Development of ZnO thin films and nanowires by Pulsed-Liquid Injection Metal-Organic Chemical Vapor Deposition for piezoelectric applications

Quang Chieu Bui

▶ **To cite this version:**

Quang Chieu Bui. Development of ZnO thin films and nanowires by Pulsed-Liquid Injection Metal-Organic Chemical Vapor Deposition for piezoelectric applications. Micro and nanotechnologies/Microelectronics. Université Grenoble Alpes [2020-..], 2022. English. NNT : 2022GRALT052 . tel-04225746

HAL Id: tel-04225746

https://theses.hal.science/tel-04225746v1

Submitted on 3 Oct 2023

HAL is a multi-disciplinary open access archive for the deposit and dissemination of scientific research documents, whether they are published or not. The documents may come from teaching and research institutions in France or abroad, or from public or private research centers.

L'archive ouverte pluridisciplinaire **HAL**, est destinée au dépôt et à la diffusion de documents scientifiques de niveau recherche, publiés ou non, émanant des établissements d'enseignement et de recherche français ou étrangers, des laboratoires publics ou privés.

THÈSE

Pour obtenir le grade de

DOCTEUR DE L'UNIVERSITÉ GRENOBLE ALPES

École doctorale : EEATS - Electronique, Electrotechnique, Automatique, Traitement du Signal (EEATS)
Spécialité : NANO ELECTRONIQUE ET NANO TECHNOLOGIES
Unité de recherche : Institut de Microélectronique, Electromagnétisme et Photonique - Laboratoire d'hyperfréquences et de caractérisation

Développement de couches minces et de nanofils de ZnO par dépôt chimique en phase vapeur aux organométalliques et à injection liquide pulsée pour des applications piézoélectriques

Development of ZnO thin films and nanowires by pulsed-liquid injection metal-organic chemical vapor deposition for piezoelectric applications

Présentée par :

Quang Chieu BUI

Direction de thèse :

Gustavo ARDILA RODRIGUEZ	Directeur de thèse
Vincent CONSONNI	Co-directeur de thèse
Bassem SALEM	Co-directeur de thèse

Rapporteurs :

Vincent SALLET

Jesus ZUNIGA-PEREZ

Thèse soutenue publiquement le **13 juin 2022**, devant le jury composé de :

Vincent SALLET Chargé de Recherche CNRS, GEMAC, Versailles	Rapporteur
Jesús ZUNIGA-PEREZ Directeur de Recherche CNRS, CRHEA, Valbonne	Rapporteur
Noëlle GOGNEAU Directrice de Recherche CNRS, C2N, Marcoussis	Examinatrice
Daniel ALQUIER Professeur des Universités Univ. de Tours, GREMAN, Tours	Examinateur
Ahmad BSIESY Professeur des Universités UGA, LTM, Grenoble	Président
Gustavo ARDILA RODRIGUEZ Maître de Conférence UGA, IMEP-LAHC	Directeur de thèse
Vincent CONSONNI Chargé de Recherche CNRS, LMGP, Grenoble	Co-directeur de thèse
Bassem SALEM Chargé de Recherche CNRS, LTM, Grenoble	Co-directeur de thèse

Acknowledgements

And so, my time as a PhD student is coming to an end. Three years is not a long, but also not short journey, where I have chances to meet many people and do different things. This manuscript is the result from many researches, tests and fails, discussions, various emotions, and the help from many people for which I am really grateful.

First of all, I would like to express my sincere gratitude and thanks to my supervisors, Gustavo Ardila, Vincent Consonni, and Bassem Salem. You gave me the chance and guided me through this PhD with your care, your kindness and your wisdom. I enjoyed discussing with you and learnt a lot from you. I also got much knowledge from the conferences, workshops that you created opportunities for me to join and articles that you sent me, which contributed big parts to my work. Thank you a lot for all your help, your support and your advice!

I would like to thank the members of the jury: Vincent Sallet and Jesus Zuniga-Perez as reviewers, Noëlle Gogneau, Daniel Alquier, and Ahmad Bsiesy as examiners, for having accepted to evaluate this thesis as well as for the constructive exchanges during the defense.

I wish to show my sincere gratitude to Thierry Baron and Maxime Besacier, director and deputy director of LTM, Audrey Dieudonné, project manager, and other actors of the NEED for IoT project, which financed my thesis. Thank you for all your work that gave me the motivation and the opportunity for me to perform this thesis.

I would like to express my appreciation to Anne Kaminski-Cachopo and Jean-Emmanuel Broquin, directors of IMEP-LaHC, who welcomed me to their lab and helped me throughout my thesis.

I would like to express my appreciation to Carmen Jimenez and Franz Bruckert, directors of LMGP, who not only allowed me to join their lab but also helped me in conducting experiments and gave me useful insights.

I would like to show my appreciation to all the collaborators for their hard work and dedications, which greatly contributed and enriched my work. I would like to give my thanks to Hervé Roussel for his help in X-ray diffraction, to Isabelle Gelard for her help in scanning electron microscope, to Eirini Sarigiannidou for her help in transmission electron microscopy, to Odette Chaix-Pluchery for her help in Raman scattering spectroscopy, to Xavier Mescot for his help in atomic force microscopy and electrical characterizations, to Youssouf Guerfi and Sarah Boubenia for their helps in lithography process, to Corinne Perret and Guillaume Gay for their helps in atomic layer deposition, to Mohammed Zeghouane for his help in XPS measurements, and to Fabrice Donatini for his help in cathodoluminescence.

I would like to thank Serge Quessada, Matthieu Jouvert, and Mikhail Anikin for supporting my experimental works and helping me in technical problems. I also would like to thank Marielle Clot, Annie Ducher, Michele San Martin, and Josiane Viboud for assisting me in administrative procedures.

I also would like to thank all my colleagues whom I have the pleasure to meet and work with during these years. I would like to give a special thank to Thomas for teaching me how to use MOCVD system, to Eléa for her assistance in transmission electron microscopy experiment, to Adou for his help in atomic layer deposition, and to Tabassom for sharing office with me as well as interesting discussions and helping me many times. I am also thankful to Huong, Pierre, Dorina, Clément, Jose, Guislain, Huy, Valia, Julius, Carlos, Chiara, Lorenzo, Maxime, Alexandre, Laetitia, Olfa, Khanh, Adrien, Lisa, Manuel, Shruti, Adeel, and Petros for their helps and good moments during lunch times. It was great to meet you guys!

Finally, I am deeply grateful to my family, who have been supporting and encouraging me for over the years. Thank you for always believing in me and being there for me.

Résumé

Développement de couches minces et de nanofils de ZnO par Dépôt Chimique en Phase Vapeur aux Organométalliques et à Injection Liquide Pulsée pour des applications piézoélectriques

L'oxyde de zinc (ZnO) est un matériau durable très intéressant pour les applications piézoélectriques en tant que semiconducteur biocompatible et composé d'éléments abondants. Cependant, l'efficacité piézoélectrique du ZnO dépend fortement de ses propriétés morphologiques, structurales et électriques. De manière intéressante, les conditions de croissance employées durant le processus de dépôt chimique en phase vapeur aux organométalliques et à injection liquide pulsée (PLI-MOCVD) peuvent influencer largement les propriétés morphologiques, structurales, électriques et piézoélectriques du dépôt de ZnO, mais leurs corrélations n'ont pas encore été explorées. L'objectif de cette thèse est de comprendre et de contrôler les facteurs clés gouvernant la formation du ZnO par PLI-MOCVD et améliorant ses performances piézoélectriques. La température de croissance, les débits des réactifs et la nature du substrat durant le processus de PLI-MOCVD sont optimisés afin d'étudier leurs effets sur la croissance de couches minces et de nanofils de ZnO ainsi que sur leurs propriétés.

En augmentant la température de la croissance de 400 à 750°C tout en fixant tous les autres paramètres de croissance, la morphologie du ZnO déposé sur des substrats de Si passe de couches minces à nanofils. Cette transition de morphologie s'accompagne d'une amélioration de l'orientation suivant l'axe *c*, du coefficient piézoélectrique et de l'uniformité de la polarité du Zn. Le post-recuit à haute température sous atmosphère d'O_2 effectué sur les couches minces de ZnO conduit également à une augmentation de l'orientation suivant l'axe *c*, du coefficient piézoélectrique et de l'uniformité de la polarité Zn. La variation du débit à 500 °C permet d'obtenir des couches minces avec des morphologies et des distributions de polarité différentes. Sur ces couches minces, la différence de propriétés et d'efficacité piézoélectrique entre les domaines de polarités Zn et O est montrée. Au contraire, la variation du débit à 700 °C mène à la formation de nanofils de longueur et de diamètre différents. Tous les nanofils présentent la polarité Zn. La corrélation entre l'efficacité piézoélectrique et la géométrie des nanofils est également présentée. En outre, l'intégration de la couche d'AZO en tant qu'électrode transparente inférieure conduit à une augmentation supplémentaire de l'efficacité piézoélectrique des nanofils de ZnO tout en ouvrant certaines perspectives orientées vers la fabrication de dispositifs piézoélectriques insensibles à l'éclairement visible et contenant seulement des matériaux durables. Ces résultats démontrent la flexibilité du système de PLI-MOCVD pour la croissance de ZnO avec différentes morphologies et différentes propriétés pour les dispositifs piézoélectriques.

Mots clés: ZnO, MOCVD, piezoelectrique, nanostructure, polarité

Abstract

Development of ZnO thin films and nanowires by Pulsed-Liquid Injection Metal-Organic Chemical Vapor Deposition for piezoelectric applications

Zinc Oxide (ZnO) is a very interesting sustainable material for piezoelectric applications as a biocompatible semiconductor composed of abundant elements. However, the piezoelectric efficiency of ZnO strongly depends on its morphological, structural and electrical properties. Interestingly, the growth conditions used during the pulsed-liquid injection metal–organic chemical vapor deposition (PLI-MOCVD) process can largely tune the morphological, structural, electrical and piezoelectric properties of ZnO deposits, but their correlations have not been explored so far. The objective of this thesis is to understand and control the key factors driving the ZnO formation by PLI-MOCVD and enhancing its piezoelectric performance. The growth temperature, reactant flow rates, and the nature of the substrate during the PLI-MOCVD process are optimized to study their effects on the growth of ZnO thin films and nanowires as well as on their properties.

By increasing the growth temperature from 400 to 750°C while fixing all other growth parameters, the morphology of ZnO deposited on Si substrates is changed from thin films to nanowires. This morphology transition is accompanied with the improvement of the *c*-axis orientation, piezoelectric coefficient and Zn-polar uniformity. The post-annealing at high temperature under O_2 atmosphere performed on ZnO thin films also leads to higher *c*-axis orientation, piezoelectric coefficient and Zn-polar uniformity. The flow rate variation at 500 °C results in the formation of thin films with different morphologies and polarity distribution. On these thin films, the differences in properties and piezoelectric efficiency between Zn- and O-polarity domains are revealed. In contrast, the flow rate variation at 700 °C results in the formation of nanowires with different lengths and diameters. All nanowires exhibit the Zn-polarity. The correlation of the piezoelectric efficiency and the nanowire geometry is also presented. In addition, the integration of the AZO layer as a bottom transparent electrode leads to further increasing the piezoelectric efficiency of ZnO nanowires while opening some perspectives towards the fabrication of visible blind piezoelectric devices containing only sustainable materials. These results eventually demonstrate the great flexibility of the PLI-MOCVD system to grow ZnO with different morphologies and properties for piezoelectric devices.

Keywords: ZnO, MOCVD, piezoelectricity, nanostructure, polarity

Table of Contents

List of acronyms

AFM	*Atomic Force Microscopy*
ALD	*Atomic Layer Deposition*
AZO	*Aluminum-Doped Zinc Oxide, ZnO: Al*
BSF	*Basal-plane Stacking Fault*
CEA	*Commissariat à l'Énergie Atomique et aux Énergies Alternatives*
CL	*Cathodoluminescence*
DEZn	*Diethylzinc, $(C_2H_5)_2Zn$*
DFT	*Density Functional Theory*
FESEM	*Field Emission Scanning Electron Microscopy*
HRTEM	*High-Resolution Transmission Electron Microscopy*
ICDD	*International Centre for Diffraction Data*
IOT	*Internet of Things*
ITO	*Indium Tin Oxide, In_2O_3: Sn*
IMEP-LAHC	*L'Institut de Microélectronique Electromagnétisme et Photonique et le LAboratoire d'Hyperfréquences et de Caractérisation*
LMGP	*Laboratoire des Matériaux et du Génie Physique*
LTM	*Laboratoire des Technologies de la Microélectronique*
NBE	*Near Band Edge*
NEED	*Nanoelectronique Durable*
NW	*Nanowire*
PFM	*Piezoresponse force microscopy*
PLI-MOCVD	*Pulsed-Liquid Injection Metal-Organic Chemical Vapour Deposition*
PMMA	*Poly(methyl methacrylate), $(C_5O_2H_8)_n$*
PTA	*Plateforme Technologique Avancée*
PZT	*Lead Zirconate Titanate, $PbZr_xTi_{1-x}O_3$ $(0 \leq x \leq 1)$*
SAED	*Selected Area Diffraction*
TES	*Two-Electron Satellites*
XRD	*X-Ray Diffraction*

Introduction

Nowadays, the Internet of Things (IoT) has become one important tool in our daily lives. Many physical objects such as sensors, actuators and everyday electronic devices (smartphones, computers, monitors in cars, etc.) are connected to the internet, allowing automatic data collection, processing, transmission and seamless communications between objects and people. The development of new technologies and IoT devices requires the usage of new materials including rare or toxic elements (Gallium (Ga), Indium (In), Lead (Pb), etc.). The continuous consumption of these critical elements can lead to a supply risk as well as other environmental and economic issues in the near future. Thus, it is necessary to find alternative ways to reduce or substitute the usage of critical elements for the IoT applications.

In this context, the NanoElectroniquE Durable (NEED) for IoT project is proposed to address this critical issue. This project aims to develop methodologies and technologies for the sustainable development of micro-nano-electronic devices. The objectives are to identify the supply chain risks of the IoT emerging devices, reduce or replace the consumption of critical elements by more abundant materials or by using more efficient designs, and integrate new technologies and materials to the production lines and devices. Concerning material technology, the challenge is to find alternative non-critical materials which also have the same function and high efficiency as the replaced one. These materials also need to be compatible for large scale industrial production. The application fields include sensors, memories, optoelectronics, spintronics, and piezoelectrics. My thesis is a part of this project, which takes part in developing a sustainable material for the piezoelectric applications.

The piezoelectric materials are present in many kinds of devices. It is used for pressure sensors, actuators, or components in surface acoustic wave (SAW) devices that are used for the accurate measurement tools and automatic systems in research and industrial production. They are used as ultrasonic transducers for navigation or in medical treatment. In daily life, they can be found in microphones, earphones, frequency filters in mobile phones, alarms, inkjet printers, ignite lighters, etc. They also have potential to be a power source for mobile devices thanks to the ability to harvest mechanical energy from the surrounding environment and convert it to electricity. Thus, the requirement of piezoelectric materials will undoubtedly keep growing in the future. One of the most common materials used for piezoelectric application is Lead Zirconate Titanate (PZT) due to its outstanding piezoelectric performance. However, Lead (Pb) element contained in this material is extremely toxic for the environment and humans. The Lead Oxide (PbO) and Pb in PZT products can be volatile and released to the environment during its life-cycle, from which Pb can enter the human body and cause severe harms. Thus, it is necessary to find another piezoelectric material that can replace PZT for the sustainable development of advanced technologies.

On the other hand, Zinc Oxide (ZnO) is a potential candidate to replace this piezoelectric material. This semiconductor compound has advantages including being an abundant, inexpensive, and biocompatible material that also possesses piezoelectric properties thanks to its Wurtzite structure. In fact, this material is not new. It is a multifunctional material that has been produced and

presented in many applications including rubbers, cosmetic products, antibacterial treatments, etc. Its properties have also been studied and used in electronic and optoelectronic applications. The study of ZnO piezoelectric properties is still quite new and have recently become attractive as a solution for sustainable development. Compared to PZT, the piezoelectric coefficient of ZnO is still quite low, but it can be improved. The main challenge of ZnO for being used in piezoelectric devices is its high residual n-type doping. Regardless of the fabrication methods, the ZnO structure contains a large amount of free electrons. When the ZnO is polarized, these free electrons can move to the positive pole, screening the piezoelectric potential and reducing the piezoelectric efficiency. Therefore, it is necessary to remove or compensate these free electrons in order to increase the piezoelectric efficiency of ZnO. The other challenges, which are less mentioned but also essential for piezoelectric performance, are the requirement of good orientation and uniform polarity. The randomness of orientation and polar domains can lead to the cancellation of piezoelectric signals between domains, resulting in the decrease or even disappearance of piezoelectric potential. Those properties of ZnO are strongly influenced by its fabrication process. Thus, its piezoelectric performance can be significantly enhanced by tailoring its formation using suitable fabrication conditions.

Among the different fabrication techniques, the pulsed-liquid injection metal-organic chemical vapour deposition (PLI-MOCVD) is selected to grow ZnO structures. This technique can grow ZnO fast, in large areas, does not require ultra-high vacuum while still achieving high structural quality, and hence, it is compatible with industrial scale production. It is also a complex process providing many controllable parameters such as the growth temperature, flow rates, pressure, dopants, and substrates, allowing to largely modify ZnO properties to be suitable for different applications. Many investigations about the effect of MOCVD parameters on ZnO growth have been performed, but most of the work focused on the ZnO structural, optical and electrical properties. Meanwhile, there was missing information about piezoelectric properties, in particular, the piezoelectric coefficient and polarity. According to the literature, the piezoelectric properties have strong correlations with other properties, suggesting that the piezoelectric properties can also be largely changed when the growth conditions are varied. In other words, it is possible to enhance the ZnO piezoelectric coefficient by adjusting the growth parameters.

In the framework of NEED project, this thesis aims to develop a piezoelectric device using only eco-friendly materials while still ensuring its performance to be comparable with existing PZT devices and its ability to integrate into the industrial production. For that, the sustainable ZnO material is chosen for the piezoelectric component. The PLI-MOCVD technique is selected for the ZnO growth as it not only has potential to improve the ZnO piezoelectric properties but also is suitable for the scale up production in the industry. The compatible material for the device electrode will be also carefully selected while taking into account the criticality of the raw materials. My work is mainly shared in three laboratories: Laboratoire des Materials and Engineering Physics (LMGP), L'Institut de Microélectronique Electromagnétisme et Photonique et le LAboratoire d'Hyperfréquences et de Caractérisation (IMEP-LAHC), and Laboratoire des Technologies de la Microélectronique (LTM). This work is also done in collaborations with Institut Néel and Plateforme Technologique Avancée (PTA).

Since understanding and controlling the PLI-MOCVD growth conditions is a key point to enhance ZnO piezoelectric performance, the main objective of my thesis is to study the influence of these growth conditions on ZnO properties. Different PLI-MOCVD parameters are systematically varied and investigated, which are the temperature, the precursor flow rates, and the substrates. The ZnO structural properties are analyzed by field-emission scanning electron microscopy (FE-SEM), X-ray diffraction (XRD), Raman scattering spectroscopy, transmission electron microscopy (TEM). The optical characterizations are performed by using cathodoluminescence (CL) and Ultraviolet–Visible–Near Infrared (UV–Vis-NIR) spectrophotometry. The resistivity, charge density and mobility are measured by using transmission line measurement (TLM) method and Hall-effect measurement. Finally, the piezoelectric properties are characterized by piezoresponse force microscopy (PFM). The PFM is a powerfull tool with the ability to mapping the topography and the piezoelectric responses simultaneously. By carefully analyzing the evolution of the ZnO piezoelectric properties (i.e. piezoelectric coefficient and polarity) with the fabrication conditions as well as its correlations with other structural, electrical properties, the method to improve the ZnO piezoelectric efficiency can be realized. The content of this thesis report is divided into 5 chapters:

Chapter 1 describes the piezoelectric phenomenon, definitions, and its application. The PZT material and its problems for sustainable development are introduced. Then, other lead-free piezoelectric materials with their advantages, drawbacks, and the motivations of choosing ZnO for piezoelectric applications are also discussed. After that, the ZnO properties and the state-of-the-art of ZnO piezoelectric devices are presented. From that, its challenges for piezoelectric applications are discussed. Finally, an overview of ZnO growth techniques and the reason to choose PLI-MOCVD for the ZnO growth are presented.

Chapter 2 describes the PLI-MOCVD techniques used to grow ZnO thin films and nanowires (NWs). The effects of growth factors on ZnO properties are reviewed, which implies the possibility of enhancing the ZnO piezoelectric efficiency. The general setup of PLI-MOCVD parameters for ZnO growths is also described here. Then, PFM technique used for analyzing the ZnO piezoelectric properties is introduced. The principle, details of experimental setup, and steps of calibrations in order to have reliable results are described. In particular, the interference of the electrostatic effect and other difficulties (background signals, tip dragging) during the PFM measurement as well as the methods to overcome these problems during the PFM measurement are presented. The information of other structural, optical, electrical characterizations used in this thesis and the methodology for analyzing ZnO properties are also given in detail.

Chapter 3 presents and discusses the first experimental result of this thesis, which is the investigation on the growth temperature effect on ZnO properties. The morphologies, structural, electrical and piezoelectric properties of ZnO thin films and NWs grown at different temperatures ranging from 400 – 750 °C are shown. The growth mechanism of ZnO NWs on Si substrate is described. The direct comparisons of properties between the thin film and NWs grown by the same PLI-MOCVD are performed. Their difference in piezoelectric properties namely the piezoelectric coefficient and polarity are also revealed. The effect of post-annealing on the ZnO piezoelectric

properties is also shown in this chapter. The change of piezoelectric coefficient and polarity along with the thin film crystallization is revealed.

Chapter 4 presents the study on the precursor flow rate effect on ZnO properties based on the results obtained in the previous chapter. The first part demonstrates the ability to reverse the polarity on the ZnO thin films by adjusting the flow rate conditions. The difference between two polarities of the ZnO structure, the mechanism and the correlation with other properties are discussed in detail. In the second part, the influence of flow rate conditions on the ZnO nanowire growth and their piezoelectric performance is discussed. The correlation of nanowire geometry with the piezoelectric coefficient is also presented.

Chapter 5 shows the effect of using aluminum-doped ZnO (Al-doped ZnO, AZO) grown by the atomic layer deposition (ALD) process as a bottom electrode on the piezoelectric performance of ZnO NWs. The morphology, structural, optical and electrical properties of AZO layers with different Al concentrations are demonstrated. Then, the impacts of these AZO layers on the following ZnO nanowire growth by PLI-MOCVD process are shown. The piezoelectric performances of these ZnO NWs/AZO layer structure are presented and discussed.

Chapter 1
Piezoelectricity, the sustainable development and challenges

This first Chapter introduces piezoelectricity, its applications and current challenges concerning sustainable development, which gives motivation for developing ZnO-based piezoelectric devices. First, the principle of the piezoelectric phenomenon is described along with the introduction of piezoelectric coefficients, which is one of the most important properties to evaluate the piezoelectric performance of the material. An overview of the most common piezoelectric material - lead zirconate titanate (PZT), its problematic for sustainability and other lead-free materials are presented. In this context, the remarkable advantages of ZnO for piezoelectric applications compared to PZT are shown. Then, the ZnO structure, its piezoelectric properties, and the state-of-the-art of ZnO-based piezoelectric devices are presented, introducing the challenges of ZnO when being used as a piezoelectric material. A special emphasis is placed on the needs for a good structural orientation, a polarity uniformity, and a low free charge carrier density to significantly enhance the ZnO piezoelectric efficiency, all of them being strongly affected by the fabrication process. Finally, different techniques for ZnO growth along with their advantages and drawbacks are reviewed.

1.1 Piezoelectricity

Piezoelectricity is a physical phenomenon produced in certain materials, in which an electric polarization is generated under a mechanical deformation. Conversely, those materials can be deformed mechanically under an electric polarization. These two phenomena are known as “direct” and “inverse” piezoelectric effects, respectively.

The direct piezoelectric effect was discovered in 1880 by Pierre and Jacques Curie using tourmaline, quartz, topaz, cane sugar, and Rochelle salt.[1] In 1881, Gabriel Lippmann predicted that there also exists the inverse piezoelectric effect,[2] which was later confirmed by Pierre and Jacques Curies during the same year.[3] In the following decades, the piezoelectric phenomenon was mostly investigated in research laboratory. Until 1917, the first practical application of piezoelectricity, which was the sonar device, was introduced by Paul Langevin and his coworkers.[4] The device employed the inverse piezoelectric effect of the quartz crystal to convert electricity into ultrasonic sound. By sending the sound wave under the water and measuring the time interval from the emitting until receiving of the echo sound reflected from an object, the distance to that object was calculated. Since the success of the sonar device, the piezoelectric phenomenon has received a great attention, leading to the intense development of piezoelectric devices. Nowadays, piezoelectric materials are available in many applications in different fields of research and industrial production. It can also be seen in applications of daily life such as inkjet printers, ignite lighters, alarms, and mobile phones.

1.1.1 Principle

Basically, the origin of piezoelectricity in a material is due to the asymmetrical distribution of charges induced by the partially ionic bond inside its crystal structure. This means the piezoelectric effect only occurs in certain materials formed by two or more types of elements. In those materials, a mechanical force causes the deformation of the crystal structure, which makes the lattice sites as well as their charges be redistributed, as shown in **Figure 1.1**. Not all charge redistributions can generate the electric polarization.

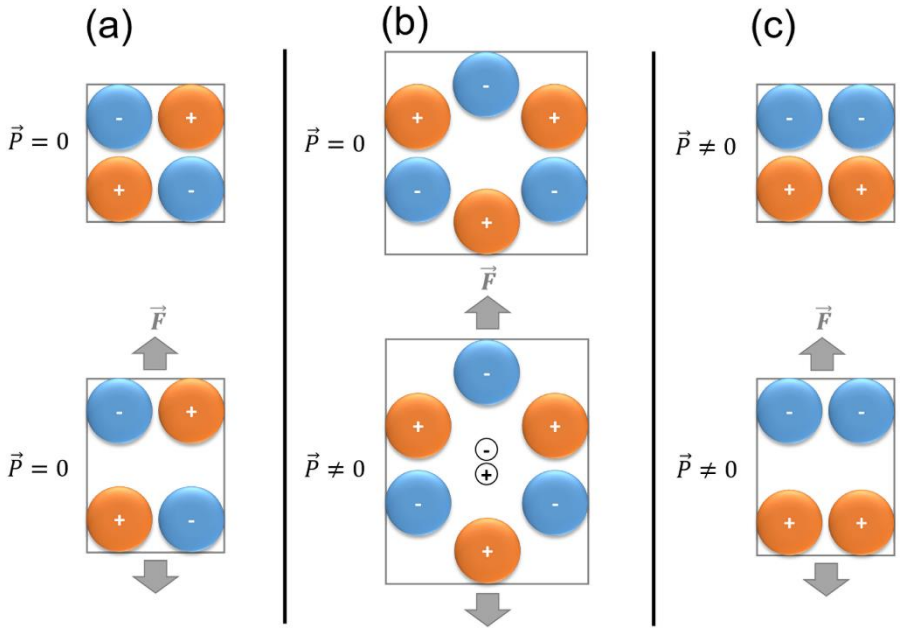

Figure 1.1: Schematic representing the effect of a mechanical force $\vec{F}$ on the electric dipole moment $\vec{P}$ in the unit cell of (a) centrosymmetric crystal, (b) non-centrosymmetric crystal, and (c) non-centrosymmetric polar crystal.

In a centrosymmetric crystal structure (**Figure 1.1a**), the lattice deformation caused by the mechanical force does not result in any net charge within the unit cell. Thus, the piezoelectric effect does not occur in centrosymmetric crystal. In a non-centrosymmetric crystal structure (**Figure 1.1b** and **c**), the lattice deformation leads to a shift of the positive and negative charges towards opposite directions, inducing the creation of an electric dipole moment within the unit cell as well as the generation of a voltage over the material.

Among the 32 existing crystal classes, 21 crystal classes are non-centrosymmetric, but only 20 crystal classes exhibit the piezoelectric effect.[5] The remaining crystal class is the cubic class with the *432* point group, where the piezoelectric polarization developed along the <111> polar axes cancel each other due to its high symmetry. Among the 20 classes with piezoelectric polarization, 10 of them do not exhibit a spontaneous polarization in their resting state (**Figure 1.1b**). In these non-polar piezoelectric crystals, the piezoelectric polarization only appears under mechanical stress, when the positive and negative charges from the constituting ions are separated into two opposite directions. The other 10 classes are polar piezoelectric crystals, which exhibit a spontaneous polarization even in their resting state due to the existence of an electric dipole moment within their

unit cell (**Figure 1.1c**). The materials belonging to those 10 crystal classes have the ability to generate a voltage when their temperature is changed, which is known as the pyroelectric phenomenon. Moreover, certain pyroelectric materials can also be ferroelectric, which is the ability to reverse their spontaneous polarization by applying an external electric field.[5] For example, the ferroelectric ceramic such as PZT usually contains many randomly oriented polar domains, in which their electric dipole moments neutralize each other. Thus, the poling process can be performed, in which an external electric field is applied across PZT. Thanks to its ferroelectric property, the polar domain states in PZT are realigned along the electric field direction (**Figure 1.2**). After removing the electric field, the ferroelectric ceramic with residual polarization can be used for piezoelectric applications.

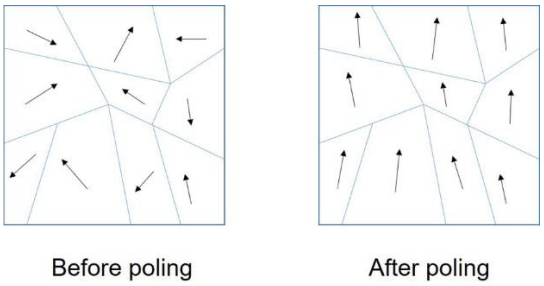

Figure 1.2: Schematic of domain states in ferroelectric material before and after poling process.

1.1.1.1 Macroscopic description of the piezoelectric phenomenon

The electrical polarization induced by the piezoelectric phenomenon leads to the change of electrical charge distribution along the polar axis. At the macro-scale, this change results in the formation of the potential difference as well as the voltage between two opposite sides of the material. By connecting the piezoelectric material to an external circuit, the potential difference can generate an electric current to be used for many applications. The mechanism of an electric current generation from a piezoelectric material when it is connected to an external circuit can be described as shown in **Figure 1.3**.

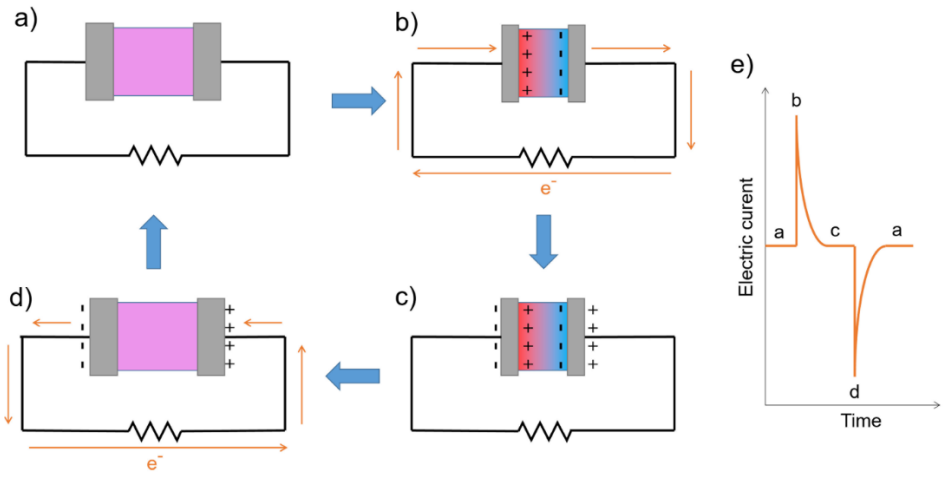

Figure 1.3: Schematic describing the generation of an external electrical current using the piezoelectric phenomenon.(a) Resting state with no current, (b) current is generated when a force is applied, (c) neutralized state with no current, (d) reverse current is generated when a force is released, (e) current signal vs time graph.

At the beginning, the piezoelectric material is not deformed, the electric charge is in equilibrium state and no current is generated (**Figure 1.3a**). When a mechanical force is applied to the material, it is deformed and a potential difference is formed between two opposite sides of the piezoelectric material (**Figure 1.3b**). This causes the movement of free electric charge along the external circuit from one side to the opposite side in order to compensate for the potential difference, hence a current is generated. As time passes by, the concentrations of the free electric charge at the two sides of the external circuit are changed and create an opposite potential with the potential inside the piezoelectric material. Thus, the new balance state is formed and no more current flows inside the external circuit (**Figure 1.3c**). When the applied mechanical force is released, the piezoelectric material goes back to its initial state and the potential inside it disappears. The potential difference of the external circuit is now a driving force that pushes the free electric charges, generating a current with opposite direction until this potential is compensated and disappears (**Figure 1.3d**). **Figure 1.3e** illustrates the current in the external circuit as a function of time, showing that an alternating-current signal is generated at the moment the mechanical force is applied and released on the piezoelectric material. By alternatively applying and releasing the force, an alternating current is generated. In inverse piezoelectric phenomenon, an alternating voltage is applied on the piezoelectric material, leading to the deformation of the material with respect to the applied voltage amplitude and sign. These direct and inverse piezoelectric mechanisms are employed in sensors and actuators for many applications.

1.1.1.2 Piezoelectric coefficients

Mathematically, the piezoelectricity phenomenon can be described as a linear interaction between the linear elastic strain and the electric displacement in the material.[6,7] The linear elastic strain can be expressed by Hooke's law equation:

$$S = sT \tag{1.1}$$

and the electric displacement can be expressed by the equation:

$$D = \varepsilon E \tag{1.2}$$

where S is the second-rank tensor of strain, s is the fourth-rank tensor of compliance (m^2/N), T is the second-rank tensor of stress (N/m^2), D is the first-rank tensor of electric displacement (C/m^2), ε is the second-rank tensor of permittivity ($C^2.N^{-1}.m^{-2}$), and E is the first-rank tensor of electric field (N/C). The coupling between the elastic strain and the electric displacement can be expressed as follows:

$$S = s^E T + d^t E \tag{1.3}$$

$$D = dT + \varepsilon^T E \tag{1.4}$$

where d and d^t are the third-rank tensors of constants presenting the direct and inverse piezoelectric coefficient of the material, respectively. The superscript t indicates the transpose of the tensor. The superscripts E and T signify that the electric field E and the stress T are constant, respectively. Due to the symmetry of the stress and strain tensors ($T_{ij} = T_{ji}$, $S_{ij} = S_{ji}$), the Voigt notation can be used to reduce the rank of the tensor.[6,7] Thus, the piezoelectric constant $d_{kij} = d_{kji}$ can be expressed by d_{km}. The subscript k = 1, 2 and 3 indicates the direction of the electric field E in the Cartesian coordinate system. The subscript m = 1, 2 and 3 represents the direction of stresses or strains along the three axes of the Cartesian coordinate system, while the subscript m = 4, 5, and 6 signifies the shear stresses or strains T_{23}, T_{13}, and T_{12}, respectively. The constant d is defined as the piezoelectric charge

or strain coefficient of the material (C/N or m/V). Similarly, the equations (1.3) and (1.4) can also be presented in different ways,[6,7] such as:

$$S = s^D T + g^t D \quad (1.5)$$

$$E = -gT + (\varepsilon^{-1})^T D \quad (1.6)$$

or:

$$T = (s^{-1})^E S - e^t E \quad (1.7)$$

$$D = eS + \varepsilon^S E \quad (1.8)$$

or:

$$T = (s^{-1})^D S + h^t D \quad (1.9)$$

$$E = -hS + (\varepsilon^{-1})^S D \quad (1.10)$$

where g is defined as the piezoelectric voltage coefficient (m^2/C or Vm/N), e is defined as the piezoelectric stress coefficient (C/m^2 or N/Vm), h is defined as the piezoelectric stiffness coefficient (N/C or V/m). The superscripts D and S denote that the electric displacement D and the strain S are constant. These piezoelectric coefficients are commonly used to evaluate the potential performance of piezoelectric materials.

Besides, another important parameter that is also used to characterize the piezoelectric properties of materials is the electromechanical coupling coefficient. The electromechanical coupling coefficient k is defined as the ratio of the mechanical energy that is converted from the electrical energy or vice versa:[6,7]

$$k = \sqrt{\frac{converted\ mechanical\ energy}{applied\ electrical\ energy}} \quad or \quad k = \sqrt{\frac{converted\ electrical\ energy}{applied\ mechanical\ energy}} \quad (1.11)$$

This parameter can be related to the piezoelectric coefficients in the equation as follows:

$$k_{ij} = \frac{e_{ij}}{\sqrt{\varepsilon_{ii}^S (s^{-1})_{jj}^D}} \quad or \quad k_{ij} = \frac{d_{ij}}{\sqrt{\varepsilon_{ii}^T s_{jj}^E}} \quad (1.12)$$

It can be seen in equation (1.12) that high efficient piezoelectric device requires a material with high piezoelectric constants, as well as low elastic and permittivity constants.

1.1.2 Piezoelectric material

Since the discovery of piezoelectricity, a large number of piezoelectric materials have been found. With the success in the sonar device, quartz got more attention for its piezoelectric property. However, its piezoelectric coefficient (d_{33} = 2.3 pC/N) is modest to be used for many practical applications.[8] In 1942 – 1947, a breakthrough in piezoelectric material was made when the ferroelectric property of ceramic barium titanate ($BaTiO_3$ - BT) was discovered by different research groups in the United States, Russia, and Japan.[9] Thanks to the ferroelectric property, the polar domains of $BaTiO_3$ are able to be realigned by applying an external electric field despite the random orientation of ceramic. The piezoelectric constant d_{33} of $BaTiO_3$ after the poling process shows a value of 190 pC/N, which is significantly higher compared to quartz.[10,11] In addition, the ceramic is also easier and less expensive to fabricate than the single crystal. This has made the ferroelectric ceramic become an attractive material for piezoelectric applications. The main drawback of $BaTiO_3$ is indicated by its low Curie temperature (T_c = 120 °C), above which the ceramic loses its ferroelectric property.[10,12] This limits $BaTiO_3$ to be used in high temperature applications. A new ferroelectric ceramic, which is PZT, was later discovered in the 1950s. This material surpasses $BaTiO_3$ not only in

superior piezoelectric constant up to 600 pC/N, but also with an higher Curie temperature.[12] The PZT with its superior piezoelectric properties compared to $BaTiO_3$ has soon led to its domination in the piezo-ceramic market. Nowadays, PZT is the most widely used piezoelectric material thanks to its outstanding piezoelectric performance.

1.1.2.1 Lead zirconate titanate

Structure

Lead zirconate titanate (PZT) is a solid solution of lead zirconate ($PbZrO_3$) and lead titanate ($PbTiO_3$). Its chemical formula is $PbZr_xTi_{1-x}O_3$ ($0 \leq x \leq 1$). The crystal structure of PZT as well as its properties can be changed depending on its temperature and Zr/Ti ratio.[12] PZT has a cubic structure when its temperature is above Curie-temperature, which is varied from 230 to 500 °C with the Zr/Ti ratio. In the cubic structure, there are 8 Pb atoms located at the corners, 6 O atoms are at the surface centers, and the Zr or Ti atom is at the body center (**Figure 1.4a**). Since this cubic structure is symmetric, PZT does not show piezoelectric property in this phase. Below Curie-Temperature, PZT has a rhombohedral structure at high Zr/Ti ratio, or a tetragonal structure at low Zr/Ti ratio. The Zr or Ti atom also shifts off the center, resulting in the occurrence of a spontaneous polarization along the <100> or <111> directions (**Figure 1.4b**). When an electric field is applied on PZT, this Zr or Ti atom can move along the electric field direction, leading to a change in the polar direction.

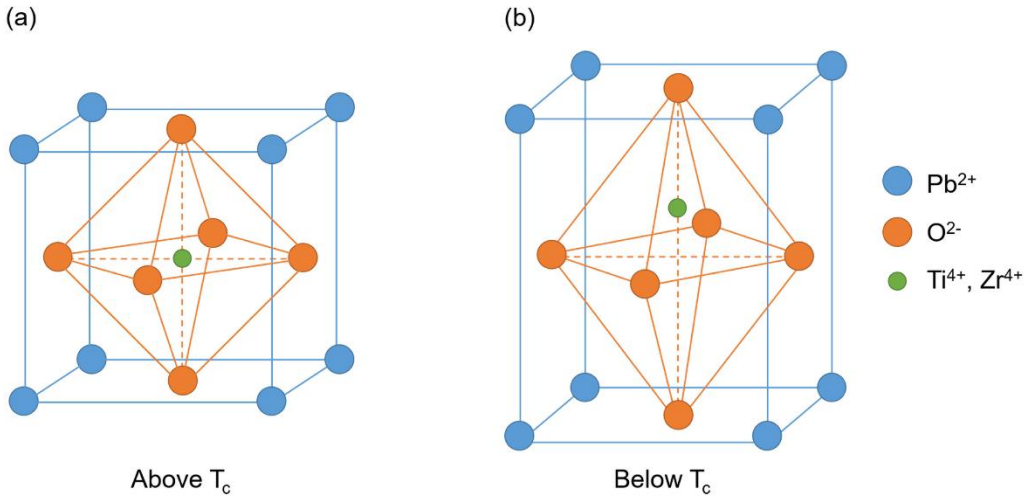

Figure 1.4: Crystal structure of PZT (a) above and (b) below its Curie temperature.

The rhombohedral structure has 8 equivalent polar <111> directions while the tetragonal structure has 6 equivalent polar <100> directions. Both rhombohedral and tetragonal phases can coexist in the PZT when the Zr/Ti is around 52/48, which is known as the morphotropic phase boundary. At this boundary, all 14 possible polar domains from both phases of PZT can be poled, allowing it to maximize the piezoelectric coefficient.[12]

Problem of lead (Pb)

One of the main problems of PZT originate from the fact it contains up to 60 weight % of lead (Pb), which is a well-known highly toxic element.[13] The component lead oxide (PbO) can be volatile at

high temperature and be released into the atmosphere during the life-cycle of PZT including its production, leakage through machining or in usage, and waste disposal.[14] This emission into the environment causes the accumulation of lead (Pb) in water, soil and organism and poisons entire food chains. From those statements, Pb can enter the human body and accumulate overtime in organs such as the brain, kidneys, liver and bones. This causes many dangerous harm such as kidney damage, brain damage, disruption of nervous systems and even death.[15]

The total identified world Pb resources is estimated to be more than 2 billion tons, according to United States Geological Survey (USGS 2020).[16] However, the new Pb production from mining has been limited and decreased in recent years due to the extreme toxicity of this element and of its production process. Currently, the raw Pb resource is usually found and extracted together with other ore such as zinc, silver and copper. Its main mineral is Galena (PbS). There are also other mineral forms such as cerussite ($PbCO_3$) and sulfuric acid galena ($PbSO_4$). The world production of new Pb from mines is 4.5 million tons in 2019.[16] Most of new Pb is mined in China, where 2.1 million tons of Pb is produced, accounting for 46.7% of the global total amount, as shown in **Table 1.1**. Other Pb deposits are in Australia, Russia, Peru, Mexico, and the United States. The total quantity of identified Pb reserves in mines are estimated around 90 million tons, which can supply for 20 years.

Table 1.1: World Mine Production and Reserves of Pb.[16]

	Mine production (thousand tons)		**Reserves (thousand tons)**
	2018	**2019**	
United States	280	280	5000
Australia	432	430	36000
Bolivia	112	100	1600
China	2100	2100	18000
India	192	190	2500
Kazakhstan	86	90	2000
Mexico	240	240	5600
Peru	289	290	6300
Russia	220	220	6400
Sweden	65	60	1100
Turkey	76	70	860
Other countries	468	430	5000
World total (rounded)	4560	4500	90000

Recently, Pb from the recycling process gradually increases and become the main Pb resource in many countries.[17] Indeed, the data of International Lead and Zinc Study Group (ILZSG) shows that 4.5 million tons of Pb from mining only accounts for 37.5% of the total 12 million tons of Pb production in 2019.[18] The rest of 62.5% comes from the secondary Pb production.[18] The percentage of recycled Pb production is even higher in developed countries. For example, it reaches 80% in the United States, and 90% in Europe.[17] The used Pb-based batteries are the main resource of secondary Pb, which comprise more than 85% the total amount of recycled Pb. It is also recycled from other waste products such as lead-pipes, lead-sheet, and glass of liquid crystal display.

There was no restriction of using Pb in the past. However, the threats of Pb-based products have been realized and its harmful effects to the environment and human health are more and more concerned due to its high toxicity. Different regulations have been made by governments in many countries in order to minimize the dangerous effects of Pb. For instance, the Restriction of Hazardous Substances Directive (RoHS) was published in 2011 in the Official Journal of the European Union, which limits the maximum concentration values by weight for Pb to 0.1 %. The limit or ban on the use of Pb element in products have pushed producers to find alternative materials to replace Pb. The Pb production also tends to decrease in recent years, in which the majority comes from recycling process as mentioned above. In particular, this has encouraged researchers in public institutes to develop lead-free piezoelectric materials that are more biocompatible and environment friendly.

1.1.2.2 Lead-free piezoelectric materials

The incentive of finding a new material to replace PZT has resulted in the development of various new lead-free piezoelectric materials. They can be categorized into different types such as ceramics, polymers, and semiconductors.

Ceramic materials

The first piezoelectric ceramic that has been discovered is $BaTiO_3$, (BT) which is also a lead-free material. However, its lower Curie temperature has limited its applications at high temperatures. To improve the piezoelectric coefficient and Curie temperature, many methods have been introduced including the use of different fabrication processes or the development of novel structures. For example, T. Karaki et al. fabricated high-density BT piezoelectric ceramics using hydrothermally synthesized nano-particles of 100 nm in size and two-step sintering process.[19] The piezoelectric coefficient of 460 pC/N was achieved. By using templated grain growth method, S. Wada et al. has obtained a [110]-oriented BT ceramics with a d_{33} of 788 pC/N.[20] A novel sandwich-structure of BT was designed by Roscow et al.[21], which includes two dense outer BT layers and a porous BT layer in middle. Their results have shown that the optimal piezoelectric coefficient d_{33} of 124.5 pC/N is achieved with the porosity at 60 vol% and a relative thickness of 0.73 of the interlayer.

Besides BT, there are other lead-free perovskite piezo-ceramics which have also been receiving a lot of attention such as bismuth potassium titanate ($(Bi_{0.5}K_{0.5})TiO_3$ – BKT), bismuth sodium titanate ($(Bi_{0.5}Na_{0.5})TiO_3$ – BNT), and potassium niobate ($KNbO_3$). Recently, the binary solid solutions combining these ceramics are developed to further improve their piezoelectric properties. For instant, the binary system of $BaTiO_3$ – $(Bi_{0.5}K_{0.5})TiO_3$ was reported with the d_{33} of 125 pC/N, which is higher than both of its components.[10,12,22] The sodium potassium niobate solid solution $(K,Na)NbO_3$ KNN) is one of the most promising candidates for lead-free piezoelectric ceramics thanks to its high Curie temperature T_c of 420 °C and good piezoelectric coefficient d_{33} of 160 pC/N. The main drawback of KNN is the volatility of potassium oxide, causing the difficulty to maintain stoichiometry.[10,12,22]

Another type of piezo-ceramic that has drawn extensive attention is bismuth layer-structured ferroelectrics (BLSFs).[12,22] This structure was discovered by Aurivillus in 1949, composed of $(Bi_2O_2)^{2+}$ layers and perovskite layers arranged alternately along the c-axis. This type of structure has modest

piezoelectric coefficient, but notable higher Curie temperatures. For example, one of the BLSFs is $BaBi_4Ti_4O_{15}$, which has a high T_c of 395 °C, but a poor d_{33} of 12 pC/N.[23] Another BLSF is Bi_3NbTiO_9, whose T_c can reach at 900 °C, but its maximum d_{33} is only 25 pC/N. Thus, this type of material is suitable for applications at high temperature.

It is important to note that many of these lead-free piezoelectric ceramics contain critical elements such as Nb and Bi, which can be subject to supply risks due to their scarcity in the natural state. In addition, the extraction processes for some of these elements can cause significant local pollution. For instance, it has been reported that the mining and extraction of KNN can be harmful to the environment.[14] Compared to PZT, the consumption of thermal and electrical energy of KNN through its fabrication activities is higher, except in milling where it consumes approximately the same amount of energy. In general, it has been shown that the production of KNN can cause more damage to ecosystem quality, resources, and human health.[14]

Organic materials

Polymers are materials composed of many macromolecules formed by smaller repeating molecules. Despite their large size structures, polymers can directly exhibit piezoelectricity phenomenon when their molecular structures are deformed by stress, generating an electric dipole moment. The most common piezoelectric polymer is Polyvinylidene Fluoride (PVDF), whose piezoelectric coefficient d_{33} is $13 - 28$ pC/N.[22] The piezoelectric properties of its copolymers such as poly(vinylidene fluoride-hexa- fluoropropylene), or P(VDF-HFP),[24] poly(vinylidene fluoride-trifluoroethylene), P(VDF-TrFE)[25] have also been explored. Although the piezoelectric coefficient of polymers is lower compared to ceramics, they have the advantages of being highly flexible, biocompatible, biodegradable, low cost, and requiring low energy consumption. In addition, the piezoelectric composites can be formed by combination of piezoelectric ceramic and polymer matrix.[22] In this case, a polymer does not need to have the intrinsic piezoelectric property. For example, a stretchable and transparent nano-generator can be formed by integrating $BaTiO_3$ powders and fibers into PDMS matrix,[26] or introducing KNN nanorods into PVDF layer.[27]

The piezoelectric phenomenon can also be observed in some other biomaterials such as M13 bacteriophages,[28] peptide nanotubes,[22] etc. For instance, A vertically aligned M13 bacteriophage nanopillars were fabricated by Shin et al., which exhibited the piezoelectric coefficient d_{33} at 10.4 pm/V.[29] In another work, Kholkin et al. demonstrated that the self-assembled diphenylalanine peptide nanotubes has a d_{33} of 60 pm/V.[30] Overall, the piezoelectric properties of these organic materials are relatively poor compared to inorganic materials, but they possess higher flexibility, environmental friendliness and biocompatibility. They are thus promising candidates for self-powered implantable, wearable electronics, or biomedical and medical applications.

Semiconductors

The piezoelectric phenomenon is commonly found in the wide-band gap semiconductors belonging to groups III-V and II-VI such as AlN, GaN, and ZnO due to their partially ionic boding and zinc-blende or wurtzite non-centrosymmetric crystal structures.[31,32] In contrast to piezo-ceramics, these semiconductors do not exhibit any ferroelectric properties. This means that the polarization direction in these structures cannot be reversed by the poling process. Thus, they require to be

grown as single crystals or highly oriented polycrystalline films to be able to exhibit the piezoelectric effect. The random orientation of grains in polycrystalline semiconductor cannot be poled and results in a poor piezoelectric effect. For example, the piezoelectric coefficient d_{33} of single crystal of AlN was reported at the value of 5.6 pm/V, which is higher than the value of 3.4 pm/V for the polycrystalline AlN deposited by sputtering.[33] Indeed, the piezoelectric properties of semiconductors largely vary with its structural and electrical properties which strongly depend on their fabrication process.[34–37] **Table 1.2** shows theoretical piezoelectric coefficient d_{33} values of single crystal AlN, GaN and ZnO estimated by using the first-principles calculation based on the density functional theory (DFT), and experimental values measured on their different morphologies.

Table 1.2: Piezoelectric coefficient d_{33} of semiconductors.

Material	**Morphology**	**d_{33} (pm/V)**	**Method**
AlN	Single crystal	5.23	First-principles calculation[38]
AlN	Single crystal	5.6	Interferometry[39]
AlN	Thin film	5.1	Interferometry[40]
AlN	Thin film	5.8	Interferometry[41]
AlN	Thin film	3.4	PFM[33]
GaN	Single crystal	2.7	First-principles calculation[42]
GaN	Single crystal	3.7	Interferometry[39]
GaN	Thin film	3.1	Interferometry[40]
GaN	Nanowire	13	PFM[43]
ZnO	Single crystal	12.84	First-principles calculation[44]
ZnO	Single crystal	9.93	PFM[45]
ZnO	Thin film	12.4	PFM[46]
ZnO	Nanobelt	26.7	PFM[45]
ZnO	Nanorod	44.33	PFM[47]

In general, the semiconductor materials exhibit a relatively modest piezoelectric effect compared to piezo-ceramics, but they possess other advantages and distinguished properties of semiconductor which cannot be replaced by other materials.[31,32,48]

First, many researches have shown that semiconductor materials show a strong enhancement in the piezoelectric coefficient d_{33} when one of their typical sizes is reduced to nanoscale dimension. For example, the d_{33} of individual GaN nanowire measured by using piezoresponse force microscopy (PFM) method has shown a value at 13 pm/V, which is 3−6 times higher than bulk GaN.[43] M.H. Zhao et al. reported the piezoelectric coefficient of bulk ZnO measured by PFM at 9.93 pm/V. With the same measurement technique, they found a significantly large d_{33} on ZnO nanobelt at 26.7 pm/V.[45] In comparison, J. Christman et al. also demonstrated an AFM measurement which shows the magnitude of the piezoelectric effect of ZnO thin films at 12.4 pm/V.[46] The research of Ghosh et.al has presented an outstanding piezoelectric coefficient d_{33} of 44.33 pm/V for vertically aligned ZnO nanorods.[47] Although a phenomenological explanation for the modification of piezoelectric properties in the nanostructure of these semiconductors has not been clearly identified, their potential for piezoelectric applications has attracted huge attention in the last

decade. In addition, the piezoelectric properties of semiconductors can be significantly increased by adding different dopants.[34–37] By doping with scandium (Sc), U. Masato et al. shown that the d_{33} of GaN thin films reaches a value of 14 pC/N, which is 4 times higher compared to the undoped thin film.[49] In the report of Y. Yang et al., a d_{33} value of 110 pC/N is obtained using PFM on V-doped ZnO thin films.[50] Those results have shown that the piezoelectric coefficient of semiconductors, especially ZnO, can be significantly increased and may be comparable to PZT.

Second, the piezoelectric effect can be combined with other optical and electrical properties of semiconductors to create a new coupled effect, opening for various innovation applications in electronics, optoelectronics, piezoelectricity, piezotronics and piezophototronics.[31,32,48]

Third, those advantages together with the maturity in micro/nanotechnologies and fabrication of these semiconductor materials is not only convenient for enhancing their piezoelectric properties, but also favorable for their integration into miniaturized devices as well as introduction into microelectromechanical systems (MEMS).

Among semiconductors, ZnO is one of the most promising candidates as an alternative lead-free material. ZnO has the highest piezoelectric coefficient compared to AlN and GaN, as shown by both theoretical and experimental values in **Table 1.2**. Besides, Ga element is rare on earth, which can lead to supply chain shortage in the future. For instance, world resources of Ga contained in bauxite is estimated to exceed 1 million tons, but less than 10% is potentially recoverable (U.S.G.S 2020).[16]

1.2 Zinc Oxide

Zinc oxide (ZnO) is a multifunctional material with many interesting properties such as high chemical, thermal, mechanical and optical stability, UV-protection, antibacterial, antifungal, and catalytic properties, which are suitable for numerous applications.[51,52] Nowadays, there are more than 50% of ZnO used in the rubber industry, where it is added during the vulcanization process to improve the resistance of rubber against heat and UV degradation.[51–53] Other applications include agent in ceramics, anti-corrosive coating in paints, water treatment, component in cosmetics, batteries, foods, etc.[51,52]

In addition, ZnO is a semiconductor with a wide direct bandgap energy (3.37 eV) at room temperature, a high exciton binding energy (60 meV), a good optical transparency, and a high electron mobility.[35,51,52,54] These properties make it attractive for a wide range of electronic, optoelectronic applications such as light-emitting diodes, transistors, and transparent conductive oxide (TCO). Particularly, it is a potential candidate for developing lead-free piezoelectric devices as an abundant, inexpensive, and biocompatible material that possesses piezoelectric properties.[35,36,48,52]

1.2.1 Biocompatibility

Unlike lead (Pb), Zinc (Zn) is an essential element for the life of all living organisms.[55,56] It is an indispensable micronutrient that is responsible for many metabolic reactions during the growth and development of plants, animals and humans. For example, the Zn deficiency in soils causes the

reduction in crop yield and crop quality.[57] Application of Zn fertilizers help improving the wheat yields, summer maize yields. In the human body, Zn plays important roles involved in growth and cell division, fertility and the immune system.[55] The Zn deficiency can result in decreasing the sense of taste, smell, appetite, affecting skin, hair, nail and eyesight.

ZnO is generally known as a non-toxic material. There is no evidence of carcinogenicity, genotoxicity or reproduction toxicity in human caused by this compound.[51] While it does not cause skin and eye irritation, inhaling or ingesting of ZnO powder can lead to zinc fever which causes chills, fever, cough, and tightness in the chest. Thus, it is required to take proper precautions when handling ZnO.

Moreover, ZnO compound are popularly used in many cosmetic and personal care products such as sunscreen, makeup, nail products, deodorant, baby lotions, bath soaps and foot powders.[56] This is due to the fact that ZnO is not only a non-toxic, non-sensitizing and bio-safe ingredient, but also possesses UV-protective, anti-acne, antibacterial, astringent, anti-odor and anti-inflammatory properties.

1.2.2 Abundancy

Zinc is basically an abundant element. According to United States Geological Survey (USGS 2020), the identified Zn resources of the world are estimated to be about 1.9 billion tons.[16] Global refined zinc production in 2019 was 13.49 million tons, which includes both mined sources (70%) and Zn from recycled materials (30%). Most of new Zn production is mined from sulfidic ore deposits, in which zinc blende/sphalerite (ZnS) is usually mixed with the sulfides of copper, lead and iron. The largest producer of Zn was made in China with 4.3 million tons, which comprises 33.7% of the global total amount, as shown in **Table 1.3**. The total reserve of Zn in mine is reported at 250 million tons.

Table 1.3: World Mine Production and Reserves of Zn.[16]

	Mine production (thousand tons)		**Reserves (thousand tons)**
	2018	**2019**	
United States	824	780	11000
Australia	1110	1300	68000
Bolivia	480	460	4800
Canada	287	300	2200
China	4170	4300	44000
India	750	800	7500
Kazakhstan	304	290	12000
Mexico	691	690	22000
Peru	1470	1400	19000
Russia	300	300	22000
Sweden	234	230	3600
Other countries	1840	1900	34000
World total (rounded)	12500	13000	250000

Since the exploration and mine development is still ongoing, the amount of Zn reserved continues increasing as additional deposits are explored, developed, or new technology improves their feasibility. Based on the USGS data, although the Zn production increased by 80 % between 1990 and 2010, the reserve amount also increased. Consequently, the ratio between produced and reserved Zn amount remained unchanged.

The Zn production also includes the secondary or recycled sources. Zn is recycled at all stages of production and from its waste products.[58] Zn waste generated during manufacturing is collected and becomes the source for recycling process. The other disposed products such as galvanized steel and Zn alloys are also the important sources of Zn recycling. In 2010, the global recycling rate of Zn at the end of life was approximately 33%. This recycling rate is higher in developed regions such as Europe (46 %) and North America (42 %).[58] New technologies are also developing to increase the efficiency of Zn production and recycling process.[58] Recycling of Zn in industry and products help conserve the natural Zn resources.

1.2.3 ZnO structure and polarity

ZnO has three different phases including the wurtzite, zinc-blend and rock salt structures.[51,54] Among them, the hexagonal wurtzite structure is the most stable form of ZnO in normal ambient conditions. The hexagonal wurtzite structure belongs to space group *P63mc* with the lattice constants a = 3.249 Å and c = 5.206 Å (**Figure 1.5a**).[34,54] In this structure, Zn^{2+} and O^{2-} ions are distributed according to two interpenetrated hexagonal compact structures. Each Zn^{2+} cation is linked to four neighboring O^{2-} anions (and vice versa), resulting in the tetrahedral coordination.[54,59] The vector collinear to the *c*-axis starting from the Zn^{2+} cation and pointing to the O^{2-} anion in the tetrahedral environment defines by convention the [0001] direction and the Zn-polarity, while the opposite [000$\bar{1}$] direction defines the O-polarity (**Figure 1.5b**). The bonding between Zn^{2+} and O^{2-} ions is ionocovalent, in which two shared electrons are shifted toward the O^{2-} ion due to the larger electronegativity of O as compared to Zn. According to Pauling, the bond between two elements is 50% ionic and 50% covalent when their electronegativity difference is 1.7.[60] In the case of ZnO, Pauling electronegativity of Zn and O are 1.65 and 3.44, respectively, resulting in the electronegativity difference of 1.79.[60] In Philips ionicity scale, the bonding formed by Zn and O has an ionicity degree of 0.616. This partially ionic bond of Zn^{2+} and O^{2-} ions along with the non-centrosymmetric structure result in the asymmetric charge distribution in ZnO crystal structure as well as the creation of a spontaneous polarization along the *c*- axis. This makes ZnO a pyroelectric and piezoelectric material. The (0001) and (000$\bar{1}$) planes (*c*-planes) are polar with opposite charges. In contrast, the directions perpendicular to the *c*-axis have zero dipole moment, and the planes perpendicular to the *c*-planes, such as the (10$\bar{1}$0) plane (*m*-planes), (11$\bar{2}$0) planes (*a*-planes) are non-polar.[36,37]

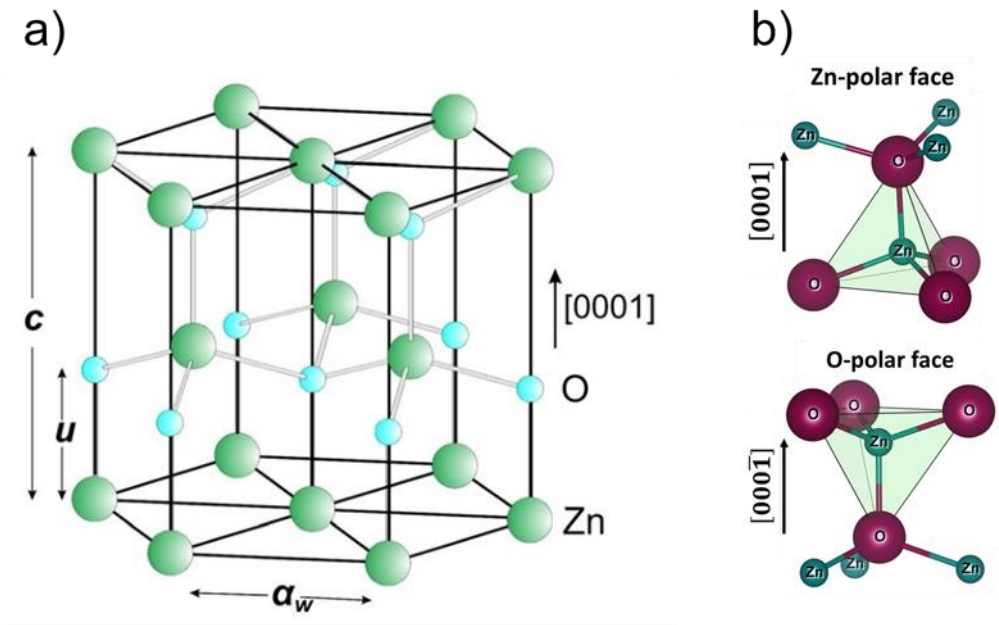

Figure 1.5: (a) Wurtzite structure of ZnO;[34] (b) Side view of the O- and Zn-polar ZnO faces with the coordination tetrahedron centered on the Zn atom.[59]

The surface energies between two polar surfaces as well as between the polar surfaces and non-polar surfaces significantly differ.[54,61] By varying different factors during the ZnO fabrication, the relative surface energy of those planes can be affected. Thus, it is possible to obtain ZnO nanostructures with various morphologies and to modify its structural, electrical as well as piezoelectric properties by controlling the fabrication process conditions during its formation.[54,61]

1.2.4 ZnO defect

A crystal defect is an interruption in the periodicity of a crystal structure. There exists bulk defects, planar defects, linear defects and point defects. ZnO structure typically contains a lot of point defects regardless of the fabrication process used.[54,62–64] Depending on the technique and conditions used, the nature and relative proportions of defects greatly vary, leading to a drastic change of the ZnO properties.

ZnO frequently exhibits n-type character with high levels of unintentional dopants. Different explanations were given to account for the origin of intrinsic n-doping in ZnO, but the subject still remains controversial. Several studies explain this phenomenon by the presence of numerous intrinsic point defects acting as donors, such as oxygen vacancy (V_O) and zinc interstitial (Zn_i) since their formation energy is low (**Figure 1.6**).[62–64] However, the most recent results of *ab initio* calculation show that the V_O defects acts as a deep donor with the energy transition far from the minimum of the conduction band. Thus, this defect is electrically inactive at room temperature. The zinc interstitial (Zn_i) is a shallow donor, but it is unstable at room temperature. The Zn vacancy (V_{ZN}) also has low formation energy but it is an acceptor, while other native defects have high formation energies (**Figure 1.6**).

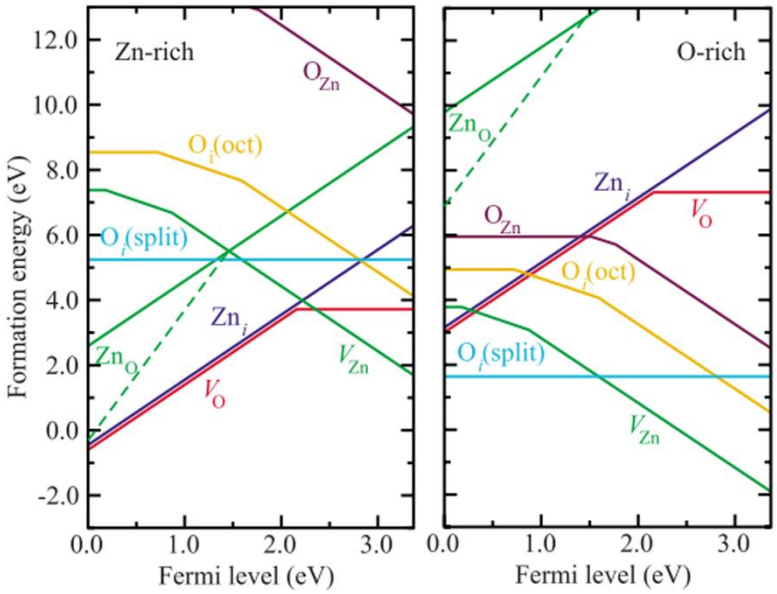

Figure 1.6: Formation energies as a function of Fermi-level position for native point defects in ZnO. The zero of Fermi level corresponds to the valence-band maximum.[62]

Other studies have proposed that the n-type character of ZnO is caused by the complexes of V_O and Zn_i with other impurities or the extrinsic defects that come from the raw material or any step of the fabrication process. Indeed, many studies have reported different types of extrinsic defects formed unintentionally during the synthesis of ZnO. For example, the formation of hydrogen-related defects is very likely since hydrogen exists in most synthetic techniques and its capacity for rapid diffusion into the crystal increases its incorporation into ZnO. Hydrogen can form shallow donor defects when it is in interstitial position between the Zn-O bond (H_i), substitutes an oxygen atom (H_O), or forms complexes with Zn vacancy (V_{Zn}-nH).[65,66] Other extrinsic defects such as Al, Ga substituting for Zn sites, or C contamination can also be the reason for the n-type character of ZnO.[62,64,67,68]

Generally, the intrinsic free electron density of ZnO typically varies between 10^{16} and 10^{19} cm^{-3} depending on the nature and amount of defects it contains.[63] Controlling the concentration of dopants inside ZnO is necessary to be able to precisely adjust its electrical properties for different applications. For this, a common strategy is to intentionally add other dopants into ZnO crystal with a controlled amount.[54] An n-type doping is achieved by substituting for Zn sites with group-III elements (Al, Ga, In) or by substituting for O sites with group-VII elements (F, Cl, Br, I). By adding more extrinsic n-type dopants, the free electron density can be significantly increased to 10^{21} cm^{-3} and a reduced resistivity down to 10^{-4} Ω.cm is obtained. For example, the high conductivity of ZnO is obtained by doping with Al, which is commonly used for transparent conductive electrodes.[69] On the contrary, p-type doping can be made by adding group IA elements (Li, Na, K), group IB elements (Cu, Ag, Au) or group VB elements (N, P, As, Sb). However, p-type doping is currently not stable and reproducible in ZnO. This problem could be due to the low solubility of p-type dopants and their compensation by abundant n-type impurities. Many p-type dopants include group-I elements (Li, Na, K), group-V elements (N, P and As) as well as copper and silver to form deep acceptors and do not produce

significant p-type conduction, while other donor defects are created significantly. Until now, p-type doping in ZnO is still a challenge that limits its applications in electronic and optoelectronic fields, which usually require the use of heterojunctions with n-type and p-type materials.[54,63]

Nevertheless, p-type compensating doping can be exploited in case where a highly resistive ZnO is desired such as piezoelectric devices.[35,36] In this case, the p-type dopants is added in order to compensate the intrinsic n-type dopants, leading to the reduction of the free charge density in ZnO crystal and to the increase in its resistivity.

1.2.5 ZnO for piezoelectric applications and challenges

ZnO is a potential candidate for lead-free piezoelectric material as it is abundant, biocompatible and possesses piezoelectric properties thanks to its non-centrosymmetric wurtzite structure together with the spontaneous polarization along the *c*-axis. Compared to PZT, the piezoelectric coefficient of ZnO is modest, but it has the advantage of being compatible with the flexibility in the fabrication process that offers an ability to largely modify the structural and electrical properties as well as significantly improve the piezoelectric efficiency. There are many different architectures of ZnO-based piezoelectric devices, but they can be classified into two main types: thin film and nanowires. Each type has the advantages as well as drawbacks when being used for piezoelectric applications.

1.2.5.1 ZnO thin film devices

ZnO thin films have been developed for many piezoelectric applications such as sensors,[70,71] surface acoustic wave (SAW),[72,73] and energy harvesting.[74–76] The ZnO thin film as a main piezoelectric component is usually deposited by sputtering,[71–74,76] hydrothermal method,[75] or chemical vapour deposition,[70] followed by the micro-fabrication steps to create the electrodes. For instance, S. Li et al. developed an acceleration sensor comprising the Si cantilever, Li-doped ZnO thin film, Pt/Ti bottom electrode and Al top electrode,[71] as shown in **Figure 1.7**. When an acceleration proceeds, the cantilever vibrates, causing the deformation and generation of electricity in ZnO thin film due to its piezoelectric property. By extracting the electric signals, the acceleration can be measured. In another study, K. Tao et al. developed a ZnO-based energy harvester using ZnO thin film.[76] They designed and fabricated a fully integrated two-degree-of-freedom MEMS, in which the ZnO thin film was deposited by sputtering and sandwiched between the top and bottom Pt/Au electrodes. Power generation of the device showed two resonant peaks at 403.8 and 489.9 Hz with the voltages of 10 and 15mV, respectively. A ZnO piezoelectric microcantilever for energy harvesting was also fabricated by D. Bhatia et al.[74] The ZnO thin film was deposited on Si substrate, while Cr/Au served as a top electrode. The deformation of the ZnO cantilever induced a voltage at 230 mV.

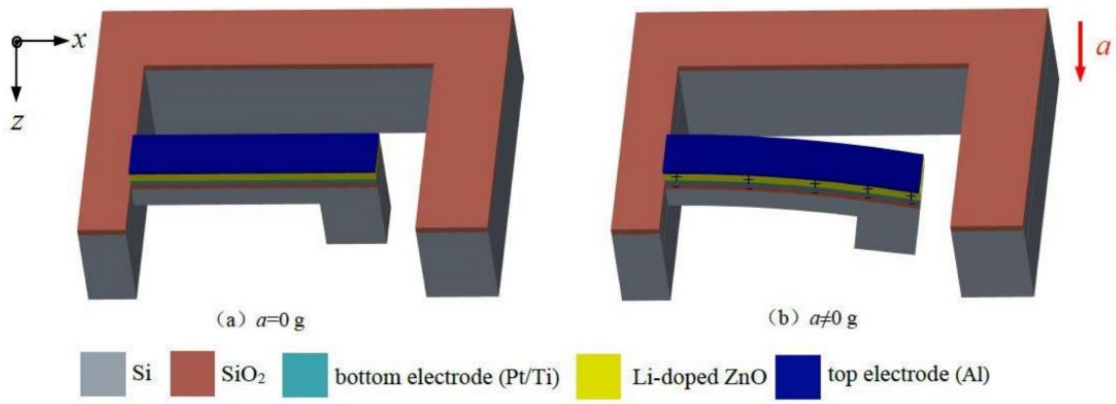

Figure 1.7: Schematic of a ZnO piezoelectric thin film based acceleration sensor.[71]

Generally, the ZnO thin film structure is simpler to be fabricated and integrated into the MEMS to develop a piezoelectric device compared to the nanowire structure. However, there are some challenges that need to be overcome in order to have a good piezoelectric performance, which is more difficult to achieve in thin films than in nanowires:

First, it is essential to have a thin film with good orientation: As a wurtzite structure semiconductor, the electrical polarization inside the ZnO crystal occurs along the *c*-axis. A polycrystalline ZnO thin film with random orientation grains can lead to a poor piezoelectric efficiency or even the disappearance of piezoelectric properties. Unlike piezo-ceramic, the ZnO polar axis cannot be changed or aligned by the poling process. Thus, it is required that the ZnO thin film has a good oriented structure after the final step of its fabrication process for piezoelectric applications. Researchers have shown that the orientation of ZnO thin film can be greatly affected and improved by its fabrication conditions. For example, L. Fanni et al. demonstrated that the preferred orientation of ZnO thin films grown by metal–organic chemical vapour deposition (MOCVD) was switched between *a*- and *c*-axis when the growth temperature and precursor flow rates were varied.[77] On the other hand, X. Cai et al. showed that a sufficient copper doping can enhance the *c*-axis orientation of ZnO thin films grown by MOCVD.[78] The structural orientation of ZnO thin film can also be improved after the growth step by using post thermal annealing, as presented in refs.[79–81] However, none of those researches studied the effect on ZnO piezoelectric properties.

Second, it is not only required that the ZnO thin film has a good orientation, but it is also necessary that its structural polarity is uniform: During the piezoelectric phenomenon, the electrical potentials generated in the Zn- and O-polarity domains are of opposite signs. A stack of grains with opposite polarities inside the ZnO thin film can cause the neutralization of piezoelectric signals, resulting in the cancellation of the piezoelectric output. Controlling the polarity of ZnO thin film is crucial for its piezoelectric applications, but there are only a few investigations about this matter.

Third, the screening effect caused by the high residual n-type doping inside the ZnO structure is also one of the major problems that reduces its piezoelectric efficiency:[35,36] Mostly, ZnO contains a large amount of free electrons generated by the incorporation of intrinsic and extrinsic point defects

during its growth. In piezoelectric materials, the piezoelectric potential is created between the electrodes at two opposite sides when a mechanical force is applied. Because there are free electrons inside ZnO, they can move freely to the positive side to reduce the voltage, thus screening the piezoelectric potential (**Figure 1.8**). Therefore, it is necessary to compensate for these free electrons in order to increase the piezoelectric efficiency.

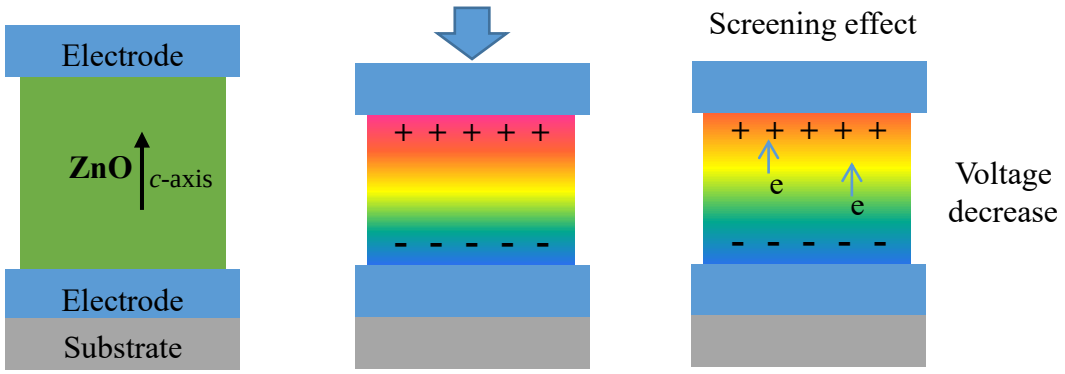

Figure 1.8: Schematic of free electrons screening the piezoelectric potential in ZnO.

One possible method is to introduce positive charges (holes) into ZnO to compensate for the residual free electrons by adding acceptor dopants, which can belong to group IA, group IB, or group V.[35,36] A positive charge carrier can be created when the atom of group IA or group IB replaces Zn atom, or atom of group V replaces O atom. However, dopants can also come to unwanted sites in ZnO so that the positive charge is not created, or form a complex structure with their neighbor atoms and introduce even more free electrons to the ZnO. It should also be noted that the difference of size between dopans and Zn or O atoms can cause the distortion of ZnO crystal structure, which can influence the structural orientation of ZnO, which in turn affects its piezoelectric efficiency. For example, X. Cai et al. reported that Cu dopants in ZnO thin films induced both acceptor and donor energy levels in the band gap.[78] They also showed that the additional Cu dopant source vapor was one of the critical factors that affect the ratio Zn/O, leading to a perfect condition for the hexagonal structure growth. As a result, the ZnO morphology changed from thin film to nanorods. X. Wang et al. fabricated different ZnO thin films doped with Cu, Ni, Co and Fe by using conventional magnetic sputtering technique.[73] Their results show that the electrical resistivity of Cu-doped ZnO thin film increased up to 10^9 Ω.cm and its polar *c*-axis orientation was also enhanced, resulting in an increase of the piezoelectric coefficient d_{33} to 13.5 pC/N. Meanwhile, the ZnO thin films with other dopants led to the degradation of the ZnO orientation and resulted in lower piezoelectric coefficients compared to the undoped one at 11 pC/N. Interestingly, J. Luo et al. reported a significant enhancement of piezoelectric coefficients d_{33} up to 127 pC/N obtained in Fe-doped ZnO thin films prepared by sputtering.[82] Since Fe is also a non-critical element, this result shows that a highly piezoelectric efficient ZnO-based device can be achieved using only sustainable materials. Besides, another strategy to enhance the ZnO piezoelectric efficiency consists in forming a p-n junction to trap free electrons. This was demonstrated in the report of K. Pradel et al., in which the p-n homojunction ZnO thin film was prepared by hydrothermal method (**Figure 1.9**).[75] The junction helped increase the piezoelectric output from 7.1 to 284 mV

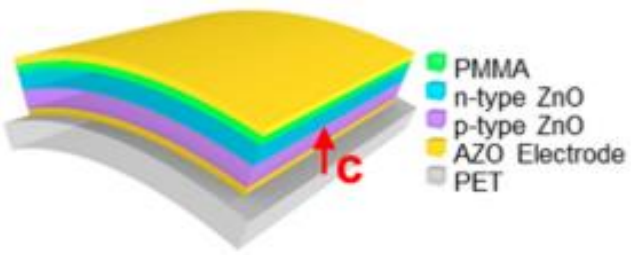

Figure 1.9: Schematic of the homojunction ZnO nanogenerator.[75]

Besides, D. Sijun et al. demonstrated an extraordinary approach to increase the performance of a ZnO-based cantilevered energy harvester by modifying the architecture of the device electrode coverage.[83] Both their simulation and the experimental results indicated that an improvement of the piezoelectric output up to 126 – 144.5 % was achieved with the optimal electrode coverage area, where the generated power collection on the cantilever was maximized.

1.2.5.2 ZnO nanowire devices

ZnO nanowire structure has received increasing attention in recent years as it has a wide range of properties which are suitable for many applications in electrical, optical and especially piezoelectric fields.[35,36,52,54,84,85] Various types of piezoelectric applications based on ZnO nanowires have been developed with diverse fabrication processes and designs.[35,36] The piezoelectric nanogenerator made of ZnO nanowires was introduced by Z. L. Wang et al., which can produce continuous direct-current output by receiving surrounding ultrasonic waves (**Figure 1.10**).[86] The vertical ZnO nanowire array was grown on either GaN or sapphire substrates covered by a ZnO layer that was used for the bottom electrode. The top electrode is a zigzag Si electrode coated with Pt. The output power per unit area of the device was estimated to be 10 mW/cm^2.

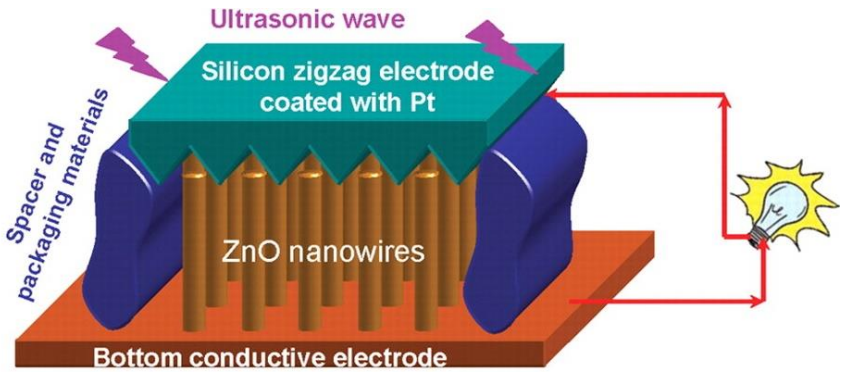

Figure 1.10: Schematic diagram showing the design and structure of the piezoelectric nanogenerator made of vertical ZnO NWs powered by an ultrasonic wave.[86]

In another work, R. Yang et al. (also from Prof. Wang group) developed a nanogenerator using a single ZnO nanowire laterally placed on a flexible Kapton polyimide substrate (**Figure 1.11**).[87] The ZnO NWs with the 3 – 5 µm diameter and 200 – 300 mm length were synthesized by a physical vapour deposition method. Then, the ZnO NW was placed on the Kapton film using a probe station and optical microscope. Both ends of the ZnO NW were tightly bonded to the substrate using silver

paste. An output voltage of up to 50 mV was generated by repeatedly stretching and releasing the NW device.

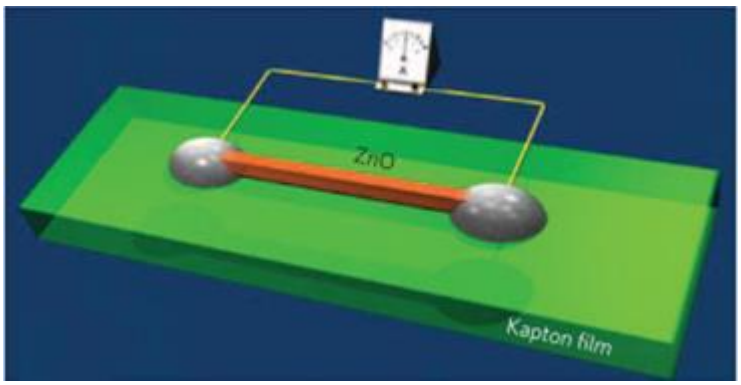

Figure 1.11: Schematic of a piezoelectric generator made of a single ZnO NW lying on a Kapton substrate with both ends tightly bonded to the substrate and outlet interconnects.[87]

Compared to thin films, it is more complicated to fabricate the NW structure-based piezoelectric device. The requirements when developing ZnO nanowire structure in order to have a good piezoelectric performance are the same as compared to the ZnO thin film structure, mainly a good orientation along the polar *c*-axis with a uniform polarity, and a low residual free electron density. However, the NW offers a better structure that is more favorable for piezoelectric performance, and its one-dimensional nanostructure allows to develop more approaches to reduce the residual free electron density as well as its screening effect problem. Many research groups have shown that the piezoelectric coefficient of ZnO NW structure is superior compared to the thin films.[47,88,89] M. Ghosh et al. reported a piezoelectric coefficient d_{33} at 44.33 pm/V measured by PFM on ZnO NWs grown by hydrothermal method,[47] which is much higher than the value at 12.4 pm/V of ZnO thin film reported in ref.[46]. One of the reasons is that the NWs possess a better crystallinity with good orientation along the polar *c*-axis. Thanks to the absence of the random orientation of grains causing the piezoelectric cancellation as seen in polycrystalline thin film, the piezoelectric coefficient is significantly enhanced in the NW structure.

Regarding the screening effect caused by the residual free electrons, the doping method can also be applied for ZnO NWs to mitigate this problem, leading to further increase the piezoelectric coefficient. In the work of Y. Chang et al., undoped and Li-doped ZnO NWs were grown by hydrothermal method.[90] The piezoelectric properties of the ZnO NWs were characterized using AFM with a Pt-coated silicon tip. When the tip scanned on the ZnO NWs, the piezoelectric output current coming through a load with the resistance of 20 MΩ was measured. While the XRD analysis expressed that both undoped and Li-doped ZnO NWs have good orientation along the *c*-axis, the piezoelectric responses measured by AFM show that the piezoelectric output current on Li-doped ZnO NWs (8 nA) is much higher than on undoped NWs (1.6 nA). Those results implied that the increase in piezoelectric response is related to the change in electrical properties of Li-doped ZnO NWs. S. Rafique et al. fabricated piezoelectric nanogenerators made of undoped and Ag-doped ZnO nanorods grown by hydrothermal method.[91] To evaluate the performance of nanogenerators, a

mechanical force of 3 kgf was applied, while the output voltage and current were measured by an oscilloscope. The Ag-doped ZnO nanogenerator provided a maximum output power density of 1.45 mW/cm^2 with a load resistance of 31 MΩ, which was three times higher compared to the undoped ZnO nanogenerator.

Besides adding dopants, other research groups also demonstrated alternative methods that can trap free electrons causing the screening effect, leading to the improvement of the piezoelectric output. Similar to thin films, this can be done by forming a p-n junction at the interface between the ZnO NWs and electrodes. For instance, Q. Wang et al. presented a nanogenerator with ZnO-CuO nano-heterojunctions fabricated by using two-step aqueous solution method (Figure 1.10).[92] By applying the same compressive strain of 1 kgf, the nanogenerator with the p-n junction showed an output current that was 25 times higher compared to the nanogenerator with pure ZnO. This was due to the fact that the p-n junction suppressed the free electrons. Furthermore, while the p-n junction can only be formed at the top or bottom surface of the thin film, the NW structure provides the possibility to form the p-n junction at their side-walls. The large surface area of NW side-wall allows this p-n junction to effectively trap a large amount of free electrons, leading to a huge boost in piezoelectric performance. By coating the ZnO NWs with copper thiocyanate (CuSCN), N. Jalaji et al. showed that the power density of a piezoelectric harvesting device was increased to 303.39 $\mu W/cm^2$, which was four time higher compared to uncoated one (**Figure 1.12**).[93]

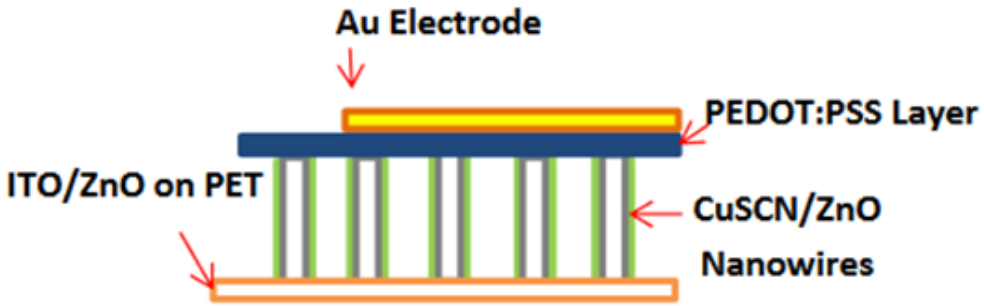

Figure 1.12: Schematic of ZnO/CuSCN/PEDOT:PSS devices.[93]

Thanks to its one-dimensional nanostructure, the change of NW geometry can have a significant effect on the free electrons residing in the structure. For example, R. Tao et al. showed *via* numerical simulations of Vertically Intergrated Nanogenerators (known as VING) that free electrons can be completely depleted by surface traps at the interface between ZnO NWs and the dielelectric polymer matrix when the diameter of the ZnO nanowire is sufficiently small, resulting in a jump of the piezoelectric potential (**Figure 1.13**).[89]

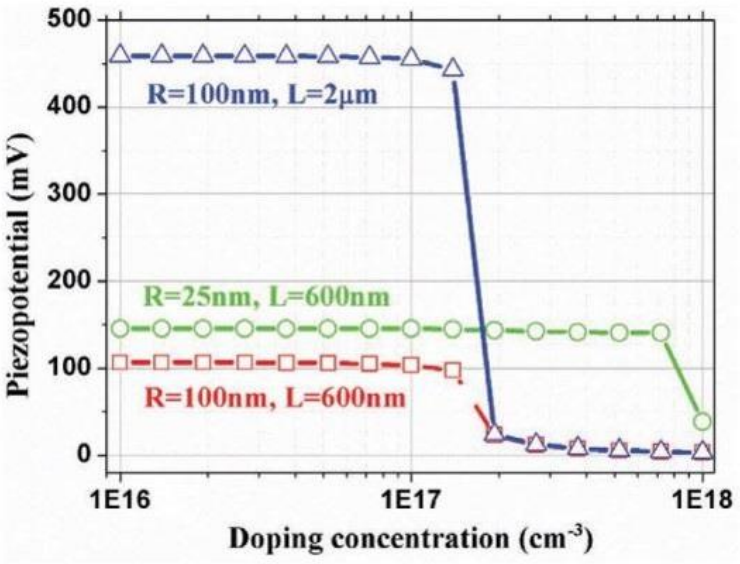

Figure 1.13: Variation of ZnO nanowire-based nanogenerator performance with doping level along with the influence of nanowire radius (R) and length (L).

Moreover, R. Yang et al. showed the important role of the contact between the piezoelectric ZnO component and electrodes in the piezoelectric performance of the device.[87] In their experiment, the Schottky contact was formed by silver (Ag), while the Ohmic contact was created by indium (In). The device exhibited stronger output signals when at least one Schottky contact was formed at one end of the device. This can be explained by the Schottky contact preventing free electrons inside the ZnO going out to the external circuit, which could reduce the piezoelectric potential.

Overall, the piezoelectric performance of ZnO thin films and nanowires are strongly dependent upon its structural and electrical properties. By improving the structural orientation as well as polarity uniformity and reducing the screening effect, the piezoelectric response of ZnO can be significantly enhanced. These can be done by controlling and combining various methods during the ZnO fabrication process. Thus, it is important to understand the synthesis technique and important factors during the ZnO growth in order to modify its structural and electrical properties in such a way that it is favorable for piezoelectric applications.

1.2.6 Synthesis methods

There is a wide variety of techniques that can be used to synthesize ZnO thin films and nanostructures. They can be categorized into physical techniques such as thermal evaporation,[94] sputtering,[95] pulsed laser deposition,[96] molecular beam epitaxy,[97] and chemical techniques including chemical bath deposition,[59,66,98] metal–organic chemical vapor deposition (MOCVD),[99,100] and atomic layer deposition (ALD)[101]. Each technique has its advantages and drawbacks. The properties of ZnO and its piezoelectric performance are also greatly dependent upon the techniques and conditions used during the growth. Various ZnO morphologies have been grown by different methods and their piezoelectric coefficient d_{33} values have been estimated by PFM measurement, which are shown in **Table 1.4**. The most common techniques used to grow ZnO for piezoelectric applications are

sputtering and aqueous solution methods thanks to their simplicity, while there is a lack of study on molecular beam epitaxy and chemical vapor deposition, especially on MOCVD.

Table 1.4: Piezoelectric coefficient d_{33} measured by PFM measurement of ZnO grown by different methods.

Growth method	**Morphology**	**d_{33} (pm/V)**
Sputtering[46]	Thin film	12.4
Sputtering[73]	Thin film	11.5
Thermal evaporation[45]	Nanobelt	14.3 – 26.7
Thermal evaporation[102]	Nanopillar	7.5
Pulsed laser deposition[103]	Thin film	8.6
Pulsed laser deposition[102]	Thin film	11.3 – 15.9
Pulsed laser deposition[103]	Micropillar	18.2 – 46.9
Aqueous solution[104]	Thin film	5.8
Aqueous solution[105]	Nanorod	2.7 – 6.1
Aqueous solution[106]	Nanorod	0.4 – 9.5
Aqueous solution[47]	Nanorod	44.3
Chemical vapor deposition[107]	Nanopyramid	13.2

1.2.6.1 Physical techniques

Thermal evaporation is the simplest process among physical vapor deposition techniques. In this process, a material source is evaporated by heating at high temperature. Then, the material vapor is carried inside the chamber to reach the substrate, where it condenses back to a solid state. This technique can be performed with or without vacuum, but it requires a very high temperature to heat the material source. For instance, B. Yao et al. have demonstrated different ZnO morphologies grown by using thermal evaporation deposition (**Figure 1.14**).[94] In their experiment, the ZnO power as a material source was heated at 1100 °C in normal atmosphere pressure. The ZnO nanostructures were formed on the inner wall of the quartz tube at temperature ranging from 500 to 800 °C.

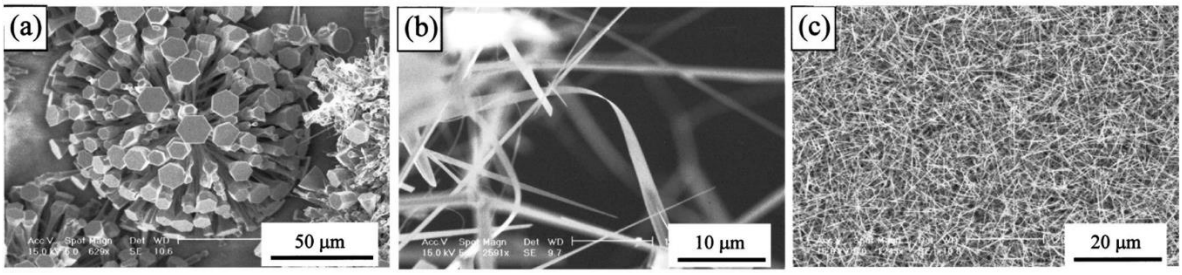

Figure 1.14: SEM images of (a) ZnO nanorods, (b) ZnO nanoribbons, (c) and ZnO nanowires grown by thermal evaporation.[94]

Sputtering is also a popular physical deposition technique. Instead of using high temperatures, this technique generates a plasma environment containing energetic atoms or ions to bombard the material source. The material is sputtered away from the source, goes through the

chamber and deposits on the substrate. The process is usually performed in O_2 and Ar environment, where O_2 is used as the reactive gas and Ar acts as the sputtering enhancing gas. The advantages of sputtering is its simplicity and the substrate can be kept at low or near room temperature. Thus, this technique is commonly used to develop ZnO-based nanogenerators on flexible substrates, which require low temperature deposition. However, the bombardment from high speed atoms or ions can damage the substrate and the growing ZnO layer. To mitigate this damaging bombardment, P. Carcia et al. used lower power and low cathode voltage to decrease the atoms and ions speed.[95] They also increased the gas pressure to 20 mTorr in order to dissipate the energy of atoms and ions by collisions.

Another physical deposition technique that does not require high temperature is pulsed laser deposition. In this technique, a high-power pulsed laser beam is used to ablate the material source. The material is vaporized from the source and deposited on a substrate. Being evaporated by the laser, the material is provided with high energy, allowing it to form a high quality structure even on low temperature substrate. E. Abdel-Fattah et al. has shown that the pulsed laser deposition of ZnO can be performed on glass substrate with temperature from room temperature to 450 °C.[96] However, their results also showed that the deposited ZnO film had better quality on higher temperature substrate, regardless of laser fluence.

Molecular beam epitaxy is an advanced physical deposition technique, in which the thin film or nanostructure is epitaxially grown by the beams of atoms in a molecular regime. The material sources of each element are evaporated from their effusion cells, where the cell temperature is adjusted to precisely control the material flow rates. Then, the beams of materials are fired at the heated substrate to grow the thin film or nanostructure. The process is usually performed in ultra-high vacuum (10^{-7} – 10^{-12} Torr), allowing to grow epitaxially thin films or nanostructure.[97] Thanks to that, the grown ZnO structure can achieve a very high purity and excellent crystal quality. Due to the requirement of extreme growth conditions such as high temperature, ultra-high vacuum, and a very low growth rate, this technique is generally not the most suitable for industrial scale production.

1.2.6.2 Chemical techniques

ZnO can be formed by chemical bath deposition technique. This technique typically includes two steps: the initial deposition of a seed layer and the subsequent ZnO growth on top of it. The seed layer deposition on the substrate can be performed using spin coating, sputtering, or atomic layer deposition. Then, ZnO growth is carried out by keeping the substrate in a zinc precursor solution, which can be zinc nitrate hexahydrate ($Zn(NO_3)_2 \cdot 6H_2O$),[59] or zinc acetate dihydrate ($(Zn(CH_3COO)_2.2H_2O$).[66] Compared to other techniques, chemical bath deposition does not require expensive infrastructure. It can also grow ZnO at low temperature, and can be scaled up for mass production, but this is achieved at the expense of the structural and optical quality.

Chemical vapor deposition is a process in which the material is grown by the reaction of precursors or agents on the substrate surface. The technique is called metal-organic chemical vapor deposition (MOCVD) when metal-organic precursors are used. For ZnO deposition, the Zn precursor

is usually dimethyl zinc ($Zn(CH_3)_2$ – DMZn),[100] or diethyl zinc ($(C_2H_5)_2Zn$ – DEZn).[99] Besides precursor nature, other parameters such as growth temperature, flow rate, pressure, etc. can be controlled, allowing obtaining various ZnO morphologies along with different properties (**Figure 1.15**). Moreover, this technique is not only able to create a high quality ZnO structure, but also can be applicable to large scale production.

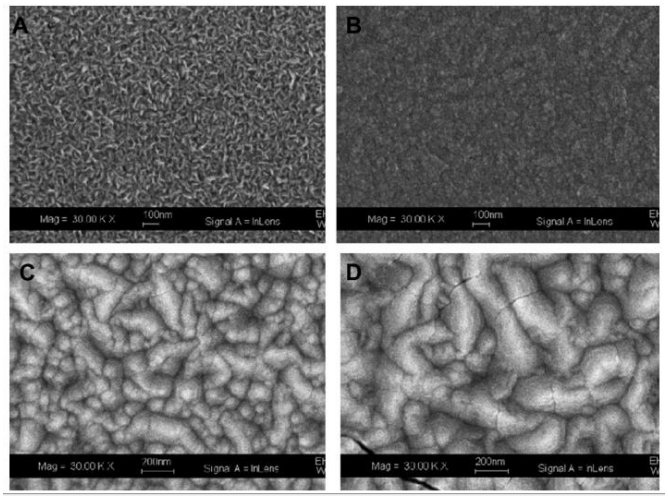

Figure 1.15: SEM images of ZnO thin film grown by MOCVD at various temperatures.[108]

Atomic layer deposition is a variant of chemical vapor deposition. Different from other techniques, the precursors are not introduced simultaneously in the chamber, but they are inserted sequentially with controlled pulses. In each pulse, the precursor reacts and saturates the surface reactive sites before the next pulse is introduced. Thus, the material is grown uniformly with highly precise thickness, but the use of vaccum is required and the growth rate is very low.

Comparing physical and chemical deposition techniques, ZnO deposited by chemical deposition techniques can exhibit a larger amount of incorporated impurities coming from by-products of reactions during the growth. However, the impurities can also originate from the material source used in the deposition. The physical techniques also usually require higher temperatures or more pronounced vacuum to obtain high quality structure. In contrast, ZnO structure grown by the chemical techniques can achieve high quality structure at lower vacuum conditions. Moreover, the ZnO growths by these techniques are also more suitable for industrial scale production. Among them, the low growth rate of ALD is not suitable to fabricate ZnO for piezoelectric applications, in which the thickness at around 1 µm is desired. In this work, we are interested in the MOCVD method, whose growth rate is much higher while exhibiting a great structural and optical quality. This technique also offers the ability to modify ZnO properties by a wide range of controlled parameters, together with the capability of adding different dopants in order to enhance the ZnO piezoelectric performance. As it is a complex process, it is important to well understand the influences of growth parameters on the ZnO formation and its properties.

1.3 Summary of the chapter

In summary, piezoelectricity is a useful phenomenon that has many applications in the industry, science and daily life. While PZT has a good piezoelectric performance and is the most common material used for piezoelectric devices, its extreme toxicity gives rise to concern about the sustainable development of piezoelectric applications. Many lead-free materials have been proposed and developed in order to replace the PZT. Among them, ZnO is a promising candidate as it is an abundant, biocompatible semiconductor compound with polar and piezoelectric properties. The piezoelectric coefficients of ZnO are lower as compared to PZT, but they may be significantly enhanced by using suitable methods. ZnO-based piezoelectric devices have recently attracted a lot of attention and various enhancement methods have been proposed. The studies on ZnO properties have indicated that important key points to improve the piezoelectric efficiency involve a good structural orientation, a uniform polarity and a low free charge carrier density, which strongly depend on the fabrication process. Among ZnO growth techniques, the MOCVD is suitable for industrial production as it allows to fabricate ZnO fast, on large surface area, and does not require high vacuum while still achieving a high structural and optical quality. Despite that, it has not been explored so far for piezoelectric applications, but mainly focused on light emitting diode applications. In this thesis, the MOCVD is selected as the ZnO fabrication process. Its ability to precisely control different factors during the growth provides a robust way to adjust the ZnO properties and to improve the piezoelectric efficiency.

Chapter 2
MOCVD growth and characterizations

In this second Chapter, the MOCVD technique used to grow ZnO thin films and nanostructures is described. The effect of MOCVD parameters on ZnO properties is reviewed. The piezoresponse force microscopy (PFM), which is the technique used for analyzing the ZnO piezoelectric properties, is also presented in detail. The principles, experimental setup and steps of calibration in this measurement technique are described sequentially. The experimental procedures dedicated to other structural, optical and electrical characterizations are also described. The methodology for analyzing ZnO properties is established.

2.1 MOCVD

Metal-organic chemical vapor deposition (MOCVD), also called metal-organic vapor-phase epitaxy (MOVPE) when an epitaxial relationship occurs, is a variant of chemical vapor deposition (CVD) used to produce thin films or nanostructures. In this technique, the material is deposited on the substrate following the chemical reactions involving metal-organic precursors and molecules in vapor phase. It was first introduced in 1968 at North American Rockwell by Harold M. Manasevit.[109] In his work, gallium arsenide (GaAs) crystals were grown on sapphire (Al_2O_3), spinel ($MgAl_2O_4$), beryllium oxide (BeO), and thorium oxide (ThO_2) substrates using triethylgallium (TEG), trimethylgallium (TMG) and arsine (AsH_3).[109,110] He also demonstrated the ability of MOCVD to grow different III-V (e.g. GaP, AlAs, AlP), II-VI (e.g. ZnS, ZnTe, CdS) and IV-VI (e.g. SnS, PbS, PbSe) semiconductor compounds.[111] In the next few decades, the MOCVD technique has been rapidly developped and become an attractive method for industrial production. This technique has several advantages including the flexibility to grow many materials with high structural and optical quality, fabricate heterostructures, and ability to perform the growth on multi-wafers. By using MOCVD technique, the GaAlAs/GaAs heterostructure solar cells were successfully fabricated by R. Dupuis et al. in 1977.[112] H. Amano et al. demonstrated the Mg-doped GaN light-emitting diode (LED) grown by MOCVD in 1989.[113] Nowadays, the MOCVD technique is employed to produce semiconductor compounds for power devices, lasers, detectors, photonic integrated circuits, solar cells, LEDs, etc.[111]

Compared to other techniques, the MOCVD process can grow ZnO thin films or nanostructures with a high growth rate and on a large surface area and offers a high repeatability and reproducibility, which are suitable for industrial scale production. The high quality ZnO deposits can be formed without requiring an ultra-high vacuum as compared to the molecular beam epitaxy technique. Although this technique is also complex, it offers a wide versatility to control the ZnO growth parameters and its doping process. Thus, the ZnO properties can thoroughly be adjusted in order to be suitable for many applications including piezoelectric devices.

2.1.1 Principle

The growth process of ZnO from the metal-oragnic precursors and molecules in vapor phase in the MOCVD chamber involves many physical and chemical processes. Generally, it can be described as follows: the metal-organic Zn precursors (such as diethylzinc, DEZn ($(C_2H_5)_2Zn$)) and oxygen agents (such as O_2) are introduced in vapor phase into the MOCVD chamber using an inert carrier gas (such as Ar). At the elevated temperature in the chamber, the Zn atom is decomposed from its organic part and reacts with the oxygen agent to form subspecies in the gas phase (**Figure 2.1**). The subspecies diffuse through the gas boundary layer and are adsorbed on the heated substrate surface. Then, the chemical reactions of the subspecies continue occurring, resulting in the deposition of ZnO species on the surface. These species diffuse on the substrate surface, nucleate and form the first ZnO layer. After that, the next coming atoms incorporate to the layer and continue the growth of the ZnO thin film or nanostructures. The other by-products from the chemical reactions are removed from the MOCVD chamber by vacuum.

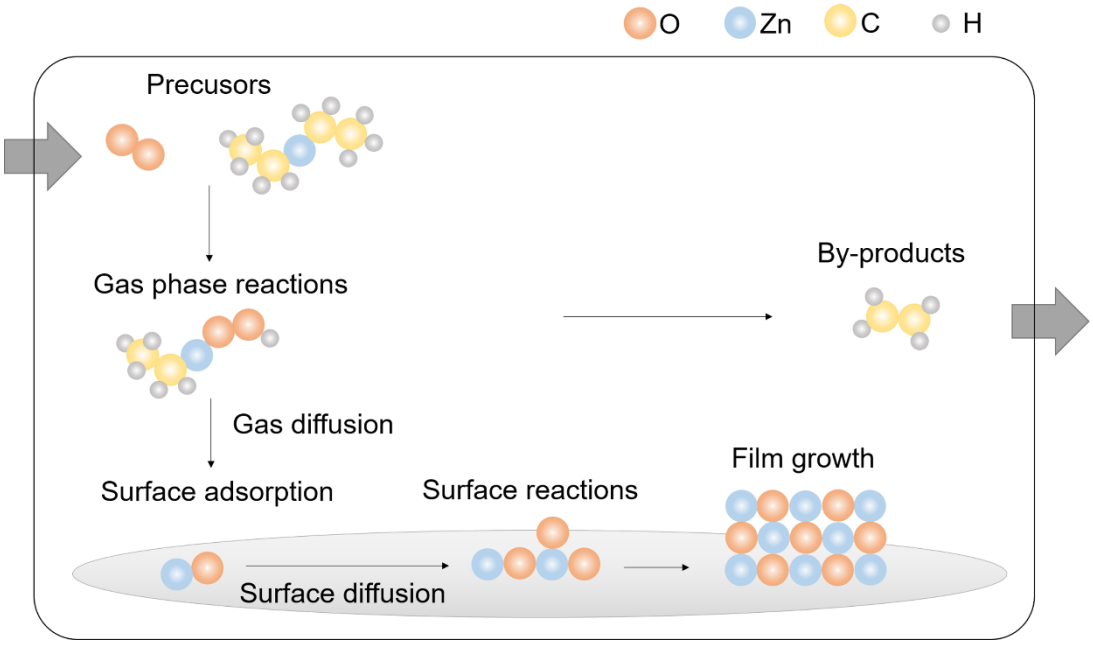

Figure 2.1: Schematic of the ZnO growth process in the MOCVD chamber.

There are also different reactions that can occur between the metal-organic Zn precursor and oxygen agent. For instance, J. Li et al. reported the different chemical reaction pathways from DEZn and O_2 precursors to ZnO as follows:[114]

i) Gas phase reaction pathways from DEZn and O_2 precursors:

$$Zn(CH_2CH_3)_2 + O_2 \rightarrow Zn(CH_2CH_3)_2 \cdot O_2$$

$$Zn(CH_2CH_3)_2 \,.\, O_2 \rightarrow {}^{\bullet}CH_2CH_2ZnC_2H_5 \cdot HOO^{\bullet}$$

$${}^{\bullet}CH_2CH_2ZnC_2H_5 \cdot HOO^{\bullet} \rightarrow HOOZnC_2H_5 + C_2H_4$$

$$HOOZnC_2H_5 \rightarrow HOCH_2CH_2ZnOH$$

$$HOCH_2CH_2ZnOH \rightarrow Zn(OH)_2 + C_2H_4$$

$$3Zn(OH)_2 \rightarrow Zn_3(OH)_6$$

$$Zn_3(OH)_6 \rightarrow Zn_3O_5H_4 + H_2O$$

$Zn_3O_5H_4 \rightarrow Zn_3O_4H_2 + H_2O$
$Zn_3O_4H_2 \rightarrow Zn_3O_3 + H_2O$

ii) Surface reaction pathways for ZnO growth:
$Zn(CH_2CH_3)_2 \,.\, O_2 \rightarrow ZnO + 2C_2H_4 + H_2O$
$\bullet CH_2CH_2ZnC_2H_5 \cdot HOO\bullet \rightarrow ZnO + 2\,C_2H_4 + H_2O$
$HOOZnC_2H_5 \rightarrow ZnO + 2C_2H_4 + H_2O$
$HOCH_2CH_2ZnOH \rightarrow ZnO + 2C_2H_4 + H_2O$
$Zn(OH)_2 \rightarrow ZnO + H_2O$
$Zn_3(OH)_6 \rightarrow 3ZnO + 3H_2O$
$Zn_3O_5H_4 \rightarrow 3ZnO + 2H_2O$
$Zn_3O_4H_2 \rightarrow 3ZnO + H_2O$

Although these physical and chemical processes are quite complicated, they are affected by some factors that can be modified by the different MOCVD parameters. By controlling the MOCVD parameters, the ZnO growth process can be adjusted with a high repeatability and reproducibility. Thus, it is important to understand the influence of these factors on the ZnO growth process to optimize the MOCVD parameters and obtain the desired ZnO properties for piezoelectric applications.

2.1.2 Effect of factors

There are many factors that are involved in the ZnO growth process in the MOCVD chamber such as the nature of precursors, growth temperature, flow rates, total pressure, use of dopants, substrate surface, etc. The effects of those factors have been investigated by different research groups, showing a large variation of ZnO properties.

2.1.2.1 Precursors

The choice of chemical precursors for the ZnO growth is a decisive factor since it affects the chemical reaction pathway that leads to the formation of ZnO in the MOCVD chamber. The metal-organic Zn precursor is usually either dimethylzinc (DMZn) or diethylzinc (DEZn). As DEZn has more carbon atoms as compared to DMZn, the bond between the Zn atom and the organic part is weaker. Thus, the DEZn is easier to decompose to react with the oxygen agent during the MOCVD process. Th. Kaufmann et al. have reported that the higher reactivity of DEZn with tertiary butanol (t-BuOH) resulted in more premature reactions, which form ZnO particles deposited on the substrate surface and cause a lower quality of ZnO films.[115] On the other hand, the study of J. Ye et al. has shown that their ZnO thin film grown with DEZn and O_2 precursors had superior structural and optical properties as compared to ZnO thin films grown with DMZn and O_2 precursors.[116] Their X-ray diffraction (XRD) results expressed that the ZnO thin film grown with DEZn exhibited a higher *c*-axis oriented structure. The Raman scattering measurements also indicated the much lower C and H impurity concentration in that thin film compared to the ZnO thin film grown with DMZn, which was explained from the different chemical reaction pathways taken between the two precursors. Although there is no discussion about the piezoelectric properties, the highly *c*-axis orientation achieved using the growth with DEZn is necessary for ZnO films to have efficient piezoelectric properties. The low C and H

impurity concentrations are also important for getting a high piezoelectric efficiency since these impurities can cause the screening effect inside the ZnO structure.[67,117]

The O_2 or H_2O molecules are commonly used as the oxygen agent in the ZnO MOCVD growth. However, many studies also reported that the high reactivity of O_2 and H_2O molecules with the Zn precursor leads to the premature reaction in the gas phase, resulting in the formation of ZnO powders that later causes the formation of defects in the grown ZnO thin film. To diminish this problem, other oxygen compounds are employed such as isopropanol (i-PrOH),[118,119] tertiary-butanol (t-BuOH),[118,120] acetone,[119] and N_2O.[119] C. Kirchner et al. investigated the ZnO growth on *c*-plane sapphire by using DEZn as Zn precursor, i-PrOH and t-BuOH as oxygen precursors.[6] By comparing the two oxygen precursors, their results showed that while the dependence of growth rate on the pressure are similar, there is a large difference in the growth rate behavior with the temperature. The ZnO film grown with t-BuOH exhibited a better optical quality compared to the one grown with i-PrOH. A comparison of ZnO growths on GaN/Si(111) templates by using i-PrOH, acetone, and N_2O was also reported by N. Oleynik et al. (**Figure 2.2**).[119] The growth with N_2O molecules needed a higher temperature due to the poor decomposition of this gas, but there was no pre-reactions and the ZnO film presented a significantly better crystallinity as compared to the ZnO layer when using the other two precursors. In the work of Y.J. Chen et al., CO_2 was chosen for oxygen precursor in order to lower the oxygen partial pressure and create a lower VI/II ratio environment during the MOCVD process.[121]

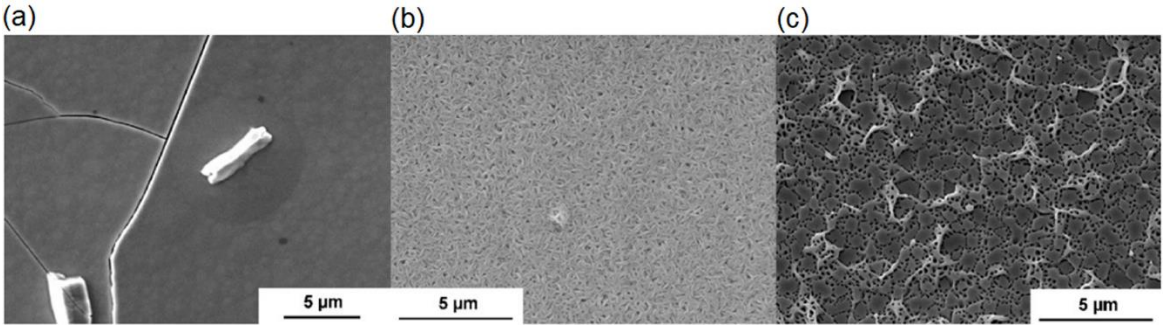

Figure 2.2: SEM images of ZnO thin film grown with different oxygen precursors: (a) iso-propanol, (b) acetone, and (c) N_2O.[119]

2.1.2.2 Temperature

The temperature is one of the most critical parameters that has a strong impact on the whole ZnO growth process in the MOCVD chamber. Generally, it provides the thermal energy required for the decomposition of chemical precursors as well as their chemical reactions, enhances the diffusion, adsorption and desorption of adatoms on the substrate. Thus, it directly affects the growth rate of ZnO on the substrate. As a consequence, the formation mechanism of ZnO significantly depends on the temperature, resulting in changing the morphology as well as the properties of ZnO. Many researchers have demonstrated the morphology transition of ZnO from thin film to nanowire-like structures when the growth temperature is increased.[122–124] This was due to the enhancement of adatom diffusion by the high temperature, which leads to the anisotropic growth. For instance, K. Bang et al. investigated the ZnO growth on GaAs substrate by MOCVD with the temperature varying in the range from 250 to 720 °C.[122] The growth rate increased with the temperature until 650 °C, then

it started decreasing at higher temperature due to the decomposition of ZnO film. Notably, the morphology of ZnO was also changed from thin film to nanorods at 650 °C, then to nanowires at 720 °C. The nanorods grown at 650 °C had the highest structural, optical quality and charge carrier mobility. J. Park et al. also reported the morphology transition of ZnO grown on sapphire by MOCVD (**Figure 2.3**).[123]

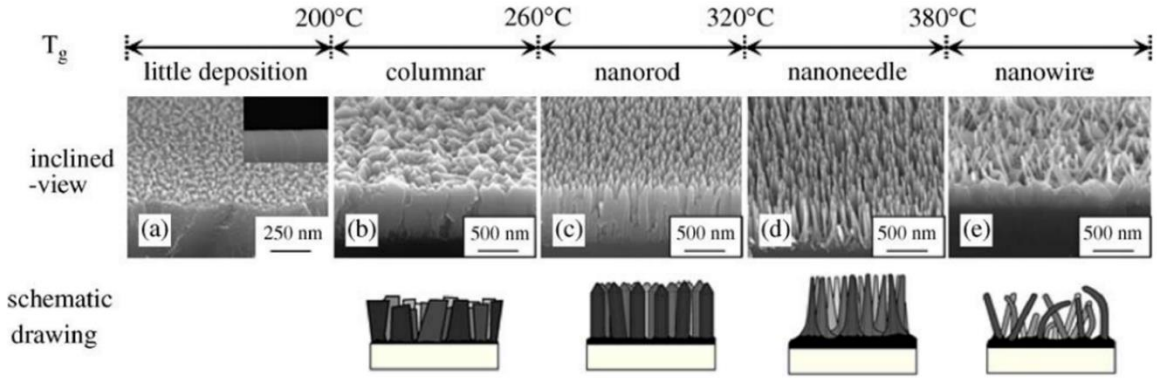

Figure 2.3: The inclined cross-sectional SEM images of ZnO grown at various growth temperature and the schematics of their morphologies.[123]

The ZnO morphology gradually changed from columnar film to nanorods, nanoneedles and nanowires (higher aspect ratio compared to nanorods) when the temperature was increased from 200 to 380 °C. Their results also showed that the nanoneedles and nanowires had a better structural, optical quality and less defects.

2.1.2.3 Flow rates

The flow rates of chemical precursors as well as their ratio also play an important role during the ZnO growth by MOCVD process. When the growth environment is changed by the flow rate variation, the surface energy of the different crystalline planes of ZnO is affected. Correspondingly, the relative growth rates on the crystalline planes are also varied, resulting in changing the main growth direction and altering the ZnO morphology. Fanni et al. obtained diverse ZnO morphologies when they modified the flow rates of DEZn and H_2O molecules.[77] The XRD analysis revealed that the preferential orientation of ZnO films was switched from the *a*-axis to the *c*-axis in different growth environment. In the other study, D.N. Montenegro et al. observed the morphology transition of ZnO from thin film to nanowires when they varied the flow rates of dimethylzinc–triethylamine (DMZn–TEN) and N_2O (**Figure 2.4**).[125] The thin films tended to be formed at high O/Zn precursor ratio, while the nanowires with a *c*-axis orientation were grown at low O/Zn precursor ratio. This implies that the low O/Zn precursor ratio enhanced the relative growth rate on the polar *c*-plane.

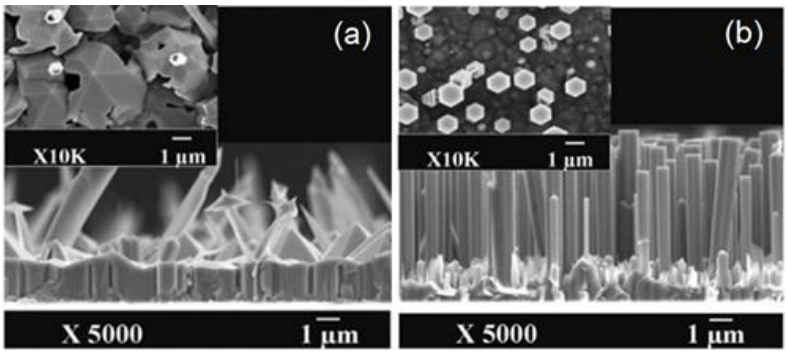

Figure 2.4: Cross and top (inset) view SEM images (a) ZnO thin film and (b) ZnO nanorods grown with different N_2O and DMZn–TEN flow rates.[125]

2.1.2.3 Other parameters

Pressure

Beside the parameters mentioned above, the pressure of the MOCVD chamber also contributes to the ZnO growth process. Together with the temperature and the flow rates, it has an influence on the diffusion of atoms as well as the growth rate and growth mechanism of the ZnO layer. In the work of C. Wu et al., the decrease of chamber pressure from 60 to 10 Torr reduced the thickness of gas boundary layer, allowing the atoms diffusing more easily to the substrate surface and resulting in the faster growth and different morphologies (**Figures 2.5a** and **b**).[126] The pre-reaction in the gas phase was also minimized at low pressure, leading to the improvement of the ZnO crystal quality.

Dopant

The nature of dopant and its flow rate also need to be carefully controlled in case it is added during the MOCVD process. As mentioned in Chapter 1, the presence of dopants inside the ZnO structure can drastically change its structural and electrical properties. Moreover, the additional dopant during the MOCVD process can also participate in varying the growth mechanism of ZnO. By performing the computational simulation, H. Chiu et al. has demonstrated that the presence of Ga-dopant can increase the surface energy of *m*-planes while decreasing the surface energy of other semi-polar planes.[127] Correspondingly, the ZnO nanostructures grown by MOCVD process had their smooth sidewall transformed to the corrugated sidewall when the Ga-dopant source was added (**Figures 2.5c and d**).

Substrate

Finally, the selection of substrate also has an effect on the ZnO growth during its nucleation step. The ZnO growths by MOCVD on *c*- and *r*- plane sapphire substrates resulted in different morphologies (**Figures 2.5e** and **f**).[128] Th. Gruber et al. also compared the growths on GaN templates and ZnO substrates.[129] The best optical and structural properties was achieved with the homoepitaxial growth on the ZnO substrate, emphasizing the strong influence of substrate at the initial growth process as well as the following ZnO formation steps. It can be seen that most of ZnO growth by MOCVD were performed on the substrate such as sapphire, GaN, or ZnO substrates because they have an epitaxial relationship with the ZnO, low lattice mismatch, or small difference in thermal expansion coefficients, which help to improve the ZnO crystal quality. However, those

substrates are not suitable for developing the piezoelectric applications since their electrical conductivity is low for being used as an electrode. The high cost of those substrates is also a drawback for industrial scale production.

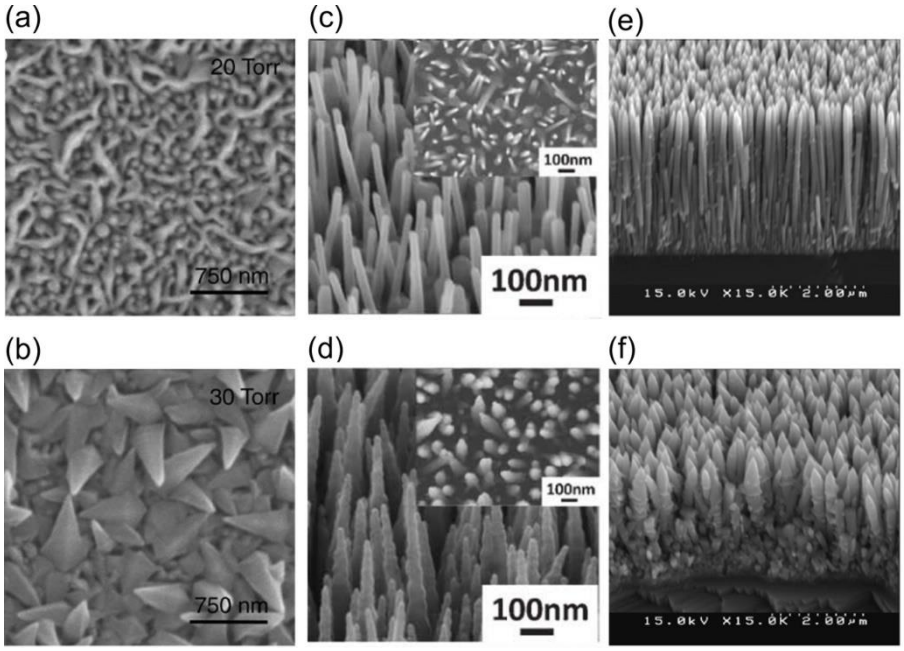

Figure 2.5: SEM images showing ZnO morphologies affected by different MOCVD growth conditions: (a, b) pressures;[126] (c, d) gallium dopant concentrations;[127] (e) *c*- and (f) *r*-plane sapphire substrates.[128]

Overall, many researches on the ZnO growth by MOCVD process have been performed with various growth conditions. A large number of ZnO morphologies from thin films to nanostructure has been reported, showing a large difference in structural, optical and electrical properties. However, there are very few studies about the effects of growth conditions on the ZnO piezoelectric properties. Since these properties have strong correlations, the change in other ZnO properties by modifying the growth condition can lead to a significant improvement of its piezoelectric efficiency. For example, those results have shown that a catalyst-free growth of ZnO nanowires on various substrates can be achieved by the MOCVD technique. The good structural quality, especially the high *c*-axis orientation of those ZnO structures is necessary for a good piezoelectric performance. Still, there is no information about the polarity of those ZnO structures on silicon. It should be noted that grains with the same *c*-axis orientation but opposite polarities (c^+- and c^--orientation) can still coexist inside the ZnO structure. Since opposite polarities can neutralize each other the piezoelectric signals, the uniformity of polarity in ZnO structure is required for good piezoelectric efficiency. Some results have shown that the improvement of crystal quality and less defects lead to the decrease of free charge carrier density and increase of mobility. While the decrease of the free charge carrier density can help reducing the screening effect, the increase of mobility can facilitate these free charge movements to screen the piezoelectric potential. Nevertheless, the correlation among the structural, electrical and piezoelectric properties need to be studied more carefully.

With the advancement of technology and industry, the new pulsed-liquid injection MOCVD (PLI-MOCVD) system is also developed in order to improve the production of high quality films. As

the normal MOCVD system uses the Zn precursor in its vapor state, it requires a constant heating on the vapor lines to prevent the condensation of precursor vapor before it can reach the reactor. In contrast, the precursor in the PLI-MOCVD system is mixed in a solvent and injected into the chamber in its liquid state. This helps to avoid the cumbersome heated system.[130] The pulsed-liquid injection also allows controlling the flow rate of the precursor more accurately. In this work, we investigate the effect of growth conditions in the PLI-MOCVD on the ZnO growth. The structural, optical, electrical, and piezoelectric properties of ZnO deposits are thoroughly investigated using different characterization techniques.

2.1.3 ZnO growth by PLI-MOCVD

The ZnO samples were grown in an Annealsys MC-200 PLI-MOCVD system. The O_2 gas was used as O precursor. For the Zn precursor, we used a solution of DEZn dissolved in hexanes provided by Sigma-Aldrich. Its concentration and mass density at 25°C are 1 mol/l and 0.726 g/ml, respectively. Due to the fact that the minimum flow rate limit for liquid in the PLI- MOCVD system is 0.1 g/min, we further diluted the DEZn solution in cyclohexane (C_6H_{12}) in order to investigate the ZnO growth with lower DEZn flow rate. Before the growth, a 100 ml of original DEZn solution was mixed with a 135 ml cyclohexane solution (anhydrous 99.5%, Sigma-Aldrich) in a glove box to have a 235 ml DEZn solution with the concentration at 0.426 mol/l. The mass density of the cyclohexane solvent and the diluted DEZn solution are 0.779 g/ml. and 0.756 g/ml, respectively. Then, the diluted DEZn solution was stored in the canister and ready for the ZnO growth. For the substrate, we performed the ZnO growth on the highly doped p-type Si (100) wafer, which was also used as a bottom electrode for the later piezoelectric characterization. The substrate was inserted into the reactor chamber by a load-lock, and was heated to a certain temperature for the growth. During the growth, the DEZn solution went from the canister through the liquid line to the injector at the top of the reactor chamber (**Figure 2.6**).

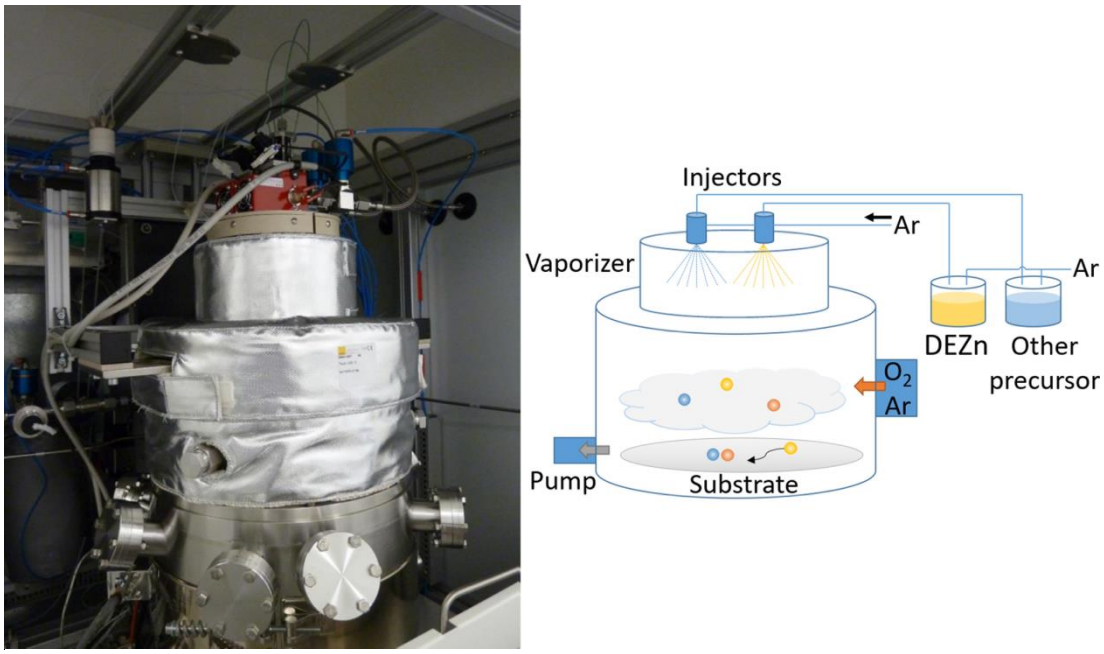

Figure 2.6: The Annealsys MC-200 PLI-MOCVD system at LMGP and its schematic diagram.

From there, it was injected into the reactor together with the Ar gas carrier. The injection rate was set to 3 Hz. After entering the chamber, the DEZn liquid is immediately vaporized by the heating at 150 °C. Then, the DEZn vapor reacted with the O_2 gas introduced from the other gas line at the lower part of the chamber. Another Ar gas was also introduced into the chamber together with the O_2 gas in order to maintain the total gas volume. The pressure in the chamber was kept constant at 3 mbar. The Zn and O atoms diffused through the gas boundary layer and deposited on the heated substrate at the bottom of the chamber, while the by-products were removed from the chamber through the vacuum line. After the growth, the substrate temperature was cooled down in Ar atmosphere using the cooling water system.

2.2 Characterizations

2.2.1 Piezoelectric characterization by piezoresponse force microscopy

Piezoresponse force microscopy (PFM) is one of the operational modes of atomic force microscopy (AFM), allowing mapping simultaneously the topography and the piezoelectric properties of materials at the micro-/nanometer scales. The AFM technique was first introduced by G. Binnig, C. Quate, and Ch. Gerber in 1986.[131] In this technique, a cantilever with a sharp tip at its end is brought into contact with (contact mode) or close to (non-contact mode) the sample surface. The tip curvature radius is on the order of nanometers. While the tip is scanned on the sample surface, the force between the tip and the sample causes a deflection of the cantilever. In case this force is changed by the different height corresponding to the contour of the sample surface, the topography of the sample can be drawn by recording the cantilever deflection. Other forces such as van der Waals forces, chemical bonding, electrostatic forces, magnetic forces, etc. can also cause the cantilever deflection, which can be employed to illustrate different phases or types of materials on the sample. Moreover, other manipulations can be performed during the scanning to extract different interesting properties of the sample. For example, a voltage can be applied on the sample using a conductive AFM tip in order to cause a deformation of the piezoelectric/ferroelectric material due to the inverse piezoelectric phenomenon. The deformation in turn leads to the cantilever deflection, which can be used to analyze the piezoelectric/ferroelectric properties of the sample. This technique is known as PFM, which was first demonstrated by P. Güthner and K. Dransfeld in 1992.[132] In their work, the PFM was used to locally polarize the ferroelectric polymer vinylidene-fluoride trifluoroethylene (PVDF-TrFE). Since then, PFM has been employed as a method to study and engineer the ferroelectric domains of various ceramics, polymers as well as semiconductor materials.

PFM have been extensively used to characterize different ZnO structures. The piezoelectric coefficient d_{33} of bulk and nanobelt ZnO was measured using PFM by Zhao et al. in 2004.[45] Their results showed that the piezoelectric coefficient of the bulk ZnO was 9.93 pm/V. On the ZnO nanobelt, it decreased from 26.7 down to 14.3 pm/V when the frequency of the applied voltage was varied from 30 kHz to 150 kHz. The dependence of the piezoelectric coefficient on the frequency was suspected due to the surface charge on the ZnO nanobelt, or the imperfect electrical contact between the bottom of the nanobelt and the conductive layer at high frequency. In 2008, Y.Yang et al. reported a giant piezoelectric coefficient d_{33} up to 110 pm/V measured by PFM in the vanadium-

doped ZnO films.[50] They also obtained a "butterfly" loop when observing the material displacement as a function of applied electrical field, suggesting a ferroelectric behavior of the film. It was suspected that the substitution of vanadium at the Zn site resulted in the appearance of switchable spontaneous polarization. However, it should be noted that there are non-piezoelectric effects such as the electrostatic effect, which can also strongly contribute to the PFM result. This is a parasitic interaction between the AFM tip/cantilever and the sample regardless of the AFM mode. D. Seol et al. have shown that the interference of the electrostatic effect can cause a misinterpretation of ferroelectric behavior on the piezoelectric material.[133] The PFM measurement on individual ZnO nanorods was performed by D. Scrymgeour et al. in 2008, which was in range of 0.4 – 9.5 pm/V.[106] Simultaneously, the resistivity of nanorods was also measured using the conductive AFM (C-AFM) mode, which is another mode of AFM that extract the current-voltage characteristics as well as the resistivity of the sample. By correlating the resistivity with the piezoelectric coefficient, they found that the piezoelectric coefficient was higher in more resistive nanorods, supporting that reduction of the screening effect can improve the piezoelectric performance. Overall, the PFM is a technique allowing characterizing the ZnO piezoelectric properties with high resolution on the nanometer scale. It does not require complex sample preparation, except on the vertical nanowire array where embedding the nanowire array in polymers is needed to avoid failed contact between the AFM tip and the sample during the scanning in contact mode. The drawbacks of PFM technique are: the scanning can be slow, the tip is worn that can affect the measurement results, piezoelectric responses need to be carefully separated with other non-piezoelectric effects to have accurate interpretation of ZnO piezoelectric properties. Nevertheless, researchers have developed new PFM setups to resolve the problems related to contact PFM. For example, Calahorra et al. demonstrated a modified PFM technique in which the tip was oscillated and "discontinuous" contacted with the sample during scanning to minimize the mechanical damage on the tip and sample.[134] S. Kim et al. performed the PFM measurement using a stiff tip and an additional applied direct current (DC) voltage to reduce the interference of the electrostatic effect to the piezoelectric responses.[135] The ability of mapping the piezoelectric responses together with the topography and other electrical properties using other AFM modes provides a powerful tool to deeply investigate the piezoelectric properties and its correlation with other properties of the ZnO structures.

2.2.1.1 Principle

The piezoelectric properties of ZnO samples were characterized by piezoresponse force microscopy (PFM) measurement using Bruker Dimension Icon atomic force microscope. This technique is based on the inverse piezoelectric phenomenon, in which a voltage is applied on the sample to cause a sample displacement. Thus, the tip has to be in contact with the sample to apply the voltage. In the PFM measurement, the AFM tip is conductive and the sample was placed directly on the chuck of the system, hence the voltage was applied to the top and bottom of the sample through the tip and the chuck (**Figure 2.7**). During the contact PFM scanning, the tip is continuously in contact with the sample surface. The tip deflection caused by the contour of the surface is recorded and eventually the topography is illustrated. At the same time, an alternating current (AC) is applied on the sample. In our setup, the bias voltage was applied from the chuck at the bottom of the sample, while the tip was grounded.

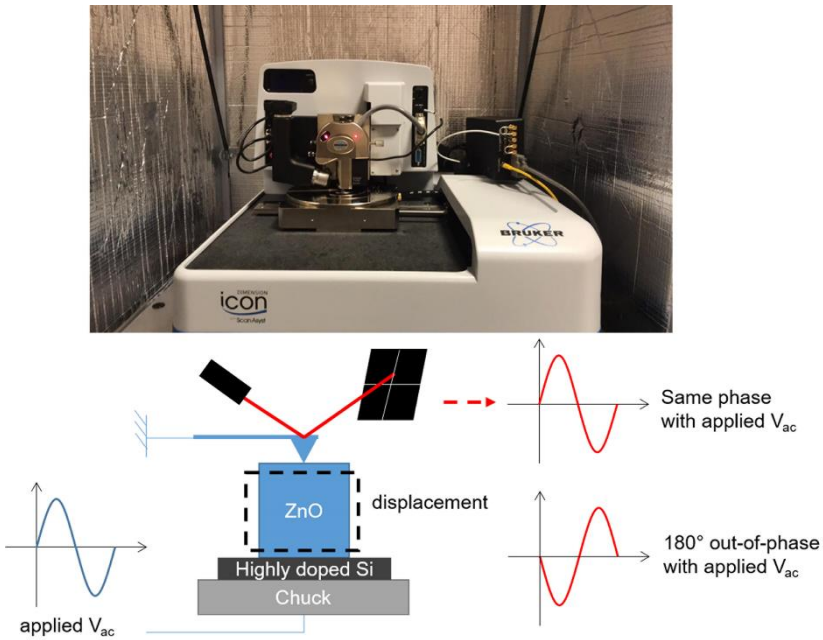

Figure 2.7: The Bruker Dimension Icon AFM system at IMEP-LAHC and its schematic.

Due to the inverse piezoelectric effect, the sample was alternatively extended and contracted with a certain amplitude and phase corresponding to the amplitude and phase of the applied AC voltage. This deformation of the sample resulted in the deflection of the probe cantilever, which was detected by the photodiode detector and demodulated using the lock-in amplifier. With this, the piezoelectric amplitude and phase images are plotted simultaneously with the topography when the tip scans over the sample surface. The tip deflection can be in the vertical and horizontal directions attributed to the combination of the piezoelectric coefficient d_{33} and d_{31} of the ZnO sample. In our work, we focus on the vertical component representing the effective d_{33} coefficient. Ideally, the amplitude of the deformation is proportional to the piezoelectric coefficient of the material, which can be expressed as follows:[133]

$$Piezoresponse\ amplitude = dV_{AC} \qquad (2.1)$$

where d is the effective d_{33} coefficient, and V_{AC} is the amplitude of the applied voltage. The deformation phase can be in-phase or 180° out-of-phase with the applied voltage, which corresponds to the polarity of the sample (**Figure 2.7**).

Electrostatic effect

Beside the piezoelectric effect, there is an electrostatic effect that can also contribute to the oscillation of the AFM cantilever during PFM measurement. This electrostatic effect originates from the interaction of charges accumulated on the AFM tip and the sample surface, which causes a force on the AFM tip.[133] The electrostatic effect signal can interfere or even dominate the measured PFM responses, leading to incorrect interpretation of piezoelectric results. Thus, it is very important to reduce the electrostatic effect signal as much as possible in the PFM measurement in order to accurately evaluate the piezoelectric properties of the material. With the electrostatic effect contribution, the piezoresponse amplitude can be described as follows:[135]

$$Piezoresponse\ amplitude = dV_{AC} + k^{-1}C_z'V_{AC}(V_{DC} - V_{SP}) \quad (2.2)$$

where k is the spring constant of the AFM cantilever, C_z' is the capacitance derivative along the z axis, V_{DC} is the direct current (DC) voltage on the tip, and V_{SP} is the surface potential difference between the tip and the sample surface. Based on the equation, the second term representing the electrostatic effect contribution can be decreased by applying an $V_{DC} = V_{SP}$, or using an AFM tip with high stiffness k.[135]

2.2.1.2 PFM measurement process

2.2.1.2.1 Tip and parameter selections

The first step before performing the PFM measurement is selecting a suitable AFM tip and parameters (applied V_{AC} frequency and amplitude) during the scanning in order to obtain correct and reliable results. Different tips, parameters were tested on various reference materials. The optimal parameters were then applied for the characterization on ZnO samples.

Tip selection

In order to reduce the interference of the electrostatic effect in the PFM measurement, the PtSi-NCH tips from Nanosensors with a high spring constant at around 43 N/m were selected. We did not use the applying V_{DC} method to reduce the electrostatic effect because the applied V_{DC} needs to be constantly calibrated to be equal to the surface potential difference V_{SP}, which can change from place to place. The applying voltage on the tip can also lead to more charge accumulation on the tip, resulting in a stronger electrostatic effect. The drawback of using high stiffness tip is more scratches can happen during PFM scanning, distorting the PFM images. However, this problem can be diminished by using datacube PFM mode, which will be described in a later section. Besides, it is necessary to change the tip when it is worn after serveral uses (**Figure 2.8**) in order to have a high resolution and good electrical contact.

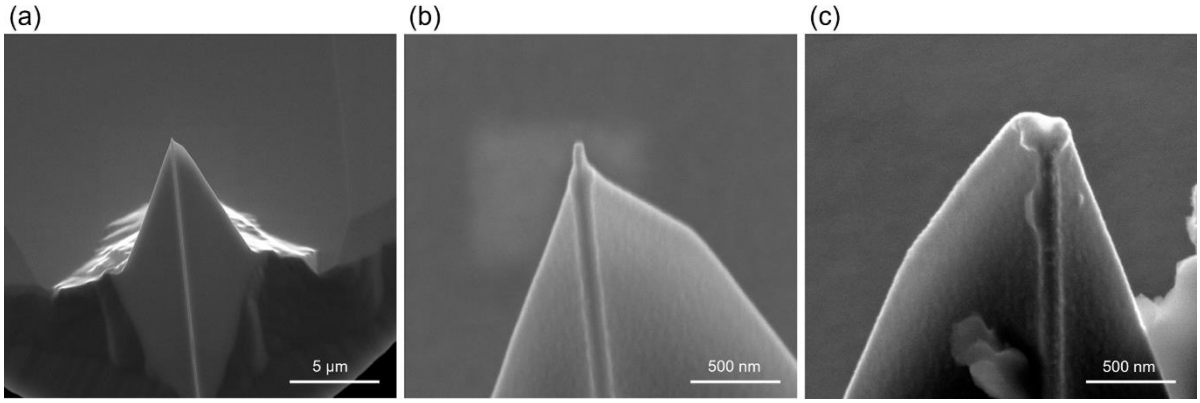

Figure 2.8: (a) FESEM image of a new PtSi-NCH tip from Nanosensors and (b) its zoom-in image, (c) FESEM images of PtSi-NCH tip after several used.

Frequency selection

To investigate the piezoresponse dependence on the applied V_{AC} frequency, the AFM tip was put in contact with the sample surface. Then, the piezoresponse – frequency relation curves were obtained by sweeping the frequency in different ranges. **Figure 2.9** shows the piezoresponse vs

frequency sweep performed on the ZnO thin film using the PtSi-NCH tip and a constant amplitude of 5 V.

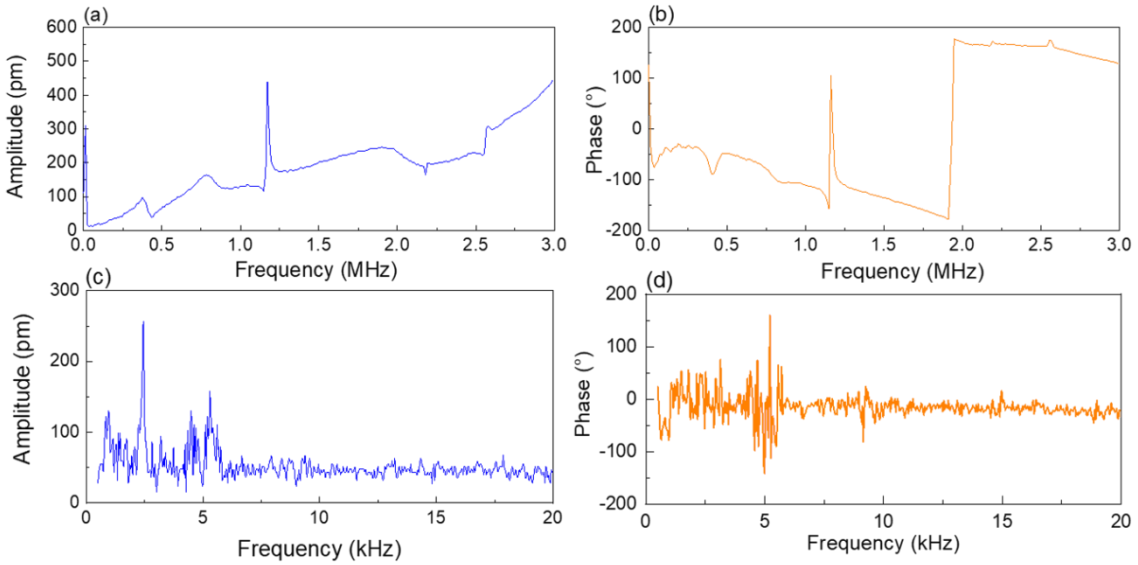

Figure 2.9: Piezoelectric amplitude and phase responses corresponding to the frequency sweep ((a) and (b)) in range of 0 – 3 MHz, and ((c) and (d)) in range of 0 – 20 kHz.

It can be seen that the piezoresponses are significantly varied with the applied V_{AC} frequency. Thus, it is important to select the suitable frequency for PFM scanning. In **Figures 2.9a and b**, the peaks are attributed to the tip resonance, contact resonance, and other mechanical mechanisms affecting output signals. The piezo amplitude and phase also exhibit abnormal values at high frequency. For instance, the phase value is supposed to be around 0 or 180°. At low frequency range, the piezo amplitude and phase responses are more stable (**Figures 2.9 c and d**). The peaks in **Figures 2.9 c and d** are caused by the background resonances coming from the system and surrounding environment, which were reported in ref.[136]. Therefore, the best frequency for PFM measurement is in the range of 7 – 20 kHz. For our experiment, we set the frequency at 15 kHz.

Amplitude selection and phase offset

After selecting the tip and frequency, we tested the piezoresponses on a reference sample periodically poled lithium niobate (PPLN) provided by Bruker. This sample has both positive (p^+) and negative (p^-) polarity domains with the same nominal piezoelectric coefficient d_{33} at 7.5 pm/V. The piezoresponse – applied V_{AC} amplitude sweeps were performed on both p^+- and p^--domains of PPLN using the PtSi-NCH tip and constant frequency at 15 kHz (**Figure 2.10**).

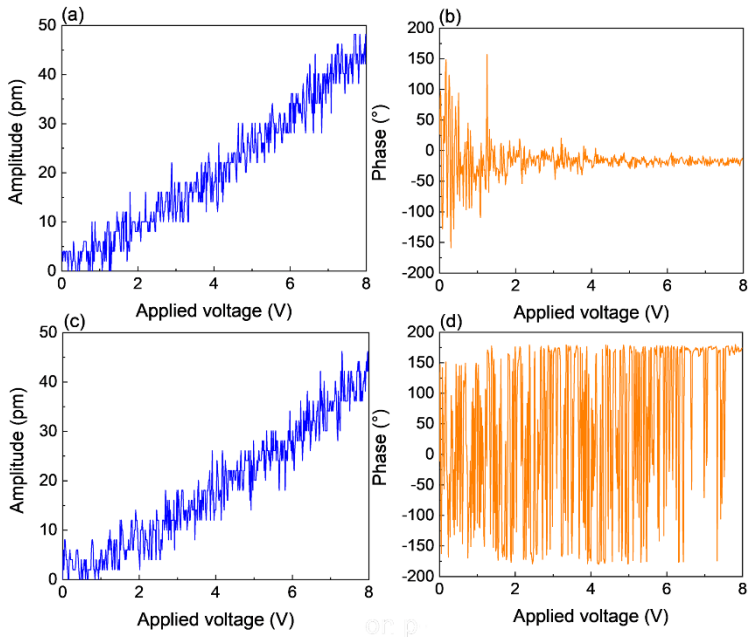

Figure 2.10: Piezoelectric amplitude and phase responses corresponding to the voltage sweep on the ((a) and (b)) p^+-domain of PPLN, and ((c) and (d)) on the p^--domain of PPLN.

The slopes on both polarity sides in **Figures 2.10a and c** have similar values around 6.25 pm/V, which is close to the nominal piezoelectric coefficient at 7.5 pm/V. The phase value on the p^+-domain is around 0°, while the phase value on the p^--domain oscillates between 180 and 180°. This is due to the display mechanism of the system, in which any phase value higher than 180° will be minus to 360°. For example, a phase value at 181° will be shown at -179°. In order to have a clearer view, we changed the phase offset in the lock-in from 0 to +90 °. With this setting, the phase value of p^+-domain was also changed from 0 to 90°, and the phase value of p^--domain is displayed at -90° (**Figure 2.11**).

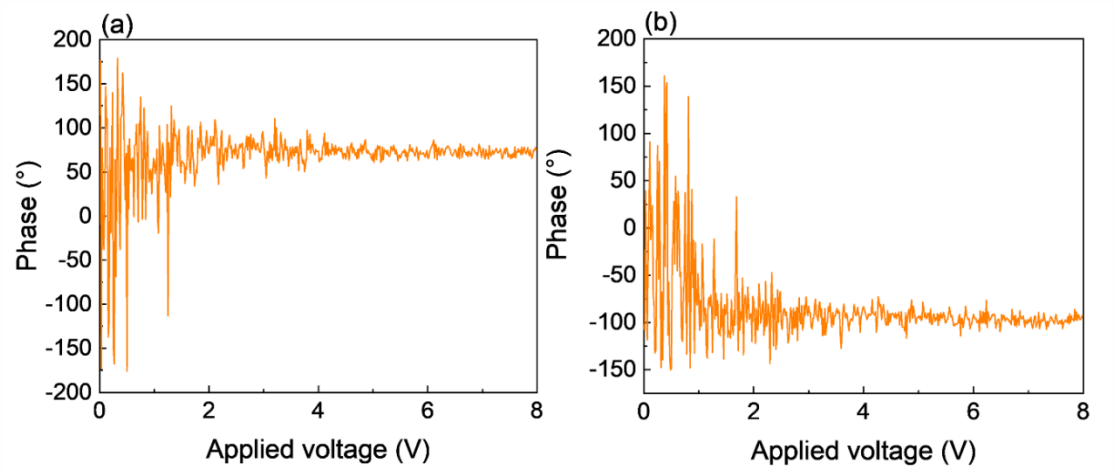

Figure 2.11: Piezoelectric phase responses corresponding to the voltage sweep on the (a) p^+-domain of PPLN, and (b) on the p^--domain of PPLN with the phase offset at +90°.

This setting also helps to distinguish more easily the polar domain from the non-polar domain. Since there is no piezoelectric effect on the non-polar domain, the unidentified phase

response on this domain has a large variation around 0°. It also can be noted in **Figure 2.11** that the phase responses are unstable at low applied voltage amplitudes due to weak piezoelectric signals. Thus, we choose a high applied voltage amplitude (5V) to reduce the noise from the measurement.

2.2.1.2.2 Signal calibration

Verification of the electrostatic effect

With the selected parameters, we verified the effectiveness of electrostatic effect removal by using the high stiffness tip. The PFM measurements on the PPLN sample using the high stiffness PtSi-NCH tip and the low stiffness SCM-PIT tip (k = 3 N/m, Bruker) were compared (**Figure 2.12**).

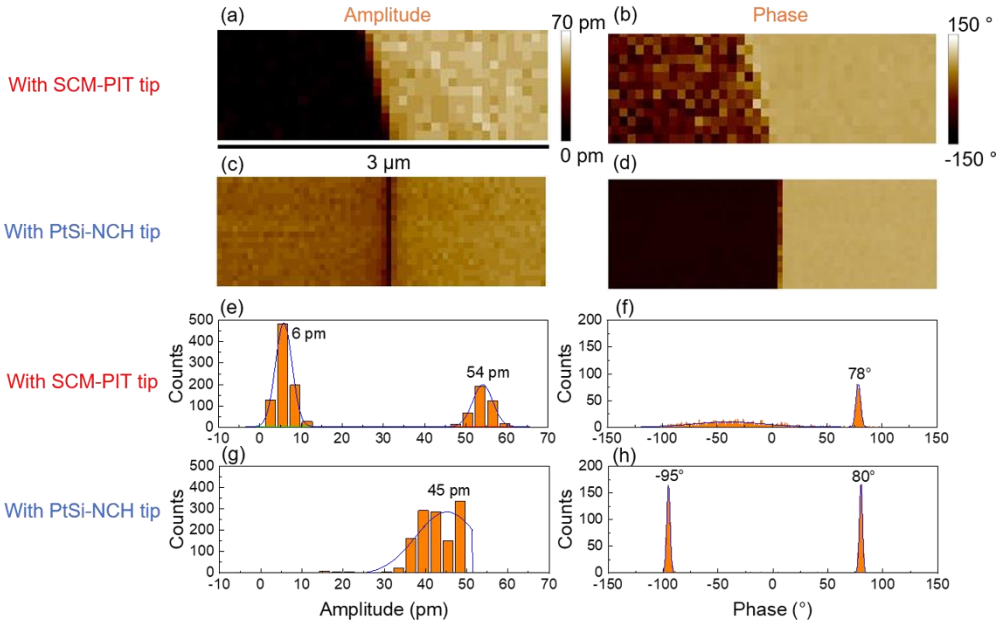

Figure 2.12: PFM scanning images on 2 polarity domains of PPLN ((a) and (b)) using SCM-PIT tip, and ((c) and (d)) using PtSi-NCH tip. (e), (f), (g) and (h) are the histograms corresponding to the PFM scanning images (a), (b), (c) and (d), respectively.

In **Figures 2.12a and e**, the piezoresponse amplitudes on two opposite polarities domains are not equal due to a strong electrostatic effect contributed to the AFM deflection when the SCM-PIT tip was used. The phase responses of p^--domain in **Figures 2.12b and f** have abnormal values. In contrast, the piezoresponse amplitudes measured by the PtSi-NCH tip are similar on both polarities, as shown in **Figures 2.12c and g**. With the applied voltage at 5V, the piezoelectric response at 45 pm corresponds to the piezoelectric coefficient at 9 pm, which is comparable with the nominal value at 7.5 pm. In **Figure 2.12h**, the phase responses on the p^+- and p^--domains show sharp values at around 80 and -95°, respectively.

We also tested the influence of V_{DC} to the electrostatic effect based on the equation (2.2). The applied V_{DC} on the AFM tips was swept from -8 to 8V (**Figure 2.13**).

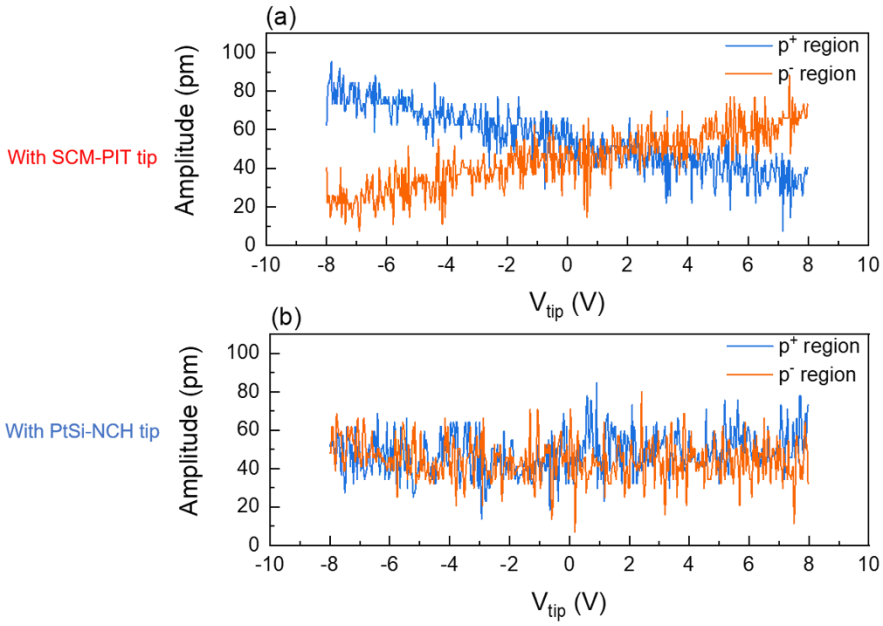

Figure 2.13: Piezoelectric amplitude responses corresponding to the applied V_{DC} sweep on two polarity domains of PPLN (a) using SCM-PIT tip, and (b) using PtSi-NCH tip.

While the SCM-PIT tip was used, the piezoelectric amplitudes are increased or decreased depending on the polarity domain with the V_{DC} variation (**Figure 2.13a**), which is in agreement with the equation (2.2). On the other hand, the piezoelectric amplitudes on both polarity domains are nearly constant regardless of the applied V_{DC} on the PtSi-tip (**Figure 2.13b**). These results show that the electrostatic effect was significantly reduced by using the high stiffness tip.

Verification of the phase response

To check the relation of the phase responses with the ZnO polarities, we performed the PFM measurements on ZnO monocrystal with identified polarities (from Crystec), and non-polar sapphire (**Figure 2.14**). The measurements were performed using the PtSi-NCH tip. The frequency and amplitude of applied V_{AC} were set at 7 kHz and 5 V, respectively.

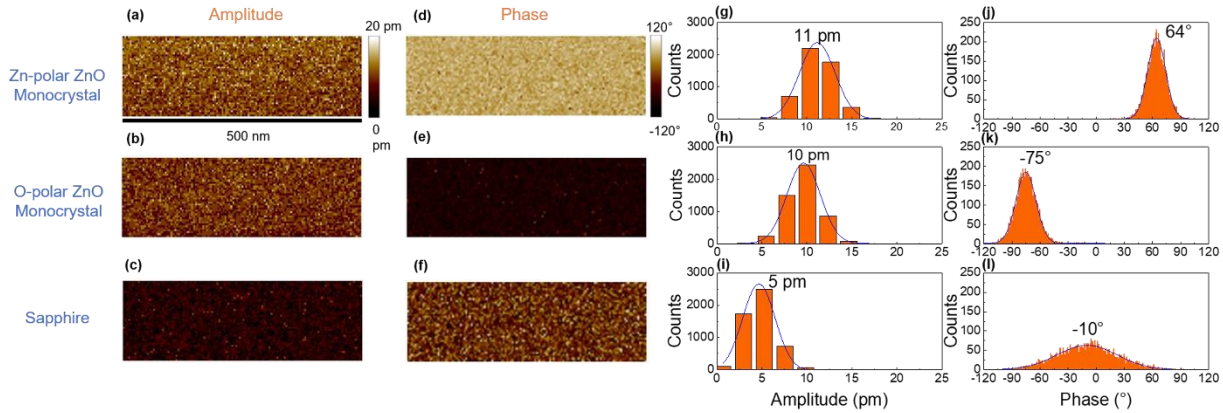

Figure 2.14: (a), (b), (c), (d), (e) and (f) PFM scanning images on different referent samples, and (g), (h), (i), (j), (k) and (l) are their corresponding histograms, respectively.

The results confirm that the ZnO with Zn polarity (positive domain) shows a positive phase response value, the ZnO with O polarity (positive domain) exhibits a negative phase response value, while the sapphire with no piezoelectric effect has its phase response broadly vary around 0 °. These results were used as references for other later PFM measurements on ZnO samples.

2.2.1.2.3 Datacube PFM

The high stiffness tip can greatly reduce the interference of the electrostatic effect during the PFM measurement. However, the tip also causes scratches on the sample surface while it is dragged during the contact PFM scanning, resulting in contact failure between the tip and the sample. To avoid this problem, the DataCube PFM mode was employed. In this mode, the tip sequentially approached, touched the sample with fixed force (i.e. 3 nN), and withdrew when moving from one position to another. For each position, the contact duration was set at 60 – 100 milliseconds to collect piezoelectric signals. The amplitude and phase data was extracted using NanoScope Analysis v200r1 software. Then, the mean values of each position were calculated and the PFM images were illustrated by using Excel and Matlab softwares.

2.2.2 Structural characterizations

2.2.2.1 Electron microscopy and atomic force microscopy

The structural properties of ZnO samples were characterized by different techniques. The morphology images of samples were captured by a FEI Quanta 250 FESEM and a Gemini300 FEI ZEISS-SEM instruments.

TEM and high-resolution TEM (HRTEM) images were captured by a JEOL 2010 LaB6 microscope operating at 200 kV with a 0.19 nm point-to-point resolution. This work was done in collaboration with E. Sarigiannidou, a research scientist at LMGP.

The topographies of ZnO samples were analyzed by AFM images, which were extracted together with the piezoelectric results from PFM measurements. The root mean square (RMS) roughness was deduced from the topography images using NanoScope Analysis v200r1 software.

2.2.2.2 X-ray diffraction and Raman spectroscopy

XRD analysis was performed by a Bruker D8 Advance diffractometer using Cu Kα1 radiation according to the Bragg−Brentano configuration. The scanning range was at 20−140° on the 2θ- scale. This work was done in collaboration with H. Roussel, a research scientist at LMGP.

Raman spectra of samples were recorded at room temperature with an excitation Ar+ laser at 488 nm using a Jobin Yvon/Horiba Labram spectrometer. The configuration using crossed polarizer and analyzer (VH) was employed to reduce the very high Si line intensity from the substrates.

2.2.2.3 Methodology of analyzing XDR results

The position, intensity and full-width-half maximum (FWHM) of diffraction peaks in the XRD pattern of ZnO samples were extracted within a fitting procedure using a Pseudo-Voigt function in Origin 2018b software. Then, their values were employed to analyze the structural orientation and quality, which are important properties for piezoelectric performance.

The orientation

The structural orientation was evaluated by the texture coefficients C_{hkl} (in percentage unit) of (hkl) plane, which was calculated by the following equation:[137]

$$C_{hkl}(\%) = \frac{\frac{I_{hkl}}{I_{0,hkl}} \times 100}{\sum_{i=1}^{N} \frac{I_{h_i k_i l_i}}{I_{0,h_i k_i l_i}}} \quad (2.3)$$

where I_{hkl} is the hkl peak intensity, $I_{0,hkl}$ is the reference hkl peak intensity from the 00-036-1451 file of the International Center for Diffraction Data (ICDD), and N is the number of peaks considered.

The homogeneous strain

The homogeneous strain expresses the mean residual strain inside the ZnO structure at the end of the fabrication process. This strain causes a variation of the lattice parameter in the whole material structure, leading to a shift of the diffraction peak from its theoretical value in the XRD pattern. Thus, the homogeneous strain can be estimated by comparing the actual value with its theoretical value. The actual *c*-lattice value was deduced from the 002 diffraction peak position by using Bragg's law equation:

$$\lambda = 2d \sin\theta \quad (2.4)$$

where λ is the wavelength of the Kα1(Cu) source equal to 0.15406 nm, θ is the Bragg angle of the 002 diffraction peak, d is the spacing between (002) planes and equal to half the *c*-lattice parameter in the wurtzite structure. Then, the homogeneous strain (in percentage) was calculated as follows:

$$\varepsilon_{hs} = \frac{c - c_o}{c_o} \quad (2.5)$$

where c_o = 5.2066 Å is the theoretical *c*-lattice parameter of wurtzite ZnO extracted from the 00-036-1451 ICDD file.

The inhomogeneous strain and crystallite size

The ZnO lattice can be locally distorted by the presence of microstructural defects, causing an inhomogeneous strain. This strain and the limit of crystallite size both contribute to the broadening of the diffraction peaks in the XRD pattern. Those characters can be estimated by using the Williamson-Hall method. By assuming that the peaks are mainly described by a Gaussian function, the FWHM of diffraction peak (β) can be expressed as follows:[138,139]

$$\beta^2 = \beta_S^2 + \beta_D^2 + \beta_{instrument}^2 \quad (2.6)$$

where $\beta_S = C\varepsilon_{IS} \tan\theta$ represents the peak broadening contribution from the inhomogeneous strain, $\beta_D = \frac{K\lambda}{D\cos\theta}$ is the peak broadening contribution from the crystallite size, $\beta_{instrument}$ is the peak broadening caused by the XRD system, θ is the Bragg angle, C is a constant equal to 4, K is a constant

depending on the shape of the particles and typically is equal to 0.9, ε_{IS} is the inhomogeneous strain, and L is the average crystallite size.[138,139] The instrument broadening was measured by using the referent iodine oxides (I_2O_3) sample, and was then subtracted from the measured FWHM of diffraction peak. After that, the equation (2.6) can be rearranged as follows:

$$(\beta \cos\theta)^2 = (C\varepsilon_{IS} \sin\theta)^2 + \left(\frac{K\lambda}{L}\right)^2 \qquad (2.7)$$

A graph of $(\beta\cos\theta)^2$ vs $(\sin\theta)^2$ was plotted and fitted with a linear curve function. Then, the inhomogeneous strain (ε_{IS}) and the crystallite size (L) were deduced from the slope and the Y-intercept of the linear curve, respectively.

2.2.3 Optical characterization

The 5 K cathodoluminescence (CL) measurements were performed with an FEI Inspect F50 FESEM instrument equipped with a liquid helium-cooled stage. A 550 nm focal length monochromator equipped with a diffraction grating of 600 grooves/mm was used to analyze the CL signal. The CL spectra were obtained with a thermoelectrically cooled silicon CCD detector. This work was done in collaboration with F. Donatini, a research scientist at Institut Néel.

Besides, a UV–Vis-NIR Perkin Elmer Lambda 950 spectrometer was used to measure the optical transmittance (250 – 1000 nm in wavelength) of some ZnO samples deposited on quartz substrate. The results will be discussed in Chapter 5.

2.2.4 Electrical characterizations

The resistivity of ZnO samples was measured by using transmission line measurement (TLM) method. Before the measurement, a series of contact electrodes with various distances between them were deposited on the ZnO sample surface using photolithography and an e-beam evaporator followed by lift-off processes. The rectangle contact electrodes were made of 50 nm-thick nickel (Ni) and 120 nm-thick gold (Au) layers. Its dimensions are around 196 µm in width (W) and 92 µm in length (L) (**Figure 2.15**). This work was done in collaboration with Y. Guerfi and S. Boubenia, postdocs at LTM.

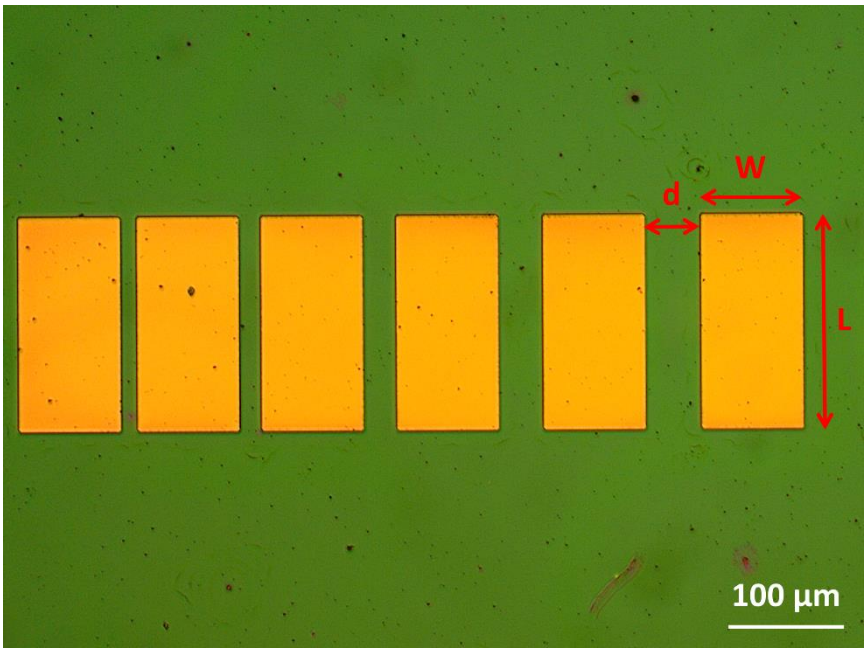

Figure 2.15: Metallic electrodes deposited on the ZnO sample surface for TLM.

Then, the electrical measurements were performed using the Karl Suss PM8 system. For each adjacent electrode pair, a constant current was applied and voltage was measured between them. The resistance (R_{Total}) obtained from the I–V curve of each electrode pair is a sum of the metallic electrode resistance (R_m), the contact resistance (R_c) at the electrode/sample interface, and the sample resistance between the electrode pair, which can be described as follows:

$$R_{Total} = 2.R_m + 2.R_c + \frac{R_S}{W}.d \qquad (2.8)$$

where R_s is the sheet resistance of the sample, and d is the distance between the electrode (**Figure 2.15**). By assuming that the electrode resistance and the contact resistance are constant, the variation of the measured resistance (R_{Total}) with the distance (d) was fitted by a linear function. The sheet resistance (R_s) as well as the resistivity of the ZnO layer was extracted from the linear curve slope.

The charge carrier density and mobility of the ZnO samples were also determined by using Van der Pauw and Hall-effect measurement method. Similar photolithography and lift-off process was carried out to form the metallic contact electrode. Then, the measurements were performed using a home-made station.

2.3. Aluminum-doped ZnO (AZO) growth by ALD

In the last part of this thesis, several AZO thin films were prepared and used as the bottom electrodes and the growth platforms for the following ZnO NW growth by PLI-MOCVD. These thin films were deposited on Si and quartz substrates by atomic layer deposition (ALD) process using a Cambridge NanoTech Fiji F200 system. Diethylzinc (DEZn) and deionized (DI) water vapor were used as as the Zn- and O- precursors. For the Al-dopant, the trimethyl aluminum (TMA) as Al-precursor

was employed. The growth was performed at 250 °C. The number of cycle was varied in order to adjust the Al-dopant concentration and the film thickness. The results willbe discussed in Chapter 5. The ALD depositions were done in collaboration with G. Gay and C. Perret, research scientists at LTM.

2.4 Summary of the chapter

The ZnO growth by MOCVD has been developed since a few decades ago, but there are very few investigations for piezoelectric applications. Despite numerous reports about the effects of growth conditions on ZnO structural, optical and electrical properties, the impacts on the piezoelectric properties as well as its correlation with other properties have not been fully explored yet. Nevertheless, some results supported that the modification of ZnO properties by adjusting the MOCVD growth condition can lead to a strong increase of its piezoelectric coefficient. In this thesis, the ZnO growth is performed by the PLI-MOCVD process. The flexibility and precision of controlling the growth conditions allows studying the effects of individual parameters on the ZnO formation. Besides, the AFM-PFM combined with other characterization techniques provide powerful tools to analyze the ZnO properties. In particular, my work focuses on investigating the influence of the growth conditions on the ZnO polarity and piezoelectric coefficient as well as their correlations with other properties, on which the information is still missing in the literature so far. Based on results, the method to improve the piezoelectric efficiency can be revealed. To do this, the first step is to study the effects of PLI-MOCVD parameters on the ZnO growth.

Chapter 3
Effect of temperature during the PLI-MOCVD growth and the post-thermal annealing on the ZnO properties

From the literature, it can be seen that the ZnO piezoelectric properties can be strongly influenced by its growth conditions. Thus, it is very important to understand as well as to control the parameters of the PLI-MOCVD process in order to improve the ZnO piezoelectric performance. The first objective of this thesis is to study the effect of the growth temperature on the ZnO growth during the PLI-MOCVD process, since it is the parameter that plays a crucial role in the ZnO formation. During the growth, it provides energy for the decomposition of chemical precursors, enhances the diffusion, adsorption, and desorption of ad-atoms on the substrate. Thus, it directly affects the chemical reactions, which in turn influences the formation mechanisms and the growth rate as well as the properties of the ZnO structure. The morphology transition from thin films to nanowires along with the improvement in crystal quality of ZnO and the enhancement of its piezoelectric efficiency were achieved when the growth temperature was raised. After that, an extended study on the effect of post-annealing at high temperature was also performed. The impact of temperature in both the growth and the post-annealing on ZnO properties is described in detail.

3.1 Effect of growth temperature

3.1.1 Introduction and objectives

Many reports have demonstrated that the temperature can significantly influence the ZnO growth using MOCVD process.[123,124,140] For example, K. Bang et al. presented the different growth regimes in MOCVD along with the variation of morphologies (**Figure 3.1**), structural, optical, and electrical properties of ZnO films by increasing the growth temperature from 250 to 720 °C.[122] In the work of G. Malandrino et al., the crystallinity of ZnO deposits on quartz was improved with the growth temperature.[124] Y. Chen et al. reported the impact of the growth temperature on the premature coalescence of nuclei and growth texture.[121] By initiating the growth at 350 °C to decrease the magnitude of the premature coalescence process, then increasing the temperature to 400 °C in following growth, the texture of ZnO films were greatly improved comparing to the single step growth either at 350 or 400 °C. Moreover, J. Park et al. demonstrated the morphology transition of ZnO from thin films to nanowires on sapphire by raising the growth temperature from 200 to 380 °C.[123] This was explained due to the enhancement of ad-atom diffusion at high temperature leading to the anisotropic growth. While the structural, optical and electrical properties were thoroughly investigated, the piezoelectric property as well as its correlation with other properties has not been completely elucidated yet.

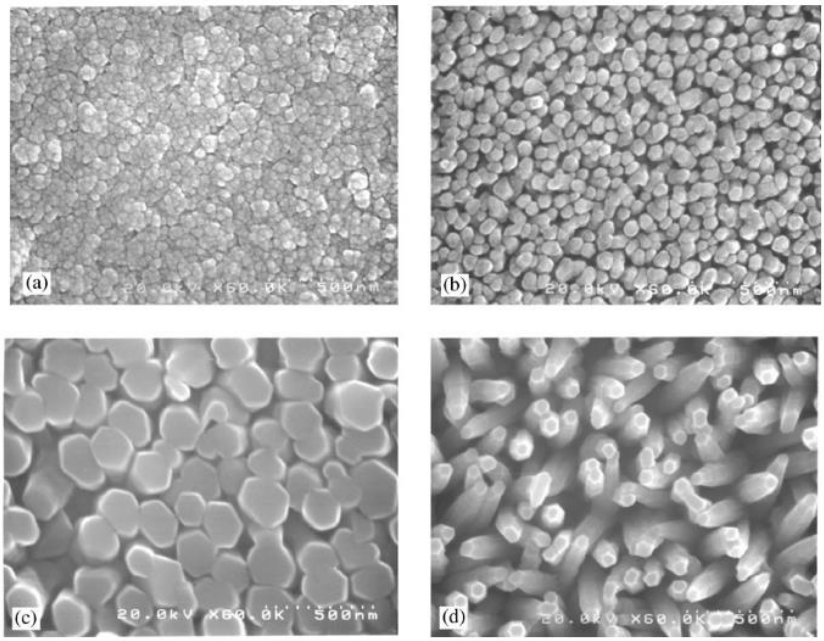

Figure 3.1: Top-view SEM images of ZnO samples grown on GaAs (001) substrates by MOCVD at (a) 450 °C, (b) 550 °C, (c) 650 °C, and (d) 720 °C.[122]

In the first part of Chapter 3, we investigated the effect of growth temperature on the properties of ZnO grown on Si substrates by PLI-MOCVD. By tuning the growth temperature in the range of 400 – 750 °C, the morphology of ZnO was gradually changed from thin film to nanowires. The structural, optical, electrical, and piezoelectric properties of ZnO deposits are analyzed in detail by using FESEM, TEM, XRD, Raman spectroscopy, CL and PFM measurements. This work was published as Q.C. Bui et al. "Morphology Transition of ZnO from Thin Film to Nanowires on Silicon and its Correlated Enhanced Zinc Polarity Uniformity and Piezoelectric Responses" in *ACS Appl. Mater. Interfaces*, 2020, **12**, 29583.

3.1.2 Experiment

3.1.2.1 ZnO thin films and nanowires grown by PLI-MOCVD

The ZnO growths were performed by using an Annealsys MC-200 MOCVD system. The heavily doped p-type Si (100) was used as a substrate and a bottom electrode for the later PFM measurements. The zinc chemical precursor was a solution of DEZn mixed with a cyclohexane solution which was injected into the chamber with the Ar gas as a gas carrier. The O_2 gas was used as the O precursor. More details about the precursors of the growth are described in **Section 2.1.3**. The flow rates of DEZn solution and O_2 molecules were fixed to 0.5 g/min and 500 sccm, respectively. The chamber pressure was kept constant at 3 mbar during the growth. These initial growth conditions were based on the works of S. Brochen and T. Cossuet, former PhD students at LMGP. They optimized the PLI-MOCVD growth process in order to have a high structural quality ZnO thin film. The substrate temperatures was varied from 400 to 750 °C for this investigation.

3.1.2.2 Characterizations

The structural, optical, electrical and piezoelectric properties of ZnO samples were analyzed by using different characterization techniques, as described in **Section 2.2**. The morphologies of ZnO

samples were studied by field-emission scanning electron microscopy (Quanta 250 FEI FEG-SEM). Their XRD patterns were recorded in the range of 20−140° at the 2θ- scale by a Bruker D8 Advance diffractometer using CuKα1 radiation according to the Bragg-Brentano configuration. Raman scattering spectra of ZnO samples were obtained at room temperature using a Jobin Yvon/Horiba Labram spectrometer equipped with a liquid nitrogen-cooled charge-coupled device (CCD) detector. It was performed in cross-polarization to reduce the signal coming from the Si substrate. A light source was the 488 nm excitation line of an Ar^+ laser with a power of about 1 mW. TEM and high-resolution TEM (HRTEM) images were captured by using a JEOL 2010 LaB_6 microscope operating at 200 kV with a 0.19 nm point-to-point resolution. TEM lamellas were prepared in cross-section by tripod polishing followed by argon ion milling according to standard techniques. The cathodoluminescence measurements were performed at 5K by using as Inspect F50 FESEM instrument equipped with a liquid helium-cooled stage. The resistivity of thin films was measured by transmission line measurement (TLM) method. The piezoelectric properties of thin film and NWs were measured by piezoresponse force microscopy (Bruker Dimension Icon AFM).

3.1.3 Results

3.1.3.1 Morphology transitions of ZnO deposits

The top-view and cross-sectional-view FESEM images in **Figure 3.2** displayed the morphology of ZnO grown by PLI-MOCVD at different growth temperatures ranging from 400 to 750 °C. In **Figures 3.2a-d**, the images exhibit that ZnO deposited at 400 – 550 °C are thin films composed of stacked grains. It also can be seen in their top-view images that the grain size is increased with the growth temperature, which is marked by the formation of highly elongated grains at 550 °C. In detail, the mean grain size measured from the top-view images of these ZnO stacked thin films increases from 51 to 60 nm as growth temperature is raised from 400 to 550 °C.

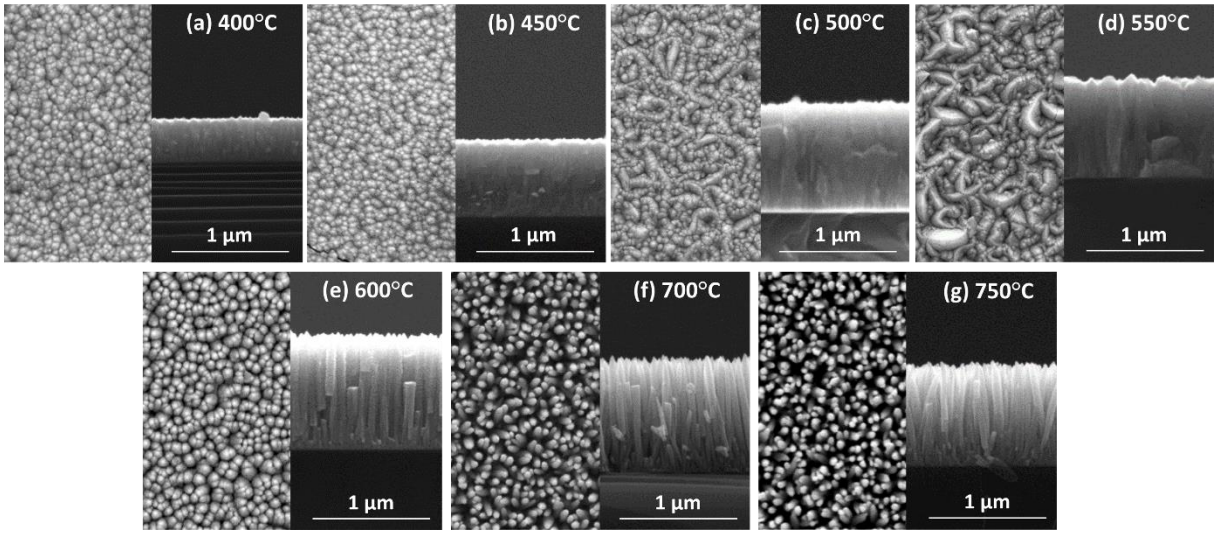

Figure 3.2: Top- (left) and cross-sectional-view (right) FESEM images of ZnO deposits grown by PLI-MOCVD for a given growth temperature of (a) 400, (b) 450, (c) 500, (d) 550, (e) 600, (f) 700, and (g) 750 °C.

In **Figure 3.2e**, the image shows that the morphology of ZnO deposited at 600 °C was changed from a stacked thin film to a columnar thin film, which is composed of vertically aligned compact nanocolumns. When the growth temperature was further increased to 700 and 750 °C, vertically aligned dense ZnO nanowire arrays were formed, as shown in **Figures 3.2f-g**. The ZnO nanowire density is 1.73 x 10^{10} nanowires/cm^2 at 700 °C, but it is slightly decreased to 1.48 x 10^{10} nanowires/cm^2 at 750 °C.

3.1.3.2 Growth rate of ZnO deposits

Figure 3.3 presents the Arrhenius plot of the ZnO deposited by PLI-MOCVD process, in which the logarithm of the growth rate is plotted against the reciprocal of the growth temperature. The mean growth rate was deduced by the ratio of film thickness over growth time, or by the ratio of nanowire length over growth time. The growth rate strongly increases from 0.4 to 1.9 nm/s when the growth temperature is increased from 400 to 550 °C, revealing the surface reaction-limited growth regime. Based on the linear fit in this regime, the activation energy of reaction in the MOCVD chamber was deduced from its slope, showing a value around 40 kJ/mol. This result is similar to the value of 38.4 kJ/mol reported in Ref.[108]. The growth rate stops increasing and is constantly maintained at around 1.9 nm/s when the growth temperature is increased from 550 to 700 °C, indicating the occurrence of the mass transport-limited growth regime. Notably, the morphology transition from stacked thin film to columnar thin films and then to nanowires also occurred in this temperature range. The growth rate of nanowires starts decreasing to the value of 1.7 nm/s when the temperature is further increased to 750 °C, indicating the strong desorption of Zn and O ad-atoms at higher growth temperature.

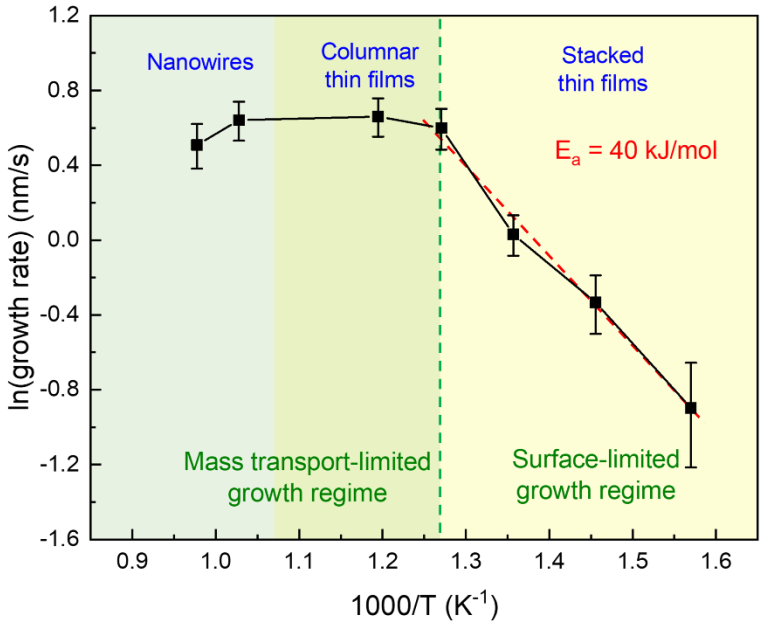

Figure 3.3: Growth rate of ZnO deposits grown by PLI-MOCVD vs reciprocal growth temperature.

3.1.3.3 Structural properties of ZnO deposits: growth texture, strain and grain size

X-ray diffraction

Figure 3.4 shows the XRD patterns of ZnO stacked thin films, columnar thin films, and nanowires deposited by PLI-MOCVD at different temperatures. Beside the diffraction peaks of the Si substrate, the diffraction peaks located at 31.8, 34.4, 36.3, 47.5, 56.6, 62.9, and 81.4° in their patterns were assigned to the 100, 002, 101, 102, 110, 103, 104 diffraction peaks of the ZnO wurtzite structure, respectively, as indicated by the International Centre for Diffraction Data (ICDD) file labeled 00-036-1451. In all ZnO samples, the 002 diffraction peak has the intensity significantly higher compared to the intensities of other ZnO diffraction peaks, signifying that the ZnO was grown preferentially along the polar *c*-axis. The 002 texture coefficients of ZnO samples were calculated based on the diffraction peak intensities, as described in **Section 2.2.2**. Additionally, the position values (θ) of diffraction peaks and their full-width-at-half-maximum (FWHM) values were also employed to analyze the strains and crystallite sizes of ZnO structures (see **Section 2.2.2**). The 002 texture coefficient, homogeneous as well as the inhomogeneous strains and crystallite size deduced from Williamson-Hall plot is represented in **Figure 3.5**. Since there are large differences in the strain and crystallite size among crystalline planes of the ZnO wurtzite structure, especially in ZnO NWs, the average inhomogeneous strain and crystallite size deduced from the Williamson-Hall plot can have a large error. To avoid this problem, we only took into account the values of 002, 004 and 006 peaks to perfom this method.

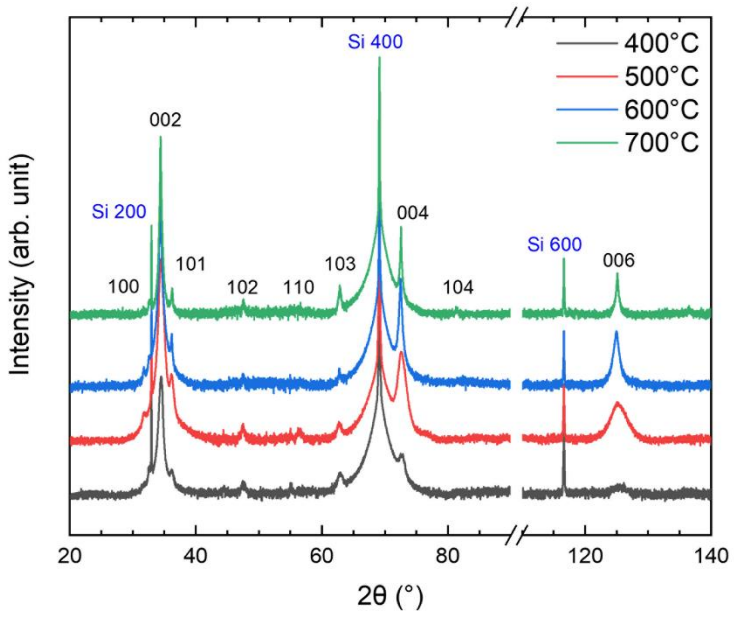

Figure 3.4: XRD patterns of ZnO deposits grown by PLI-MOCVD for a given growth temperature in the range of 400 – 700 °C. The intensity is plotted in logarithm scale.

In **Figure 3.5a**, the 002 texture coefficients of all ZnO samples are higher than 94%, suggesting their highly *c*-axis oriented structures. As the growth temperature is increased from 400 to 600 °C, the 002 texture coefficient increases from 94.5 to 99.7 %, corresponding to the improvement of structure orientation along the polar *c*-axis when the ZnO morphology changes from

stacked to columnar thin film. However, the 002 texture coefficient slightly decreases to 99.0 % when the growth temperature is increased to 750 °C. This is due to the morphology of ZnO grown at 700 and 750 °C comprises of isolated nanowires, which is less dense compared to the columnar thin film grown at 600 °C. In addition, the signal of (002) plane from the inclined nanowires are absence in the pattern due to the XRD configuration. Those reasons lead to the lower 002 peak intensity as well as lower 002 texture coefficient in ZnO nanowire arrays.

In **Figure 3.5b**, the residual homogeneous strain along the polar *c*-axis in stacked thin films grown at 400 – 500 °C shows a negative value at around -0.15%. This indicates a compressive strain of stacked thin films originates from the Volmer-Weber growth mode: The growth of polycrystalline ZnO thin film initiates with the formation of isolated islands, followed by the coalescence process of these islands, during which a significant tensile biaxial stress is generated and converted into the compressive strain along the *c*-axis.[141] Interestingly, the compressive strain along the polar *c*-axis is relieved and progressively becomes tensile when the growth temperature is increased from 500 to 600 °C, correlating to the morphology transition from stacked thin film to columnar thin film. The homogeneous strain of nanowire array grown at 700 and 750 °C has the value close to zero thanks to the efficient strain relaxation on their lateral surfaces.[142]

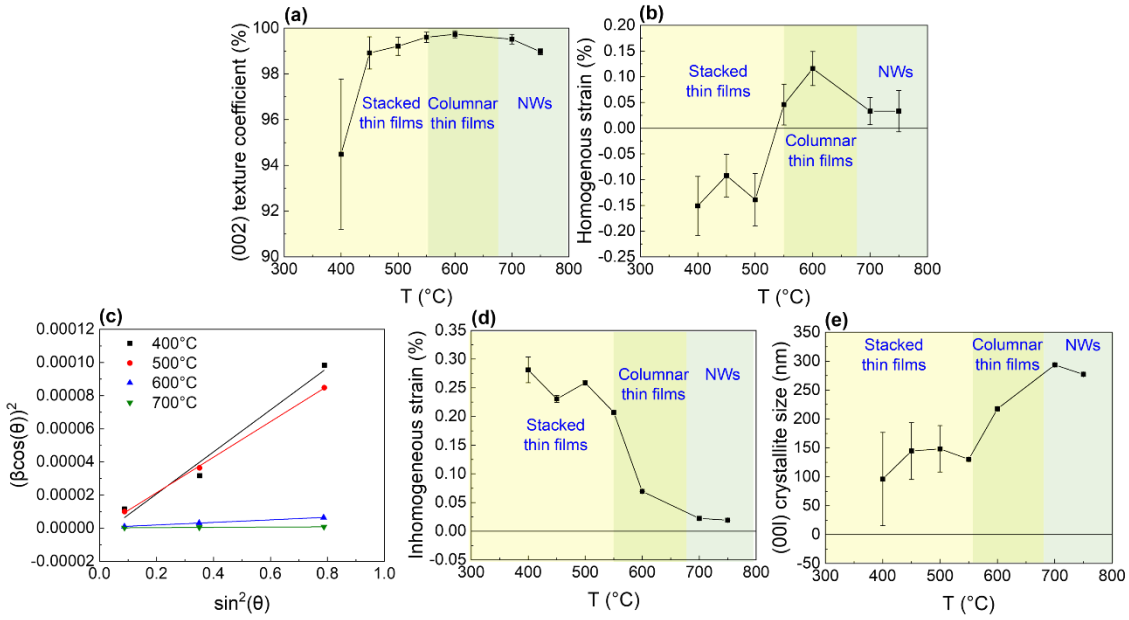

Figure 3.5: (a) Texture coefficient of the (002) diffraction peak vs growth temperature. (b) Homogeneous strain vs growth temperature. (c) Williamson-Hall plot of ZnO deposits grown by PLI-MOCVD for a given growth temperature in the range of 400 – 750 °C. (d) Inhomogeneous strain vs growth temperature deduced from the Williamson-Hall plot. (e) (00*l*) crystallite size vs growth temperature inferred from the Williamson-Hall plot.

The position and FWHM of the 002, 004, and 006 diffraction peaks in the XRD patterns of stacked thin films, columnar thin films, and nanowires in **Figure 3.4** were employed to estimate the crystallite size and inhomogeneous strain of these ZnO samples estimated by using the Williamson-Hall method (see **Section 2.2.2**). The Williamson-Hall plots are presented in **Figure 3.5c**. The inhomogeneous strain and mean crystallite size was deduced from the fitted linear curve slope and

Y-intercept,[138,139] respectively, and presented in **Figure 3.5d-e**. The results in **Figure 3.5d** show that the inhomogeneous strain caused by the microstructural defects decreases from 0.28 to 0.01 % as growth temperature is increased from 400 to 750 °C. This suggests that the density of defects inside ZnO structure was gradually decreased with the morphology transition from stacked thin films to nanowires. In **Figure 3.5d**, the mean crystallite size of stacked thin films in the vertical direction increases from 82 to 128 nm when the growth temperature is increased from 400 to 550°C. Then, it increases rapidly from 128 to 277 nm when the growth temperature is increased from 550 to 750 °C, corresponding to the transition from stacked thin film to columnar thin film and nanowires.

Raman scattering spectra

The Raman spectra of ZnO samples grown by PLI-MOCVD are shown in **Figure 3.6**. Two Raman lines located at 99 and 438 cm^{-1} are assigned to the E_2^{low} and E_2^{high} modes of the wurtzite structure, respectively.[143] It can be seen that their intensities increase dramatically with the increase of the growth temperature as well as the morphology transition from stacked thin film to nanowires, indicating a strong improvement of the ZnO crystallinity. The position of the E_2^{high} line in the ZnO nanowire array grown at 700 °C also has its value of 438.3 cm^{-1}, which is closer to the value of bulk ZnO at 438 cm^{-1}. This again expresses the strain relaxation in the ZnO nanowire array. Other Raman lines of ZnO wurtzite structure such as A_1(LO) and E_1(TO) modes are hardly detected due to the low signal of the ZnO layer as compared to the signal of the Si substrate, even when the cross-polarization was used. Furthermore, two broad bands centered around 1360 and 1580 – 1600 cm^{-1} present in the Raman spectra of all ZnO samples. These are signals of the C-C bonds, originating from the remaining organic molecules related to the by-products of DEZn chemical precursor and cyclohexane solvent after the PLI-MOCVD process.[144]

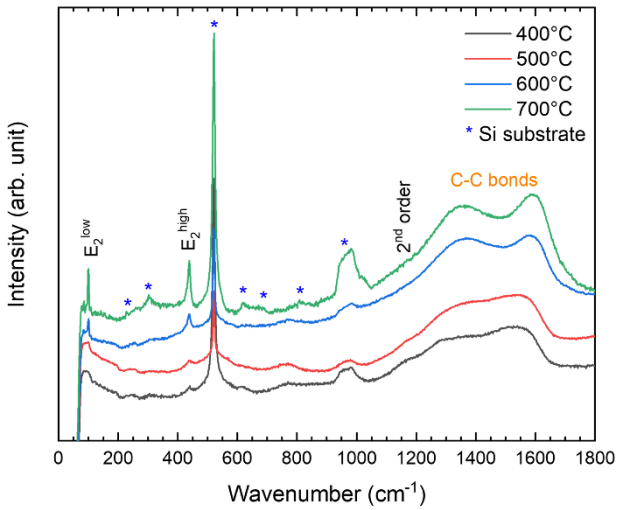

Figure 3.6: Raman spectra of ZnO deposits grown by PLI-MOCVD for a given growth temperature in the range of 400 – 700 °C.

3.1.3.4 Nucleation mechanisms of ZnO nanowires

Figures 3.7d-e present the TEM images ZnO nanowires grown at 700 °C by PLI-MOCVD, demonstrating that the nucleation of nanowires occurred directly on a very thin, amorphous, native

SiO_x layer without the formation of a continuous ZnO wetting layer. The transition from thin films to nanowires by increasing the growth temperature was demonstrated in the work of J. Park et al., where the ZnO was deposited by MOCVD on sapphire substrate.[123] Since the sapphire substrate has an epitaxial relation with the ZnO, the sapphire substrate orientation can strongly affect the morphology of ZnO.[145] The nucleation and the growth mechanism of ZnO on the sapphire substrate were driven by the epitaxial relation between them. In our case, the ZnO nanowires were grown directly on Si substrates, in which there is no epitaxial relationship between the substrate and the ZnO layer, as shown in **Figure 3.7e**. It is also worth to mention that our ZnO nanowires were grown directly on Si substrates by the PLI-MOCVD process without using any seed/wetting layers, which is opposite to the deposition of ZnO nanowires by chemical bath deposition where the polycrystalline ZnO seed layer is required.[146] The HRTEM image in **Figure 3.7e** and the selected area diffraction (SAED) patterns in **Figure 3.7c** at the bottom of ZnO nanowires displays that a polycrystalline thin layer with a thickness of several tens of nanometers was formed at the beginning of the nanowire growth. With the thickening of the growth, the grains with the *c*-axis orientation prevailed over the grains oriented along other directions during a competitive process. Consequently, the growth was developed vertically along the *c*-axis, leading to the formation of isolated *c*-axis oriented nanowires with a high density, as revealed in the TEM image in **Figure 3.7a** and the SAED pattern in **Figure 3.7b**. The formation of nanowires at 700 and 750 °C can be explained as follows: The strong desorption of zinc and oxygen ad-atoms at high growth temperature causes the creation of isolated grains. The high growth temperature also enhances the surface diffusion of zinc and oxygen ad-atoms along their sidewalls to reach the (001) growth plane, leading to the elongation along the *c*-axis on those isolated grains, resulting in the formation of isolated nanowires.

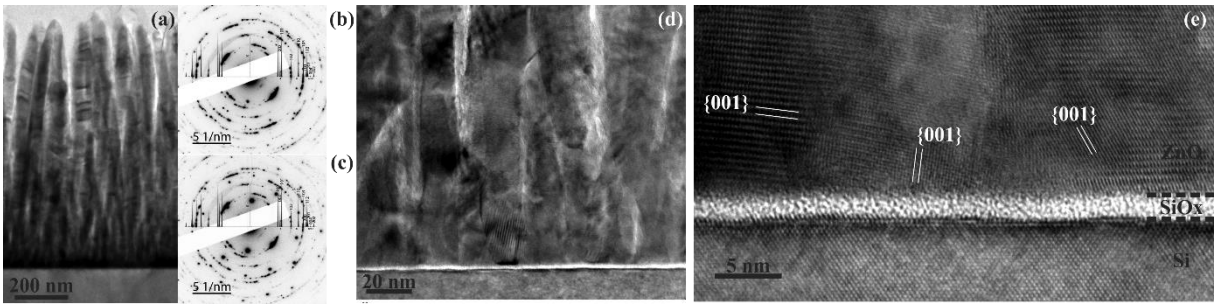

Figure 3.7: (a) Low magnification TEM image of nanowires grown at 700 °C by PLI-MOCVD. (b-c) SAED patterns recorded at the top and at the bottom of nanowires, respectively. (d-e) TEM and HRTEM images at the ZnO/Si interface, respectively.

3.1.3.5 Optical properties of ZnO deposits.

The CL spectra in **Figure 3.8** shows that the near-band-edge (NBE) emissions of the stacked and columnar thin films grown at 400 – 600 °C are the asymmetric bands lying in the range of 3.0 – 3.7 eV. The NBE emission becomes a highly structured, sharp band in nanowires grown at 700 and 750 °C. Correspondingly, the CL intensity of the NBE emission significantly increases 650 times in nanowires compared to the thin films. These observations again signify a great improvement of the crystallinity together with the optical quality of ZnO structure as the growth temperature is raised, which is in agreement with XRD and Raman scattering measurements.

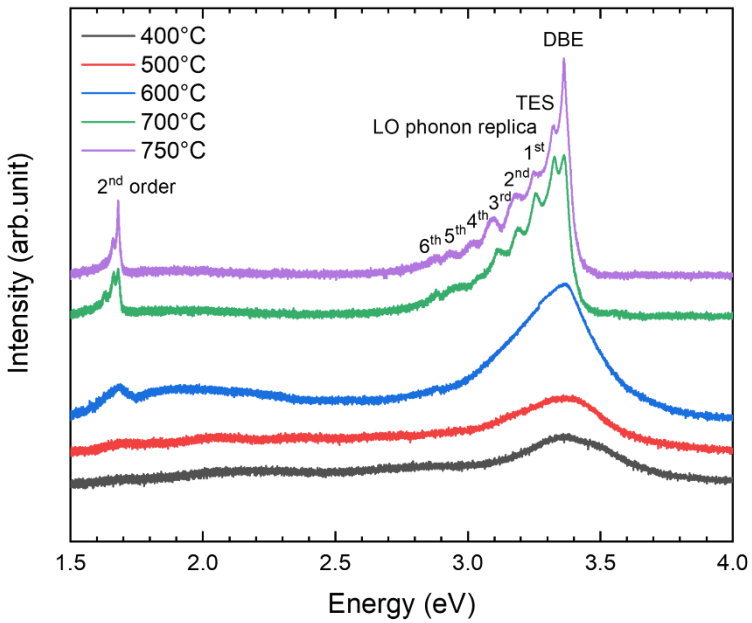

Figure 3.8: 5 K CL spectra of ZnO deposits grown by PLI-MOCVD for a given growth temperature in the range of 400 – 750 °C. The intensity is plotted in logarithm scale.

In the CL spectra of nanowires, the NBE emission line with the highest intensity located at 3.362 eV is attributed to radiative transitions involving neutral donor-bound A-excitons (DBE). In the I nomenclature,[147,148] this radiative transitions can be assigned to the I_6 line caused by the existence of Al substituting for Zn sites (Al_{Zn}), which can acts as shallow donors with an ionization energy of 51.5 meV. This line can also be assigned to the Z_3 and Z_4 lines, which are due to the incorporation of carbon species.[67] The presence of Al_{Zn} defects may be due to the residual contamination in our MOCVD chamber, and the incorporation of carbon species can be generated by the decomposition of the DEZn and cyclohexane solvent during the growth, which is also suggested in Raman spectra. However, no signal of hydrogen-related defect was detected in Raman spectra. Thus, this excludes the roles of I_4 and I_5 lines,[149,150] which is different from the ZnO nanowires grown by chemical bath deposition.[117] The second-most intense line located at 3.326 eV is attributed to radiative transitions involving two-electron satellites (TES), which could be generated by the 2s state relating to Al_{Zn} or the 2p state relating to Z_3 line. Since the theoretical position is around 3.323 eV, the shift of this line suggests that there is an additional contribution. Interestingly, the existence of basal-plane stacking faults (BSFs) in the center of nanowires was revealed by the TEM and HRTEM images in **Figure 3.9**, which is identified as a I_1-type stacking fault with the plane stacking sequence …ABABABCACACA….[151] The formation of these I_1-type BSFs creates quantum-well-like structures, which can confine excitons and induce an emission around 3.321 eV in ZnO thin films and 3.329 eV in ZnO nanowires.[152,153] Thus, the contributions of the TES line (*i.e.* Al_{Zn} and carbon species) at 3.323 eV and the BSF line (*i.e.* I_1) at 3.329 eV result in the intense line located at the middle energy of 3.326 eV.

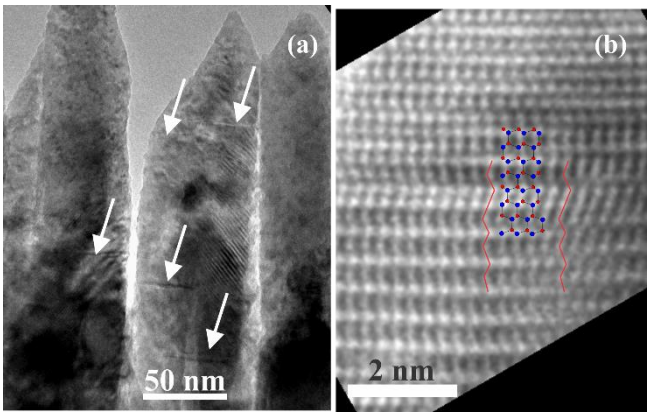

Figure 3.9: (a) Low-magnification TEM image of ZnO nanowires grown at 700 °C by PLI-MOCVD. The arrows indicate the presence of BSFs (b) HRTEM image where the stacking sequences and atomic model of an I_1-type stacking fault have been superimposed.

The other emission lines located at 3.259, 3.187, 3.116, 3.042, 2.956, and 2.879 eV (**Figure 3.8**) are assigned to the first, second, third, fourth, fifth, and sixth longitudinal-optical (LO) phonon replica of the TES and BSF lines, respectively. The different energy between each two adjacent lines is 72 meV, which is equal to the phonon energy in ZnO. The intensity of these LO phonon replica basically follows the Poisson distribution:[148]

$$I_n = \frac{e^{-S}.S^n}{n!} I_0 \qquad (3.1)$$

where *n* is the number of the LO phonon replica, I_0 is the intensity of the zero-phonon TES/BSF lines, I_n is intensity of the nth LO phonon replica, and *S* is the Huang-Rhys constant assessing the coupling strength of the electronic transition to the LO polarization field (*i.e.* phonon coupling). By plotting the ratios of I_n over I_0 in nanowires as a function of LO phonon replica number (n) and fitting the curves with Eq. (3.1), the *S* values of about 0.8 are deduced (**Figure 3.10**). For a comparison, a typical *S* value for the TES line related to Al_{Zn} is equal to 0.058.[148] The significantly higher values in our results expresses a stronger phonon coupling in nanowires, which could be locally enhanced by the additional contribution of the BSF line.

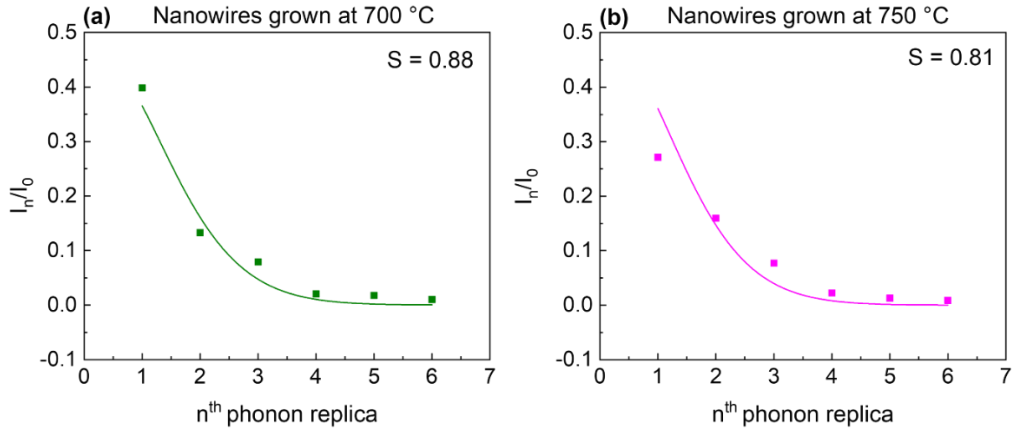

Figure 3.10: Ratios of LO phonon replica intensities to zero-phonon TES line intensity on nanowires grown at (a) 700 °C and (b) 750 °C, which follow the Poisson distribution with S is Huang-Rhys constant.

In addition, several low intensity and broad peaks in the range of visible band lying from 2 – 3 eV are observed in stacked and columnar thin films (**Figure 3.8**). These peaks originates mainly from the complexes formed by the zinc vacancy with hydrogen and/or residual donors, as suggested by the most recent theoretical calculations.[68,154] In the opposite, the absence of those peaks in nanowire samples indicates the higher optical quality[123] and excludes the significant role of hydrogen-related defects in the nanowire structures.

3.1.3.6 Piezoelectric properties and polarity of ZnO deposits

As the stacked thin film, columnar thin film and nanowires were grown by the same PLI-MOCVD system, the piezoelectric properties of different ZnO morphologies can be directly compared. By only changing the growth temperature while fixing other growth conditions (*e.g.* total pressure, flow rate, and nature of chemical precursors), we also decoupled the geometrical and dimensional effects from other electrical effects on the ZnO piezoelectric properties, which is basically not possible when comparing the ZnO thin films and nanostructures deposited by different deposition techniques. The DataCube PFM measurements were performed on the stacked thin film, columnar thin film, and nanowires grown at 500, 600 and 700 °C, respectively.

Before the PFM measurement, a specific preparation process was performed on the ZnO NW array sample to avoid artifacts caused by the gaps between NWs during PFM measurement. The NWs were spin coated by using two different types of polymethyl methacrylate (A2 and A6 from MicroChem 495PMMA) in order to completely immerse the NWs into the polymer.[155] PMMA A2 with low viscosity was used to easily penetrate between the nanowires. Then, the 6 A with a higher viscosity was used for planarization. After that, the polymer was etched by reactive ion etching (RIE) under Ar/O_2 at 60 W until the nanowire tips were visible, as shown in **Figure 3.11**. This work was done in collaboration with G. Ardila, a research scientist at IMEP-LAHC.

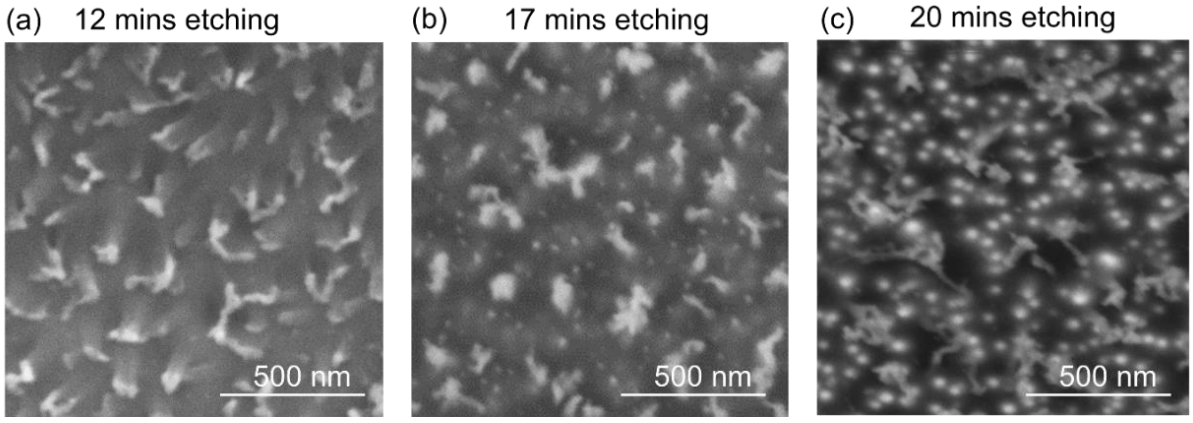

Figure 3.11: FESEM images of PMMA covered nanowires after etching during (a) 12 mins (b) 17 mins and (c) 20 mins.

Figure 3.11a shows that there is no visible tips of nanowires after 12 minutes of etching. The wire-like structures are part of the PMMA. After 17 minutes of etching, the tips of nanowires start to be seen beneath the PMMA layer, as shown in **Figure 3.11b**. After 20 minutes of etching, many tips of nanowires protrude from the PMMA layer with some remaining PMMA on top, as shown in **Figure 3.11c**.

Figure 3.12 presents the topography of a 1 μm^2-area on the stacked thin film, columnar thin film, nanowires, and reveals the correlated piezoelectric amplitude and phase responses as measured by DataCube PFM. The corresponding histograms of these piezoelectric response images are presented in **Figure 3.13**. Since the interference of the electrostatic effect was drastically reduced by using the high stiffness tip during PFM scanning, the piezoelectric amplitude is proportional to the piezoelectric coefficient and applied voltage amplitude (see **Section 2.2.1**).

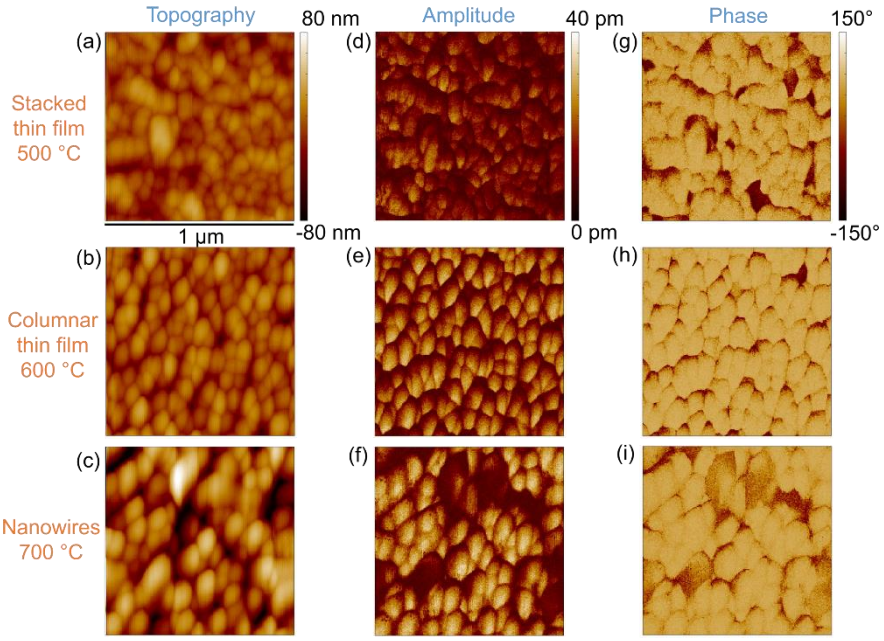

Figure 3.12: Topography of ZnO deposits grown at (a) 500 °C, (b) 600 °C and (c) 700 °C; piezoelectric amplitude of ZnO deposits grown at (d) 500 °C (e) 600 °C and (f) 700 °C; piezoelectric phase of ZnO deposits grown at (g) 500 °C (h) 600 °C and (i) 700 °C.

The piezoelectric amplitude on the surface of three ZnO morphologies in **Figures 3.12d-f** is varied from 0 to 35 pm when an AC drive voltage of 5 V was applied, expressing that the piezoelectric coefficient on these ZnO samples is from 0 to 7 pm/V. This value is lower compared to the values reported in Ref.[54]. We suspect that this could be due to the ineffective applying voltage on the highly-doped Si substrate used as the bottom electrode. During the PFM measurement, the actual voltage applied on the ZnO deposits could be smaller than the setting value at 5 V. As result, the piezoelectric coefficient of ZnO samples could be underestimated. Another reason could be the high density of charge carriers inside ZnO structures, causing the screening effect that leads to the decrease of piezoelectric amplitude. Among three morphologies, the stacked thin film has the lowest amplitude which is suggested by its darker amplitude image compared to the columnar thin film and nanowires. This can also be seen in their amplitude histograms, in which the amplitude on stacked thin film is

distributed at lower values than on other two morphologies (**Figures 3.13a-c**). The amplitude image of the nanowire sample in **Figure 3.12f** includes domains with piezoelectric response and non-piezoelectric response. The non-piezoelectric response is due to the scanning on the remaining PMMA after etching (see **Figure 3.11c**). On the domains with piezoelectric response, the amplitude of the nanowires exhibit even higher value than on the columnar thin film. Correspondingly, the amplitude distribution also shifts towards higher values when the morphology changes from stacked thin film to columnar thin film, and then to nanowires (**Figures 3.13a-c**). This increase of piezoelectric amplitude can be correlated to the improvement of growth texture along the polar *c*-axis when the morphology evolves from stacked thin film to nanowires, as shown in previous XRD analysis.

The piezoelectric phase responses in **Figures 3.12g-l** reveal the piezoelectric polar domains on ZnO samples. In these images, the domains with the phase values around 70° (*i.e.* bright domains) and -90° (*i.e.* dark domains) are attributed to the Zn- and O-polarity, respectively (see **Section 2.2.1**). The phase image of the stacked thin film in **Figure 3.12g** shows both dark and bright domains, demonstrating the coexistence of Zn- and O-polarity. On the other hand, the phase image of the columnar thin film in **Figure 3.12h** presented that most of its domains are Zn-polar. In **Figure 3.12i**, excluding the non-piezoelectric response caused by the PMMA (see **Figure 3.10c**), the phase responses on the nanowires indicate that all of them are Zn-polar. This result is different from ZnO nanowires grown by the chemical bath deposition method, in which both Zn- and O- polar nanowires were formed.[156] The corresponding phase histograms of ZnO samples in **Figures 3.13d-f** present the peaks at 70° attributed to Zn-polar domains.

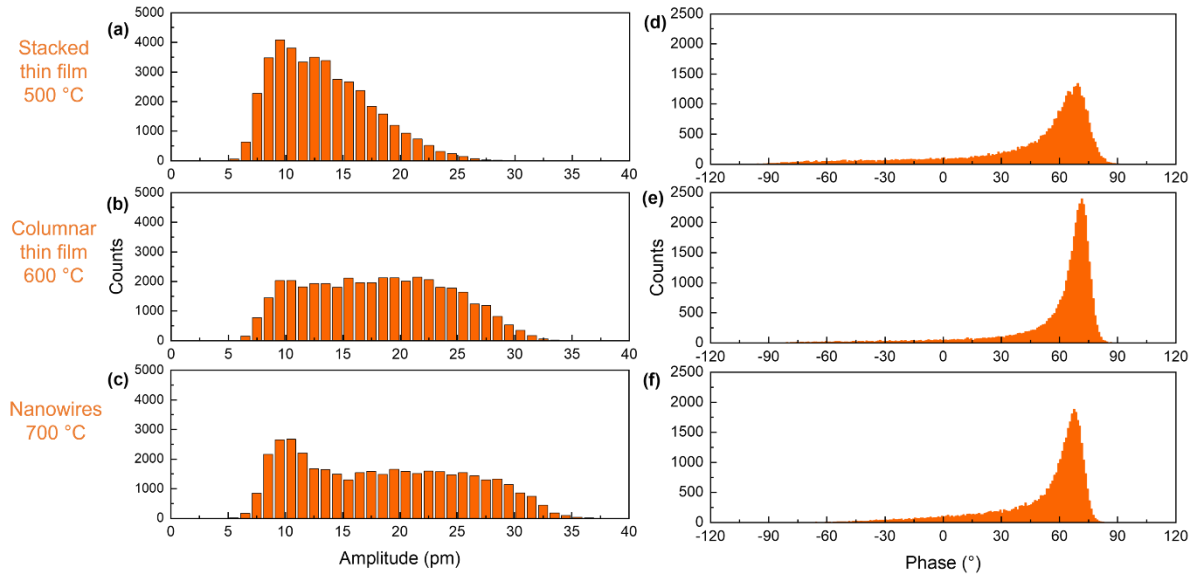

Figure 3.13: Raw piezoelectric amplitude histograms of ZnO deposits grown at (a) 500°C, (b) 600°C and (c) 700°C. Raw piezoelectric phase histograms of ZnO deposits grown at (d) 500°C, (e) 600°C and (f) 700°C.

The small negative phase response signifying to O-polar domains can be seen in the phase histogram of the stacked thin film in **Figures 3.13d**. On the phase responses of the columnar thin film and nanowires in **Figures 3.13e-f**, this signal is negligible. The other signals ranging from -180 ° to 180

° in these phase histograms are the noise caused by non-piezoelectric signals (see **Section 2.2.1**). These non-piezoelectric signals are generated when the AFM tip scanned at the grain boundaries on the thin film or on the PMMA remaining on the top of the nanowire sample (**Figures 3.13a-c**), which also contribute to the piezoelectric amplitude histograms. Consequently, the estimation of amplitude can be inaccurate, specifically in the case of nanowires where a considerable amount of PMMA still remains. Thus, we performed a PFM data treatment to remove the data points of these non-piezoelectric domains and separate the amplitude response of O- and Zn-polar data points in order to have a more accurate comparison of the piezoelectric responses among the ZnO morphologies. In this data treatment, data points with the phase response higher than 50° (attributed to the Zn-polar response) were kept without modification, while data points with the phase response lower than -50° (attributed to the O-polar response) had their amplitude value multiplied by -1. Other data points (attributed to the non-polar response) were removed from the histograms. The amplitude histograms after data treatment are shown in **Figure 3.14**.

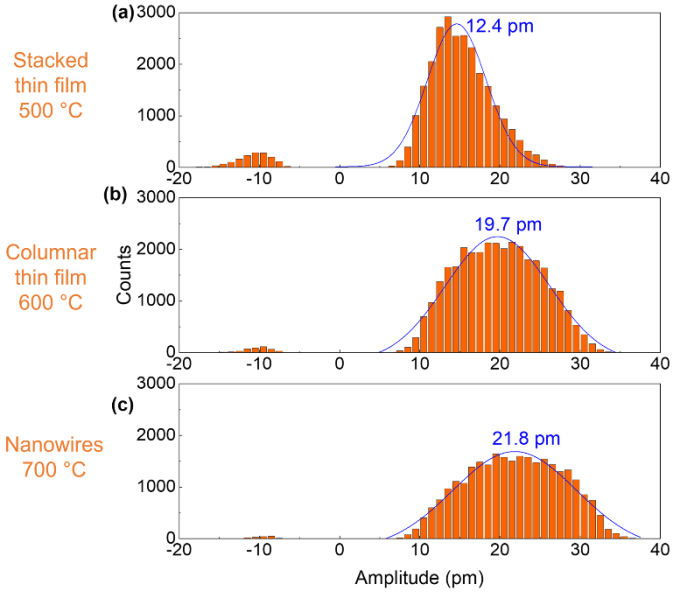

Figure 3.14: Piezoelectric amplitude histograms of ZnO deposits grown at (a) 500°C, (b) 600°C and (c) 700°C after the data treatment.

After the data treatment, it can be clearly seen that the amplitude of the Zn-polar domains increases when the ZnO morphology changes from stacked thin film to nanowires, expressed by the shift of their distribution peaks from 12.4 to 21.8 pm (**Figure 3.14**). As the applied voltage was maintained at 5 V during PFM measurements, this also expresses the increase of the piezoelectric coefficient d_{33} from 2.5 to 4.4 pm/V. Unlike the Zn-polar response, the amplitude response of the O-polar domains is maintained at a value around -10 pm. The number of O-polar response is also reduced and depleted in the columnar thin film and nanowires, indicating the predominance of Zn-polarity in these morphologies. Since the Zn- and O-polar domains are two polarities generating opposite electric potential, the coexistence of both polarities on the stacked thin film can result in the neutralization of total piezoelectric output when it is integrated into devices. The Zn-polar

uniformity on the nanowires can lead to the significantly higher piezoelectric output of this nanostructure compared to the stacked thin film.

3.1.3.7 Electrical resistivity of ZnO deposits

Moreover, the electrical resistivity of ZnO samples were measured. At first, the 4 probe method was used for the measurement, in which the probes were put directly on the ZnO surface. However, the Schottky contact between the metallic probe and the ZnO surface interfered with resistivity measurement. Thus, TLM method was employed to extract the electrical resistivity. In this method, the Au/Ni electrodes were deposited on the ZnO surface, allowing an Ohmic contact to be formed at the interface of metallic probe/electrode/ZnO. The resistivity of the ZnO thin film can be separated with the resistivity of electrodes and interfaces by TLM method (see **Section 2.2.4**). The drawback of this method is it cannot be applied to vertical NW array.

The total resistance between each metallic electrode pair was plotted against their distance, as shown in **Figure 3.15**. The resistivity values of the stacked thin film and columnar thin film were deduced from the slope of the linear fit curves in **Figure 3.15**. Both values are around 6.5 Ω.cm. Since the resistivity is similar between two morphologies, this result suggests that the enhancement of the piezoelectric amplitude with the morphology transition is more related to the improvement of the structural orientation rather than their electrical resistivity. In case of the nanowire array, its high aspect ratio nanostructure can lead to the creation of a depletion layer at the sidewalls of nanowires, resulting in decreasing the screening effect and hence increasing the piezoelectric efficiency.[89]

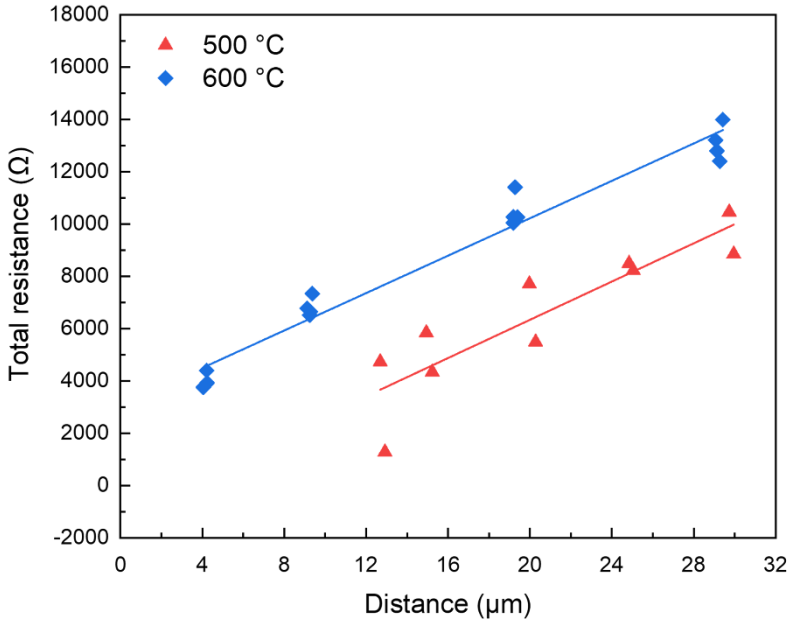

Figure 3.15: Total resistance versus Distance in TLM performed on stacked thin film and columnar thin film grown at 500 and 600 °C, respectively.

3.1.4 Discussion

Generally, the morphology transition of ZnO grown by PLI-MOCVD by raising the growth temperature is illustrated in **Figure 3.16**. This phenomenon is due to the strong anisotropy growth of

the wurtzite structure. Driving by the tendency of minimizing the free energy of the system, the ZnO growth develops the fastest on the polar *c*-plane, while it is the slowest on the non-polar *m*-plane.[157,158] When the growth temperature is increased, not only the stronger desorption of zinc and oxygen ad-atoms are occurred that leads to form the isolated islands, but also surface diffusion of ad-atoms is enhanced which helps their anisotropic growth.[159] As result, the isolated nanowire is formed. Along with the morphology transition of ZnO from stacked thin film to nanowires is the improvement in its piezoelectric amplitude. This could be attributed to the better orientation along the *c*-axis in nanowires, which is a main piezoelectric polar axis of ZnO wurtzite structure. Furthermore, the transition of morphology into nanowires also leads to the predominance of the Zn-polarity over the O-polarity. This polarity uniformity has a significant impact on the piezoelectric performance as the cancellation of piezoelectric potential of two opposite polarities is avoided, which results in greatly increasing the piezoelectric efficiency. Surprisingly, this has not been investigated in details yet. In our results, ZnO nanowires grown by PLI-MOCVD exhibit the uniform Zn-polarity, which is in general agreement with the literature reporting that ZnO nanowires spontaneously grown by vapor phase techniques are systematically Zn-polar,[34,160] and opposite to the O- and Zn-polar ZnO nanowires grown by the chemical bath deposition.[156] The piezoelectric amplitude on the Zn-polar domains is also higher than on the O-polar domains. This could be due to the less incorporation of impurities (i.e. Al_{Zn}) in Zn-polar domain, resulting in lower free charge carrier density as well as the screening effect caused by them. The difference in impurity incorporation between two polarities during the chemical vapor deposition of ZnO has been reported in ref.[161], which may be opposite to what is commonly reported in the case of ZnO nanowires grown by chemical bath deposition.[117] Another reason that can also contribute to the piezoelectric amplitude enhancement of nanowires is its high aspect ratio nanostructure, in which a surface Fermi Level pinning on the large surface area of nanowire sidewalls can efficiently deplete the free charge carriers inside it, resulting in reducing the screening effect.[89] Overall, those results show that ZnO nanowires grown by PLI-MOCVD have a great potential for the piezoelectric applications. The well controlling of the growth direction, which affects the structural orientation as well as the nature and the uniform polarity of the deposited ZnO nanostructure, is the key point to enhance the piezoelectric performance.

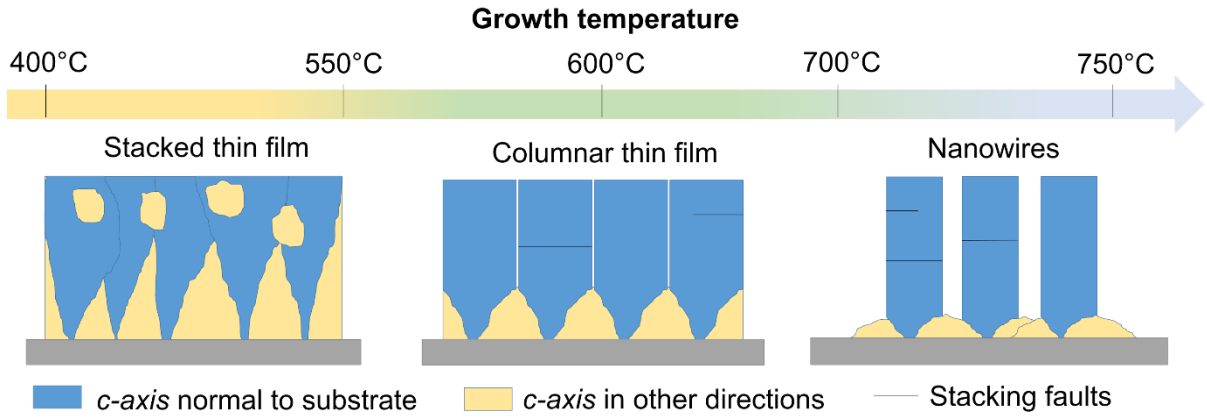

Figure 3.16: Schematic of the formation mechanisms of ZnO deposits grown by PLI-MOCVD for a given growth temperature in the range of 400 – 750°C.

3.2 Effect of annealing temperature

3.2.1 Introduction and objectives

After the growth of ZnO thin films, an investigation on effects of thermal post-annealing was also carried out. The first target is to remove the remaining carbon contamination on ZnO samples as indicated by Raman spectroscopy result in **Section 3.1**. The second target is to further enhance the piezoelectric amplitude of ZnO by the crystallization during the annealing process. Indeed, many researches supported that the effects of thermal annealing on the structural and electrical properties can lead to the performance enhancement of the ferroelectric materials such as PZT,[162] $(Bi_{0.5}Na_{0.5})TiO_3$–$(Bi_{0.5}K_{0.5})TiO_3$–$BaTiO_3$,[163] and $LiNbO_3$,[164] or the piezoelectric materials such as AlN,[165] and ZnO.[107] By using post-deposition thermal annealing under oxygen atmosphere, not only the crystallinity and *c*-axis orientation of ZnO nano-pyramidal structures were improved, but also some defects were removed, resulting in better piezoelectric response as reported in Ref.[107]. Many research groups have studied the effects of thermal annealing on the structural, optical, and electrical properties of ZnO thin films grown by different techniques such as sputtering,[79,81] molecular beam epitaxy,[97] wet chemistry[166] or MOCVD.[167] They have shown that the thermal annealing can improve the crystallinity of ZnO thin films and reduce the density of extended defects in their center. The ZnO thin film properties after the thermal annealing in air, inert nitrogen atmosphere, and in vacuum were investigated by L. Gritsenko et al.[167] Since the O_2 gas is present in air, the thermal annealing causes oxygen chemisorption onto grain boundaries, which could lead to the more drastically decrease in free charge carrier density and mobility compared to the annealing in nitrogen atmosphere and in vacuum (**Figure 3.17**).[167] These consequences would be favorable to improve the piezoelectric performance. Despite those encouraging results, the effects of thermal annealing on the piezoelectric coefficients, and especially the crystal polarity of ZnO thin films as well as their correlation with the structural and electrical properties have not been investigated yet.

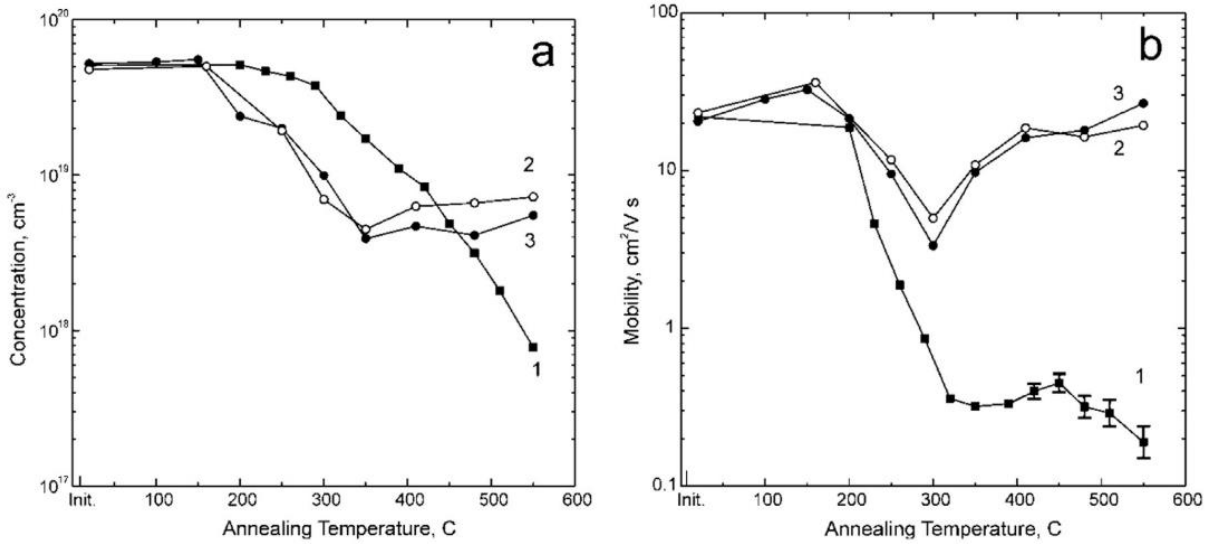

Figure 3.17: Evolution of (a) the carrier concentration and (b) mobility in MOCVD-ZnO films as a function of annealing temperature in air (1), in nitrogen atmosphere (2), and in oil vacuum (3).[167]

In this section, we systematically study the effects of thermal annealing under oxygen atmosphere on the structural, electrical, and piezoelectric properties of ZnO thin films grown by PLI-MOCVD. By varying the annealing temperature from 600 to 1000 °C, the recrystallization and grain coarsening processes accompanied by the change of electrical resistivity, piezoelectric amplitude, and polarity distribution are described in detail. The structural properties of ZnO thin films are thoroughly investigated by using FESEM, XRD, and Raman spectroscopy. Their electrical resistivity and piezoelectric properties are measured by TLM and piezoresponse force microscopy PFM, respectively. This work was published as Q.C. Bui et al. "Effects of thermal annealing on the structural and electrical properties of ZnO thin films for boosting their piezoelectric response" in *J. Alloys Compd.*, 2021, **870**, 159512.

3.2.2 Experiment

3.2.2.2 ZnO thin film growth and thermal annealing

The ZnO thin films were grown by PLI-MOCVD in an Annealsys MC-200 MOCVD system. Heavily doped p-type Si (100) wafers were used as substrates and as bottom electrodes during PFM measurements. The zinc chemical precursor solution used was DEZn diluted in cyclohexane solvant (see **Section 2.1.3**). The flow rate of DEZn solution and O_2 gas flow rate was set to 0.5 g/min and 500 sccm, respectively. The Ar gas was used as a gas carrier. The chamber pressure was maintained at 3 mbar and the growth temperature was kept at 500 °C. The ZnO thin films were grown in 10 minutes, resulting in a thickness of 1100 nm.

After that, the as-grown ZnO thin films were annealed in a horizontal quartz tubular furnace. The annealing temperature was varied from 600 to 1000 °C. The pressure in the furnace was close to 1 atm. The temperature was ramped up from room temperature to the annealing temperature with a rate of 25 °C/min, then it was maintained for 1 hour. Finally, the temperature was cooled down to room temperature naturally. The whole process was carried out under a pure oxygen atmosphere.

3.2.2.2 Characterizations

Different characterizations were performed to study the annealed ZnO thin film samples, as described in **Section 2.2**. The structural properties were investigated by field-emission scanning electron microscopy (Gemini300 FEI ZEISS-SEM), X-ray diffraction (Bruker D8 Advance diffractometer), and Raman scattering measurements (Jobin Yvon/Horiba Labram spectrometer). The resistivity of thin films was measured by using the TLM method. Their piezoelectric property images were scanned by using piezoresponse force microscopy (Bruker Dimension Icon AFM).

3.2.3 Results and discussion

3.2.3.1 Crystallization and morphology of ZnO thin films

The top-view (left) and cross sectional-view (right) FESEM images of ZnO thin films before and after being annealed at different temperatures are presented in **Figure 3.18**. It can be seen that the ZnO thin films after annealing have larger and sharper grains, indicating the crystallization of ZnO films. The cross sectional-view images reveal that ZnO thin films are composed of stacked grains, as shown in **Section 3.1** for stacked thin films. In the top-view images, a hexagonal shape of the grains in all annealed ZnO thin films can be clearly seen, suggesting the *c*-plane of the wurtzite structure,

which is the most stable phase of ZnO in these conditions. As the annealing temperature is increased from 600 to 1000 °C, the grains coalesce and coarsen to form large-sized grains. The mean grain sizes of ZnO thin films were measured from SEM images and presented in **Figure 3.19**.

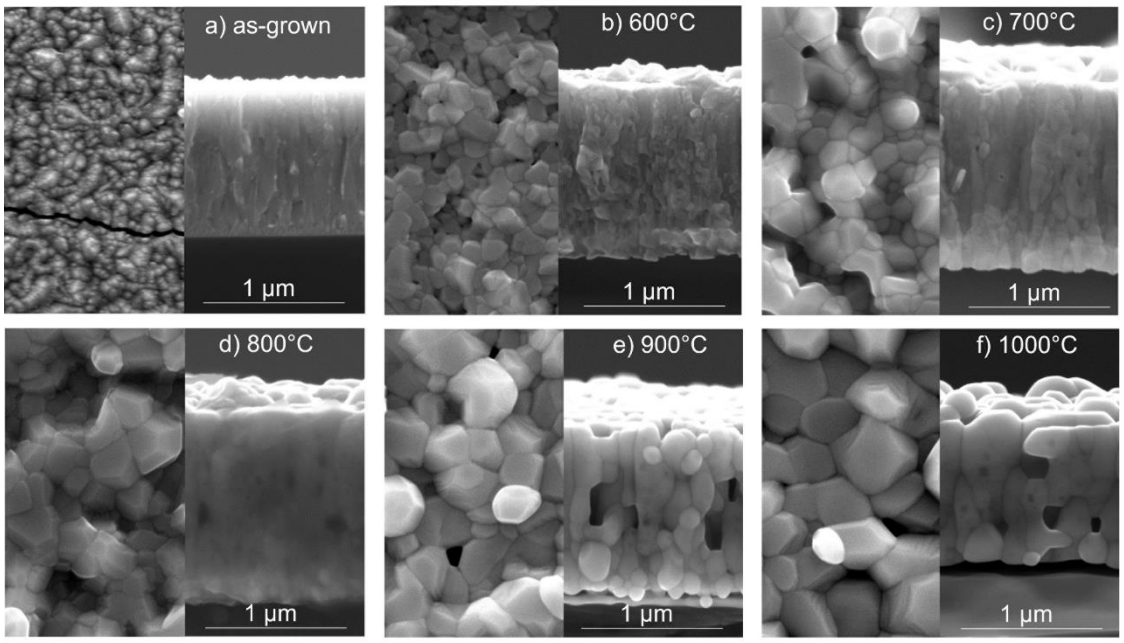

Figure 3.18: Top- (left) and cross-sectional-view (right) FESEM images of ZnO thin film grown by PLI-MOCVD at 500 °C (a) and ZnO thin films after being annealed at (b) 600, (c) 700, (d) 800, (e) 900, and (f) 1000 °C.

The result in **Figure 3.19** exhibits a continuous increase of mean grain size from 44 to 319 nm on ZnO thin films before and after being annealed at 600 – 1000 °C. Accompanying with the increase of the grain size, the root mean square roughness measured by AFM also increases from 13 to 76 nm. The grain coarsening and growth processes can be described by the migration of zinc and oxygen atoms to minimize the free energy at the grain boundaries.[141] Besides, the formation of large pores also occurred at high temperature annealing. Some pores and dots with lower contrast can be observed in the top- and cross-sectional view images of thin films annealed at 900 and 1000 °C. The similar pore formation in ZnO thin films after thermal annealing has been reported in Refs,[166,168,169] which could have an impact on the electrical properties of ZnO thin films.

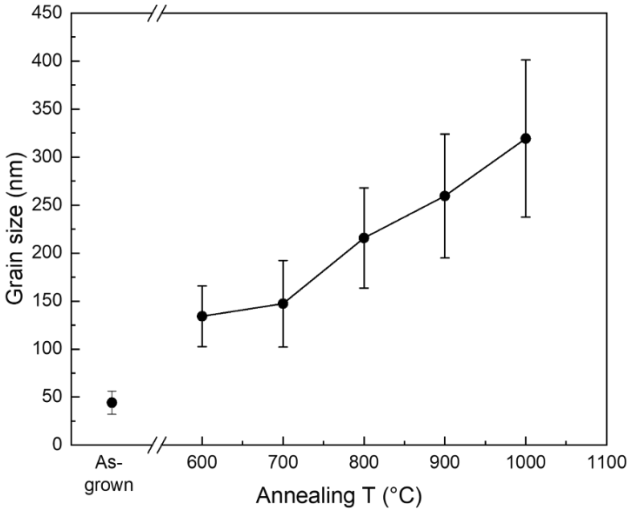

Figure 3.19: Mean grain size on ZnO thin films before and after being annealed at 600 – 1000 °C measured from top-view SEM images.

3.2.3.2 Structural properties: orientation, strain and crystallite size

X-ray diffraction

Figure 3.20a presents the XRD patterns of ZnO thin films before and after being annealed at different temperatures. All patterns are similar and show typical diffraction peaks of ZnO wurtzite structure. Beside the diffraction peaks of Si substrate, the peaks located at 31.8, 34.4, 36.3, 47.5, 56.6, 62.9, and 81.4° are attributed to the 100, 002, 101, 102, 110, 103, and 104 diffraction peaks of ZnO, respectively, according to the ICDD file labelled 00-036-1451. Similar to thin films shown in our results in **Section 3.1**, all thin films here also have a high orientation along the polar *c*-axis, indicated by the highest intense 002 diffraction peak compared to other peaks. As the annealing temperature is raised, the intensity of 002 and other diffraction peaks are significantly increased, while their FWHM of the diffraction peaks is simultaneously decreased (**Figure 3.20b**), suggesting an improvement of the crystallinity of the thin films. The peaks also shift with the increase of annealing temperature, indicating the variation of the lattice parameter as well as the strain inside the ZnO structure. To study the evolution of ZnO structural properties as a function of the annealing temperature, we analyzed their XRD patterns using the methodology as described in **Section 2.2.2**. The orientation of thin films is evaluated by calculating the texture coefficients C_{hkl} of a (hkl) planes based on their diffraction peak intensities. The homogeneous strain representing the residual strain in ZnO thin films at the end of the growth and annealing processes is extracted from the diffraction peak position value θ. In addition, the diffraction peak position and their FWHM values are employed to estimate the inhomogeneous strains caused by the microstructural defects as well as the crystallite size based on the Williamson-Hall method. The 002 texture coefficients, homogeneous strains, Williamson-Hall plots, inhomogeneous strains and crystallite size were presented in **Figure 3.21**.

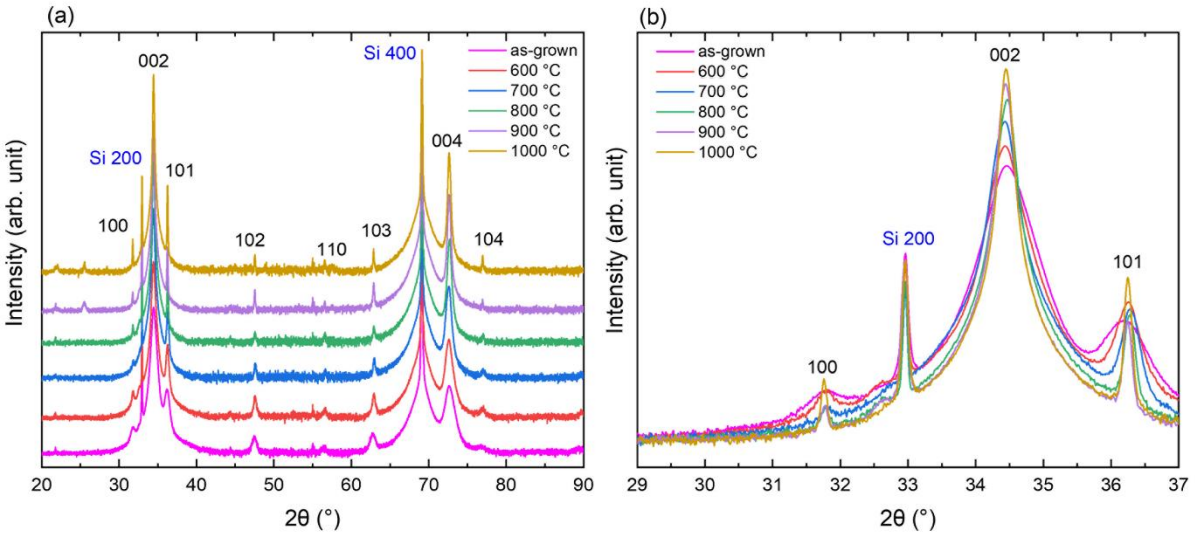

Figure 3.20: XRD patterns of ZnO thin films plotted in the range of 2θ (a) from 20 to 90° and (b) from 29 to 37° after its intensity normalization using the baseline. The intensity is plotted in logarithm scale.

In **Figure 3.21a**, the 002 texture coefficient increases from 98.9 % in as-grown thin film to 99.9 % in 900 °C-annealed thin film, indicating that grains with the polar *c*-axis normal to the Si substrate become more dominant in the ZnO thin film after be annealed at higher temperature. This describes that during the grain coarsening at elevated temperature, the *c*-axis oriented grains grew and developed into larger grains while the grains with other orientations are progressively consumed. The reason is due to the abnormal grain growth in polycrystalline thin films,[141] depending on the processing parameters.[170,171] In this phenomenon, the grain growth rate represented by the grain boundary velocity is dependent on both the grain boundary mobility and the difference in the total free energy per unit volume. These factors are strongly affected by the grain orientation. Since the *c*-axis oriented grains exhibiting the highest surface energy were developed in our case,[158] this means that the grain growth was mainly driven by the anisotropy in the grain boundary mobility. By further increasing the annealing temperature to 1000 °C, the 002 texture coefficient slightly decreases to 99.8%, expressing the deterioration of the structural quality due to the formation of large pores, as reported in Ref.[79].

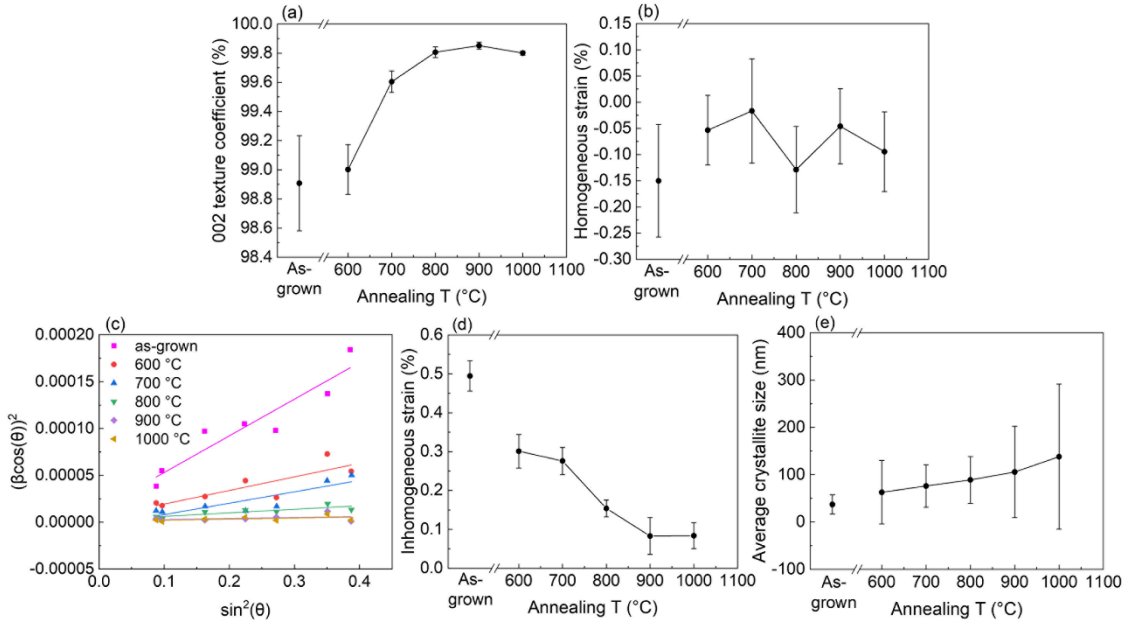

Figure 3.21: (a) Texture coefficient of the 002 diffraction peak vs annealing temperature. (b) Homogeneous strain vs annealing temperature. (c) Williamson-Hall plot of ZnO thin films. (d) Inhomogeneous strain vs annealing temperature deduced from the Williamson-Hall plot. (e) Average crystallite size vs annealing temperature inferred from the Williamson-Hall plot.

In **Figure 3.21b**, the homogeneous strain of the as-grown thin film at 500 °C shows a negative value of -0.15%, indicating a compressive strain generated during the Volmer-Weber growth mode,[172,173] as presented in our previous result in **Section 3.1**. By annealing at 700 °C, this compressive homogeneous strain decreases down to -0.02 % thanks to the grain coarsening and growth. However, it suddenly increases to -0.13% in 800 °C-annealed thin films. The increase in residual strain could be due to the contribution of extrinsic stress, namely the thermal stress induced by the thermal expansion coefficient mismatch between ZnO thin film and Si substrate. Indeed, the thermal expansion coefficient of hexagonal ZnO in *a*-axis is around 3.2 – 6.05 x 10^{-6} °C^{-1}, while the thermal expansion coefficient of Si is 2.5 x 10^{-6} °C^{-1} at room temperature.[174] The thermal stress could be generated during the cooled down process from high annealing temperature to room temperature.[79,81] During the cooling down process, the ZnO shrinks faster than the Si substrate since the thermal expansion coefficient of ZnO is higher compared to the Si substrate. As result, a residual tensile strain is generated in the *a*-axis of ZnO (ε_{xx}) at the interface with the Si substrate, which can be expressed as follows:

$$\varepsilon_{xx} = (\alpha_{ZnO} - \alpha_{Si})\Delta T \qquad (3.2)$$

where α_{ZnO} and α_{Si} are the thermal expansion coefficients of ZnO and Si, respectively, and ΔT is temperature difference. Based on Eq. (3.2), a residual tensile strain in the *a*-axis of ZnO was deduced around 0.05 – 0.28 % after the substrate temperature was cooled down from 800 to 25 °C (room temperature). The tensile strain in the *a*-axis can be converted into the compressive strain in the *c*-axis (ε_{zz}) as follows:[175,176]

$$\varepsilon_{zz} = -2\frac{C_{13}}{C_{33}}\varepsilon_{xx} \qquad (3.3)$$

where C_{13} and C_{33} are elastic constants of ZnO, which are equal to 104.2 and 213.8 GPa, respectively.[177] A compressive strain along the *c*-axis (ε_{zz}) was estimated to be from -0.27 to -0.05 %, which is comparable to the homogenous strain extracted from XRD analysis. This indicates that the thermal expansion coefficient mismatch generated after the cooling down process can cause a significant residual strain in the ZnO thin film, especially at higher annealing temperature. When annealing temperature is increased to 900 and 1000 °C, the residual strain again decreases. The large pores observed in these thin films (**Figure 3.18**) could be responsible for this strain relaxation.

The Williamson-Hall plots along with the deduced inhomogeneous strain and average crystallite size of the ZnO thin films before and after being annealed are presented in **Figures 3.21c-e**. Different from the evolution of the homogeneous strain, the inhomogeneous strain in **Figure 3.21d** continuously decreases from 0.49 to 0.08 % as the annealing temperature is raised to 1000 °C, suggesting that the density of extended defects such as dislocations and stacking faults are removed after the high temperature annealing process. Besides, **Figure 3.21e** shows that the average crystallite size also constantly increases from 37 to 138 nm when the annealing temperature is increased. It should be noted that the crystallite size here is measured in the dimension normal to the Si substrate due to the XRD configuration (see **Section 2.2.2**). This together with the grain size increase as shown in **Figure 3.19** describe that the grain coarsening and growth occur both in the plane of the film and all along its thickness. The grain growth along the film thickness results in replacing the stacked thin films to form an almost columnar thin film, which can be observed in cross-sectional view FESEM images in **Figure 3.18**.

Raman scattering spectra

The Raman scattering spectra of ZnO thin films before and after annealing at different temperatures are presented in **Figure 3.22**. The E_2^{low} and E_2^{high} lines of the ZnO wurtzite structure are detected at 99 and 438 cm^{-1}, respectively.[143] Their intensities significantly increases as the annealing temperature is raised, indicating a great improvement of the crystallinity with annealing temperature, which is consistent with the previous XRD analysis. A shift of the E_2^{high} line to the bulk value at 438 cm^{-1} after annealing expresses a strain relaxation in annealed thin films. Moreover, the ratio of E_2^{high}/E_2^{low} intensity is also continuously increasing when the annealing temperature is increased to 1000 °C. As the E_2^{high} line is associated with the oxygen lattice, while the E_2^{low} line is associated with the zinc lattice,[143,178] the increase of E_2^{high}/E_2^{low} intensity ratio describes that the oxygen vacancies are progressively filled and disappeared as the thermal annealing proceeds. Besides the E_2^{low} and E_2^{high} lines, no other Raman line of the ZnO wurtzite structure can be seen in the Raman scattering spectrum of as-grown thin film. As the annealing temperature is raised, the Raman lines such as E_2^{high} - E_2^{low}, A_1(TO), E_1(TO) and A_1(LO) located at 333, 378, 410 and 574 cm^{-1},[143] respectively, gradually appear. Simultaneously, two large broad bands centered at around 1360 cm^{-1} and 1580-1600 cm^{-1} gradually decreased and completely disappeared when the annealing temperature is increased to 800 °C. These broad bands are assigned to C-C bonds,[144] evidencing the remaining carbon impurities in the ZnO thin film grown by PLI-MOCVD process, as shown in **Section 3.1**. The vanishing of these signals in Raman spectra means that those carbon impurities are removed from ZnO thin films after annealing at sufficiently high temperature.

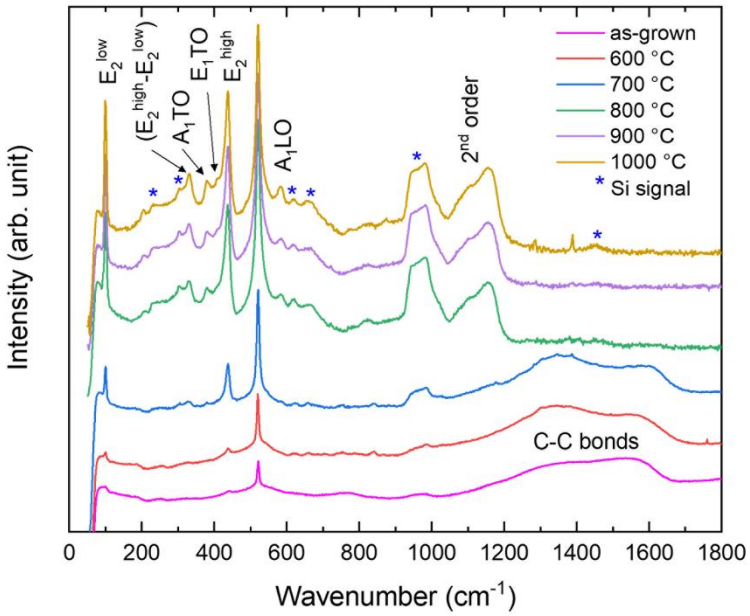

Figure 3.22: Raman scattering spectra of ZnO thin films. The intensity is plotted in logarithm scale.

3.2.3.3 Electrical resistivity of thin films

The results of TLM in **Figure 3.23** show that the electrical resistivity of ZnO thin film basically increases after being annealed at high temperature in O_2 atmosphere. In detail, it increase constantly from 6.3 Ω.cm in as-grown thin film to 50.7 Ω.cm in 800 °C-annealed thin film, decreases to 31.3 Ω.cm in 900 °C-annealed thin film, then increases again to 81.0 Ω.cm at 1000 °C-annealed thin film. The repeat of resistivity measurements within several months gave similar results, confirming that the electrical resistivity of ZnO thin films is stable with time.

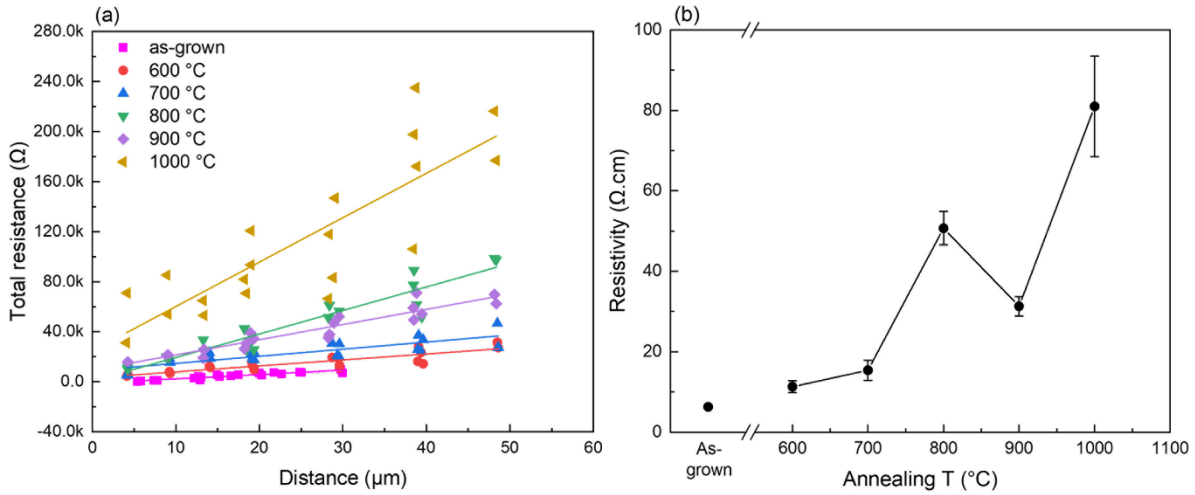

Figure 3.23: (a) Measured resistance vs distance in transmission line measurement and (b) deduced resistivity of ZnO thin films.

The effects of annealing in the O_2 atmosphere on the electrical resistivity of ZnO thin film as well as its charge carrier density and mobility have been demonstrated by different research groups.[80,97,167,168] In the report of M. Asghar et al., they showed that the resistivity of ZnO increased

with the annealing temperature due to the relocation of atoms during thermal annealing, which leaded to reducing amount of shallow donor defects as well as the charge carrier density inside ZnO.[80] The increase of ZnO resistivity by O_2 annealing was also reported in the work of L. Gritsenko et al., in which they showed that the oxygen adsorption at the grain boundary after annealing created depletion zones, resulting in the decrease of both charge carrier density and mobility.[167] In contrast, the ZnO resistivity was decreased after the annealing process in Refs.[97,168], which was explained by the enhancement of carrier mobility thanks to the improvement of crystallinity with less grain boundary density and defects, helping mitigate the carrier scattering. In our results, since the thin films were annealed in the O_2 atmosphere, the oxygen adsorption at the grain boundaries is expected. This could form the depletion zones, leading to the increase of the electrical resistivity when the annealing temperature was increased to 800 °C. In addition, the Raman spectra in **Figure 3.22** shows that the carbon impurities in ZnO thin films were reduced and removed after the annealing at 800 °C. Since those impurities can act as shallow donors in ZnO structure,[67] the decrease of carrier density could also contribute to the large increase in the electrical resistivity. On the other hand, our XRD and Raman results show that the ZnO crystallinity was improved after annealing thanks to the grain coarsening and growth processes, suggesting the increase of charge carrier mobility. However, this could not overcome the decrease in the charge carrier density, resulting in the increase of resistivity as the annealing temperature was raised up to 800 °C. By increasing the annealing temperature to 900 °C, the electrical resistivity suddenly decreases. This could be explained by a no significant decrease of charge carrier density occurred in ZnO thin film when the annealing temperature was increased from 800 to 900 °C, since the carbon impurities acting as a shallow donors[67] were completely removed in 800 °C-annealed thin film, as suggested in their Raman spectra (**Figure 3.22**). Meanwhile, the constant crystallinity improvement by raising the annealing temperature as suggested in previous structural analysis could increase the carrier mobility, resulting in the decrease of resistivity when annealing temperature increased from 800 to 900 °C. The electrical resistivity increases again with further increase of annealing temperature to 1000 °C is due to a significant impact of pores that interrupted the charge carrier motion.[168]

3.2.3.4 Piezoelectric properties and polarity of ZnO thin films

The PFM scannings were performed on the ZnO thin films before and after annealing. The topography of 6 x 6 μm^2 area and the correlated piezoelectric amplitude and phase responses are presented in **Figure 3.24**. The corresponding histograms of piezoelectric amplitude and phase are shown in **Figure 3.25**. In piezoelectric amplitude images, the brighter domains express higher the piezoelectric amplitude, which is proportional to the piezoelectric coefficient (see **Section 2.2.1**). As the annealing temperature is increased, the piezoelectric amplitude images of ZnO thin films present brighter domains (**Figure 3.24g-l**), indicating an increase of piezoelectric amplitude as well as the piezoelectric coefficient with annealing temperature. Correspondingly, the piezoelectric amplitude histograms in **Figure 3.25a-f** shift and stretch to a higher value at higher annealing temperature.

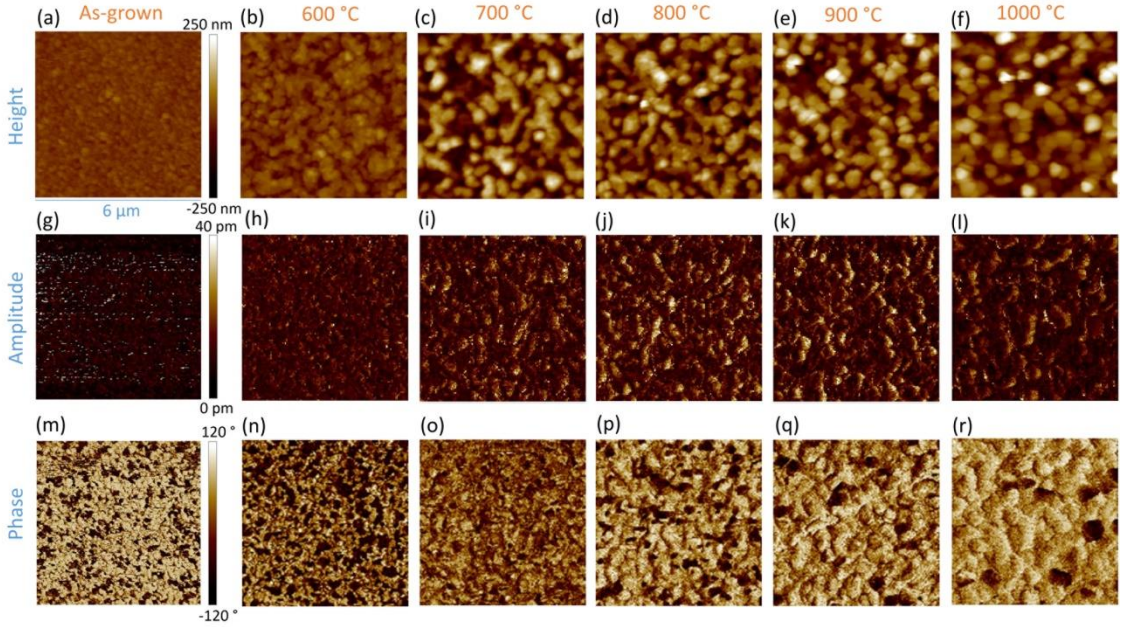

Figure 3.24: Topography of ZnO thin films (a) before and after being annealed at (b) 600, (c) 700, (d) 800, (e) 900 °C, and (f) 1000 °C. Piezoelectric amplitude of ZnO thin films (g) before and after being annealed at (h) 600, (i) 700, (j) 800, (k) 900 °C, and (l) 1000 °C. Piezoelectric phase of ZnO thin films (m) before and after being annealed at (n) 600, (o) 700, (p) 800, (q) 900 °C, and (r) 1000 °C.

In the piezoelectric phase images, phase responses identify the polarities of ZnO wurtzite structure. The domains with the phase at around 70° (bright area) represent the Zn-polarity, while the domains with the phase at around -90° (dark area) indicate the O-polarity (see **Section 2.2.1**). The phase response images of the thin films before and after annealing in **Figures 3.24m-r** revealing both dark and bright domains, demonstrating the Zn- and O-polar domains on these samples. Correspondingly, their phase histograms in **Figures 3.25g-l** present the positive peaks around 70° and the negative peaks around -90°, which are assigned to Zn- and O-polar domains, respectively. The other phase signals stretching from -180 to 180° are noise caused by non-polar signals with unidentified phase (see **Section 2.2.1**). It can be seen in **Figures 3.24m-r** and **Figures 3.25g-l** that there is a difference in the distribution of two polarities among thin films. Compared to the phase response image of the as-grown thin film in **Figure 3.24m**, the phase response image of the 600 °C-annealed thin film in **Figure 3.24n** shows more O-polar domains (dark area). In **Figures 3.25g-h**, their phase histograms also show a decrease on the positive side and an increase on the negative side after the thin film was annealed at 600 °C, revealing a development of O-polar domains. On the phase image of thin film annealed at 700 °C (**Figure 3.24o**), the distinction between dark and bright domains becomes unclear, implying a dark-bright mixed area. Correlatively, its phase histogram in **Figure 3.25i** exhibits a broad peak centered at nearly 0°. The reason could be due to the coarsening process between grains with Zn- and O-polarity during the annealing process. Since they are the opposite polarities, the coarsening and growth processes lead to the formation of domains with neutralized polarity, resulting in diminishing the piezoelectric signals. Consequently, the 700 °C-annealed thin film composed of large non-piezoelectric area gives phase signals randomly distributed from negative to positive values, which is displayed by a broad peak centered at 0° in its histogram

(**Figure 3.25i**). In the phase images of thin films annealed at higher temperature (**Figures 3.24p-r**), the borders between two opposite polar domains can be clearly seen again. Moreover, the phase images show that the bright domains become more dominant when the annealing temperature increases from 800 to 1000 °C. Their phase histograms in **Figure 3.25j-l** also present a higher distribution on the positive side, implying the predominance of the Zn-polar polarity over the O-polar polarity. This observation expresses that the Zn-polar grains prevailed over the O-polar grains after the annealing process at these high temperatures. Since the surface energy of Zn-polar *c*-plane is significantly higher compared to the O-polar *c*-plane,[179] the prevalence of Zn-polar grains again signify that the grain coarsening and growth processes at high temperatures is not mainly driven by the minimization of the free energy on the surfaces, but it is instead governed by the anisotropy in the grain boundary mobility.[141]

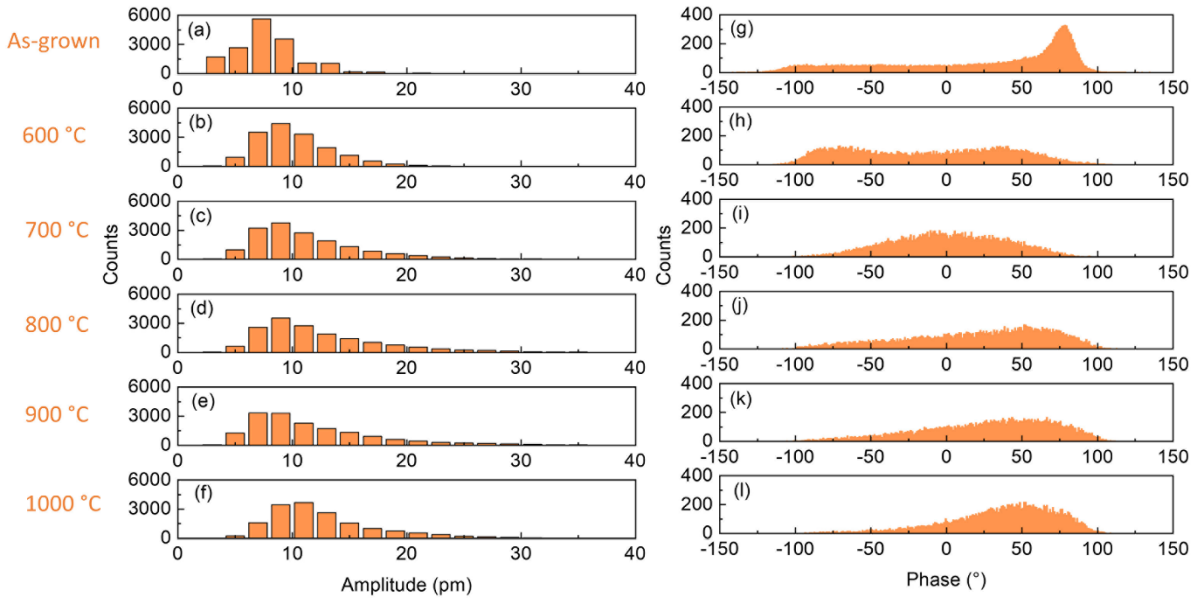

Figure 3.25: Raw piezoelectric amplitude histograms of ZnO thin films (a) before and after being annealed at (b) 600, (c) 700, (d) 800, (e) 900 and (f) 1000 °C. Raw piezoelectric phase histograms of ZnO thin films (g) before and after being annealed at (h) 600, (i) 700, (j) 800, (k) 900 and (l) 1000 °C.

In other to separate the piezoelectric responses from the Zn- and O-polar domains, and remove noise from non-polarity areas, a PFM data treatment (see Section 3.1) was performed: the data points with the phase response higher than 50° representing Zn-polar signals were kept without modification; in contrast, data points with the phase response lower than -50 ° representing the O-polar signals had their amplitude value multiplied by -1. Other data points were assigned to non-polarity areas and were removed.

The amplitude histograms after data treatment of ZnO thin films before and after annealing at different temperatures are presented in **Figure 3.26**. It can be seen that the amount of Zn-polar signals on thin films decreases after being annealed at 600 and 700 °C (**Figures 3.26a-c**). As the annealing temperature is further increased to 800, 900, and 1000 °C, the distribution on Zn-polar domains increases again along with the amplitude stretching to higher value (**Figures 3.26d-f**). Meanwhile, the amount and amplitude on O-polar domains increases on the 600 °C-annealed thin

film, but then decreases at higher annealing temperatures. This again describes that the O-polar grains were developed on 600 °C-annealed thin film, then they competed with Zn-polar grains during the grain coarsening and growth at 700 °C, and were consumed at higher annealing temperature.

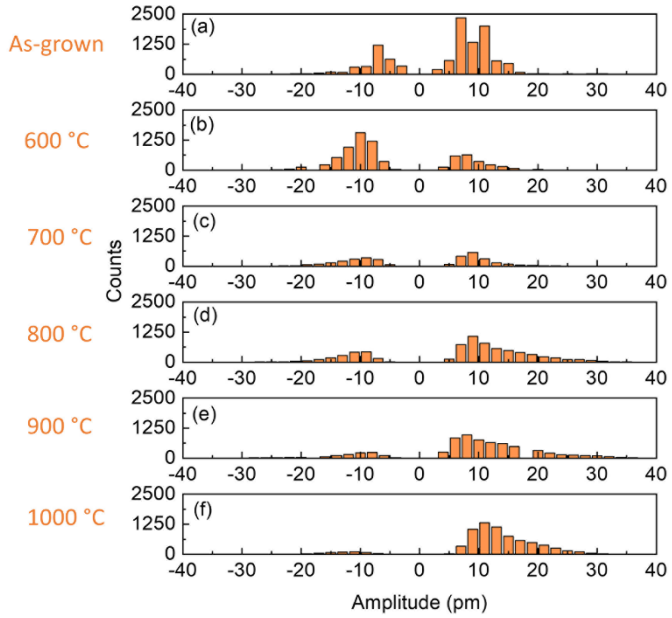

Figure 3.26: Piezoelectric amplitude histograms of ZnO thin films (a) before and after being annealed at (b) 600, (c) 700, (d) 800, (e) 900 and (f) 1000 °C after the data treatments.

Furthermore, the average piezoelectric amplitude responses of the Zn- and O-polar domains and the percentage of the Zn-polar domains on thin films were calculated to have more accurate comparison. The calculation was performed after the data treatment, in which the contribution of non-polar domains was removed. The Zn-polar percentage is the ratio of Zn-polar data point amount to the total amount of Zn- and O-polar data points, excluding the non-polar data point amount. The calculation results are presented in **Figure 3.27**. The average piezoelectric amplitudes on both polarities are at around 7.5 – 13.5 pm, corresponding to the piezoelectric coefficients at around 1.5 – 2.7 pm/V. On the Zn-polar domains, the average piezoelectric amplitude in as-grown, 600 °C- and 700 °C- annealed thin films is similar and around 9.5 pm (**Figure 3.27a**). Then, it increases significantly to 13.2 pm at 800 °C, and does not change at higher annealing temperature. On the O-polar domains, the average piezoelectric amplitude in the as-grown thin film is 7.5 pm, which increases to 11.3 pm just after the thin film is annealed at 600 °C. After annealing at 700 °C, the amplitude decreases slightly to 10.8 pm. Then, it increases again to 12 pm at 800 °C and remains at the same value at higher temperature. It should be mentioned that the highly doped Si substrate used as the bottom electrode were partially oxidized after the annealing at high temperature, evidencing by the appearance of a pink-color-Si oxide layer at the backside of the Si substrate after the annealing at 1000 °C. The 1000 °C-annealed thin film also started being peeled off from the substrate as observed in FESEM image (**Figure 3.18f**). These caused a poor electrical contact between the ZnO thin film and the Si bottom electrode, leading to decreasing the applied voltage during the PFM measurement and causing an underestimation of the piezoelectric amplitude of this ZnO thin film. Generally, the evolutions of the average piezoelectric amplitudes on both Zn- and O-polar domains in **Figure 3.27a**

shows that they increase with annealing temperature. This could be due to the increase of polar *c*-axis oriented domains inside ZnO thin films after being annealed at higher temperature,[107] as indicated in the XRD analysis (**Figure 3.21a**). In addition, the TLM results in **Figure 3.23** imply that the higher temperature annealing could also reduce the charge carrier density acting as shallow donors inside the ZnO thin films, decreasing the screening effect and improving the piezoelectric efficiency.[107]

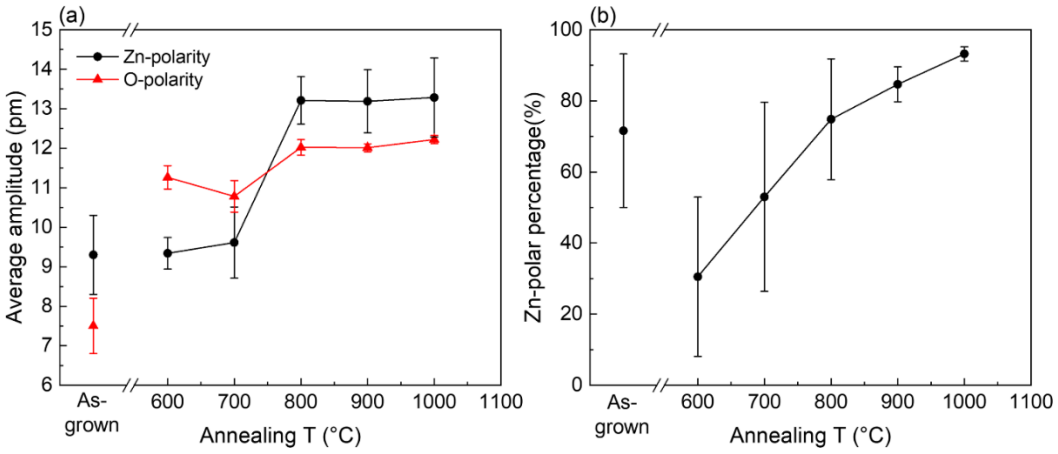

Figure 3.27: Average piezoelectric amplitude on (a) Zn-polar and O-polar area, and (b) percentage of Zn-polar area of ZnO thin films.

Figure 3.27b shows that the Zn-polar percentage decreases from 71.7 % in the as-grown thin film to 30.5 % in the thin film annealed at 600 °C, expressing the development of O-polar domains after annealing at this temperature. Then, the Zn-polar percentage increases continuously up to 93.2 % as the annealing temperature is raised to 1000 °C, indicating the predominance of Zn-polar domains. The behavior of Zn-polar percentage with the annealing temperature can be explained as follows: The development of Zn- and O-polar grains in the ZnO stacked thin film during the annealing process is driven by the minimization of free energy per unit volume and the grain boundary mobility. Both of them are strongly anisotropic and can be varied with annealing temperature. While being annealed at 600 °C, the O-polar grains on ZnO thin film were more developed compared to the Zn-polar grains during the grain coarsening and growth process. This is thanks to its lower surface energy,[179] which is favorable for minimizing the free energy of the thin film, leading to faster grain growth of O-polarity. However, the Zn-polar grains were more developed and became predominant at higher annealing temperature. This indicates that the grain coarsening and growth at those higher annealing temperatures were mainly driven by the anisotropy of grain boundary mobility, in which the grain boundary mobility of the Zn-polar grains is faster compared to the O-polar grains. A comparison between grain boundary migrations along Zn- and O-polarity was performed by J. Lee et al..[180] Their results showed that the migration rate is significantly faster in the Zn-polar domains than in the O-polar domains, which is in agreement with our observation. These results show that the high temperature annealing not only helps increase the local piezoelectric amplitude, but also leads to the Zn-polar uniformity in ZnO stacked thin films grown by MOCVD, which can result in significant improvement of overall piezoelectric output.

3.3 Summary of the chapter

By raising the growth temperature from 400 to 750 °C, the SEM image revealed that the ZnO morphology was changed from stacked thin films to columnar thin films, and then to nanowires. The structural analysis also showed an improvement in the orientation along the *c*-axis and crystallinity in nanowires compared to thin film. This is accompanied with the increase of piezoelectric amplitude while the electrical resistivity is very similar among ZnO samples, implying that the enhancement of piezoelectric coefficient is more related to the morphology transition. Moreover, the PFM images presented that Zn-polarity prevailed over O-polarity in ZnO nanowires grown at high temperature. Those results described the strong impact of temperature on the ZnO growth process, which in turn affects its morphology, growth texture, and polarity as well as piezoelectric properties.

On the other hand, increasing the annealing temperature from 600 to 1000 °C also resulted in the improvement of the *c*-axis orientation and crystallinity along the crystallization of ZnO thin film. The carbon impurity from the MOCVD growth process was removed after annealing from 800 °C. Regarding the resistivity, it is significantly increased after the annealing process under O_2 atmosphere, which is in agreement with other reports in literature. Accordingly, the piezoelectric amplitude also increases with the annealing temperature thanks to the better structural orientation and low charge carriers that could screen the piezoelectric potential. Interestingly, the PFM images also revealed that the Zn-polar grains become predominant as the annealing temperature is raised. These results again show the preferable development along the c^+-direction of ZnO at high temperature.

The evolutions of morphology, structural orientation, polarity, resistivity and piezoelectric amplitude with the growth and annealing temperature are studied, revealing a strong correlation of ZnO structural, electrical and piezoelectric properties. The *c*-axis orientation, polarity uniformity as well as high piezoelectric amplitude are improved at higher growth and annealing temperature, showing that high temperature can be employed to fabricate ZnO structures with high piezoelectric performance. In particular, the ZnO nanowires show superior properties for piezoelectric application compared to thin films. A comparison in mechanical properties between the ZnO thin film and nanowire structures can be performed when integrating them into the piezoelectric devices.

Chapter 4
Effect of flow rates on the structural and piezoelectric properties of ZnO thin films and nanowires

In order to improve the ZnO piezoelectric performance, it is necessary to study the effect of growth conditions on the ZnO formation process. Based on that statement, the optimal growth parameters can be found and applied to tune the ZnO properties in such a way that is favorable for the piezoelectric aplications. In Chapter 3, the effect of temperature during the growth and the post-thermal annealing process on the ZnO properties was revealed. The ZnO thin films in the stacked configuration were formed at 500 °C, while the vertisally aligned ZnO nanowires were grown at 700 °C. In this chapter, we systematically varied the O_2 gas and DEZn solution flow rates while maintaining other parameters in order to investigate their influences on the properties of ZnO thin films and nanowires grown by PLI-MOCVD. The ZnO growths were sequentially performed at 500 and 700 °C, for which the ZnO thin films and nanowires were formed, respectively, as previously shown in Chapter 3. Different morphologies of ZnO thin films and nanowires were obtained. The impact of flow rate conditions at each growth temperature was thoroughly analyzed, showing the large variation of the structural, electrical and piezoelectric properties as well as their strong correlation. The results demonstrate the ability of the PLI-MOCVD system to modify the ZnO properties in order to improve its piezoelectric efficiency by carefully adjusting the O_2 gas and DEZn solution flow rates combined with dedicated growth temperatures.

4.1 Effect of flow rates at low growth temperature

4.1.1 Introduction and objectives

Besides the temperature, the flow rates of reactants also play important roles that can greatly affect the ZnO formation during the MOCVD process. By varying the flow rates of DEZn and H_2O used as precursors, Fanni et al. obtained ZnO thin films with different morphologies.[77] The XRD investigation revealed that there was a large variation of structural orientation from the non-polar *a*-axis to the polar *c*-axis when the flow rates were changed (**Figure 4.1**). On the other hand, D. Montenegro et al. showed that ZnO thin films and nanowires with different lengths and diameters were grown by changing the nitrous oxide (N_2O) and dimethylzinc–triethylamine (DMZn–TEN) flow rates.[125] This described that the relative growth rate along the polar *c*-axis and along other directions was influenced by the variation of precursor flow rates. It has been shown that the flow rates of reactants can change the value of the surface energy as well as the relative growth rates of the ZnO crystalline planes during its growth, leading to changing the main growth direction and resulting in various ZnO morphologies and properties.[62,127,181] The growth direction involves the ZnO structural

orientation and polarity, which are important properties that strongly affect the ZnO piezoelectric performance. Up to now, there is no report about the impact of the flow rates on the crystal polarity and piezoelectric properties as well as their correlation with other properties in ZnO thin films and nanowires.

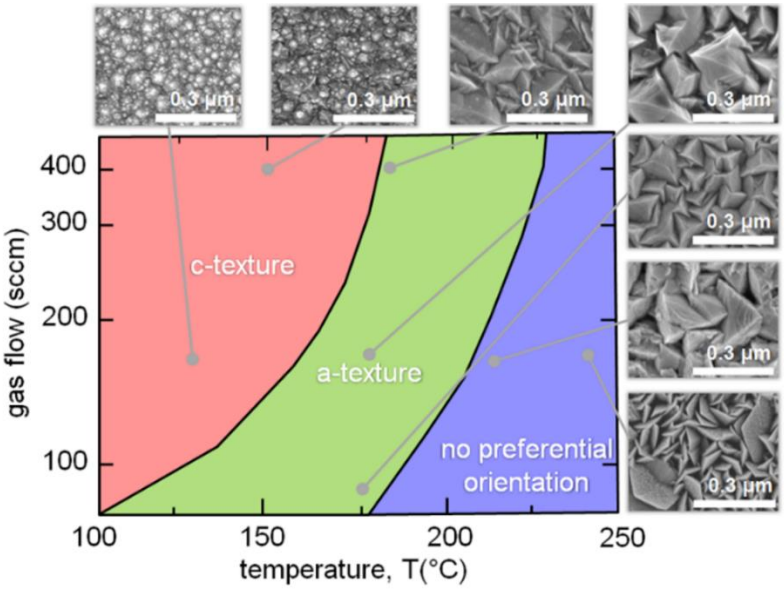

Figure 4.1: Combined effects of gas flow and temperature on the morphology and the preferential orientation of ZnO films grown on glass substrates by MOCVD.[77]

In the first part of Chapter 4, the DEZn solution and O_2 gas flow rates are varied while the growth temperature is kept at 500 °C in the regime where ZnO stacked thin films are formed. The objective is to investigate the effects of flow rates on ZnO growth in the PLI-MOCVD process in that regime. By sequentially varying each flow rate, different morphologies of ZnO thin films are observed by FESEM. The PFM imaging revealed that there is a large variation of crystal polarity distribution along with the morphology change. The structural, electrical properties and their strong correlations with piezoelectric properties are further demonstrated by XRD, Raman spectroscopy, and TLM. This work was partly published as Q.C. Bui et al. "Tuneable polarity and enhanced piezoelectric response of ZnO thin films grown by metal – organic chemical vapour deposition" in *Mater. Adv.*, 2022, **3**, 498.

4.1.2 Experiment

4.1.2.1 ZnO thin films grown by PLI-MOCVD

The ZnO samples were grown in the Annealsys MC-200 PLI-MOCVD system using DEZn and O_2 gas as reactants, while Ar gas was used as a gas carrier and mixed gas with O_2 to maintain the gas volume. The chamber pressure was maintained at 3 mbar, and the growth temperature was kept at 500 °C for both series. The DEZn solution was prepared in cyclohexane solvent as shown in **Section 2.1.3**. The DEZn solution and O_2 gas were also introduced into the reactor chamber with various flow rates. The heavily doped p-type Si (100) wafers were used as substrates and as bottom electrodes during PFM measurements.

In the first series of samples, the O_2 gas flow rate was varied in the range of 100 – 700 sccm, while the DEZn solution flow rate was maintained at 0.5 g/min. The flow rate of mixed Ar gas was

also adjusted in the opposite way of O_2 flow rate variation in order to maintain the total gas volume introduced into the reactor chamber. In the second series of samples, the DEZn solution flow rate was varied between 0.2 and 0.5 g/min, while the O_2 gas flow rate was kept at 500 sccm. The reference sample for both series is the one grown with the 0.5 g/min DEZn solution and 500 sccm O_2 gas flow rates. Correspondingly, the O_2/DEZn molar flow rate ratio was varied from 16 to 198 in the two series of samples.

At first, all ZnO thin films were grown with the same duration. However, the growth rate was varied depending on the flow rate condition, leading to different thickness among thin films. Since the thickness also strongly influences the structural, electrical as well as piezoelectric properties of ZnO thin films, it can interfere with the investigation on flow rate effects. **Figure 4.2** presents the FESEM images of ZnO thin films grown with the same flow rate condition (i.e 100 sccm O_2 gas and 0.5 g/min DEZn solution flow rates) but different growth time. The images reveal that the morphology of ZnO thin films are changed with different growth time as well as thickness. To decouple the flow rate effects with the thickness effects, the growth time was adjusted for each sample to fix their thickness to a value of around 900 nm. The details of O_2 gas and DEZn solution flow rates as well as their molar flow rate ratios and the growth time used for each sample are presented in **Table 4.1**.

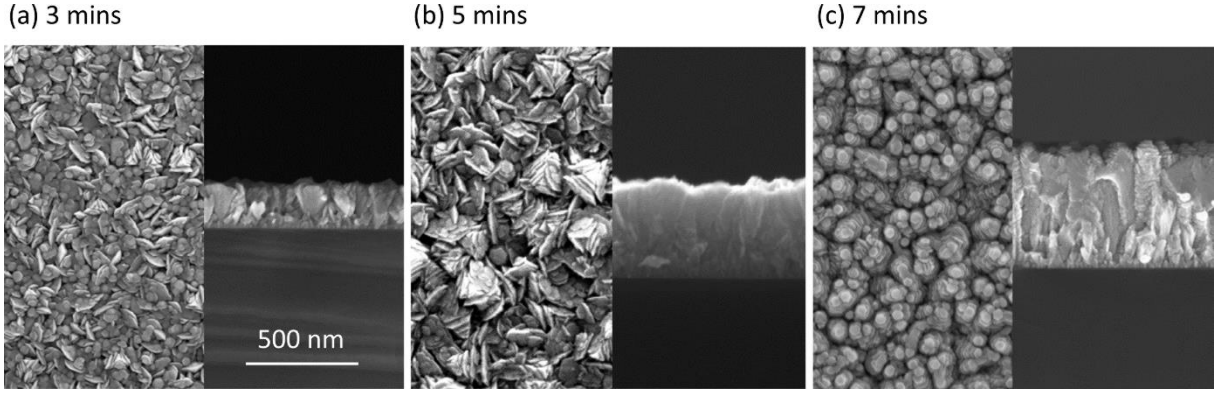

Figure 4.2: Top-view (left) and cross-sectional-view (right) FESEM images of ZnO thin films grown by PLI-MOCVD with 100 sccm O_2 gas and 0.5 g/min DEZn solution flow rates in (a) 3, (b) 5, and (c) 7 minutes.

Table 4.1: The O_2 gas and DEZn solution flow rates, the O_2/DEZn molar flow rate ratios and the growth time of ZnO samples. The growth temperature is fixed at 500 °C.

	O_2 flow rate (sccm)	**DEZn flow rate (g/min)**	**O_2/DEZn ratio**	**Growth time (second)**
Sample 1	100	0.5	16	647
Sample 2	300	0.5	48	692
Sample 3*	500	0.5	79	795
Sample 4	700	0.5	111	948
Sample 5	500	0.4	99	942
Sample 6	500	0.3	132	1050
Sample 7	500	0.2	198	1580

** The ZnO sample grown with 500 sccm O_2 gas and 0.5 g/min DEZn solution is the common sample for both series.*

4.1.2.2 Characterizations

After the growths, the structural, electrical and piezoelectric properties of ZnO samples were investigated by using different characterization techniques (see **Section 2.2**). The morphology of ZnO samples was investigated by FESEM using a Gemini300 FEI ZEISS-SEM. The structural properties were analysed by Raman scattering and XRD measurements. The resistivity was measured using the TLM method. The piezoelectric properties of ZnO samples were studied by datacube PFM.

4.1.3 Results

4.1.3.1 Morphological properties

Figure 4.3 shows the FESEM images of two series of ZnO thin films grown by PLI-MOCVD corresponding to their O_2 gas and DEZn solution flow rate growth conditions. By carefully adjusting the growth time for each growth, the thickness of all thin films grown with different flow rates are kept similar at around 900 nm, as shown in their cross-sectional view images. Thus, the effect of flow rates on ZnO properties is decoupled from the thickness influence, which is a major issue since the ZnO thin films grown at 500 °C are composed of stacked grains, as shown in **Figure 4.3**. While the thickness of all thin films are similar, their top-view images display different morphologies, indicating the impact of flow rate conditions on the ZnO growth processes as well as the properties of the final products. In the series with O_2 flow rate variation, the top-view image of the thin film grown with the 100 sccm O_2 gas flow rate in **Figure 4.3a** presents flat hexagonal shape grains, suggesting the polar *c*-plane of the wurtzite structure. When the O_2 flow rate is increased to 300 and 500 sccm, the hexagonal shape becomes less sharp and the grain size is decreased (**Figures 4.3b-c**). Together with these changes, the cross-sectional view images in **Figures 4.3a-c** also show that the top facet of grains changes from flat to sharp surfaces, expressing the reduction of this surface area. This implies that the ZnO growth proceeded in such a way that minimized this top hexagonal surface area, which is likely the *c*-plane since it has the highest surface energy.[61] The RMS roughness measured by AFM gradually decreases from 21 nm in the thin films grown with 100 sccm O_2 to 8 nm in the thin films grown with 500 sccm O_2, which is related to the decrease of grain size and grain gap when the O_2 flow rate is increased from 100 to 500 sccm. Different from other thin films in the same series, the top-view image of the thin film grown with 700 sccm O_2 in **Figure 4.3d** displays that it comprises many large-sized clusters formed of smaller grains. The RMS roughness also increases back to 21 nm on this thin film.

Among thin films in series with DEZn flow rate variation, the thin film grown with the 0.4 g/min DEZn solution and 500 sccm O_2 gas flow rates (**Figure 4.3g**) shows a similar morphology compared to the thin film grown with the 0.5 g/min DEZn solution and 700 sccm O_2 gas flow rates (**Figure 4.3d**). The presence of large-sized clusters can also be seen on the top-view images of thin films grown with lower DEZn solution flow rate (**Figures 4.3e-f**). Correlatively, the roughness of these three thin films grown are similar and around 21 nm due to the presence of large-sized clusters. However, the density of those large-sized clusters decreases when the DEZn solution flow rate is decreased to 0.3 and 0.2 g/min. Meanwhile, the formation of small round-shaped grains increases

with the decrease of the DEZn solution flow rate (**Figures 4.3e-f**). By referring to the O_2/DEZn molar flow rate ratio, it can be noted that the preferential range for the large-sized cluster formation is from 99 to 111. The change of ZnO thin film morphology with the variation of the DEZn solution and O_2 gas flow rates as well as their ratio expresses the influence of flow rate conditions on the ZnO formation during the PLI-MOCVD process through alternating the free energies and relative growth rates of crystalline planes.[62,127,181]

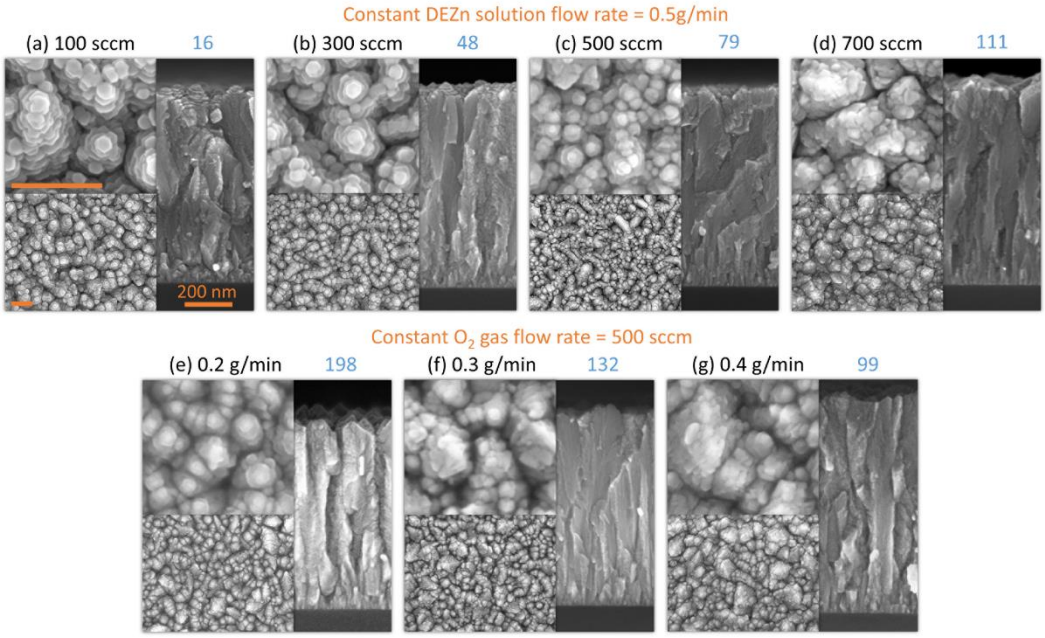

Figure 4.3: Top-view (left) and cross-sectional-view (right) FESEM images of ZnO thin films grown by PLI-MOCVD with the (a) 100, (b) 300, (c) 500, and (d) 700 sccm O_2 gas flow rate for a given DEZn solution flow rate of 0.5 g/min; or with the (e) 0.2, (f) 0.3, and (g) 0.4 g/min DEZn solution flow rate for a given O_2 gas flow rate of 500 sccm. The corresponding O_2/DEZn molar flow rate ratios are indicated in blue. The scale bars correspond to 200 nm.

4.1.3.2 Growth rate of ZnO thin films

Figure 4.4 shows the mean growth rate of ZnO thin films with respect to the O_2 gas and DEZn solution flow rates as well as the O_2/DEZn flow rate ratio. The mean growth rate is deduced from the ratio of the thickness of ZnO thin films over the growth time. **Figure 4.4a** reveals that the ZnO thin film is grown faster when the DEZn solution flow rate is increased while the O_2 gas flow rate is kept constant at 500 sccm. This indicates that the growth rate is limited by the amount of available Zn reactant in our PLI-MOCVD growth process.

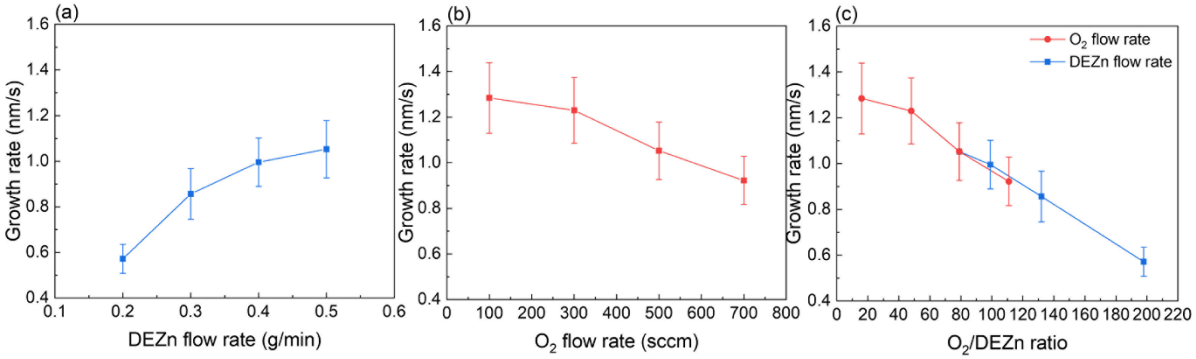

Figure 4.4: Evolution of the mean growth rate of ZnO thin films grown by PLI-MOCVD as a function of (a) the DEZn solution flow rate for a given O_2 gas flow rate of 500 sccm, (b) the O_2 gas flow rate for a given DEZn solution flow rate of 0.5 g/min and (c) the O_2/DEZn flow rate ratio.

On the other hand, increasing the O_2 gas flow rate while maintaining the DEZn solution flow rate at 0.5 g/min leads to a decrease of the growth rate (**Figure 4.4b**). It should be mentioned that the total gas volume introduced into the PLI-MOCVD reactor chamber was kept at constant for all growth conditions by using and adjusting the flow rate of Ar gas mixed with O_2 gas. When the O_2 flow rate was increased, the mixed Ar flow rate was decreased with the same amount. Along with this, the reactor chamber pressure was also maintained at 3 mbar. Thus, the DEZn flow rate introduced into the chamber should be stable and not be pushed out by the increasing O_2 gas flow rate. However, the increase of oxygen reactant amount could increase the probability of reaction between the O and Zn reactants in their gas phase, reducing the Zn reactant amount reaching the substrate to form the ZnO film and resulting in decreasing the ZnO growth rate. Interestingly, **Figure 4.4c** shows that the mean growth rate monotonically decrease when the O_2/DEZn flow rate ratio is increased, signifying again that it is the Zn reactant playing a role of limiting species during the PLI-MOCVD growth process in both series despite the two different ways of varying the flow rate conditions.

4.1.3.3 Structural properties: composition, orientation, strain and grain size

Raman scattering spectra

Figure 4.5a shows the Raman scattering spectra of ZnO thin films grown with different O_2 gas and DEZn solution flow rates. In all thin films, the E_2^{low} and E_2^{high} lines of the ZnO wurtzite structure are detected at 99 and 438 cm^{-1},[143,178] which is similar to other ZnO samples grown by PLI-MOCVD shown in our previous results in Chapter 3. Two large broad bands at around 1360 and 1580 cm^{-1} attributed to C-C bonds present in Raman spectra regardless of the flow rate conditions, evidencing the remaining carbon impurities on ZnO thin films after the growth due to a large amount of organic compounds used during the PLI-MOCVD process.[144] This carbon impurities can be removed by using the high temperature annealing in oxygen atmosphere as shown in **Section 3.2**. Among thin films in the series with O_2 flow rate variation, the E_2^{low} and E_2^{high} lines of the thin film grown with 100 sccm O_2 exhibit the highest intensity compared to other thin films, expressing a better crystallinity of this thin film. In the series with DEZn flow rate variation, it is the thin film grown with 0.2 g/min DEZn which has the highest intense E_2^{low} and E_2^{high} lines compared to other thin films. Interestingly, the thin film grown with 100 sccm O_2 has the highest mean growth rate, while the thin film grown with 0.2 g/min

DEZn has the lowest mean growth rate, as presented in **Figure 4.4**. These observations express that a high crystallinity ZnO thin film can be fabricated within a broad range of growth rate.

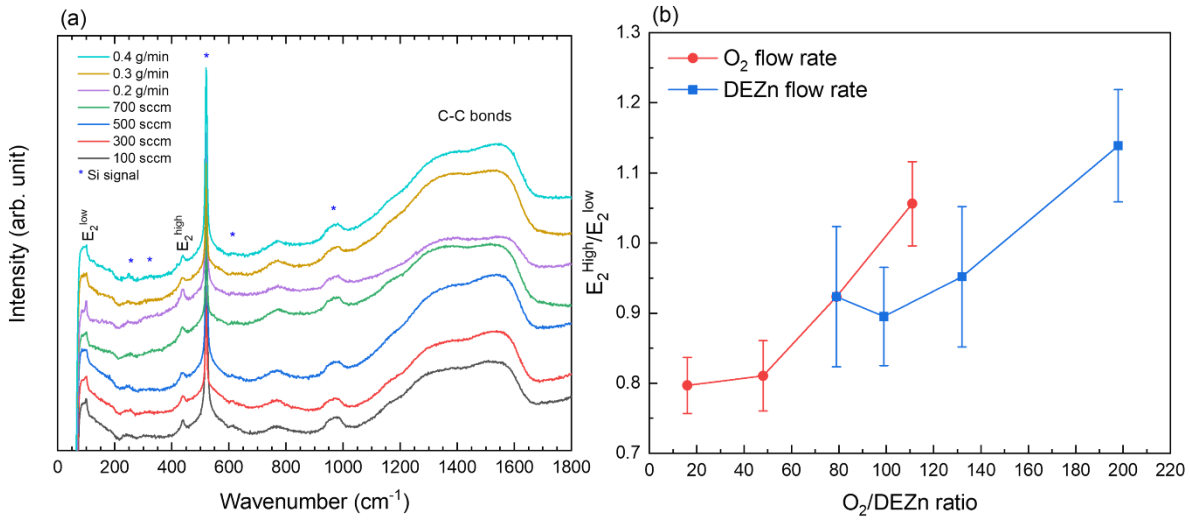

Figure 4.5: (a) Raman scattering spectra of ZnO thin films grown by PLI-MOCVD with various O_2 gas and DEZn solution flow rates. The intensity is plotted in logarithmic scale. (b) Evolution of the E_2^{high}/E_2^{low} intensity ratio as a function of the O_2/DEZn flow rate ratio.

As the E_2^{high} mode corresponds to the O atom lattice vibration and the E_2^{low} mode is associated with the Zn atom lattice vibration in the ZnO wurtzite structure,[143,178] the change of E_2^{high}/E_2^{low} intensity ratio in the ZnO thin films grown with different flow rate conditions reflects the variation of chemical composition (i.e: the O/Zn atomic ratio) inside ZnO thin films. The variation of the E_2^{high}/E_2^{low} ratio in the ZnO thin films with respect to the O_2/DEZn molar flow rate ratio was recorded and presented in **Figure 4.5b**. The result reveals that the E_2^{high}/E_2^{low} ratio tends to increase when the O_2/DEZn flow rate ratio is increased from 16 to 198. The increase of E_2^{high}/E_2^{low} ratio implies an increase of O/Zn atomic ratio inside the ZnO thin film structure, in which the amount of O atoms is relatively higher compared to the Zn atoms. The reason could be due to the stronger oxidizing environment in the PLI-MOCVD chamber as well as the increase of oxygen chemical potential when the O_2/DEZn flow rate ratio is increased. This growth condition is favourable for the formation of Zn vacancies thanks to its low formation energy when the Fermi level is close to the conduction band minimum, as reported by density-functional theory calculations in Ref.[62]. A larger concentration of Zn vacancies formed inside ZnO structure grown at higher O_2/Zn flow rate ratio leads to increasing the O/Zn atom, deduced by the raising of E_2^{high}/E_2^{low} ratio as seen in **Figure 4.5b**.

X-ray diffraction

Figure 4.6 shows the XRD patterns of ZnO thin films grown with different O_2 gas and DEZn solution flow rates. Beside the diffraction peaks of Si substrates, the other diffraction peaks located at 31.8, 34.4, 36.3, 47.5, 62.9, 72.6, and 125.1° are assigned to the 100, 002, 101, 102, 103, 004, and 006 reflections of the ZnO wurtzite structure, respectively, according to the ICDD file labelled 00-036-1451. In **Figure 4.6a**, the XRD patterns of all the ZnO thin films are fairly similar despite the difference in their morphology. A significantly higher intensity of the 002 diffraction peak compared to other ZnO peaks indicates the highly *c*-axis oriented structure of thin films regardless of their different O_2

and DEZn flow rate growth conditions. However, the zoom-in of the XRD patterns in **Figure 4.6b** reveals that there is a considerable peak shift and change in the FWHM of diffraction peaks when the O_2 gas and DEZn flow rates are varied. The intensity, position, and FWHM of the diffraction peaks were then employed to carefully study the effect of O_2 and DEZn flow rate conditions on the structural properties of ZnO thin films using the method as described in **Section 2.2.2**.

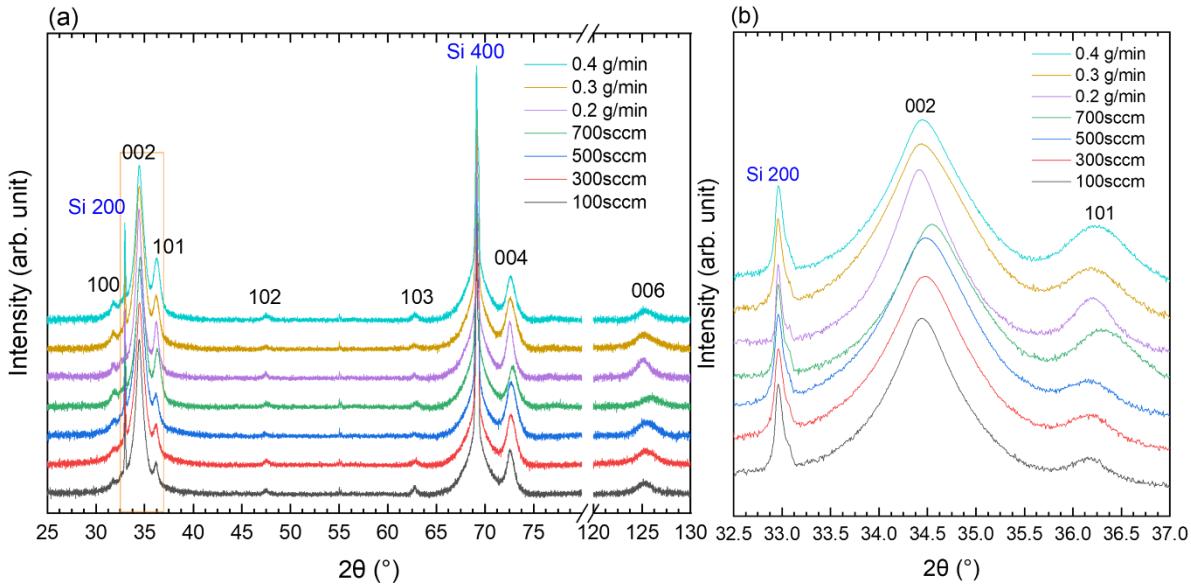

Figure 4.6: (a) XRD of ZnO thin films grown by PLI-MOCVD with various O_2 gas and DEZn solution flow rate conditions; (b) Zoom-in in the area of interest ranging from 32.5 to 37° in the XRD pattern. The intensity is plotted in logarithmic scale.

The texture coefficients of ZnO diffraction peaks were calculated based on the relative intensities of diffraction peaks and presented in **Figure 4.7**, showing a slight variation among thin films. In series with O_2 flow rate variation, **Figure 4.7a** shows that 002 texture coefficient increases from 99.5 to 99.7 % when the O_2 flow rate is increased from 100 to 500 sccm, expressing a small enhancement of the structural orientation along the *c*-axis. Correlatively, the change in morphology where the flat hexagonal shape grains become the smaller and sharper shape grains as observed in **Figures 4.3a-c** also implies a more aggressive growth along the *c*-axis. At 700 sccm O_2, the 002 texture coefficient suddenly decreases down to 98.8%, while the other texture coefficients increase, especially in the direction normal to the (101) plane (**Figure 4.7d**). This describes a decrease of the growth rate along the polar *c*-axis as compared to the growth rate in other directions. In series with DEZn flow rate variation, a similar tendency of texture coefficients is observed when the DEZn flow rate is decreased from 0.5 to 0.4 g/min. In that growth condition, the 002 texture coefficient decreases down to 98.6% (**Figure 4.7b**), while the other texture coefficients increase, mostly the 101 texture coefficient (**Figure 4.7e**). It can also be notably seen that the thin film grown with 0.4 g/min DEZn and the other one grown with 700 sccm O_2 not only exhibit the similar behaviour in their texture coefficients, but also have similar morphologies comprised of many large-sized clusters (**Figures 4.3d and g**). The 002 texture coefficient gradually increases again to 99.4 % when the DEZn flow rate is further decreased down to 0.2 g/min (**Figure 4.7b**), while the texture coefficients along other directions decrease (**Figure 4.7e**). Along with this, the density of large-sized clusters also

decreases on thin films grown with 0.3 and 0.2 g/min DEZn (**Figures 4.3e-f**). Even though the 002 texture coefficient increases again with the decrease of the large-sized cluster density, the thin film grown at 0.2 g/min DEZn exhibiting the lowest density of large-sized cluster still has a lower 002 texture coefficient compared to other thin films which contain no large-sized cluster in their morphology. These results emphasize the strong correlation between the morphology and the structural orientation of thin films, in which the hexagonal or round grains signify a high orientation along the polar *c*-axis, while the large-sized clusters indicate a lower orientation. Nevertheless, the 002 texture coefficients of all ZnO thin films grown with various flow rates are above 98%, indicating their highly *c*-axis oriented structure. In comparison, L. Fanni et al. demonstrated that the growth direction of the ZnO thin film was switched between the non-polar *a*-axis to the polar *c*-axis when the DEZn and H_2O vapour flow rates were varied.[77] Since there are many differences in our growth conditions such as the MOCVD systems, the nature of precursors, the growth temperature and the pressure, a significant difference between our results is not unexpected.

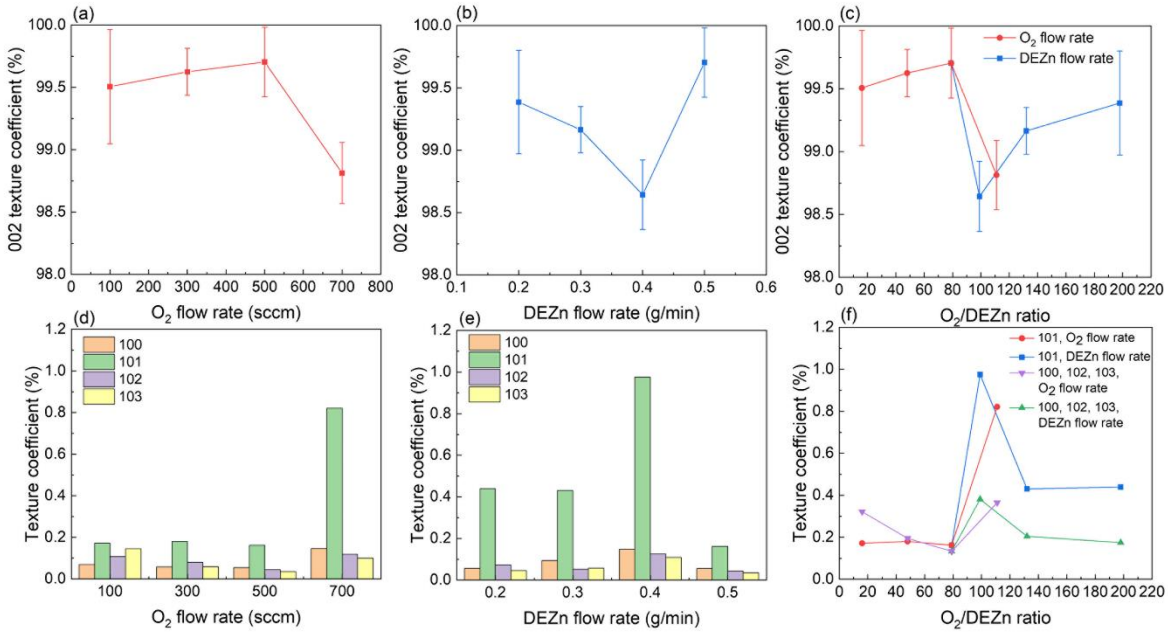

Figure 4.7: Evolution of the 002 texture coefficient as a function of the (a) O_2 gas flow rate, (b) DEZn solution flow rate, and (c) O_2/DEZn flow rate ratio. Evolution of the 100, 101, 102 and 103 texture coefficients as a function of the (d) O_2 gas flow rate, (e) DEZn solution flow rate, and (f) O_2/DEZn flow rate ratio.

The residual homogeneous strains of ZnO thin films were deduced from the shift of 002 peak from its theoretical value and presented in **Figure 4.8**. In all ZnO thin films, the residual strains show negative values, indicating a compressive strain along the polar *c*-axis regardless of the flow rate conditions. Similar to ZnO thin film growths in our previous results shown in Chapter 3, this out-of-plane compressive strain induced by the in-plane biaxial stress is generated during the Volmer-Weber growth mode of polycrystalline ZnO thin films. In this growth mode, the growth imitates by the formation of isolated islands, followed by the coalescence process, during which a significant tensile biaxial stress is developed inside the thin films.[172,173,182] After that, the stress can partially or entirely be relieved during the film thickening process due to the excess incorporated atoms at grain

boundaries.[172,173,182] In our results, only the thin film grown with 0.2 g/min DEZn exhibits the total strain relaxation (**Figure 4.8b**). This thin film also shows a better crystallinity compared to other thin films as suggested by Raman scattering spectra (**Figure 4.5**). Among thin films in series with the O_2 flow rate variation, an efficient strain relaxation is also observed in the thin film grown with the 100 sccm O_2 (**Figure 4.8a**). Overall, it can be seen that the mean homogeneous strain decreases when either the O_2 gas or DEZn solution flow rates are decreased, as shown in **Figures 4.8a-b**. Besides, the strains of thin films could also be related to their grain morphologies. In particular, the thin film grown with 100 sccm O_2 exhibiting a small homogeneous strain also has large grain size and grain gap as revealed in **Figure 4.3a**. In comparison, larger homogeneous strains are shown in thin films grown with 300 and 500 sccm O_2, of which morphologies present smaller grain sizes and grain gaps (**Figures 4.3b-c**). The thin film grown with 700 sccm O_2 containing compact large-sized clusters form small grains (**Figure 4.3d**) has the largest homogeneous strain. These observations express that the morphology with less compact and bigger grains should exhibit a smaller tensile biaxial stress as well as residual strain. This could be explained by the grains growth and coalescence to form bigger grains in the Volmer-Weber growth mode, during which the surface free energy at grain boundaries are removed and the intrinsic stress inside the film is relieved.[172] On the other hand, the thin film grown with the 0.4 g/min DEZn solution and 500 sccm O_2 gas flow rates shows a much lower homogeneous strain compared to the thin film grown with 0.5 g/min DEZn solution and 700 sccm O_2 gas flow rates (**Figures 4.8b-c**), while both their morphologies exhibits compact large-sized clusters of small grains (**Figures 4.3d and g**). A significant difference in homogeneous strains between these two thin films despite their similar morphologies implies that the homogeneous strain is more influenced by the flow rates rather than by the morphology or the O_2/DEZn ratio (**Figure 4.8c**). The flow rate is related to the atom density and the morphology is related to the surface roughness, both of which can affect the surface free energy and the diffusion of atoms at the grain boundaries as well as the variation of the homogeneous residual strain inside thin films during its thickening stage.[182] As the O_2 gas and DEZn solution flow rates are increased, the homogenous strain is increased. The largest homogeneous strain is observed in the thin film grown with the 700 sccm O_2 gas flow rate and 0.5 g/min DEZn solution flow rate, which are the highest flow rates in both series (**Figure 4.8c**). This could be due to the high flow rate environment preventing the surface diffusion of atoms out of or into the grain boundaries favouring the relaxation.

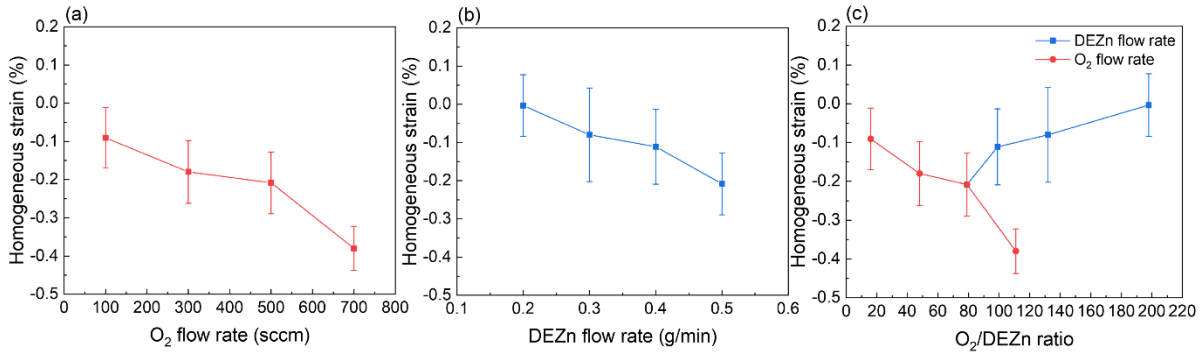

Figure 4.8: Evolution of the mean homogenenous strain as a function of the (a) O_2 gas flow rate, (b) DEZn solution flow rate, and (c) O_2/DEZn flow rate ratio.

The mean inhomogeneous strain and average crystallite size of ZnO thin films are estimated by using Williamson-Hall method as described in **Section 2.2.2**. The Williamson-Hall plot of thin films grown with different flow rate conditions are presented in **Figure 4.9**. The inhomogeneous strain and crystallite size are deduced from the slope and the Y-intercept of the linear curves, respectively, and shown in **Figure 4.10**. In the series with O_2 flow rate variation, the result in **Figures 4.10a** shows that the inhomogeneous strain increases as the O_2 flow rate is increased from 100 to 500 sccm, then decreases at 700 sccm. In the series with DEZn flow rate variation, it increases when the flow rate is raised from 0.2 to 0.3 g/min, slightly decreases at 0.4 g/min, and then increases again at 0.5 g/min (**Figures 4.10b**). These results suggest that the inhomogeneous strain tends to be smaller in the thin films grown with lower O_2 and DEZn flow rates. In the lower flow rate environment, the atom arrangement during the growth is enhanced thanks to the higher surface diffusion, resulting in the formation of thin films with a better crystallinity and less defects.[77] The thin films grown with the 100 sccm O_2 and the thin film grown with 0.2 g/min DEZn, which are the best crystallinity thin films among their series as shown in Raman scattering spectra, also exhibit the lowest inhomogeneous strain. However, in **Figure 4.10c**, it can be seen that the increase tendency of the inhomogeneous strain with the O_2 gas and DEZn solution flow rates is disrupted when the O_2/DEZn ratio is in the range of 99 – 111, corresponding to the two thin films whose morphologies comprise of a high number density of large-sized clusters (**Figures 4.3d and g**). The inhomogeneous strains in the thin film grown with the 700 sccm O_2 and 0.5 g/min DEZn and in the thin film grown with the 500 sccm O_2 gas and 0.4 g/min DEZn solution flow rates are notably similar and equal to 0.44 and 0.43 %, respectively. This implies that the inhomogeneous strain is more affected by the morphology or the O_2/DEZn ratio rather than by the flow rates, which is different from the homogeneous strain. As the mean inhomogeneous strain is caused by microstructural defects in the ZnO thin films, its variation implies a change in the type and density of incorporated defects inside the thin films grown with different O_2 and DEZn flow rates.

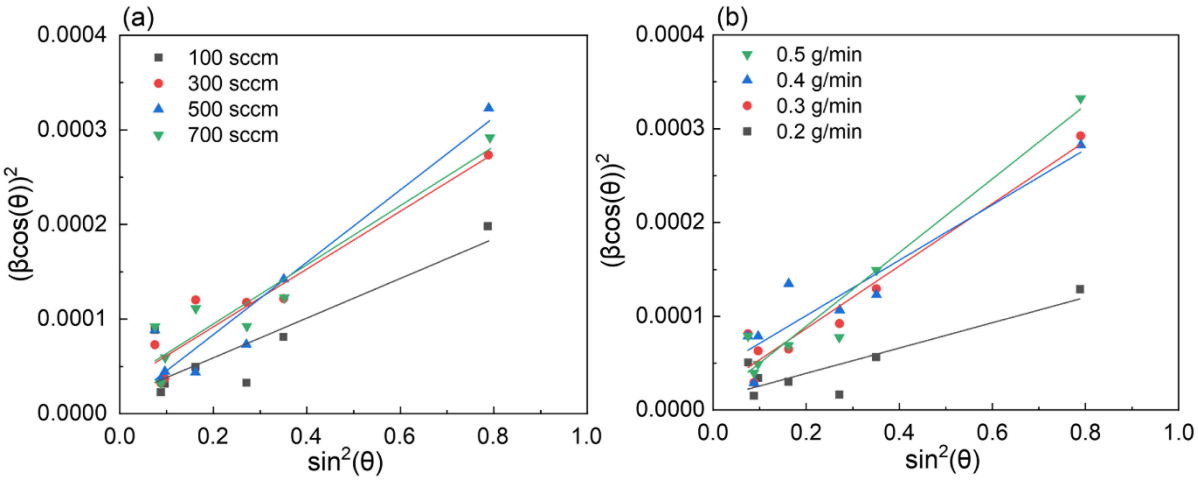

Figure 4.9: Williamson-Hall plots of ZnO thin films as a function of the (a) O_2 gas and (b) DEZn solution flow rates.

The average crystallite size of thin films were estimated by Williamson-Hall method and presented in **Figures 4.10d-f**. As the XRD patterns were scanned with the out-of-plane configuration,

the average crystallite size presented here is calculated in the vertical dimension that is perpendicular to the Si substrate. The result shows values around 20 – 52 nm, which is similar to Ref.[183]. The thin film grown with the 500 sccm O_2 and 0.5 g/min DEZn has the highest average crystallite size at around 52 nm, which is related to its aggressive growth along the polar *c*-axis compared as indicated by its highest 002 texture coefficient (**Figures 4.7c**). In contrast, the thin films grown with the 700 sccm O_2 gas and 0.4 g/min DEZn solution flow rates have the smallest average crystallite size at around 24.5 and 21.5 nm due to their lowest growth rate along the *c*-axis as implied by their lowest 002 texture coefficients (**Figures 4.7c**). These results indicate that the average crystallite size of ZnO thin films strongly depends on the growth rate along the *c*-axis.

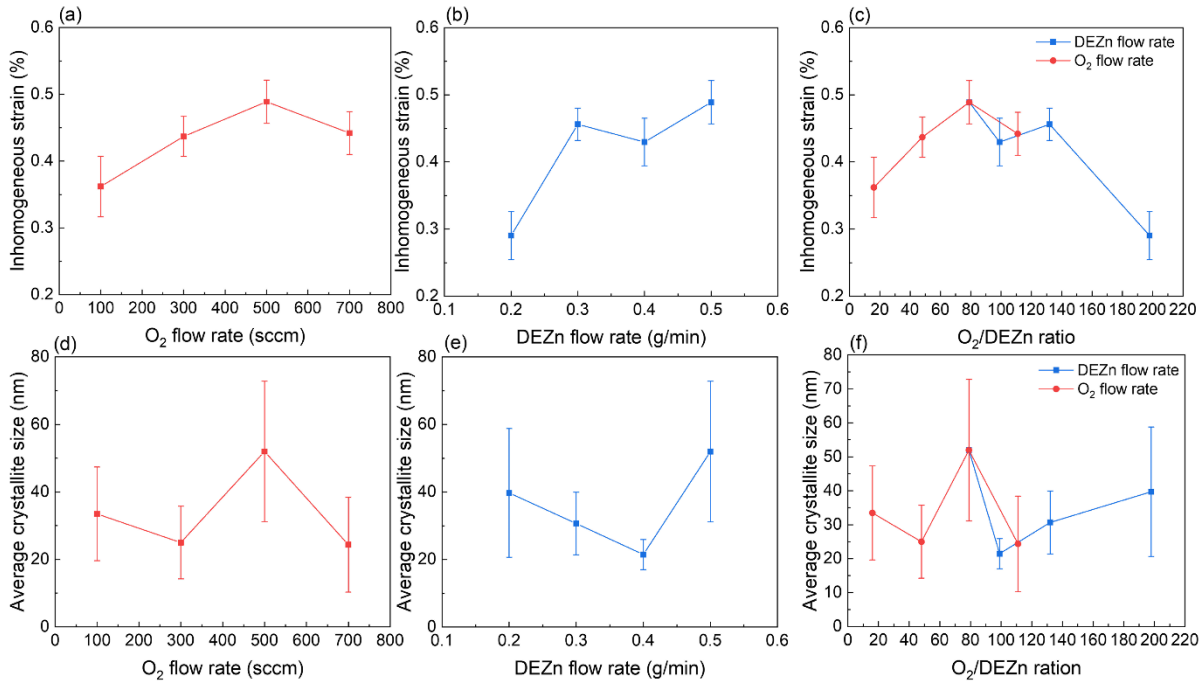

Figure 4.10: Evolution of the mean inhomogeneous strain as a function of the (a) O_2 gas flow rate, (b) DEZn solution flow rate, and (c) O_2/DEZn flow rate ratio. Evolution of the average crystallite size as a function of the (d) O_2 gas flow rate, (e) DEZn solution flow rate, and (f) O_2/DEZn flow rate ratio.

Overall, the XRD analysis shows the impacts of the O_2 gas and DEZn solution flow rate as well as the O_2/DEZn ratio conditions on the structural properties of ZnO thin films, namely the orientation, homogeneous strain, inhomogeneous strain and crystallite size. While the homogeneous strain is more dependent on the flow rates rather than the O_2/DEZn ratio, the orientation and inhomogeneous strain exhibit a stronger relation with the O_2/DEZn ratio. For instance, the disrupted variation in the orientation in **Figure 4.7c** and the inhomogeneous strain in **Figure 4.10c** occur when the O_2 gas flow rate is increased from 500 to 700 sccm, or when the DEZn solution flow rate is decreased from 0.5 to 0.4 g/min, corresponding to the O_2/DEZn ratio lying in range of 99 – 111. A remarkable morphology change from flat hexagonal/round grains to large-sized clusters is also observed around this O_2/DEZn ratio (**Figures 4.3d and g**).

4.1.3.4 Crystal polarity, piezoelectric response, and resistivity of ZnO thin films

Crystal polarity

Figure 4.11 illustrates the topography of thin films along with their piezoelectric amplitude and phase responses. The corresponding amplitude and phase histograms are shown in **Figure 4.12**. As the interference of the electrostatic effect is removed by using the high stiffness tip during PFM scanning (see **Section 2.2.1**), the piezoelectric amplitude is proportional to the piezoelectric coefficient and applied voltage amplitude.[135,136] This means that the brighter domain in the piezoelectric amplitude image corresponding to the higher amplitude response indicates the higher piezoelectric coefficient, and vice versa. In the phase images, the piezoelectric phase response with respect to the applied voltage phase identifies the polarity of the ZnO thin film. The bright area with the phase at around 70° represents the Zn-polar domain, and the dark area with the phase at around -90° represents the O-polar domain (see **Section 2.2.1**). The piezoelectric phase images reveal a striking difference in the polar domain distribution on ZnO thin films when the O_2 gas and DEZn solution flow rates are varied. On thin films grown with the 100 and 300 sccm O_2 gas flow rates, their phase images display the predominant Zn-polarity (**Figures 4.11c and f**). The phase image of thin film grown with the 500 sccm O_2 gas flow rate in **Figure 4.11i** shows some domains with the mix of dark and bright piezoelectric phases, caused by the neutralization of two opposite polar domains when they are stacked together. In **Figure 4.11l**, the phase image of the thin film grown with the 700 sccm O_2 shows the predominant O-polarity. By comparing the topography with the piezoelectric phase images, it can be seen that the hexagonal and round shape grains exhibit the Zn-polarity (**Figures 4.11a-i**). On the thin film grown with the 700 sccm, the large-sized clusters exhibit the O-polar signals, while surrounding smaller grains show the Zn-polar signals (**Figures 4.11j-l, v-x**). Similarly, the phase images of the thin films grown with the 0.2, 0.3, and 0.4 g/min DEZn also revealed that the O-polar signals is related to the large-sized clusters while the Zn-polar signals are shown by the smaller round shape grains (**Figures 4.11m-u**). These images display the difference in the grain sizes and shapes between two opposite polarities, indicating their distinct growth mechanism.

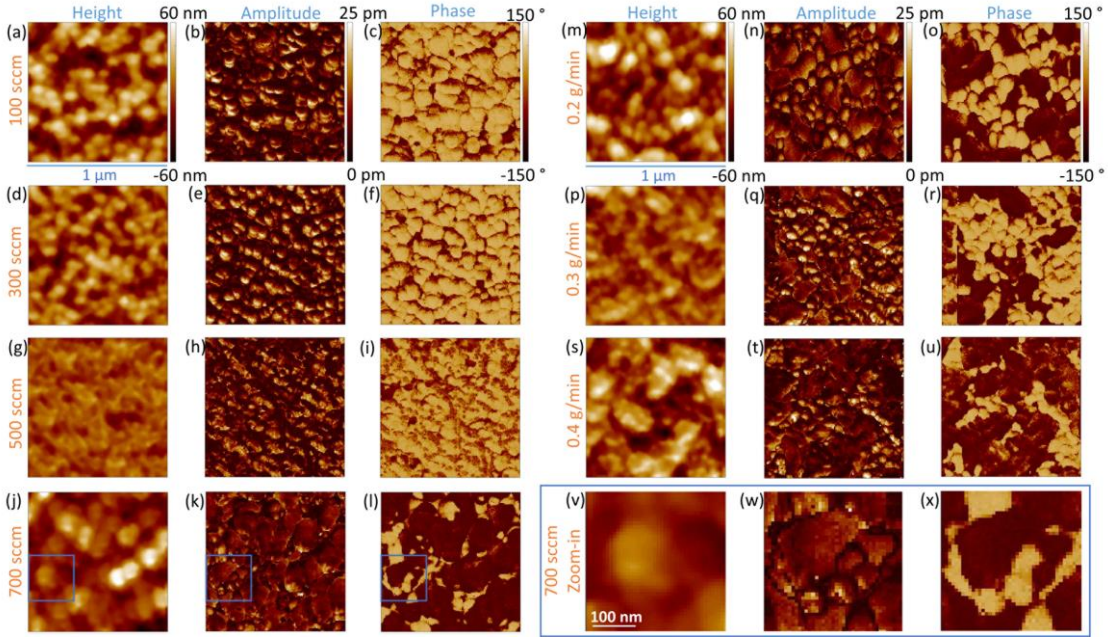

Figure 4.11: Topography, piezoelectric amplitude, and piezoelectric phase of ZnO thin films grown by PLI-MOCVD with the (a-c) 100, (d-f) 300, (g-i) 500, and (j-l) 700 sccm O_2 gas flow rate for a given DEZn solution flow rate of 0.5 g/min; or with the (m-o) 0.2, (p-r) 0.3, (s-u) 0.4 g/min DEZn solution flow rate for a given O_2 gas flow rate of 500 sccm. (v-x) Zoom-in in the area of interest in the thin film grown with the O_2 gas flow rate of 700 sccm.

Correspondingly, their phase histograms in **Figures 4.12h-j** also exhibit the large change of the polarity distribution with the flow rate conditions. On the phase histograms of thin films grown with 100, 300 and 500 sccm O_2 in **Figures 4.12h-j**, only the positive peak representing the Zn-polarity is clearly seen. In contrast, the phase histogram of the thin film grown with 700 sccm O_2 in **Figures 4.12k** shows the negative peak representing the O-polarity that is higher than the positive peak of Zn-polarity, indicating the O-polar predominance. The phase histograms of thin films grown with 0.2, 0.3 and 0.4 g/min DEZn in **Figures 4.12l-n** show both positive and negative peaks with similar distribution. It can also be seen in **Figures 4.11 and 4.12** that the large change of the polarity distribution occur when the O_2 gas flow rate is increased from 500 to 700 sccm or when the DEZn flow rate is decreased from 0.5 to 0.4 g/min, corresponding to the sudden morphology change from round shape grains to highly dense large-sized clusters. This implies that the polarity switch could be related to the change in surface energies of crystalline planes affected by the variation of O_2 gas and DEZn solution flow rates. With DFT calculation, C. Tang et al. have shown that the O-polar *c*-plane is more stable than the Zn-polar one in the O-rich conditions,[179] which corresponds to the high O_2/DEZn ratio in our case. As the growth of ZnO proceeds in such a way that minimizes the free energy of the system,[184] the development of O-polar *c*-plane possessing a lower surface energy is more favourable compared to Zn-polar *c*-plane during the thickening stage in the high O_2/DEZn ratio conditions. This leads to the development of O-polar domains when the O_2/DEZn ratio is increased, as seen in **Figures 4.11l**, **o**, **r** and **u**.

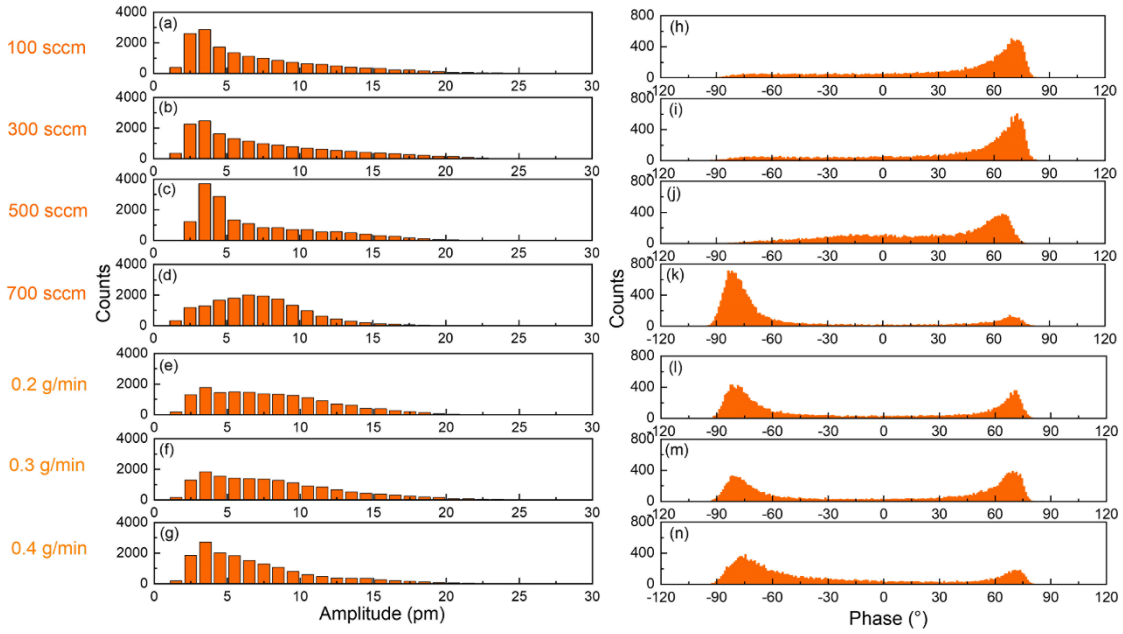

Figure 4.12: (a-g) Raw amplitude and (h-n) phase histograms of ZnO thin films deduced from PFM measurements.

Piezoelectric amplitude and coefficient

Furthermore, a data treatment was performed in order to separate the piezoelectric amplitudes of the Zn-polarity, O-polarity, and non-polar domains. The data points with the piezoelectric phase higher than 50° assigned to the Zn-polar signals had their piezoelectric amplitude unchanged, while the data points with the piezoelectric phase lower than -50° assigned to the O-polar signals had their piezoelectric amplitude multiplied by -1. Other data points assigned to non-polar domains were removed. **Figure 4.13** presents the piezoelectric amplitude histograms of thin films after data treatment. In **Figures 4.13a-c**, the histograms of thin films grown with the 100, 300 and 500 sccm O_2 show that most of the piezoelectric signals are Zn-polar coming from the hexagonal and round shape grains. In the opposite, the histogram of the thin film grown with the 700 sccm O_2 shown in **Figure 4.13d** exhibits that most of the piezoelectric signals are O-polar generated on the large-sized clusters. The thin film grown with 0.4 g/min DEZn exhibiting the similar high density of large-sized clusters also presents the large number of the O-polar signals in its histogram (**Figure 4.13g**). Meanwhile, the histograms of thin films grown with the 0.2 and 0.3 g/min DEZn in **Figures 4.13e-f** express the coexistence of Zn-polar signals from small round-shaped grains and O-polar signals from large-sized clusters. Notably, the histograms show that the piezoelectric amplitude distribution of the Zn-polar signals stretches to higher values (i.e over 20 pm) as compared to the O-polar signals. On the amplitude images, these high amplitude signals are illustrated by the very bright spots, which are only observed on the Zn-polar domains. This implies that the piezoelectric coefficient of the Zn-polar domains is higher compared to the O-polar domains. The difference in the piezoelectric coefficient between two polarities could be due to the difference in the impurities contained in each polar domain. S. Lautenschlaeger et al. have shown that there are larger amount of impurities incorporated in ZnO films grown by chemical vapour deposition on O-polar ZnO substrate than on the Zn-polar ZnO substrate.[161] The higher density of impurities that can act as shallow donors in the O-polar domains leads to the severe screening effect, resulting in lower piezoelectric efficiency as compared to the Zn-polar domains.[22,35,36,48]

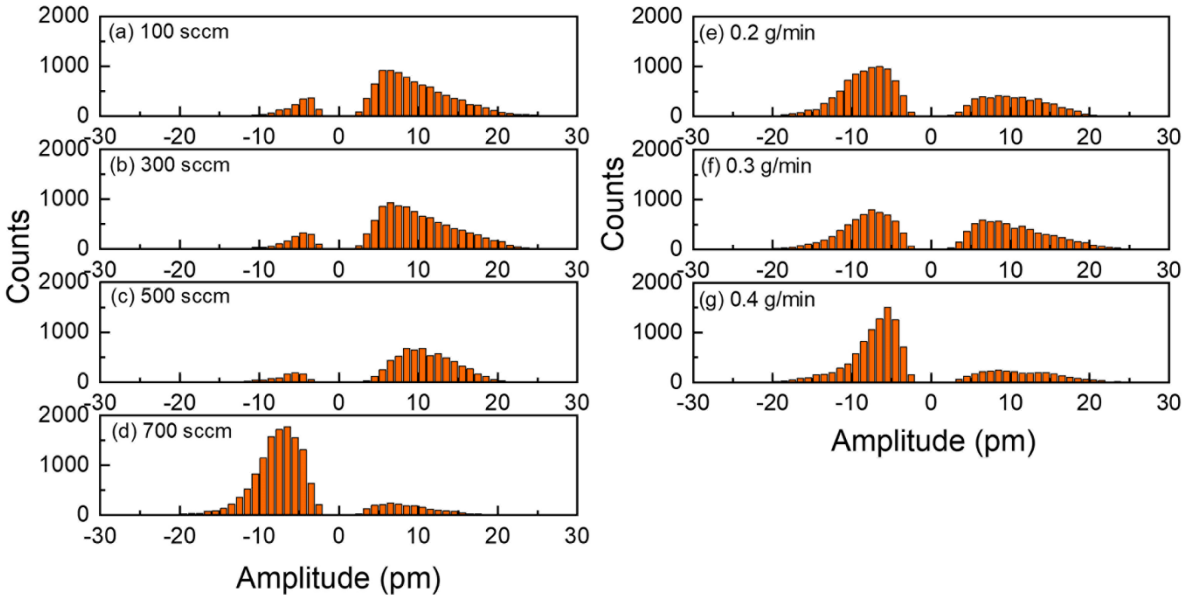

Figure 4.13: Piezoelectric amplitude histogram after data treatment of ZnO thin films grown by PLI-MOCVD with the (a) 100, (b) 300, (c) 500, (d) 700 sccm O_2 gas flow rate for a given DEZn solution flow rate of 0.5 g/min; or with the (e) 0.2, (f) 0.3, (g) 0.4 g/min DEZn solution flow rate for a given O_2 gas flow rate of 500 sccm.

In order to study more carefully the evolution of piezoelectric properties with the flow rate conditions, the mean piezoelectric amplitude on the Zn- and O-polar domains were calculated using the data after treatment. The Zn-polar percentage was also deduced from the ratio of the Zn-polar signal amount to the total amount of Zn- and O-polar signals, excluding the non-polar signals. In **Figures 4.14a-c**, the mean piezoelectric amplitudes on both polarities are varied in range of 5 – 11 pm, corresponding to the piezoelectric coefficients d_{33} at around 1 – 2.2 pm/V. The results presented in **Figures 4.14a-c** also clearly show that Zn-polar amplitude is higher than O-polar amplitude. On Zn-polar domains, the piezoelectric amplitudes are fairly similar at around 10 pm among the thin films, except the thin film grown with the 700 sccm O_2 in which the amplitude decreases to 8.7 pm (**Figures 4.14a-c**). On O-polar domains, the piezoelectric amplitude increases from 5.2 to 7.7 pm as the O_2 flow rate is increased from 100 to 700 sccm. It further increases from 6.6 to 8.4 pm as the DEZn flow rate is decreased from 0.5 to 0.2 g/min. It can also be seen that the piezoelectric amplitude of O-polar domains continuously increases when the O_2/DEZn ratio is higher (**Figure 4.14c**). This can be explained by the less incorporation of impurities acting as shallow donors such as Al_{Zn} and Ga_{Zn} at higher oxygen chemical potential as the O_2/DEZn ratio is increased,[68] resulting in decreasing the screening effect.[22,35,36,48] Regarding the Zn-polar percentage (**Figures 4.14d-f**), the thin films grown with the 100, 300, and 500 sccm O_2 show values at around 85%, expressing the predominant Zn-polarity. As the O_2 gas flow rate is increased to 700 sccm, the Zn-polar percentage significantly decreases to 14.5%, indicating the predominant O-polarity. The thin film grown with 0.4 g/min DEZn exhibiting similar morphology also has a low Zn-polar percentage at 25%. As the DEZn solution flow rate is decreased to 0.3 and 0.2 g/min, the Zn-polar percentages of thin films are around 40 – 50%, expressing the coexistence of both polarities.

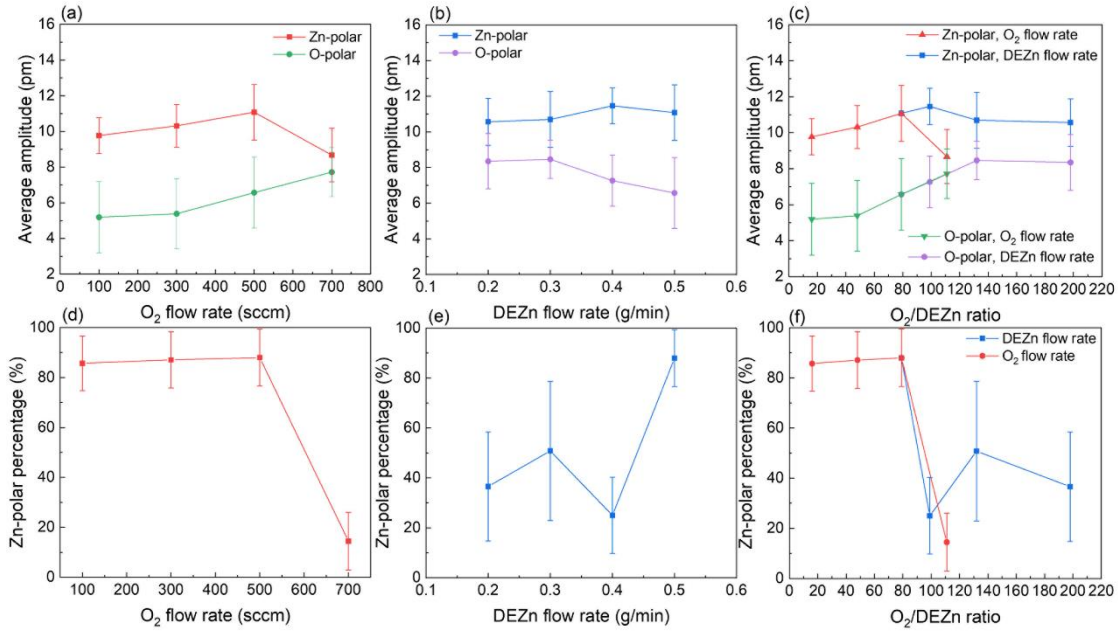

Figure 4.14: Evolution of the mean piezoelectric amplitude on the Zn- and O-polar domains as a function of the (a) O_2 gas flow rate, (b) DEZn solution flow rate, and (c) O_2/DEZn flow rate ratio. Evolution of the Zn-polar domain percentage as a function of the (d) O_2 gas flow rate, (e) DEZn solution flow rate, and (f) O_2/DEZn flow rate ratio.

On the thin film grown with the 700 sccm O_2, its lower Zn-polar piezoelectric amplitude compared to other thin films as shown in **Figures 4.14a-c** can be related to its very low Zn-polar percentage (**Figures 4.14d-f**), corresponding to the strongly predominant O-polarity. In this film, the Zn-polar grains could be so small that the measured amplitudes on these Zn-polar grains can be interfered with and reduced by the amplitude with opposite phase coming from the O-polar grains underneath them. In the opposite case, the thin films grown with the 100 and 300 sccm O_2 exhibit the lowest O-polar piezoelectric amplitude, which could be due to the fact that the measured piezoelectric amplitudes on O-polar grains are compensated by the piezoelectric amplitudes of Zn-polar grains underneath them. The thin films grown with the 0.2 and 0.3 g/min DEZn have the highest O-polar piezoelectric amplitudes and similar Zn-polar piezoelectric amplitudes as compared to other thin films. This implies that both polarities coexist on these thin films without amplitude neutralization as the grain sizes of both polarities are large enough, suggested by their Zn-polar percentages at 40 – 50%.

Electrical resistivity

Figure 4.15 presents the TLM results and the resistivity of ZnO thin films grown with different flow rate conditions. The results show that the resistivity of ZnO thin films is varied from 0.5 to 11.7 Ω.cm (**Figures 4.15b-d**). In the series with O_2 variation, the resistivity increases from 2.7 to 11.7 Ω.cm when the O_2 gas flow rate is increased from 100 to 500 sccm, but then significantly decreases to 0.5 Ω.cm at 700 sccm. In the series with DEZn variation, the resistivity decreases from 11.7 to 2.2 Ω.cm as the DEZn solution flow rate is decreased from 0.5 to 0.4 g/min, then slightly increases 3.9 Ω.cm at 0.2 g/min. It is worth to mention that the thin films with the resistivity higher than 10 Ω.cm are also those exhibiting strongly predominant Zn-polarity. In contrast, the thin film with the resistivity lower than 1 Ω.cm is also the one exhibiting strongly predominant O-polarity. These again suggest that the Zn-polar domains could have a lower density of impurities acting as shallow donors as compared to the O-polar domains, which could be the reason for the higher piezoelectric amplitude response on Zn-polar domains. Nevertheless, the variation of ZnO morphology with the flow rate conditions can also greatly influence its resistivity.

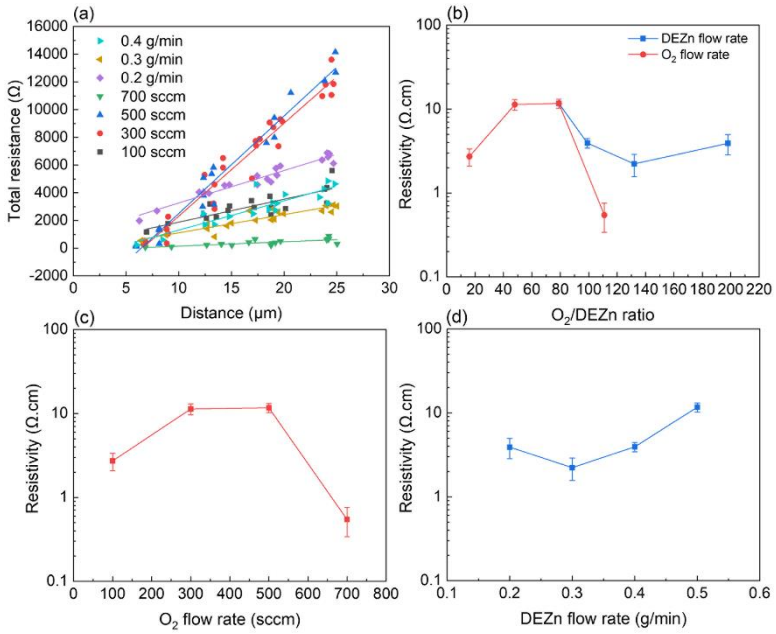

Figure 4.15: (a) Evolution of the total resistance of ZnO thin films grown by PLI-MOCVD as a function of the distance between electrode pairs using the TLM method. Evolution of the resistivity of ZnO thin films as a function of the (b) O_2/DEZn flow rate ratio, (c) O_2 gas flow rate, and (d) DEZn solution flow rate.

These PFM and TLM results show that the piezoelectric properties of the ZnO thin films grown by PLI-MOCVD are greatly influenced by the variation of the flow rate conditions, and have a strong correlation with its morphological, structural, and electrical properties. Along with the morphology transition as observed in FESEM images, the phase response images from PFM scanning reveals that there is also a remarkable change in crystal polarity of ZnO thin films when the O_2 gas and DEZn solution flow rates are varied. Simultaneously, the Raman spectrum analysis implies that the variation of O_2/DEZn flow rate ratio as well as the oxygen chemical potential during the growth can affect the O/Zn atomic ratio in ZnO thin films. This alters the surface energy of ZnO crystalline planes as well as their relative growth rate resulting in changing the growth direction and the crystal polarity. The difference in the shape between the O- and Zn-polar grains as shown in the topography and piezoelectric phase images (**Figure 4.11**) indicates their different growth mechanisms resulted from the growth direction change. By comparing the PFM results with the XRD analysis, it can be seen that the switch of the crystal polarity of ZnO thin films from predominant Zn-polarity to predominant O-polarity occurs concomitantly with the disrupted changes of the texture coefficient (**Figure 4.7c**) and the inhomogeneous strain (**Figure 4.10c**) when the O_2/DEZn flow rate ratio is in the range of 99 – 111. The increase in the density of O-polar large-sized clusters comes along with the decrease in the 002 texture coefficient, expressing the lower *c*-axis crystal orientation of the O-polar large-sized clusters compared to the Zn-polar hexagonal/round grains. In addition, the strong correlation of the polarity switch with the disrupted change of the inhomogeneous strain relating to the microstructure defects suggest the difference in the nature and density of incorporated defects between the O- and Zn-polar domains. The difference in the incorporation of impurities between the O- and Zn-polar domains can lead to their difference in resistivity,[46] and the piezoelectric efficiency

by influencing the free charge carriers causing the screening effect.[89,185] The difference in resistivity is suggested by TLM results, and the lower piezoelectric amplitude of the O-polar domains compared to the piezoelectric amplitude of the Zn-polar domains is observed by PFM measurements.

4.1.4 Discussion: schematic diagram of the processes

In summary, the evolution of the morphological, structural, and piezoelectric properties of ZnO thin films grown by PLI-MOCVD with the DEZn solution and O_2 gas flow rates as well as with the O_2/DEZn flow rate ratio is illustrated in **Figure 4.16**.

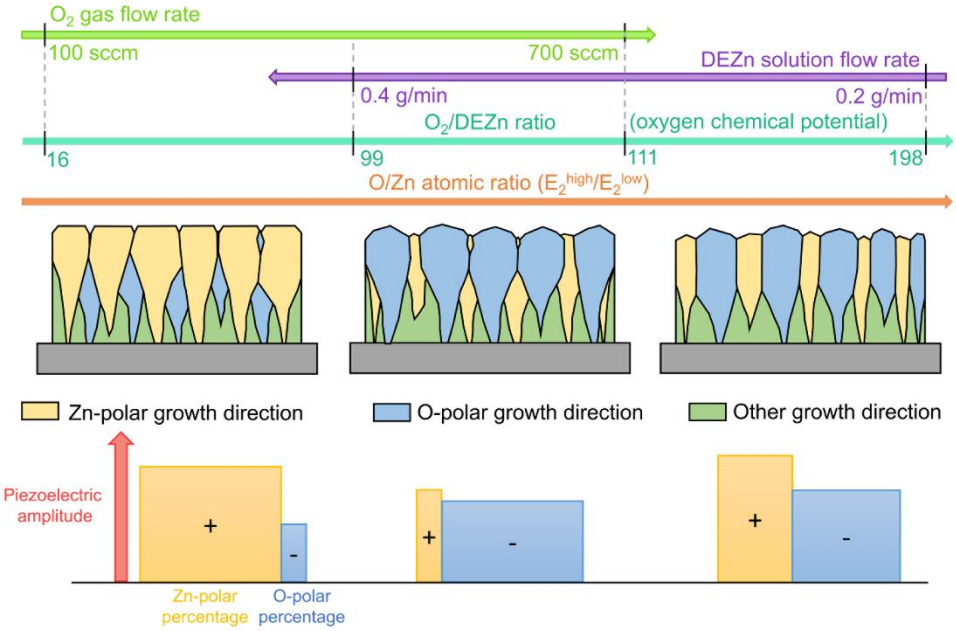

Figure 4.16: Schematic representing the dependence of the morphological, structural, and piezoelectric properties of ZnO thin films grown by PLI-MOCVD on the DEZn solution and O_2 gas flow rate conditions.

In all flow rate conditions, ZnO thin film growths are highly oriented along the polar *c*-axis thanks to the highest surface energy of *c*-planes as well as their growth rates compared to other directions.[61] However, there is a difference between the relative growth rates on c^+-and c^--planes, which can be varied as the DEZn and O_2 flow rates are changed. When the O_2 gas flow rate is low, corresponding to the O_2/DEZn ratio ranging from 16 to 99, the growth on the c^+-plane is faster due to its higher surface energy in a low oxygen chemical potential condition.[45] This leads to the predominance of Zn-polar hexagonal and round shape grains on thin films. When the O_2/DEZn ratio is in range of 99 – 111, the relative growth rate on the c^--plane becomes higher than on the c^+-plane since it has higher surface energy as the oxygen chemical potential is increased.[45] Consequently, the O-polar large-sized clusters are strongly developed in this range. With further increase of the O_2/DEZn ratio above 111, the growth rates on both polar planes are fairly similar, resulting in the coexistence of Zn- and O-polar domains. Since the ZnO thin film is grown with a very low Zn flow rate compared to the O_2 flow rate in this condition, the growth strongly depends on the incorporation of limited Zn reactant on the growing front.[186] As the Zn-polar domains provide three dangling bonds per O atom while the O-polar domains have one dangling bond per O atom on their surface, the

incorporation rate of Zn atoms is much faster on the Zn-polar domains.[59] As a result, the development of Zn-polar domains is increased again, which coexists with the O-polar domains at very high O_2/DEZn ratio condition. The variation of DEZn and O_2 flow rate also have an impact on the incorporation of impurities into the ZnO thin film, which can in turn affect its piezoelectric efficiency. At high O_2/DEZn ratio or strong oxidizing condition, the incorporation of shallow donors such as Al_{Zn} and Ga_{Zn} on the O-polar domains is reduced.[68] Thus, piezoelectric amplitude on the O-polar domains is enhanced thanks to the decrease of the screening effect.[89,185] The piezoelectric amplitude of Zn-polar domains is less affected since the incorporation of shallow donors is less pronounced on these polar domains.[161] Generally, the piezoelectric amplitude on the Zn-polar domains is higher compared to the O-polar domains. This implies that the ZnO structure with the Zn-polar uniformity can exhibit a high piezoelectric efficiency. The piezoelectric efficiency of ZnO can be further improved by introducing dopants to reduce the screening effect.[36]

4.2 Effect of flow rate at high growth temperature

4.2.1 Introduction and objectives

After investigating the effect of flow rates at 500 °C, we continue to study the flow rate effect at 700 °C, for which the ZnO nanowires are expected to be formed, according to our result in **Section 3.1**. The effect of flow rates at different temperatures is worth to study carefully since both parameters have strong influence throughout the multi-steps of ZnO formation inside the MOCVD chamber.[54] L. Fanni et al. showed that different combinations of flow rates and temperatures can lead to different growth regimes, which significantly changed the ZnO growth directions and its properties.[77] Their results presented that ZnO structure had no preferential orientation at 250 °C, while it was mainly grown along the *c*-axis at 100 °C regardless of the flow rates. At intermediate temperature, the growth direction strongly depended on the flow rates. Furthermore, D. Montenegro et al. demonstrated that different flow rate conditions resulted in the formation of nanowires with various lengths and diameters (**Figure 4.17**).[125] The variation of nanowire geometry can lead to a significant change of piezoelectric potential, which has been observed in the simulation results performed by R. Tao et al..[89] To the best of our knowledge, there is no systematic experimental investigation about the correlation of nanowire geometry with their piezoelectric coefficient.

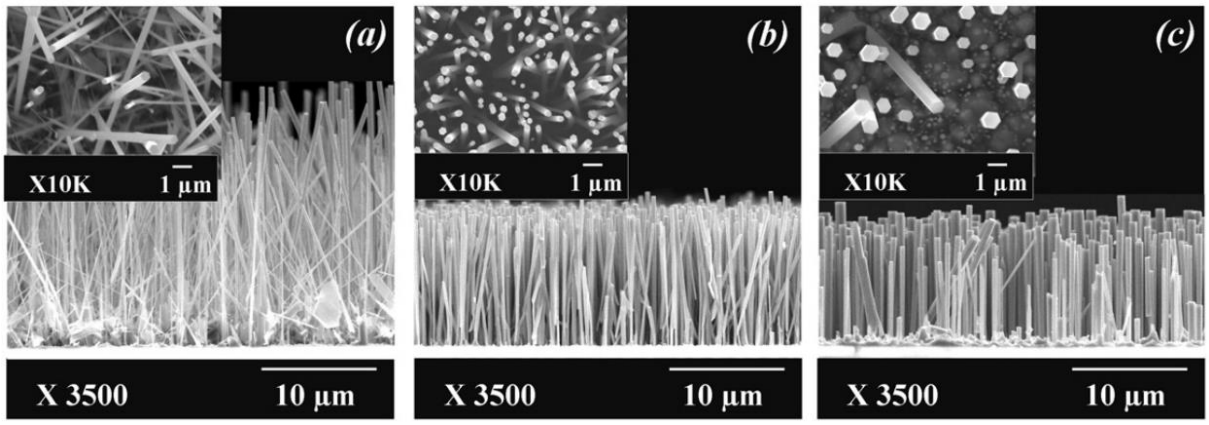

Figure 4.17: Cross-sectional- and top- (inset) view SEM images of ZnO NW arrays grown by MOCVD with different flows rates of N_2O and DMZn–TEN: (a) 109 sccm and 28 sccm, (b) 153 sccm and 39 sccm, (c) 214 sccm and 54 sccm of N_2O and DMZn–TEN, respectively.[125]

In this study, the temperature was maintained at 700 °C while the DEZn solution and O_2 gas flow rates were sequentially varied. The FESEM images showed that all ZnO deposits are composed of nanowires with different dimensions. The evolution of piezoelectric amplitude and coefficient measured by the PFM technique as a function of the ZnO nanowire geometry is presented. The structural properties of nanowires were also analyzed using XRD, and Raman spectroscopy.

4.2.2 Experiment

4.2.2.1 ZnO grown by PLI-MOCVD

The ZnO samples were grown on heavily doped p-type Si (100) substrates by an Annealsys MC-200 PLI-MOCVD system. The DEZn diluted in cyclohexane solvent was used as Zn precursor (see **Section 2.1.3**), and the O_2 gas was used as O precursor. Similar to the experiment in **Section 4.1**, two sample series were prepared, in which the flow rates of O_2 gas and DEZn solution were varied in the range of 100 – 700 sccm and 0.2 – 0.5 g/min, respectively, but the growth temperature was set at 700 °C instead of 500 °C. The flow rate of mixed Ar gas was also adjusted to maintain the total gas volume introduced into the reactor chamber. The common sample of two sample series is the one grown with the 0.5 g/min DEZn solution and 500 sccm O_2 gas flow rates. The chamber pressure was kept at 3 mbar during the growths. The growth time was fixed at 8.45 minutes for all samples. The details of precursor flow rates, their ratio and the growth time used for ZnO depositions are shown in **Table 4.2**.

Table 4.2: The O_2 gas and DEZn solution flow rates, the O_2/DEZn molar flow rate ratios and the growth time of ZnO samples. The growth temperature is fixed at 700 °C.

	O_2 flow rate (sccm)	**DEZn flow rate (g/min)**	**O_2/DEZn ratio**	**Growth time (second)**
Sample 1	100	0.5	16	507
Sample 2	300	0.5	48	507
Sample 3*	500	0.5	79	507
Sample 4	700	0.5	111	507
Sample 5	500	0.4	99	507
Sample 6	500	0.3	132	507
Sample 7	500	0.2	198	507

** The ZnO sample grown with 500 sccm O_2 gas and 0.5 g/min DEZn solution is the common sample for both series.*

4.2.2.2 Characterizations

The morphology, structural and piezoelectric properties of ZnO samples were studied using different characterization techniques (see **Section 2.2**). The morphology of ZnO samples was observed by FESEM using a Quanta 250 FEI FEG-SEM. The XRD patterns were acquired by a Bruker D8 Advance diffractometer using CuKα1 radiation according to the Bragg-Brentano configuration. The

Raman spectra were collected by using a Jobin Yvon/Horiba Labram spectrometer equipped with a liquid nitrogen-cooled charge-coupled device (CCD) detector. The topography along with piezoelectric response images were obtained by datacube PFM measurement using a Bruker Dimension Icon AFM.

4.2.3 Results

4.2.3.1 Morphological properties

Figure 4.18 displays the FESEM images of ZnO deposits grown on Si substrate at 700 °C using the PLI-MOCVD system, showing that all the growths result in the formation of vertically aligned NW arrays regardless of flow rate conditions.

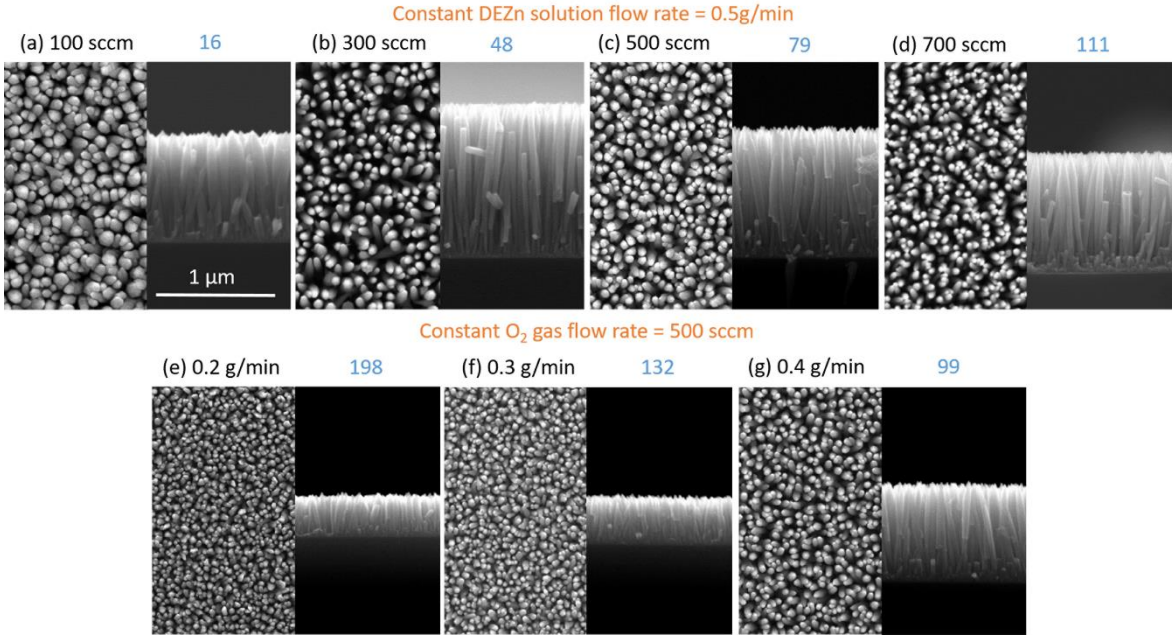

Figure 4.18: Top-view (left) and cross-sectional-view (right) FESEM images of ZnO NWs grown by PLI-MOCVD with the (a) 100, (b) 300, (c) 500, and (d) 700 sccm O_2 gas flow rate for a given DEZn solution flow rate of 0.5 g/min; or with the (e) 0.2, (f) 0.3, and (g) 0.4 g/min DEZn solution flow rate for a given O_2 gas flow rate of 500 sccm. The corresponding O_2/DEZn molar flow rate ratios are indicated in blue.

In our previous results shown in **Section 4.1**, while using the same system and growth conditions except the growth temperature was set at 500 °C, all the growths at that temperature led to the formation of ZnO thin films. The transition of ZnO morphology from stacked thin film to nanowires when the growth temperature increased from 500 to 700 °C was demonstrated in **Section 3.1**. The reason is due to the strongly anisotropic growth of ZnO along the polar *c*-axis combined with the significant desorption of Zn and O atom at high growth temperature, leading to the formation of isolated islands with high *c*-axis orientation, followed by the elongation of NWs on those islands thanks to the enhanced surface diffusion of Zn and O atoms. The length, diameter, aspect ratio (length/diameter ratio) and density of NWs were extracted from their FESEM images and presented in **Table 4.3**. Their evolutions as a function of the O_2/DEZn flow rate ratio are shown in **Figure 4.19**.

Table 4.3: The length, diameter, aspect ratio and density of NW arrays.

Flow rates	Length (nm)	Diameter (nm)	Aspect ratio	Density (10^9 NWs/cm^2)
100 sccm O_2 0.5 g/min DEZn	962 ± 78	82.3 ± 9.8	11.7 ± 2.3	9 ± 1
300 sccm O_2 0.5 g/min DEZn	1429 ± 55	74 ± 11.2	19.3 ± 3.7	13 ± 1
500 sccm O_2 0.5 g/min DEZn	1125 ± 31	72.9 ± 12.2	15.4 ± 3.0	13 ± 1
700 sccm O_2 0.5 g/min DEZn	1096 ± 32	61.7 ± 5.05	17.8 ± 2.0	14 ± 1
500 sccm O_2 0.2 g/min DEZn	362 ± 45	42.2 ± 3.8	8.6 ± 1.8	36 ± 1
500 sccm O_2 0.3 g/min DEZn	446 ± 75	50.5 ± 6.2	8.8 ± 2.6	30 ± 1
500 sccm O_2 0.4 g/min DEZn	865 ± 86	53.4 ± 7.3	16.2 ± 3.8	16 ± 1

The difference in the geometry among NW arrays expresses the impact of the flow rate condition on the formation process of ZnO NWs as well as their growth rate.[62,127,181] The NW length is attributed to the growth rate in the axial direction, and the NW diameter is attributed to the growth rate in the radial direction. Thus, the difference in the NW length, diameter as well as the aspect ratio among NW arrays in **Figures 4.19** describes the variation of the relative growth rates in the axial and radial directions. In the work of D.N. Montenegro et al., the lengths and diameters of ZnO NWs grown by MOCVD were varied by changing the flow rates of nitrous oxide (N_2O) and dimethylzinc–triethylamine (DMZn–TEN).[125] They also demonstrated that the ZnO morphology transformed from NWs to a thin film when the N_2O flow rate was increased, while the flow rate of dimethylzinc–triethylamine (DMZn–TEN) was maintained, corresponding to the increase of O/Zn flow rate ratio. Normally, the *c*-plane on the top of NWs has the highest surface energy,[61] the Zn and O atoms tend to diffuse and develop on this plane, driven by the minimization of the free energy during the ZnO formation process. However, their results showed that the higher O/Zn flow rate ratio led to a less anisotropic growth, explained by the reduction of Zn atom diffusion to its growing surface (i.e. the *c*-plane on the NW tip), resulting in the 2D thin film formation. In our case, a similar tendency is

observed when the O_2 flow rate was decreased from 500 to 300 sccm, while the DEZn solution flow rate was maintained. This change of flow rate condition results in the increase of the NW length from 1125 to 1429 nm, while the diameter is kept at around 73 – 74 nm (**Figures 4.19a and b**). Correspondingly, the aspect ratio increases from 15.4 to 19.3 (**Figure 4.19c**). When the O_2 gas flow rate was further decreased to 100 sccm, the NW length drastically decreased down to 962 nm, while its diameter increased to 82.3 nm, leading to the decrease of the aspect ratio to 11.7. These results describe that the relative growth rate decreases in the axial direction while it increases in the radial direction at the 100 sccm O_2 gas flow rate, expressing that the growth is less anisotropic when the O_2/DEZn flow rate ratio is decreased. This also implies that a ZnO thin film may be obtained by further decreasing the O_2 gas flow rate, but we did not perform this test due to the limitation of the MOCVD system. The decrease of the NW length indicates the slower growth rate due to the insufficient O_2 gas flow rate at 100 sccm. The increase of the diameter could also be due to the fact that an insufficient O reactant reaches the most reactive site at the top of NWs when the O_2 gas flow rate was decreased down to 100 sccm. Thus, the Zn reactants started attaching to other planes at the sidewall of NWs where the surface energy is lower, leading to the development of ZnO in the radial direction.

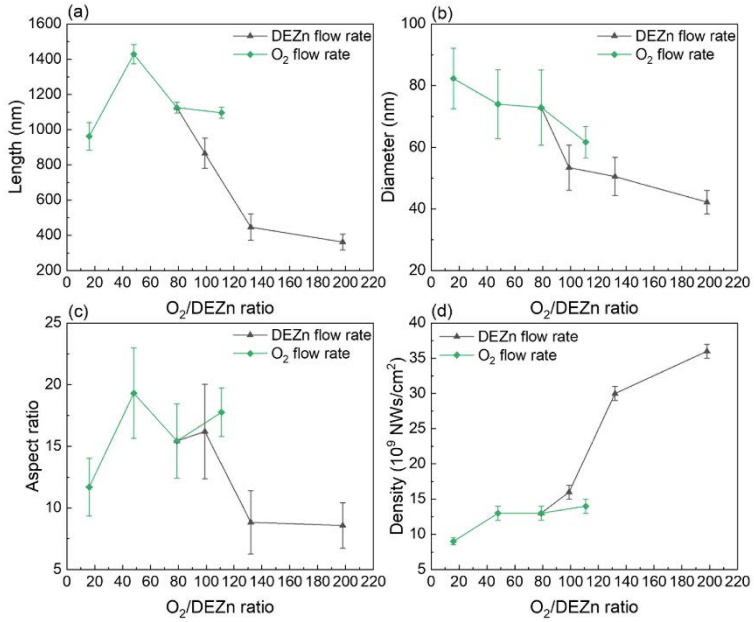

Figure 4.19: Evolution of (a) the length, (b) the diameter, (c) the aspect ratio, and (d) the density of ZnO NW arrays as a function of the O_2/DEZn flow rate ratio.

In contrast, when the O_2 gas flow rate increased from 500 to 700 sccm, the NW length was not increased (**Figure 4.19a**), expressing the saturation of the O_2 reactant. Meanwhile, the diameter of NWs grown with the 700 sccm O_2 gas flow rate decreased, leading to the increase of the aspect ratio (**Figures 4.19b and c**). In the series reporting the DEZn solution flow rate variation, both length and diameter of NWs are drastically decreased when the DEZn solution flow rate is decreased from 0.5 to 0.2 g/min (**Figures 4.19a and b**). As the NW samples were grown with the same growth time, this reflects the significant change of the growth rate when the flow rate condition is varied. In

Figures 4.19d, the NW array grown with the 100 sccm O_2 gas flow rate has the lowest density. This can be explained by its largest diameter resulting from the merging of smaller NWs into a larger NW during the growth process. As a consequence, the number of NW per area unit or the density are decreased. In comparison, the decrease of the DEZn solution flow rate to 0.3 and 0.2 g/min leads to slower growth rates. These samples have smaller NWs before merging, and hence, their density values are the highest one.

4.2.3.2 Growth rate of ZnO NWs

The growth rate of NWs depending on the flow rate conditions was approximately estimated by calculating the ratio of the NW length over the growth time, which is presented in **Figure 4.20**.

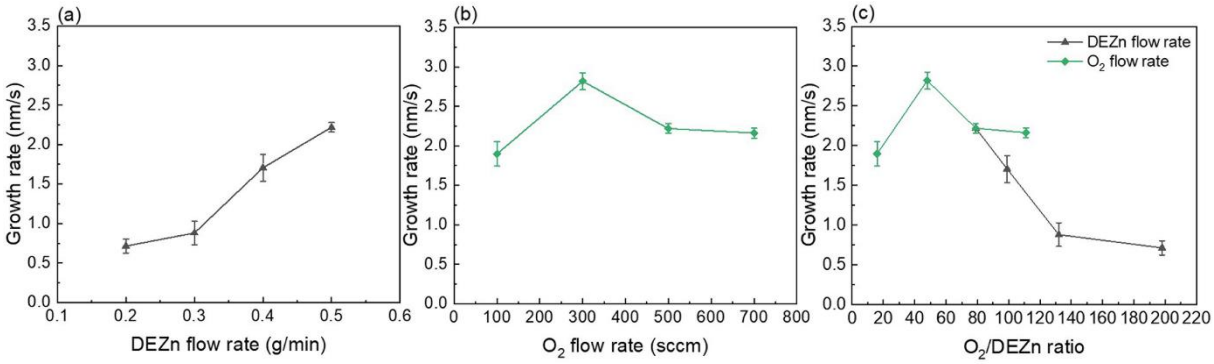

Figure 4.20: Evolution of the mean growth rate of ZnO NWs grown by PLI-MOCVD as a function of (a) the DEZn solution flow rate for a given O_2 gas flow rate of 500 sccm, (b) the O_2 gas flow rate for a given DEZn solution flow rate of 0.5 g/min and (c) the O_2/DEZn flow rate ratio.

Figure 4.20a shows that the growth rate increases rapidly from 0.7 to 2.2 nm/s when the DEZn solution flow rate is increased from 0.2 to 0.5 g/min, while the O_2 gas flow rate is kept constant at 500 sccm. On the other hand, while the DEZn solution flow rate is maintained at 0.5 g/min, the growth rate increases from 1.9 to 2.8 nm/s when the O_2 gas flow rate is increased from 100 to 300 sccm, but then it decreases and maintains at 2.2 nm/s when the O_2 gas flow rate is further increased to 500 and 700 sccm (**Figure 4.20b**). The increase of growth rate with the DEZn solution flow rate indicates that the NW growth at 700 °C is limited by the DEZn amount in the PLI-MOCVD chamber, which is similar to the behaviour of thin film growth rate at 500 °C as shown in **Section 4.1**. However, the evolution of growth rate at 700 °C is different compared to its evolution at 500 °C shown in **Section 4.1** when the O_2 gas flow rate is varied. In our previous result, the growth rate at 500 °C was constantly decreased when the O_2 gas flow rate was increased from 100 to 700 sccm (see **Figure 4.4b** in **Section 4.1**). The pressure was maintained at 3 mbar and the total gas volume introduced into the PLI-MOCVD chamber was kept constant by adjusting the flow rate of Ar gas to compensate for the amount of O_2 gas that was varied. Thus, the decrease of growth rate at higher O_2 gas flow rate was due to the increase of reaction between the O and Zn reactants in their gas phase, preventing the Zn reactant from reaching the substrate to form ZnO. Unlike the growth rate at 500 °C, the growth rate at 700 °C decreases when the O_2 gas flow rate is decreased from 300 to 100 sccm, showing that O reactants also become insufficient at low O_2 gas flow rate due to the faster reactions between reactants at this high temperature. The growth rate at 700 °C increases when the O_2 gas flow rate is

increases from 300 to 500 sccm, which is similar to the behaviour of the growth rate at 500 °C and could be caused by the same reason: the increase of O_2 gas caused more reactions in the gas phase and interfered with the Zn reactants diffusing to the substrate. Further increasing the O_2 gas flow rate to 700 sccm seems to have less effect on the growth rate. Nevertheless, **Figure 4.20c** shows that the NW growth at 700 °C is limited by O reactants when the O_2/DEZn flow rate ratio is below 48, while it is limited by Zn reactants when the O_2/DEZn ratio is higher. Within the same range of DEZn solution and O_2 gas flow rate, the mean growth rate of NWs grown by PLI-MOCVD at 700 °C is varied from 0.7 to 2.8 nm/s, which is faster compared to the growth rate ranging from 0.6 to 1.3 nm/s for thin films grown at 500 °C using the same system as well as other parameters (see **Figure 4.4** in **Section 4.1**).

Besides, the growth rate of a NW array could be underestimated/overestimated when their growth rate is deduced from only their length over the growth time while there is also the difference in their NW diameter and density as well as their area coverage. Another way to estimate an equivalent growth rate of NW arrays consists in calculating the ratio of total ZnO volume per cm^2 over the growth time. To simplify, we assume the NW section as being a cylindrical shape, then the growth rate can be calculated as follows:

$$growth\ rate_{(\text{volume per cm}^2\ /\ \text{growth}\ time)} = \frac{l \times \pi r^2 \times density}{t} \qquad (4.1)$$

where l is the NW length, r is the NW radius (half of diameter), density is the number of NW per cm^2, and t is the growth time. In this equation, (πr^2 x density) is the defined as the area coverage of the NW array:

$$Area\ coverage = \pi r^2 \times density \qquad (4.2)$$

In other words, the area coverage is the total area of NWs per cm^2. Since there are voids between NWs, the area coverage values of NW samples is less than 1. In case of the thin film, the area coverage value is equal to 1 as there are no void, hence the equation (4.1) becomes the film thickness/growth time ratio and is equivalent to the growth rate for a 2D layer. The area coverage and the growth rate of NW arrays deduced from equations (4.1 & 4.2) are shown in **Figure 4.21**. Overall, there is no large change in the area coverage when the flow rates are varied (**Figure 4.21a**). Correspondingly, the evolution of the growth rate deduced from the volume/growth time with the flow rate condition in **Figure 4.21b** is similar to the growth rate calculated from the lenght/growth time in **Figure 4.20c**, verifying the analysis of the NW growth rate influenced by the DEZn and O_2 flow rates as shown above. It can be notably seen that the area coverage of NW array is the lowest when the DEZn/O_2 flow rate ratio is in the range of 99 – 111, which is the same range where the predominant O-polar ZnO thin films were formed using the same PLI-MOCVD process except at lower growth temperature, as shown in **Section 4.1**.

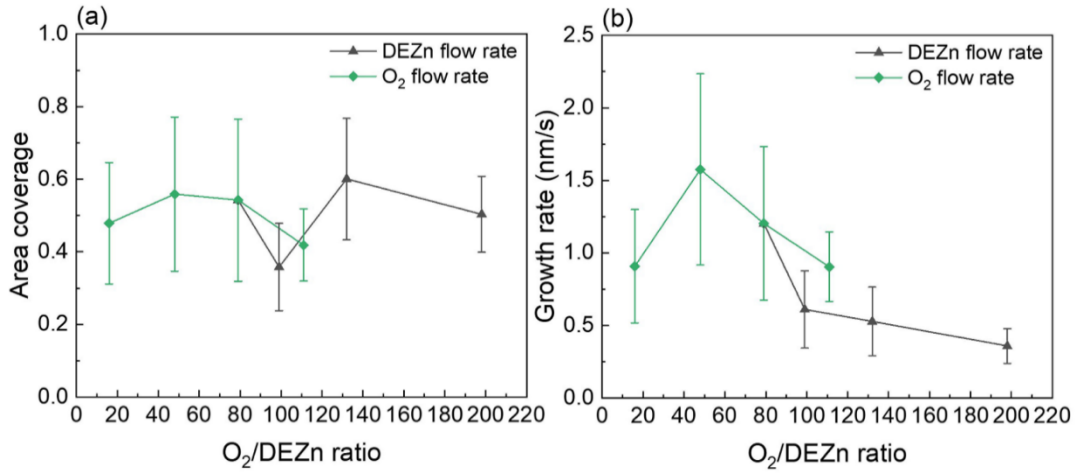

Figure 4.21: Evolution of (a) the coverage area and (b) the growth rate (volume per cm^2/s) of NW arrays as a function of the O_2/DEZn flow rate ratio.

4.2.3.3 Orientation and strain of ZnO NW arrays

The structural properties of NW arrays grown at 700 °C were analyzed by XRD and Raman spectroscopy. The XRD patterns of ZnO NWs in **Figure 4.22a** show the 100, 002, 101, 102, 103, and 004 diffraction peaks of the ZnO wurtzite structure located at 31.8, 34.4, 36.3, 47.5, 62.9, and 72.6°, respectively, according to the ICDD file labelled 00-036-1451. Correlatively, their Raman spectra in **Figure 4.22b** also show the E_2^{low} and E_2^{high} lines of the ZnO wurtzite structure positioned at 99 and 438 cm^{-1}.[143,178] The signals detected at around 1360 and 1580 cm^{-1} in their Raman spectra are assigned to the C-C bonds, indicating that carbon impurities remain in ZnO NWs after the growth by PLI-MOCVD process,[144] which is similar to our results shown in **Section 3.1** and **Section 4.1**.

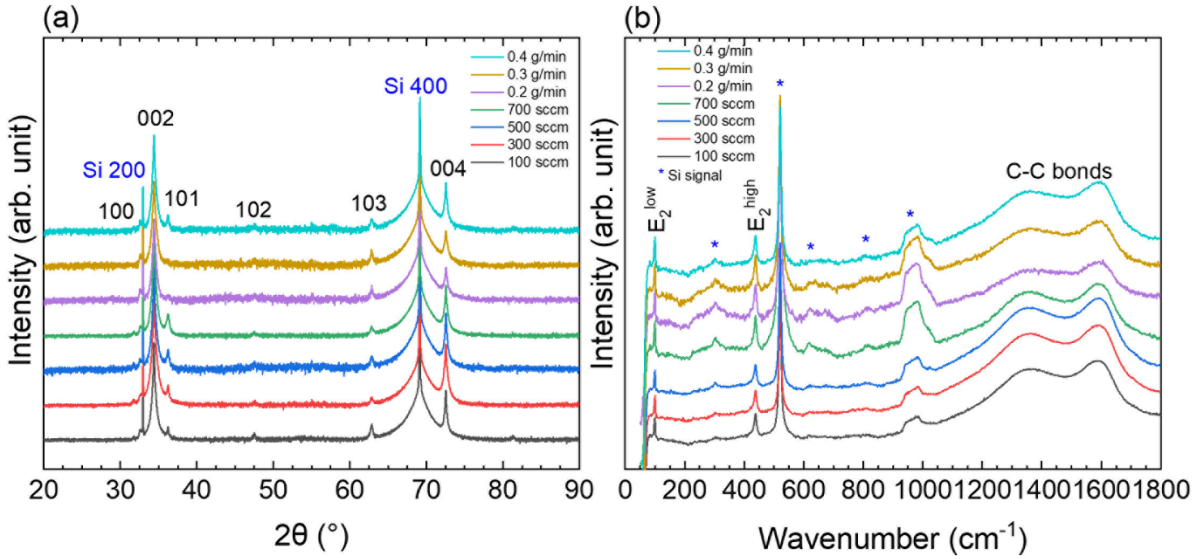

Figure 4.22: (a) XRD patterns and (b) Raman spectra of ZnO NW arrays grown with different flow rate conditions.

In XRD patterns, the 002 peak exhibits a significantly higher intensity compared to other diffraction peaks, expressing a highly *c*-axis oriented structure of ZnO NWs. Compared to the thin films grown by

the same process in **Section 4.1**, the XRD patterns of NWs show sharper peaks with smaller width, indicating the superior crystallinity of NWs compared to the thin films. This is also supported by the results in Raman spectra, where the E_2^{low} and E_2^{high} lines of NWs are more intense than those of thin films. The stronger intensity of signals from Si substrates observed in the Raman spectra of four NW arrays grown with the 700 sccm O_2 gas flow rate and the 0.2, 0.3 and 0.4 g/min DEZn solution flow rates compared to other NW arrays is due to their lower area coverage and NW length, which make the signals from the Si substrate underneath the ZnO NW array be more detectable. Similar to our previous studies, the intensity and the position of diffraction peaks in XRD patterns of NW arrays were exploited to evaluate their orientation and the residual homogeneous strain (see **Section 2.2.2**). In overall, the 002 texture coefficients of NW arrays are above 99.4%, expressing their very high orientation along the *c*-axis. The increase of the 002 texture coefficient with the NW length can be observed in **Figure 4.23**, which is due to the fact that there are more signals of 002 diffraction peak coming from the longer NW. This again implies that the ZnO NW becomes more oriented along the *c*-axis during its elongation, which was indicated by the SAED patterns in **Section 3.1** showing a random orientation at the bottom of the NW, but a high *c*-axis orientation at the top of the NW.

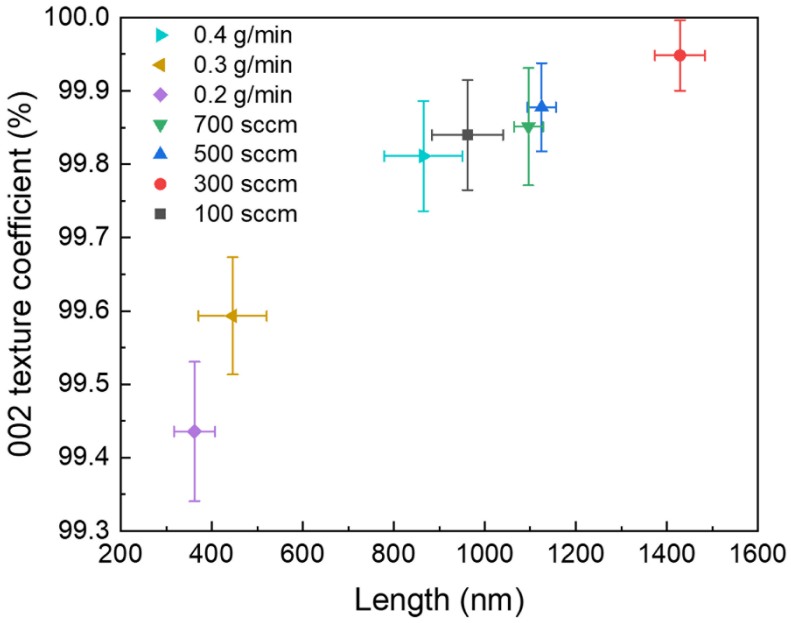

Figure 4.23: Evolution of 002 texture coefficient as a function of the ZnO lenght.

The residual homogeneous strains of NW arrays lie in the range of 0.02 – 0.07%, which are very close to 0, implying the efficient strain relaxation thanks to their nanowire structures. In comparison, the residual homogeneous strains of thin films grown by the same process in **Section 4.1** are varied from -0.01 to -0.4%. In agreement with the XRD analysis, the Raman spectra of NW arrays have the E_2^{high} line position very close to the bulk value at 438 cm^{-1}, indicating again the relaxed strain in NW structures. Besides, the Williamson-Hall method was also employed to estimate the inhomogeneous strain and the crystallite size of ZnO NW arrays (see **Section 2.2.2**). It should be mentioned that the Williamson-Hall method is less accurate when applied on the sample with larger crystallite size, especially on NW samples, in which the strain and size are highly anisotropic. This

causes large error bars in the strain and size estimation that makes the comparison among NW arrays more difficult. However, similar to the homogeneous strain, all inhomogeneous strains are less than 0.01 %, which are very close to 0 thanks to their nanowire structure. The deduced crystallize size are varied around 100 – 200 nm, which are significantly higher than those of ZnO thin films shown in **Section 4.1**. These results indicate a better crystallinity of ZnO NW structure compared to their thin film counterpart grown by the same PLI-MOCVD process.

4.2.3.4 Crystal polarity and piezoelectric response

Crystal polarity

The PFM mappings of NW arrays are shown in **Figure 4.24**, in which the piezoelectric amplitude is proportional to the piezoelectric coefficient and applied voltage amplitude, while the piezoelectric phase with respect to the applied voltage indicates the polarity. The positive phase value at around 70° (bright area) corresponds to the Zn-polarity, and the negative phase value at around -90° (dark area) corresponds to the O-polarity (see **Section 2.2.1**). The amplitude images of NW arrays grown with different flow rate conditions exhibit different brightness, expressing the variation of the amplitude as well as the piezoelectric coefficient among NW samples.

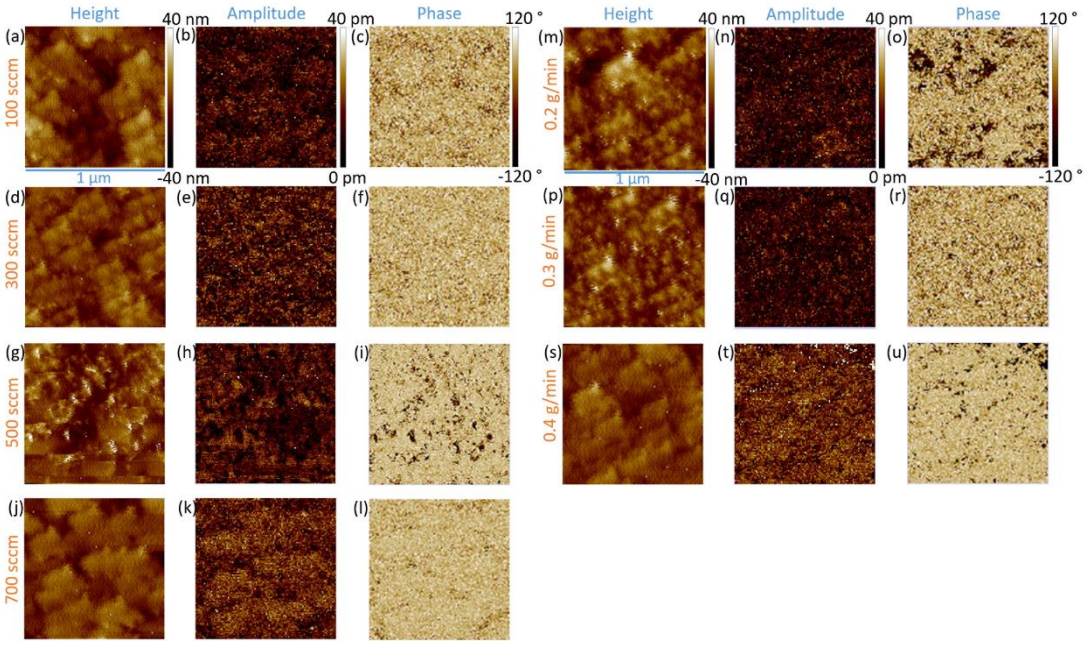

Figure 4.24: Topography, piezoelectric amplitude, and piezoelectric phase of ZnO NW arrays grown by PLI-MOCVD with the (a-c) 100, (d-f) 300, (g-i) 500, and (j-l) 700 sccm O_2 gas flow rate for a given DEZn solution flow rate of 0.5 g/min; or with the (m-o) 0.2, (p-r) 0.3, (s-u) 0.4 g/min DEZn solution flow rate for a given O_2 gas flow rate of 500 sccm.

In their phase images, the predominance of the positive phase (bright area) indicates that ZnO NWs have Zn-polarity. Some small dark areas in those phase images do not represent the O-polar ZnO NWs, but they are artifacts resulting from the contact failure when the AFM approached the void between NWs. This is due to the fact that we did not fill the void in NW arrays before performing the PFM measurement. In **Section 3.1**, the void in the NW array was filled by PMMA, on top of which the PFM measurement gave non-polar responses since the PMMA is a non-piezoelectric material. The

PFM results of ZnO NW arrays show that all NWs grown by PLI-MOCVD process at 700 °C are Zn-polar regardless of the flow rate conditions. This is different from the thin films grown by the same process but at 500 °C, where there was a large variation of ZnO polarity when the flow rate condition was changed, as shown in **Section 4.1**. The predominant Zn-polar-, predominant O-polar-, and coexisted two-polar-thin films were formed at different O_2/DEZn flow rate ratio. To verify if the O-polar ZnO NWs can be grown by our PLI-MOCVD process, we performed another NW growth on ZnO substrates with an identified Zn- and O-polarity. These ZnO substrates (from Crystec) are the same as those used in the PFM calibration shown in **Section 2.2.1**. The DEZn solution and O_2 gas flow rates were set to 0.5 g/min and 500 sccm, respectively. Other parameters were kept constant as those NW growths on Si substrates. **Figure 4.25** presents the FESEM images and PFM maps of ZnO NW arrays on ZnO substrates after the growth for 7 minutes.

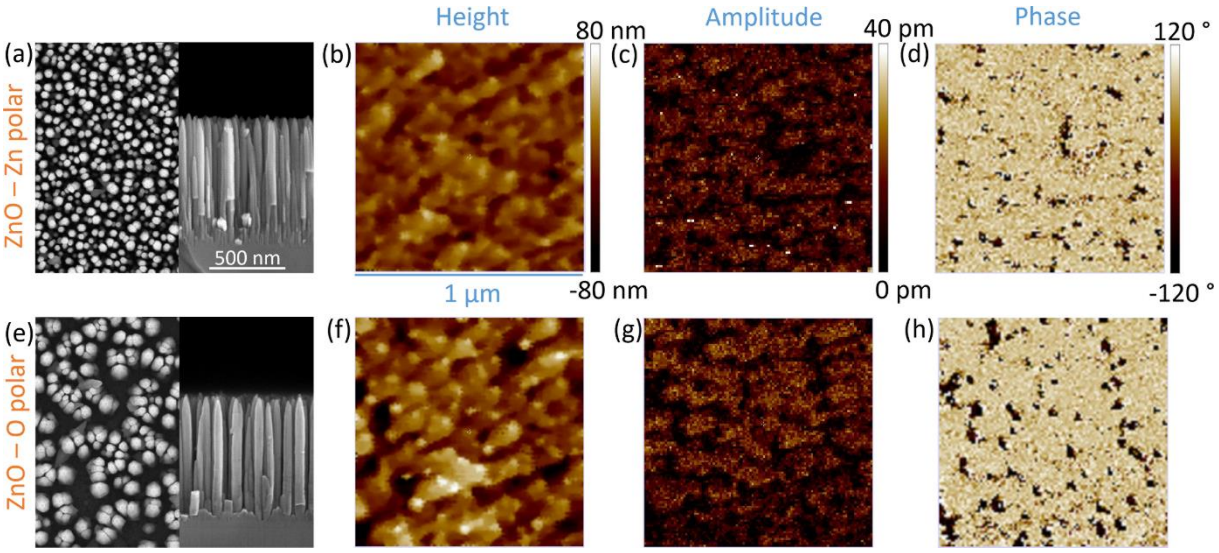

Figure 4.25: Top- (left) and cross-sectional-view FESEM images of ZnO NW arrays grown on (a) Zn- , and (e) O-polar ZnO substrates. PFM scanning images of ZnO NW arrays grown on (b-d) Zn- , and (f-h) O-polar ZnO substrates.

The FESEM images (**Figures 4.25a** and **e**) display the well-aligned ZnO NW arrays formed on the Zn- and O-polar ZnO substrates. The NW length is similar between the two arrays and around 870 nm. However, it can be seen that the NWs grown on the Zn-polar ZnO substrate have a smaller diameter and a higher density as compared to the NWs grown on the O-polar ZnO substrate. In detail, the diameters of NWs on the Zn- and O-polar ZnO substrates are around 49 and 53 nm, respectively. The density of NW array on the Zn-polar ZnO substrate is around 25 x 10^9 NWs/cm^2, while it is 12 x 10^9 NWs/cm^2 on the O-polar ZnO substrate. The difference in the diameter and density between the two arrays reveals the impact of the substrates on the nucleation step at the beginning of the growth.[34,37] In PFM results (**Figures 4.25d** and **h**), the phase images again show that the ZnO NWs grown on ZnO substrates have Zn-polarity, even on the O-polar ZnO substrate. This confirm that only Zn-polar ZnO NWs were grown by the PLI-MOCVD process, which is in agreement with Ref.[34].G Perillat-Merceroz et al. performed the ZnO NW growth on O-polar ZnO substrate by MOCVD using DEZn as the Zn precursor and N_2O as the O precursor.[187] Their convergent beam electron diffraction result also demonstrated that ZnO NWs are Zn-polar, which sit on top of O-polar

pyramids. In the work of V. Sallet et al., they also showed that the catalyst-free ZnO NW growth by MOCVD resulted in Zn-polar ZnO NWs, while the O-polar ZnO NWs were only formed using the catalyst-assisted approach with the gold droplet.[188] Z.L. Wang et al. showed that the Zn clusters as well as the Zn local enrichment at the growth front only occurred on the Zn-terminated ZnO (001) polar surface, leading to the self-catalyzed growth of the ZnO NW during the vapor-liquid-solid (VLS) growth process.[189] Meanwhile, the O-terminated ($00\bar{1}$) polar surface was chemically inert and did not initiate any growth. By using the plasma-assisted molecular beam epitaxy (PAMBE) to fabricate the p-GaN/n-ZnO heterojunction nanowires, F. Schuster et al. observed a polarity inversion from N-polar GaN (negative polarity) to Zn-polar ZnO (positive polarity), which was explained due to the high binding energy of the N-O bonds.[190] Different from the catalyst-free growth of MOCVD process, the ZnO NWs grown by the chemical bath deposition can be controlled to be along both Zn- or O-polar direction by using the identified-polar ZnO substrates.[156] In the other work of P. X. Gao and Z. L. Wang, they also showed that both O- and Zn-polar ZnO surfaces were chemically active when the tin (Sn) element was added as a catalyst for the VLS growth,[191] which is opposite to their previous work in Ref.[189]. Although the ZnO NWs grown by our PLI-MOCVD is limited to the Zn-polarity, the polar uniformity of the NW array is essential for high efficient piezoelectric devices. It also should be mentioned that the ZnO substrates were also used as bottom electrodes during the PFM measurements. Since the conductivity of ZnO substrates is lower compared to highly doped Si substrates, the piezoelectric amplitude of NWs grown on ZnO substrates could be underestimated compared to NWs grown on highly doped Si substrates.

Piezoelectric amplitude and coefficient

In order to study the influence of flow rate conditions on the piezoelectric amplitude of ZnO NWs, the mean piezoelectric amplitude on the Zn-polar NWs were extracted from their piezoelectric amplitude images. The mean amplitude calculation only took into account data points with the piezoelectric phase higher than 50° assigned to the Zn-polar signals from NWs. Other data points were assigned to artifacts from the void in NW array and were removed. **Figure 4.26** presents the evolution of the mean piezoelectric amplitude of ZnO NWs as a function of the length, diameter, aspect ratio, and density of NW arrays, corresponding to their flow rate growth conditions. In **Figure 4.26a**, the graph shows that the amplitude seems to be higher on the longer NWs, except two NW arrays grown with the 0.4 g/min DEZn solution and 700 sccm O_2 gas flow rates. On the other hand, there is a clearer tendency of decrease in amplitude when the NW diameter is increased, as presented in **Figure 4.26b**. Two NW arrays grown with the 0.2 and 0.3 g/min DEZn solution flow rate exhibit the lowest amplitude despite their smaller diameters, which could be due to their shortest length as observed in **Figure 4.26a**. Similarly, the amplitude also exhibits a strong dependence on the NW aspect ratio in **Figure 4.26c**, in which it increases when the aspect ratio increases. The NW array grown with the 300 sccm O_2 gas flow rate has the highest aspect ratio, but it has the lower amplitude compared to two NW arrays grown with the 0.4 g/min DEZn solution and 700 sccm O_2 gas flow rates, for which the NW diameters are smaller (**Figure 4.26b**). In **Figure 4.26d**, except two NW arrays grown with the 0.2 and 0.3 g/min DEZn solution flow rate, the piezoelectric amplitude likely increases as the NW density is increased.

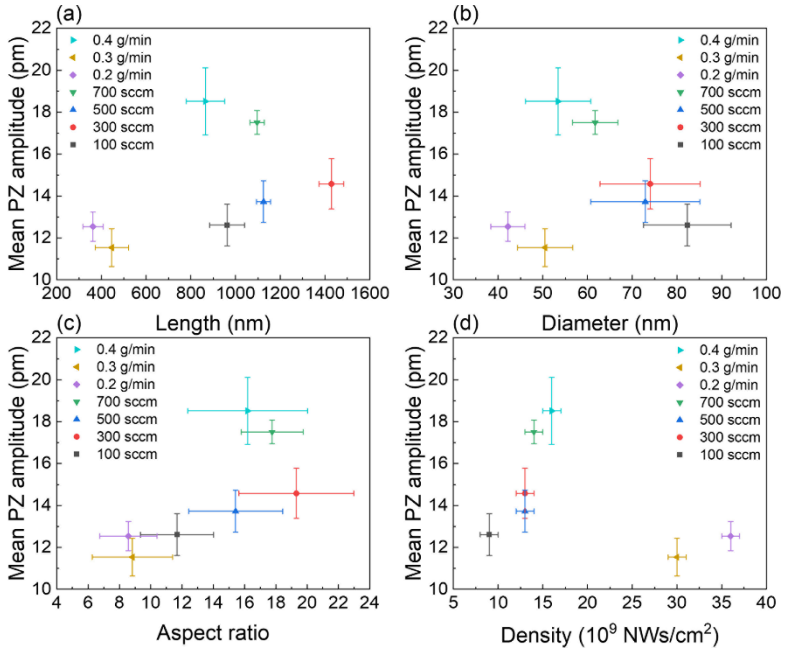

Figure 4.26: Evolution of mean piezoelectric amplitude as a function the (a) length, (b) diameter, (c) aspect ratio, or (d) density of NW arrays.

4.2.4 Discussion

The variation of the piezoelectric amplitude as well as its correlation with the geometry of NW arrays grown with different flow rate conditions can be attributed to several reasons. First, it is shown by XRD results that the orientation along the polar *c*-axis is improved with the increase of the NW length (**Figure 4.23**), which is favourable for enhancing the piezoelectric amplitude. This could be a reason for the lowest piezoelectric amplitude in the shortest NWs grown with the 0.2 and 0.3 g/min DEZn solution flow rate. Second, NWs with a small diameter or a high aspect ratio can provide large sidewall surface area, on which the surface Fermi level pinning occurs, which traps and depletes the free charge carriers inside the NWs.[89] This reduces the screening effect and results in increasing the piezoelectric potential.[89] Thus, the piezoelectric amplitude tends to increase with the decrease of diameter or the increase of aspect ratio (**Figures 4.26b-c**). The degree of influence of those phenomena on the piezoelectric amplitude also depends on the length and diameter of NWs, which can be illustrated by three regimes as shown in **Figure 4.27**.

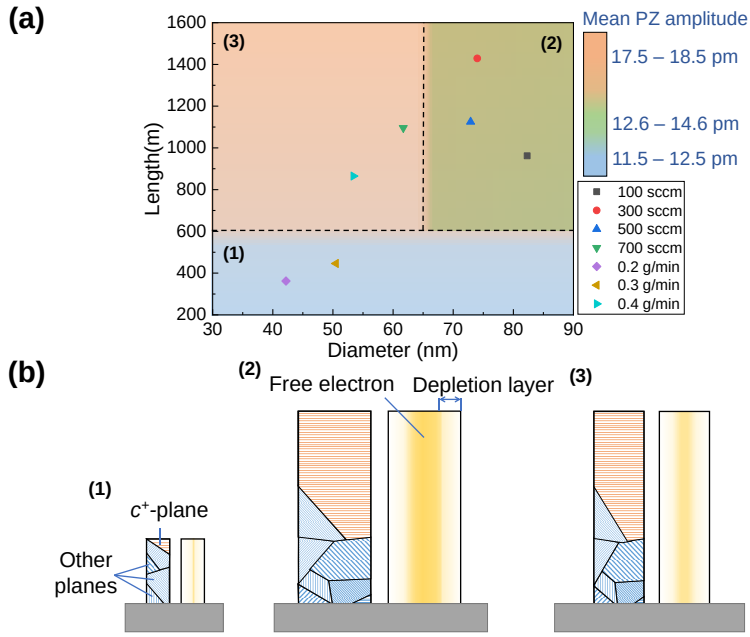

Figure 4.27: (a) Graph representing the lengths, diameters and PZ amplitudes of ZnO NW arrays grown with different flow rate conditions. (b) Schematic illustrating the influence of NW geometry on its structural (left) and electrical (right) properties.

For instance, in the regime (1), the NW arrays grown with the 0.2 and 0.3 g/min DEZn solution flow rate have very short lengths (362 and 446 nm), on which the piezoelectric amplitude is the lowest despite their smallest diameter. This implies that the piezoelectric amplitude is limited by the short length of NWs rather than their diameter. In contrast, in the regime (2), the NWs grown with the 300 sccm O_2 gas flow rate has the longest length and the highest aspect ratio, but it has larger diameter and exhibits a lower piezoelectric amplitude compared to the NW array grown with the 700 sccm O_2 gas flow rate and the other one grown with the 0.4 g/min DEZn solution flow rate. The highest piezoelectric amplitude is observed in NWs grown with the 0.4 g/min DEZn solution flow rate, which has the 3rd-smallest diameter but has the length above 800 nm. This NW array is situated in the regime (3), where the NW has a better *c*-axis oriented structure thanks to its longer length and less residual free electrons due to the more efficient depletion phenomenon on the thinner NW. These results express that the piezoelectric amplitude is stronger for the NWs with the length above 800 nm and the diameter smaller than 65 nm. Besides, since the area coverage among NW arrays is similar (**Figure 4.21a**), the NW density is approximately inversely proportional to the diameter square, as shown in equation (4.2). Thus, the evolution of the piezoelectric amplitude with the NW density observed in **Figure 4.26d** is due to its correlation with the diameter. Third, the variation of the flow rate condition can influence the incorporation of defects and impurities into the ZnO structure during its growth,[68] which in turn affects the screening effect as well as the piezoelectric response.[89,185] The investigations about the doping concentration and surface traps on ZnO NWs could be done to further understand their effects on the NW piezoelectric properties. Nevertheless, the mean piezoelectric amplitude of ZnO NWs is varied from 11 to 19 pm. In comparison, the ZnO thin films grown with the same PLI-MOCVD process but at a lower growth temperature have their mean piezoelectric amplitudes on the Zn-polar domain in the range of 8 – 11 pm, as shown in **Section**

4.1. Since the applied voltage amplitude in PFM measurement was kept at 5 V, the deduced piezoelectric coefficient d_{33} lies in the range of 2.2 – 3.8 pm/V for ZnO NWs and 1.6 – 2.2 pm/V for ZnO thin films. This emphasizes that the NW structures have superior piezoelectric efficiency compared to thin films.

4.3 Summary of the chapter

In summary, ZnO thin films and nanowires were formed with different combination of O_2 gas, DEZn solution flow rates and growth temperatures. The ZnO thin films were deposited at 500 °C with various morphologies when the flow rate conditions were changed. While the XRD analysis shows that all ZnO thin films are highly *c*-axis oriented, the PFM results further revealed that there is a large different in polarity distribution among thin films. In details, some thin films exhibit Zn-polar predominance indicating the development in c^+-axis direction, while some others present O-polar predominance responding to the development in c^--axis direction. The thin films with coexistence of both polarities are also formed at certain growth condition. This can be explained by the influence of the O_2/DEZn flow rate ratio on the oxygen chemical potential during the PLI-MOCVD growth process, affecting the surface energies of crystalline planes as well as the growth directions. The O-polar predominant thin films are only formed in a narrow range of O_2/DEZn flow rate ratio from 99 to 111, implying that this O-polar domain is less stable compared to the Zn-polar domain, which is also supported by previous results in Chapter 3. The appearance of O-polar predominant thin films is accompanied with a large change in grain size and shape, notable disruption in structural orientation and microstructural defects, and resistivity. This indicates that O-polar grains have different growth mechanism and properties compared to Zn-polar grains. In particular, the results suggest that O-polar grains could have more impurities that can screen the piezoelectric potential. Correspondingly, the PFM results also reveal that the Zn-polar domains exhibit higher piezoelectric amplitude than the O-polar domains.

At 700 °C, ZnO NWs were grown regardless of the flow rate conditions. Unlike the thin films grown at 500 °C, all NWs exhibit the Zn-polarity, which is in agreement with other reports showing that the self-assembled growth of ZnO NWs in the MOCVD process is only developed through Zn-polar domains. Compared with thin films grown at 500 °C, the NWs grown at 700 °C have higher piezoelectric amplitudes. The piezoelectric amplitude also tends to be higher in longer and thinner NWs confiming theoretical trends. Overall, the results show the importance of controlling the flow rate conditions to enhance the performances. The Zn-polarity uniformity along with the higher piezoelectric amplitude demonstrated that ZnO NWs are promising for piezoelectric applications. Nevertheless, a deeper study on electrical properties, especially for ZnO NWs, are required to understand clearly the effect of flow rate conditions on their doping concentration that in turn greatly affects their piezoelectric performance.

Chapter 5
AZO electrode grown by ALD and its influence on ZnO nanowire piezoelectric performance

In the previous Chapters, we have demonstrated that ZnO nanowires (NWs) with a high crystallinity can be grown directly on Si substrate by PLI-MOCVD. The heavily doped Si substrate was employed as a platform for the growth and also for the bottom electrode since it is compatible with the industrial scale production. In this Chapter, we investigated the possibility to use other material as a bottom electrode for ZnO NW-based piezoelectric devices, while also taking into account the criticality of the material. Based on literature review, the aluminum-doped ZnO (AZO) is selected for bottom electrode as it has advantages including eco-friendly material, well-known transparent electrode that is used for many electrical and optical devices, further having epitaxial relationship with ZnO NWs which can lead to high structural quality. The AZO electrode was formed using the atomic layer deposition (ALD) process, followed by ZnO NW growth using PLI-MOCVD. The Al dopant concentration was varied to study its effect on the AZO properties as well as the piezoelectric performance of ZnO NWs grown on top of it in the following step. The growth condition of ZnO NWs is based on the optimized condition deduced from previous results targeting the high structural quality and high aspect ratio, which is expected to give a good piezoelectric efficiency. The structural, electrical properties and optical transmittance of the AZO layer influenced by the Al dopant concentration were measured. Then, the properties of ZnO NWs/AZO layer structure were also analyzed.

5.1 Effect of AZO layer as a bottom electrode

5.1.1 Introduction and objectives

In electronics industry, the indium tin oxide (ITO) is one of the most common material used as an electrode for many applications thanks to its high electrical conductivity (~10^{-4} Ω.cm) and visible light transmittance (> 85%).[192,193] However, indium is a critical element and its compound is toxic.[193–195] Besides ITO, there are other transparent conductive electrode such as aluminum-doped zinc oxide (AZO),[196] fluorine-doped zinc oxide (FZO),[197] fluorine-doped tin oxide (FTO),[198] silver nanowires,[199] and graphene.[200] Among of them, aluminum-doped ZnO (AZO) is an attractive material for the electrode as it is not only low cost, non-toxic, but also has a high electrical conductivity and optical transmittance, making it be considered as a replacement for ITO.[193] For instance, R. Mereu et al. showed that the optical transmittance and the electrical conductivity of AZO thin films grown by sputtering were comparable to those of ITO thin films (**Figure 5.1**).[201] The AZO thin film has been

developed for different applications such as transistor,[202] solar cell,[88] organic light-emitting device (OLED),[203] gas sensor,[204] and piezoelectric nanogenerator.[205]

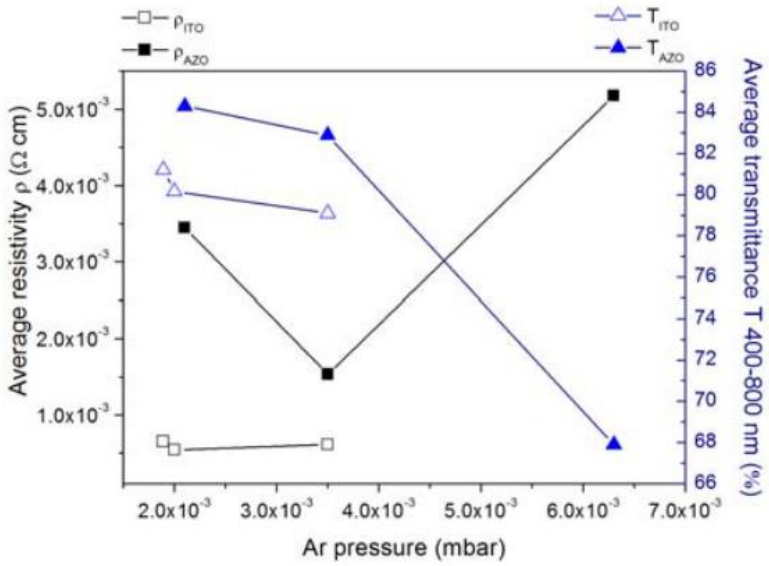

Figure 5.1: Evolution of the average resistivity and visible light transmittance of the AZO and ITO thin films as a function of the Ar pressure condition during the sputtering.[201]

AZO is a good electrode for developing the eco-friendly ZnO-based piezoelectric devices, but its effect on the device performance needs to be studied carefully. While the ZnO deposition on Si substrate follows a non-epitaxial growth, the ZnO deposition on the AZO layer proceeds through a homogenous epitaxial growth, in which the surface and structure of the AZO layer can significantly affect the ZnO NW growth process. For instance, S. Pung et al. demonstrated that the growth direction of ZnO NWs were changed depending on the orientation of ZnO thin film used as a platform.[206] Thus, it is very important to control both the structural and electrical properties of AZO electrode during its fabrication process, which can greatly affect the properties as well as the piezoelectric efficiency of the ZnO NWs grown in the following step.

Among various deposition techniques, the atomic layer deposition (ALD) process can grow AZO thin films in a large area with precisely controlled thickness, and uniformity while not requiring ultra-high vacuum. The AZO grown by ALD can also have high conductivity that is comparable with ITO. For example, an AZO thin film with the resistivity at 5.37 x 10^{-4} Ω.cm was fabricated by J. Kim et al. using the ALD process at 250 °C.[207] Many researchers have investigated the effects of different growth parameters in ALD process, such as the growth temperature,[206,208] aluminum (Al) doping concentration,[208,209] and substrates.[210] While their results showed that the AZO thin film has good properties for electrode that can be used in many applications, there are only a few reports about its piezoelectric applications, especially its combination with ZnO NWs.

In this work, we studied structural and electrical properties of the AZO electrodes deposited on Si substrates by ALD process with different Al doping concentration. Then, these AZO electrodes were then used as platforms for the following ZnO NWs growths using the PLI-MOCVD process. The influence of the AZO layer on the ZnO NW properties and the piezoelectric efficiency of the whole

structure were investigated. The structural properties of AZO thin films and ZnO NWs were analyzed by field-emission scanning electron microscopy (FESEM), X-ray diffraction (XRD), and Raman spectroscopy. The electrical properties of AZO electrodes were measured by Hall-effect measurement. The optical transmittance were recorded by a UV–Vis-NIR spectrophotometer. The piezoelectric properties were characterized by datacube piezoresponse force microscopy (PFM). A comparison of the ZnO NW growth on the AZO layer to its growth on ZnO substrates was also performed.

5.1.2 Experiment

5.1.2.1 AZO electrodes grown by ALD

The undoped ZnO and AZO thin films were synthesized by atomic layer deposition (ALD) method in the Cambridge NanoTech Fiji F200 system (see **Section 2.3**). Diethylzinc (DEZn), trimethyl aluminum (TMA) and water vapor (DI) were used as the Zn, Al and O precursors, respectively. The thin films were formed by many super cycles. For the AZO thin films, a super cycle consisted of n cycles for ZnO deposition and 1 cycle for Al_2O_3 deposition. The n was varied at 40, 30, 20, and 10 to have the AZO thin films with different Al doping concentration, which are denoted as AZO40, AZO30, AZO20, and AZO10. The undoped ZnO was grown by removing the cycle for Al_2O_3 deposition from the super cycle. The total number of cycles were kept at around 1320 for every growth to obtain the same thickness (180 nm). The substrate temperature was set at 250 °C. The growths were performed simultaneously on the standard Si (100) with resistivity around 10 Ω.cm, heavily doped p-type Si (100) with the resistivity at 2 x 10^{-3} Ω.cm, and quartz. The thin films on the standard Si substrates were used for the electrical measurements, while the thin films on the heavily doped p-type Si substrates were used for the PFM measurements, and the thin films deposited on quartz were used for the optical transmittance measurements.

5.1.2.2 ZnO NWs grown by PLI-MOCVD

The ZnO NWs were grown using PLI-MOCVD technique in an Annealsys MC-200 MOCVD system. The as-grown AZO layers on a heavily doped p-type Si (100) substrate in the previous step were used as platforms for the ZnO NW growths. The ZnO NW array grown directly on a heavily doped Si substrate was also prepared for a reference sample. The Zn precursor was a solution of diethylzinc ($Zn(C_2H_5)_2$, DEZn, Sigma-Aldrich) diluted in cyclohexane at 0.4 mol/l. This solution was injected to the reactor chamber at a flow rate of 0.5 g/min with 500 sccm Ar as gas carrier. The O_2 gas as an O precursor was introduced into the chamber with the flow rate set at 300 sccm. The temperature of the substrate and the chamber pressure were kept constant at 700 °C and 3 mbar during the growth, respectively. The growths on AZO layers and Si substrate were performed simultaneously in 10 minutes. On each AZO layer, a small AZO area was covered by a piece of Si in order to protect that area from the ZnO NW deposition. Those AZO areas without ZnO NW deposition were used for electrical connection in the later PFM measurements.

5.1.2.3 Characterizations

The properties of AZO thin films grown by ALD and ZnO NWs grown by PLI-MOCVD were characterized using different techniques (described in **Section 2.2**). The structural properties of

undoped ZnO, AZO thin films, and ZnO NWs were analyzed by field-emission scanning electron microscopy (Gemini300 FEI ZEISS-SEM), X-ray diffraction (Bruker D8 Advance diffractometer), and Raman scattering measurements (Jobin Yvon/Horiba Labram spectrometer). The electrical properties of thin films were investigated by Hall-effect measurement using a home-made station. The optical transmittance of ZnO and AZO films deposited on quartz were measured by a UV–Vis-NIR spectrophotometer (Perkin Elmer Lambda 950 spectrometer). The piezoelectric properties of NWs were measured by piezoresponse force microscopy (Bruker Dimension Icon AFM).

5.1.3 Results and discussion

5.1.3.1 AZO electrodes

In the 1st part, we studied the effect of Al doping concentration on the properties of AZO40, AZO30, AZO20 and AZO10 layers. The undoped ZnO grown by the ALD process was also prepared as a reference sample. The structural properties measurements were performed on undoped ZnO and AZO layers deposited on heavily doped Si substrates, which were used for the following ZnO growths and their PFM scanning. The electrical properties were carried out on ZnO and AZO layers deposited on standard Si substrates.

Morphology of ZnO and AZO thin films

The FESEM images of undoped and Al-doped ZnO thin films grown by ALD with different concentrations are presented in **Figure 5.2**. By maintaining the total super cycle for every ALD growth, the thickness of thin films are kept similar at around 180 nm, as shown in the cross-sectional-view images. However, the morphologies presented in the top-view images are different, indicating that it is mainly affected by the Al dopant concentration variation. The undoped ZnO film presents the big irregular shape grains along with other smaller round grains. The small round shape grains and the elongated grains observed especially on AZO30 and AZO20 express the (002) and (100) planes of ZnO wurtzite structure, respectively, which are similar to the results in refs.[208,211,212]. Correspondingly, the root mean square (RMS) roughness measured by AFM of the undoped ZnO films shows the highest value at 2.8 nm. The roughness is decreased to 2.3 nm on the AZO40 film, and to around 1.3 nm on other samples.

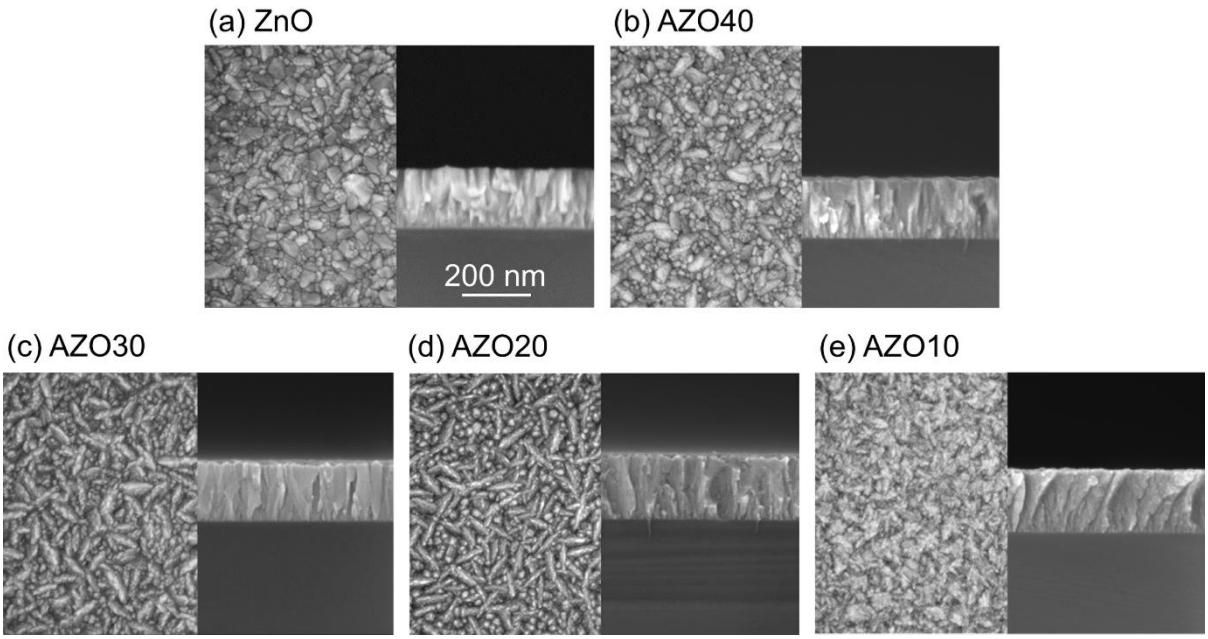

Figure 5.2: Top-view (left) and cross-sectional-view (right) FESEM images of AZO thin films grown by ALD with different Al doping concentration.

Growth Texture and Strain of ZnO and AZO thin films

Figure 5.3 shows the XRD pattern of ZnO and AZO thin films. The peaks located at 31.8, 34.4, 36.3, 47.5, 62.9, and 72.6° are attributed to the 100, 002, 101, 102, 103, and 004 diffraction peaks of the ZnO wurtzite structure, as indicated by the International Center for Diffraction Data (ICDD) file labelled 00-036-1451. Besides the peaks of Si and ZnO, no other peak of Al-related compound is observed, showing that Al atom only acts as a dopant inside ZnO thin films. The XRD pattern of undoped ZnO thin film has many diffraction peaks with similar intensities, expressing a random orientation in this thin film (**Figure 5.3a**). This is different from the ZnO grown by MOCVD as shown in our previous results, in which the structure is highly *c*-axis oriented as indicated by the superior intensity of the 002 peak as compared to other peaks. Normally, the ZnO growth is expected to be the fastest on the polar *c*-planes since they have the highest surface energy in the wurtzite structure.[158] The suppression of ZnO growth along the *c*-axis during ALD process was also observed in the report of S. Pung et al., in which they explained that it was due to the interference of organic molecules dissociated from DEZn.[206] Particularly, the negatively charged CH_3CH_2- group can attach to the positively charged Zn-polar surface, disturbing the growth on this plane. Due to the limited reactive sites during the ALD growth process, the Zn and O adatoms move to other reactive sites on other planes. In addition, our ZnO growth was performed on Si substrate which has no epitaxial relation with ZnO, and the growth temperature in ALD chamber (250 °C) is lower as compared to MOCVD chamber (500 – 700 °C) leading to a lower diffusion length of adatoms. Thus, all these reasons cause the ZnO crystal to develop in random directions.

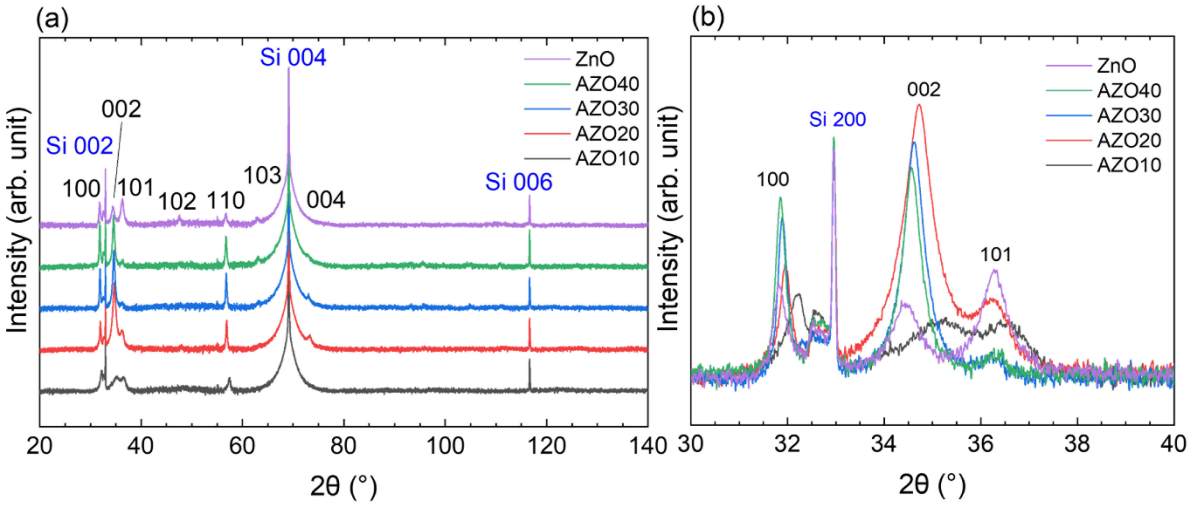

Figure 5.3: (a) XRD of AZO thin films grown by ALD with various Al doping concentration; (b) Zoom-in in the area of interest ranging from 30 to 40° in the XRD patterns. The intensity was plotted in logarithmic scale.

When the Al dopant was added in the AZO40 sample, the 002, 100 and 110 peaks become more intense, demonstrating the preferential growth on the polar *c*-plane, non-polar *m*- and *a*-planes (**Figure 5.3**). By increasing the Al amount in AZO30 and AZO20 samples, the 002 peak intensity continues increasing while the 100 and 110 peak intensities are decreased. Simultaneously, the intensities of 101, 102 and 103 representing the semi-polar plane are reduced and disappear. This also corresponds to the predominance of the round and elongated grains and the disappearance of other irregular shape grains as seen in the AZO30 and AZO20 morphologies (**Figures 5.2c-d**). The AZO thin films with a highly *a*-axis oriented structure grown by ALD has been reported by several research groups.[208,212,213] They explained that the participation of Al^{3+} ions increases the surface energy of non-polar planes, resulting in a faster growth in this direction. The results in refs.[212,213] demonstrated that the growth along the *c*-axis was suppressed regardless of the Al dopant concentration. In contrast, our results show that the ZnO thin films were even grown faster on the *c*-planes with the increase of Al dopant concentration, which is similar to the results in refs.[208,214] Although the used precursors are the same, there are differences in ALD systems, the growth temperatures and flow rates among our work and the works of other groups. These factors also strongly influence the Al incorporation inside ZnO structure, causing a distortion of ZnO lattice and largely varying the relative surface energies as well as the growth rate of ZnO crystalline planes.[208]

In AZO10 thin film, the intensities of 002 and all other peaks are suddenly decreased while their widths are increased (**Figure 5.3b**). This indicated that the Al dopant concentration was so high that it disrupted the formation of ZnO, resulting in a poor crystal quality. Combining with the SEM image in **Figure 5.2e**, the result expresses that the AZO10 is partially crystallized, which is similar to the observation in ref.[215] In **Figure 5.3b**, it can also be seen that the diffraction peaks are strongly shifted to higher θ value when the Al concentration is increased. To have a more accurate evaluation, the texture coefficients of crystallite planes and the homogeneous residual strain were calculated based on the intensities and the positions of diffraction peaks, as shown in **Figure 5.4**. Due to the low thickness of AZO thin films (< 200 nm), the signals of diffraction peaks at high 2θ angle (i.e. 004 and

006 peaks of the ZnO wurtzite structure) nearly cannot be detected in XRD patterns (**Figure 5.3**). Thus, there is not enough data to apply the Williamson-Hall method for estimating the inhomogeneous strain and crystallite size in these AZO thin films.

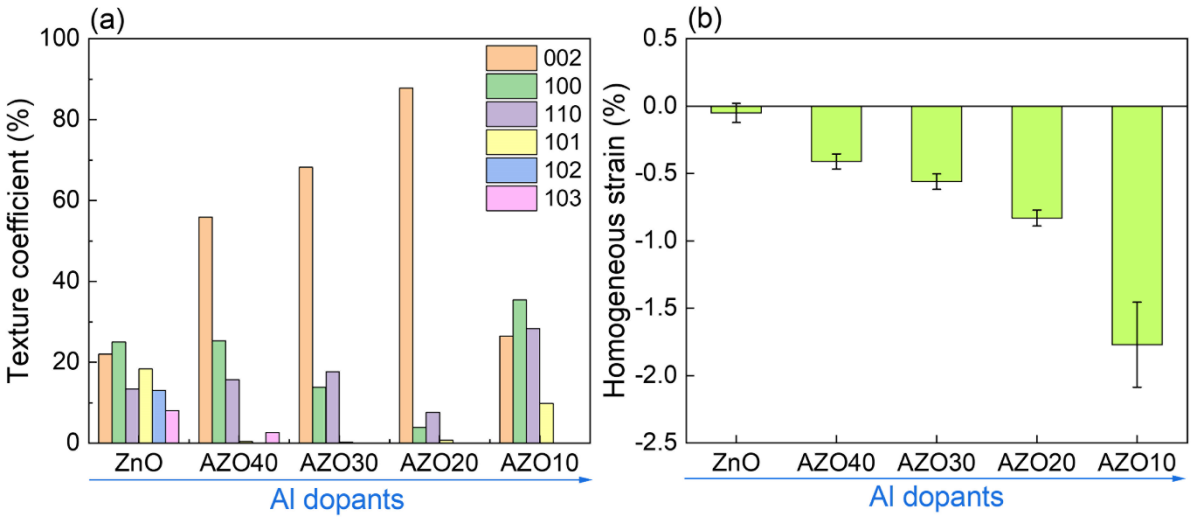

Figure 5.4: (a) The texture coefficients and (b) the mean homogeneous strain of AZO thin films grown by ALD as a function of Al doping concentration.

When the Al dopant concentration is increased, the 002 texture coefficient is continuously increased from 22.0 % in ZnO thin film to 87.8 % in AZO20 thin film, as shown in **Figure 5.4a**. Simultaneously, the texture coefficients of semi-polar (101), (102) and (103) planes are decreased close to 0 when a small amount of the Al dopant is added in the AZO40 thin film. The texture coefficients of non-polar (100) plane starts being decreased when more Al dopants are added in the AZO30 thin film, and the texture coefficients of non-polar (110) plane is also decreased in the AZO20 thin film. Further adding Al dopants leads to the formation of partially crystallized AZO10 thin film, for which the 002 texture coefficient is decreased drastically to 26.4 % while other plane texture coefficients are increased again. In **Figure 5.4b**, the residual strain is increased constantly with the Al doping concentration, indicating the participation of the Al dopants into the ZnO lattice that causes its distortion. In details, the residual strain is rapidly increased from -0.05 % in ZnO to -1.77 % in AZO10. It can be noticed that the ZnO thin film grown by the ALD process has a nearly strain-free state, which is opposite to the ZnO thin film grown by MOCVD process. As shown in previous results, ZnO thin film after MOCVD growth undergoes a significant compressive strain, which was generated during the 3D Volmer− Weber growth mode. In the ALD process, ZnO formation is forced to grow in 2D layer-by-layer mode by limiting the number of reactive sites on the substrate surface during each cycle. Thus, the strain is easier to be relaxed when the adatoms are well-arranged on the surface. The negative (compressive) strain appears and increases when the Al dopant is added, indicating that the Zn^{2+} ions are substituted by Al^{3+} ions inside the ZnO lattice. Since the Al^{3+} ion radius (0.53 Å) is smaller than the Zn^{2+} ion radius (0.74 Å), the lattice parameter is reduced when Al^{3+} ions replace Zn^{2+} ions, resulting in the peak shift to higher θ value as well as a compressive biaxial strain.[208,209,216] The significant compressive strain in AZO10 thin film is due to a larger amount of Al dopant introduced in its structure, which leads to the degradation of its crystallinity. However, a sufficient Al dopant

concentration helped improve the *c*-axis orientation as shown in AZO20 thin film, which can be favorable for the following ZnO NW growth.

Electrical properties of ZnO and AZO thin films

Figure 5.5 shows the electrical resistivity, charge carrier mobility and charge carrier density of ZnO and AZO thin films grown by ALD on standard Si substrate. The electrical measurements performed on thin films grown on quartz showed similar results. Moreover, we also fabricated metallic electrodes on the sample layer surfaces in order to ensure the good electrical contact between the probes of the measurement station and the thin films. The metallic electrodes were made of 50 nm-thick nickel (Ni) and 120 nm-thick gold (Au) layers, which were deposited on the thin film surfaces using photolithography followed by lift-off processes. The measurements with and without the metallic electrodes gave the similar results. In **Figure 5.5a**, the undoped ZnO thin film grown by the ALD process shows a resistivity at 7.8 x 10^{-3} Ω.cm, which is notably low compared to our ZnO thin films grown by the MOCVD (see **Section 3.1** and **Section 4.1**). This could be due to the incorporation of hydrogen inside ZnO structure. Many studies have shown that hydrogen impurities can be generated from the decomposition of DEZn precursor or water vapor during the ALD process, leading to an unintentional hydrogen doping in ZnO film.[217–219] These hydrogen dopants can act as shallow donors inside the ZnO structure and decrease its resistivity.[117,218] By adding Al dopant, the resistivity is further decreased to 0.6 – 0.7 x 10^{-3} Ω.cm in AZO40, AZO30 and AZO20, expressing the contribution of Al dopant to the thin film resistivity. This is also evident by an increase of the charge carrier density from 1.6 x 10^{20} cm^{-3} in undoped ZnO film to around 2.6 x 10^{21} cm^{-3} in AZO40, AZO30 and AZO20 (**Figure 5.5b**), signifying that Al dopant acts as a shallow donor inside the ZnO structure. **Figure 5.5c** shows that the charge carrier mobility is decreased from 5.1 $cm^2/(V.s)$ in undoped ZnO thin film to around 3.5 $cm^2/(V.s)$ in AZO40, AZO30 and AZO20 despite the higher structural quality of AZO films compared to the undoped ZnO film. This could be due to the increase of ionized impurity scattering when the Al dopant is added into ZnO lattice, causing a decrease of mobility in AZO films.[220] With further doping in AZO10 film, the resistivity is not decreased but it is increased to 5.5 x 10^{-3} Ω.cm in AZO10 film (**Figure 5.5a**), which could be due to partially crystallized structure of this film as revealed in XRD result. In this structure, there are many defects with incomplete atomic bonding, which can trap and immobilize the charge carriers.[221] The charge carrier mobility and density of AZO10 film could not be measured using the Van der Pauw method. We suspect that the mobility in AZO10 film is decreased drastically to such a small value that is out of the limit for the measurement system. It is worth mentioning that the resistivity of 0.6 – 0.7 x 10^{-3} Ω.cm in our AZO40, AZO30 and AZO20 films is lower compared to most of AZO films grown by ALD demonstrated by other groups,[203,212,213,215,216] showing that these AZO films are good candidate to be used as bottom electrode.

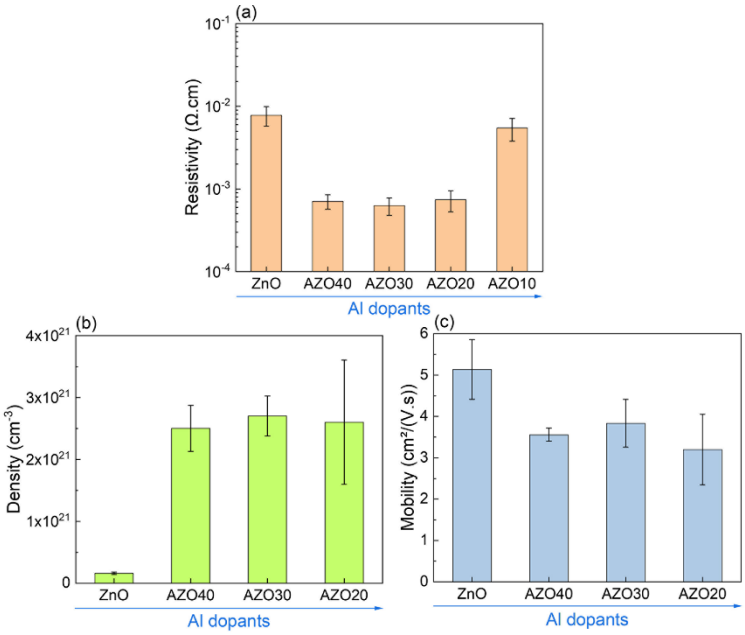

Figure 5.5: (a) The electrical resistivity, (b) the charge carrier density and (c) the charge carrier mobility of AZO thin films grown by ALD on standard Si substrate as a function of Al doping concentration.

Optical transmittance of ZnO and AZO thin films

The optical transmittance spectra in **Figure 5.6a** show that the ZnO and AZO thin films grown on quartz are highly transparent in the visible light region (400 – 700 nm). At around 650 nm, their transparency is up to 92 – 93 %, which is close to the transmittance of the quartz substrate. In the range of 400 – 700 nm, the average transmittance of ZnO and AZO thin films lies in the range of 84 – 87%, showing that these thin films have a good transparency for optical applications. Besides, it can be noticed in **Figure 5.6a** that the absorption edge shifts to lower wavelength (higher energy) as the Al dopant is increased. To clarify this, the optical band gaps of ZnO and AZO thin films were extracted using Tauc's relationship:[208]

$$(\alpha h\nu)^n = A\left(h\nu - E_g\right) \qquad (5.1)$$

where α is the absorption coefficient, $h\nu$ is the photon energy, n is equal to 2 for direct bandgap of semiconductor (i.e. ZnO), A is a constant, and E_g is the optical bandgap. The absorption coefficient α can be calculated from the optical transmittance as follows:[222]

$$\alpha = \frac{-\ln(T)}{t} \qquad (5.2)$$

where T is the optical transmittance, and t is the thickness of thin films. By plotting the $h\nu$ versus $(\alpha h\nu)^2$ (Tauc plot) and fitting a linear part of the curve, the optical bandgap E_g can be deduced from the X-intercept of the linear curve. The Tauc plots and the deduced optical band gaps of ZnO and AZO thin films are shown in **Figures 5.6b** and **c**, respectively. The result shows that the optical band gap energy constantly increases from 3.29 eV in undoped ZnO thin film to 3.91 eV in AZO10 thin film. This increase of optical band gap with the Al doping content in AZO thin films has been observed and reported by many research groups, which can be attributed to the Moss-Burstein effect: the

additional donor Al^{3+} dopants fills the lowest states of conduction band, causing a shift of the Fermi level to the higher energy.[196,208,212,213,215]

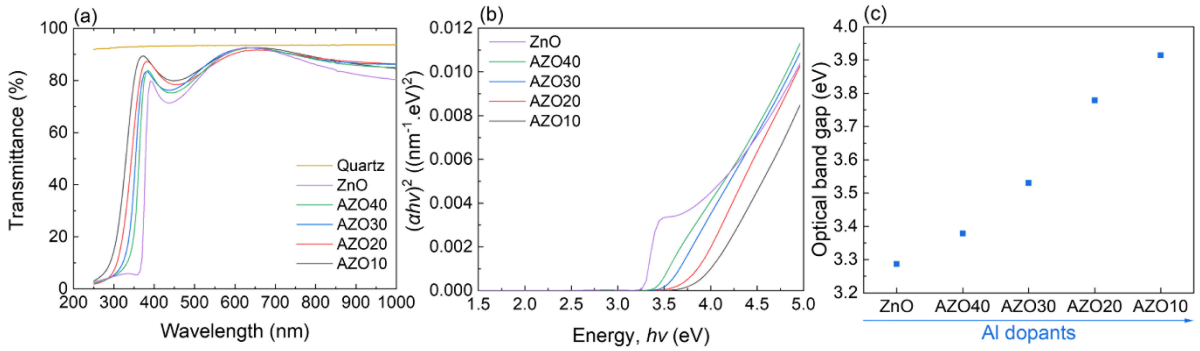

Figure 5.6: (a) The optical transmittance of undoped ZnO and AZO thin films grown on quartz by ALD with various Al doping concentration; (b) Tauc plot of ZnO and AZO thin films; (c) Optical band gaps of ZnO and AZO thin films deduced from Tauc plot.

To quantitively evaluate and compare the performance of the transparent electrodes, a figure of merit (FOM) is usually used. It is a numerical value involving the visible light transmittance and the electrical conductivity, which are two most important properties of the transparent electrode. In this work, the figure of merit values (Φ_{TC}) of the AZO films were calculated as follows:[196,223,224]

$$\Phi_{TC} = \frac{T^{10}}{R_{Sh}} \qquad (5.3)$$

where T is the average transmittance in the light wavelength ranging from 400 – 700 nm, and R_{Sh} is the sheet resistance of the thin films. It can be seen that the figure of merit value is higher when the optical transmittance or the electrical conductivity is higher, expressing a better performance of the transparent electrode. The detail of thickness, sheet resistance, transmittance and figure of merit values of undoped ZnO and AZO thin films are shown in **Table 5.1**. Moreover, a comparison of the sheet resistance and the optical transmittance of our AZO thin films with other AZO and ITO thin films grown by other research groups are shown in **Figure 5.7**.

Table 5.1: The average thickness, sheet resistance, transmittance and figure of merit values of undoped ZnO and AZO thin films grown by ALD.

Sample	Mean transmittance T (%)	Thickness (nm)	Sheet resistance (Ω/□)	Figure of merit (Ω^{-1})
ZnO	84.2	176	443.8	0.41 x 10^{-3}
AZO40	85.4	177	40.1	5.13 x 10^{-3}
AZO30	86.1	181	34.8	6.40 x 10^{-3}
AZO20	85.9	196	37.8	5.81 x 10^{-3}
AZO10	87.1	187	291.4	0.86 x 10^{-3}

The results show that the FOM values of our AZO thin films is around 10^{-3} Ω^{-1}, which is average as compared to FOM values of AZO thin films ranging from 10^{-4} to 10^{-2} Ω^{-1} shown in refs.[196,201,224]. In **Figure 5.7**, our AZO thin films, especially the AZO40, AZO30 and AZO20 thin films, have fairly good

sheet resistance and optical transmittance, which are comparable to those of ITO thin films. Although the sheet resistances of our AZO films are lower than those of some AZO films grown by sputtering, they are still fairly high as compared to AZO films grown by ALD or other growth techniques reported by other groups. These properties of our AZO thin film can be further improved by optimizing the fabrication conditions in future work. As a more eco-friendly material, these AZO thin films have a high potential to replace ITO in transparent conductive oxide (TCO) applications.

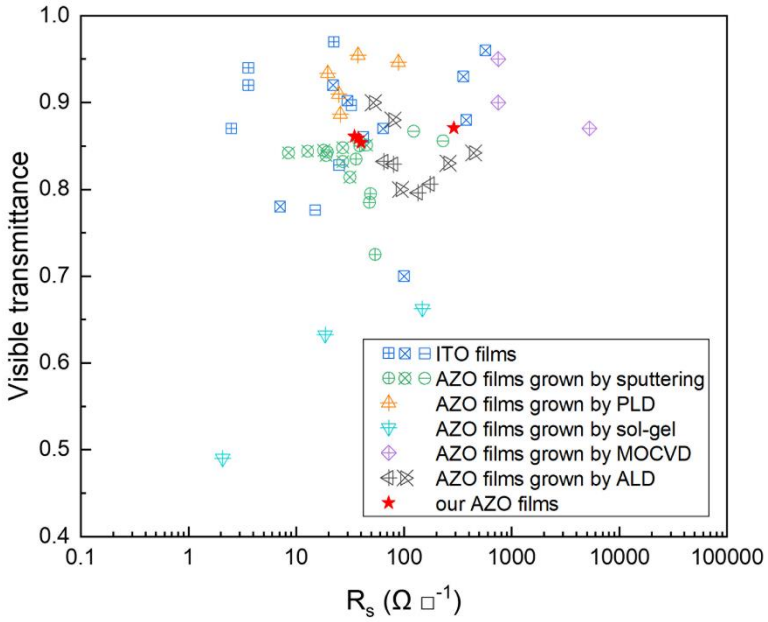

Figure 5.7: Visible transmittance as a function of the sheet resistance for conductive transparent electrodes: ITO films from refs.[201,225,226], AZO films grown by sputtering from refs.[196,201,224], by pulsed laser deposition (PLD) from ref.[227], by sol-gel method from ref.[222], by MOCVD from refs.[228], by ALD from refs.[203,229], and our AZO films.

5.1.3.2 ZnO NWs grown on AZO layers

For the next part, we studied the growth of ZnO NWs on AZO30, AZO20 and AZO10, and compared with the ZnO growth on Si substrates. Then, we compared piezoelectric properties of these NWs using PFM. All AZO layers and Si substrates were put in the PLI-MOCVD chamber and growth at the same time. The heavily doped Si substrates were used as the bottom electrodes in PFM measurements.

AZO layers after PLI-MOCVD process

Before discussing about the ZnO NWs grown on AZO layers, it is worth to mention that the AZO layers were also affected by the growth conditions in the PLI-MOCVD process. During the ZnO NW growth, the AZO30, AZO20 and AZO10 layers as substrates in the PLI-MOCVD reactor chamber were heated from room temperature to 700 °C at the beginning of the process and were cooled down at the end of the process in Ar atmosphere. When the DEZn and O_2 gas were introduced to the chamber for NW growth, these AZO layers were also exposed to the O_2 gas while being heated at 700 °C in 10 minutes due to the NW growth conditions. The pressure inside the reactor chamber was maintained at 3 mbar. This means the AZO layers were annealed throughout the NW growth process, which can affect their properties. To test the structural and electrical properties of AZO layers after

the growth, we repeated the growth process on the as-grown AZO layers using the similar conditions but without injecting DEZn precursor. These samples are denoted as annealed AZO thin films. The properties of annealed AZO layers were measured and compared with the as-grown AZO thin films. **Figure 5.8** shows the FESEM images and XRD patterns of these annealed AZO thin films.

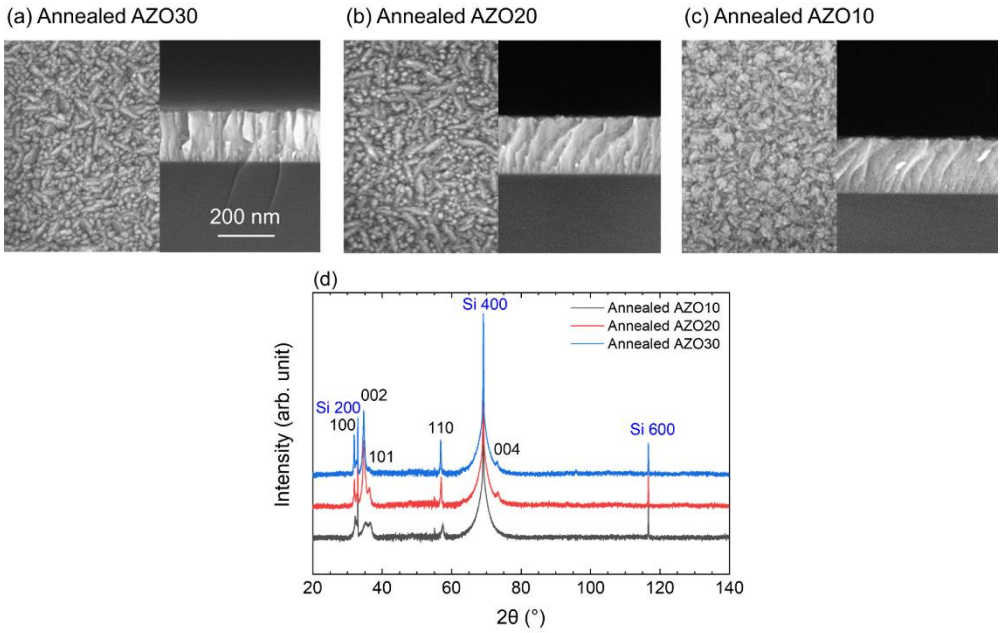

Figure 5.8: Top-view (left) and cross-sectional-view (right) FESEM images of (a) annealed AZO30, (b) annealed AZO20 and (c) annealed AZO10 thin films. (d) XRD of annealed AZO thin films; the intensity was plotted in logarithmic scale.

Figures 5.8a-c shows that there is no change in morphology of AZO30, AZO20 and AZO10 layers after the annealing process. **Figure 5.8d** also presents XRD patterns of these layers, which are similar to the XRD patterns of as-grown films (**Figure 5.3**). The 002 texture coefficients before and after the annealing are also similar, but the homogeneous compressive strains are slightly increased. In detail, the strains are increased from -0.56, -0.83 and -1.77% to -0.67, -0.99 and -2.05% in AZO30, AZO20 and AZO10 layers, respectively. This could be due to the adsorption of oxygen during the annealing at high temperature created defects or local segregation of Al oxide, which further induced more internal strain in ZnO lattice.[220,221]

Different from the structural properties, the resistivity of AZO30 and AZO20 layers is increased 1 order (from 0.6 – 0.7 x 10^{-3} to around 5 x 10^{-3} Ω.cm) after the annealing. Since they are annealing in O_2 atmosphere, the reason could be: (1) the adsorption of O at the grain boundary can trap the electrons,[220] or (2) the formation of Al oxide reduces the shallow donors formed by Al_{Zn} defects as well as the carrier density.[221] On the other hand, the resistivity of AZO10 layers remains around 5.5 x 10^{-3} Ω.cm after the annealing. This could be due to the carriers inside the AZO10 layer had been trapped even before the annealing due to its partially crystallized structure. Nevertheless, the resistivity of AZO layers after the annealing is still decent and comparable with the resistivity of the heavily doped Si substrate, which is around 2 x 10^{-3} Ω.cm.

Morphology of ZnO NWs grown on AZO thin films

The FESEM images in **Figure 5.9** shows that the ZnO NWs formed on Si substrate, AZO30 and AZO20 layers are well aligned, except on the AZO10 layer. As shown in the previous result, the ZnO NW formation on Si substrate is a non-epitaxial growth. In that growth, a very thin polycrystalline ZnO layer was formed at the beginning, followed by the prevalence of 002 direction over other directions at high growth temperature, leading to the vertical ZnO NW growth. In contrast, the ZnO NW formation on the AZO layer is a homogeneous epitaxial growth, where the direction of the initial layer strongly affects the direction of structure grown above it.

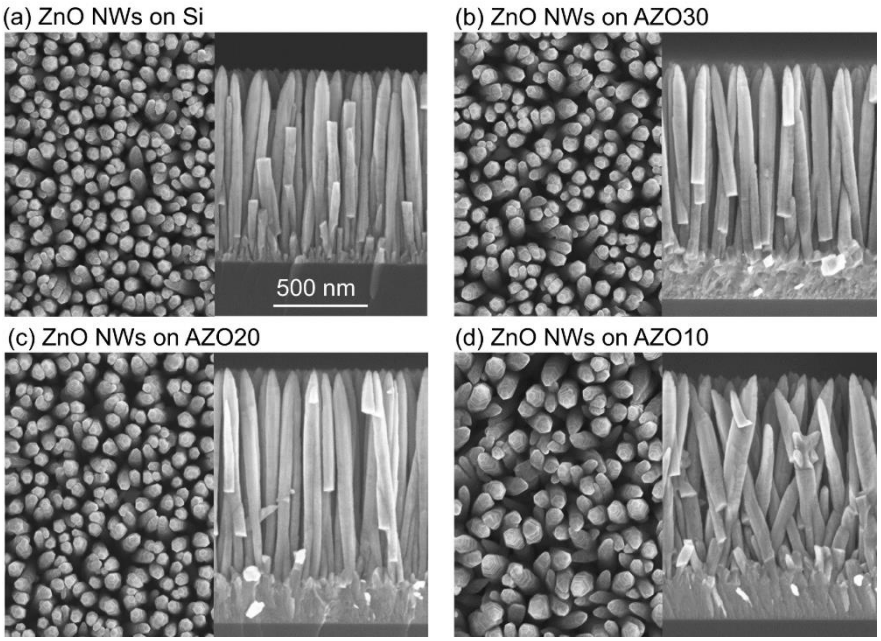

Figure 5.9: Top-view (left) and cross-sectional-view (right) FESEM images of ZnO NWs grown by PLI-MOCVD on (a) Si substrate, (b) AZO30, (c) AZO20 and (d) AZO10 layers.

Since the AZO30 and AZO20 layers have a good 002 orientation perpendicular to the substrate (**Figure 5.4a**), ZnO NWs deposited on these layers are also vertically developed. Meanwhile, the random orientation of AZO10 layer influences the growth direction that leads to the inclined NWs. A similar observation has been shown in ref.[206], where ZnO NWs were grown on AZO templates by chemical vapour deposition process. The length and diameter of NWs were measured from the cross-sectional images, which are shown in **Table 5.2**.

Table 5.2: Lengths and diameters of ZnO NWs grown by PLI-MOCVD on Si substrate and AZO layers.

Sample	Length (nm)	Diameter (nm)
ZnO NWs on Si	1029 ± 83	72 ± 10
ZnO NWs on AZO30	1072 ± 92	77 ± 14
ZnO NWs on AZO20	1174 ± 74	77 ± 13
ZnO NWs on AZO10	1092 ± 63	95 ± 16

The result shows that the ZnO NW lengths are similar among samples, but the diameter of NWs on AZO10 is notably larger than NWs on other platforms. As the NWs on AZO10 were grown

with different tilt angles, these NWs can cross and merge into bigger NWs. These results demonstrate that the AZO surfaces have a strong impact on the nucleation of ZnO at the beginning of the growth, which in turn leads to different NW formation in the following growth step.

A comparison with ZnO NWs grown on ZnO substrates

A comparison of ZnO NW growth on the AZO layer and on ZnO substrates (from Crystec) were also performed. The AZO20 layer on Si substrate, Zn-polar ZnO and O-polar ZnO substrates were put in the PLI-MOCVD chamber and ZnO NW arrays were simultaneously grown on them in 7 minutes. The AZO20 thin film was selected for this comparison because it has the highest 002 texture coefficient among our AZO thin films (**Figure 5.4**), which is the most suitable to grow a well-vertical aligned NW array. Besides, it also has a good conductivity that is similar to AZO30 and AZO40 thin films, of which the resistivity values are the lowest among AZO series (**Figure 5.5**). **Figure 5.10** displayed the FESEM images of the NW arrays with the length at around 870 nm.

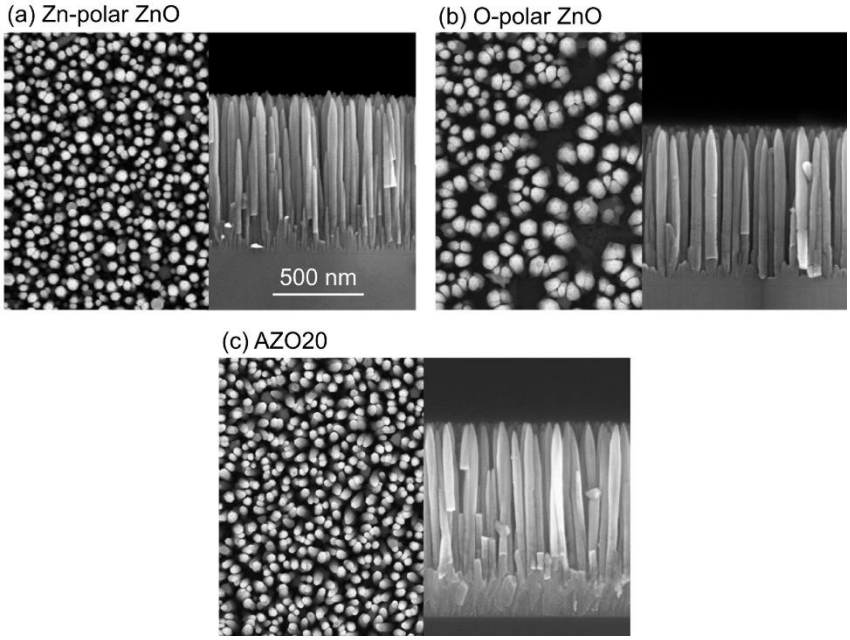

Figure 5.10: Top-view (left) and cross-sectional-view (right) FESEM images of the ZnO NWs grown by PLI-MOCVD on (a) Zn-polar ZnO substrate, (b) O-polar ZnO substrate and (c) AZO20 thin film.

Thanks to the homogeneous growth, the vertically well-aligned ZnO nanowire arrays were formed on ZnO substrates. The NW array on Zn-polar ZnO substrate has the smaller diameter, which is around 49 nm. On the O-polar ZnO substrate, the NW array diameter is around 53 nm. Some large gap can also be seen between NWs on in this NW array (**Figure 5.10b**). This could be caused by the defects existing on the O-polar ZnO substrate before the growth.[34] On AZO20 layer, the ZnO NW array also achieved a good vertical alignment with the diameter at around 56 nm. This shows that the AZO layer can be used as alterative platform to grow vertically well-aligned ZnO NWs, which is less expensive compared to ZnO substrate and can be extended to the industrial scale production.

Growth direction and strains of ZnO NWs

Figure 5.11 shows the XRD patterns of ZnO NWs grown on Si and AZO layers. Besides the diffraction peaks of Si substrate, other peaks are attributed to the diffraction peaks of ZnO wurtzite

structure, according to the ICDD file labelled 00-036-1451. In all samples, the 002 peak exhibits a significantly higher intensity compared to other peaks, indicating that NWs were grown along this direction during the MOCVD process. It can be also noticed in **Figure 5.11b** that most peaks are the convolution of 2 peaks: the one at higher θ value is the peak of the AZO layer grown by the ALD process, and the other one at the lower θ value is the peak of the ZnO structure formed by the MOCVD process. In **Figure 5.11a**, the pattern of ZnO NWs on the AZO10 layer shows many different diffraction peaks. The 104, 105 and 106 peaks located at 81.4, 104.1 and 136.5 ° were not seen in AZO10 film pattern due to low thickness film, but now are also detected. The increase of these peak intensities after the MOCVD process describes that different orientation growths continued to develop on the AZO10 surface, leading to the inclined ZnO NWs formation. Consequently, the 002 peak intensity of NWs on the AZO10 layer is lower compared to other samples. This is due to the XRD patterns were recorded in Bragg–Brentano configuration, in which only the planes that are parallel to the substrate have their signals collected. Thus, only the (002) planes of vertically aligned NWs are shown in the pattern, while the (002) planes of other inclined NWs are not scanned.

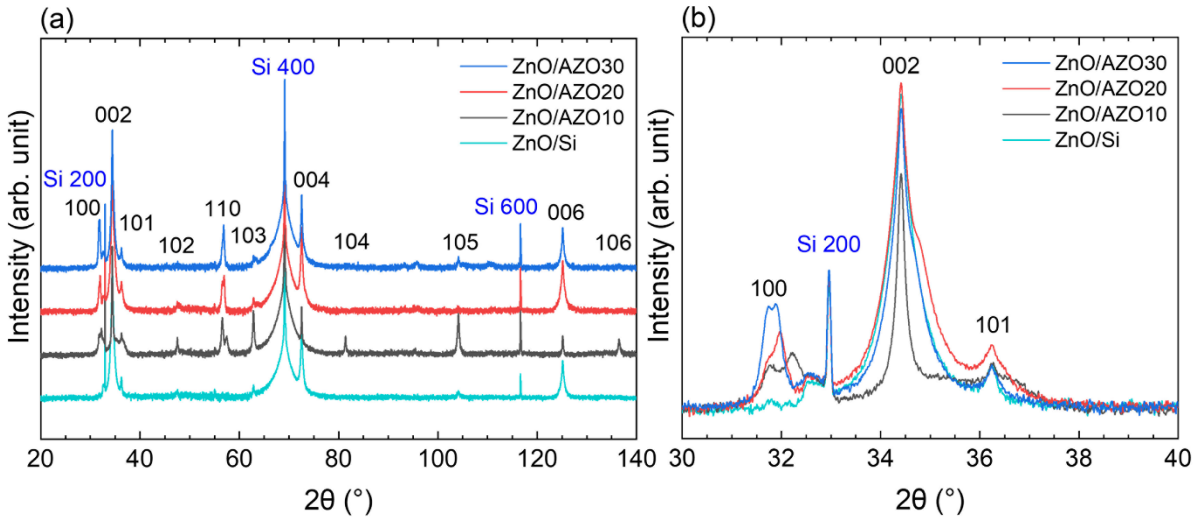

Figure 5.11: (a) XRD of ZnO NWs grown by PLI-MOCVD on Si substrate and AZO layers; (b) Zoom-in in the area of interest ranging from 30 to 40° in the XRD patterns. The intensity was plotted in logarithmic scale.

The 002 texture coefficients and residual homogeneous strains of ZnO NW samples are also extracted from the XRD results, as shown in **Figure 5.12**. In **Figure 5.12a**, the 002 texture coefficients on Si and other AZO30 and AZO20 layers are higher than 99 %. It is also more than 97 % on AZO10. This confirms that the ZnO NWs were grown along the *c*-axis. In **Figure 5.12b**, the residual strain of all samples are close to 0, indicating the strain relaxation thanks to the NW structure.

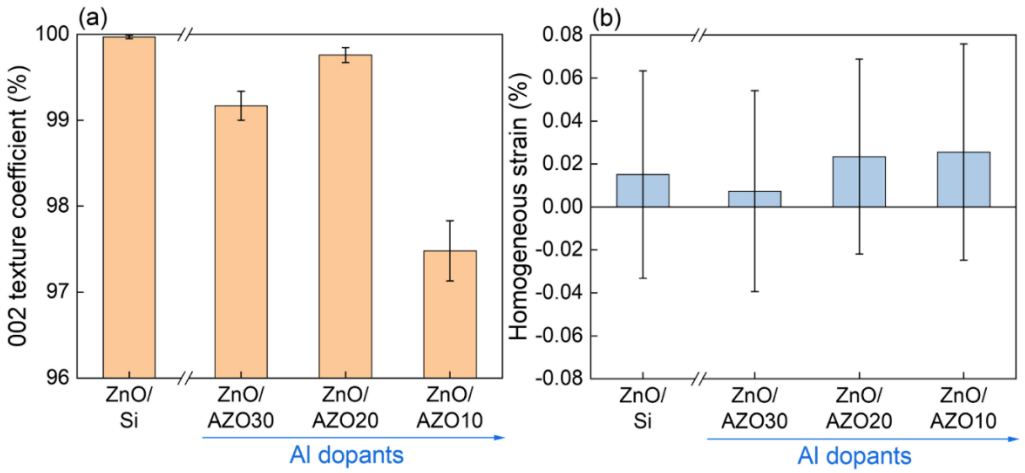

Figure 5.12: (a) The 002 texture coefficient and (b) the mean homogeneous strain of ZnO NWs grown by PLI-MOCVD on Si substrate and AZO layers.

Raman scaterring spectra

The comparison in the Raman spectra of the as-grown AZO layers, annealed AZO layers and ZnO NWs were also performed, as shown in **Figure 5.13**. Besides the signals from Si substrates, the E_2^{low} and E_2^{high} modes of ZnO wurtzite structure are detected at 99 and 438 cm^{-1} on all samples. The spectra of AZO layers before and after annealing are similar (**Figures 5.13a-b**), which again shows no evidence of change in their structures. In **Figure 5.13c**, the remarkably higher intensities of these two lines on ZnO NWs emphasized their superior crystallinity compared to AZO layers. It can also be seen that the strong signals of C-C bonds only appear on ZnO NWs grown by MOCVD process, but not in AZO films grown by ALD process despite the DEZn precursors were used in both techniques. This indicated that those carbon impurities were mostly removed after the ALD process and hence they do not contribute to the electrical conductivity of the AZO layers.

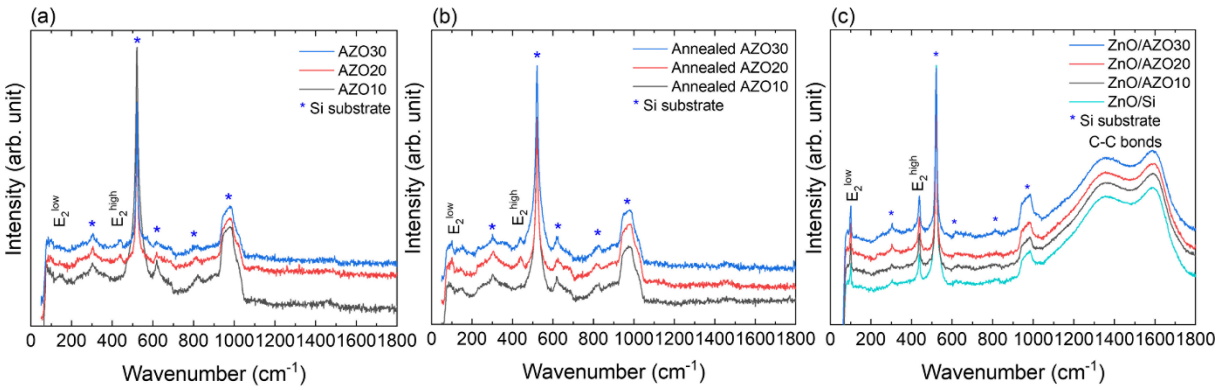

Figure 5.13: Raman scattering spectra of (a) as-grown AZO thin films grown by ALD, (b) annealed AZO thin films and (c) ZnO NWs grown by PLI-MOCVD on Si substrate and AZO layers. The intensity was plotted in logarithmic scale.

Optical transmittance of ZnO NWs/AZO thin film structure

The ZnO NW growth by PLI-MOCVD was also performed on AZO20 layer, which was deposited on quartz by ALD. The optical transmittance of this sample was measured and shown in **Figure 5.14.** Compared to the as-grown AZO20 thin film, it can be seen that the optical transmittance decreased after the ZnO NWs were grown on the AZO20 layer. However, this ZnO NWs/AZO20 layer

structure still has a high average transmittance in the range of 400 – 700 nm, which is 81.2%. This shows that the ZnO NWs/AZO20 layer structure is suitable for visible-blind and transparent optical applications.

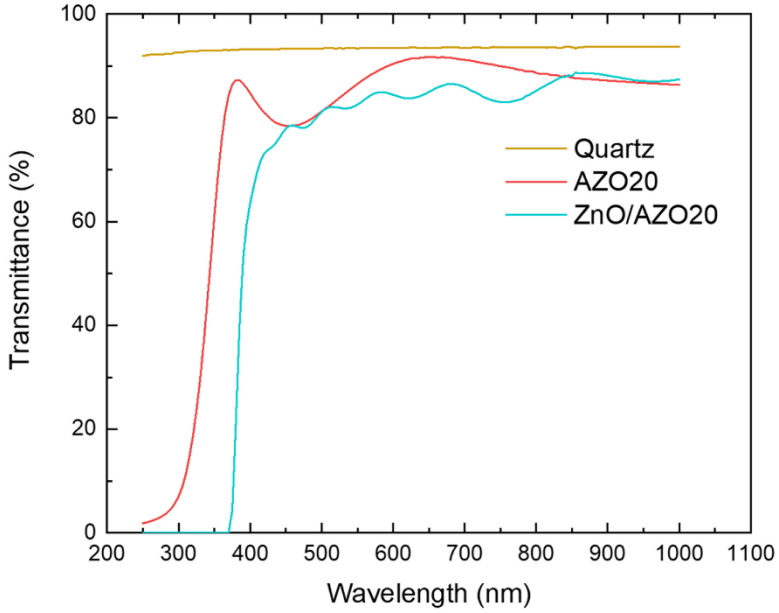

Figure 5.14: The optical transmittance of AZO20 thin film and ZnO NWs/AZO20 thin film grown on quartz. The AZO20 thin film was first grown on quartz by ALD process, the ZnO NWs were then grown on AZO20 thin film by PLI-MOCVD process.

Piezoelectric responses of ZnO NWs on AZO thin films

The PFM measurements were performed on ZnO NWs grown on AZO layers and Si substrates using 2 setups. In the 1st setup, the samples were in contact with the chuck of the AFM-PFM system (**Figure 5.15a**). The voltage was applied directly on the heavily doped Si substrate, through the AZO layer at the bottom and the conductive tip at the top. This setup is also the one that was used for all PFM measurements on ZnO deposited on the highly doped Si susbtrates demonstrated in previous Chapter 3 and 4, in which the highly doped Si substrates were used as the bottom electrodes. However, the objective of Chapter 5 is to integrate the AZO layer as a bottom electrode. To verify that our AZO thin films are able to be used as bottom electrodes for the piezoelectric applications, a 2nd setup was used for the PFM measurement. In this new setup, the heavily doped Si substrate was electrically isolated with the chuck by an empty plastic box placed between them (**Figure 5.15b**). The voltage was applied on the AZO layer through the copper (Cu) tape. Thus, the voltage was applied directly to the AZO layer instead of indirectly through the Si substrate. Then, the datacube PFM was performed.

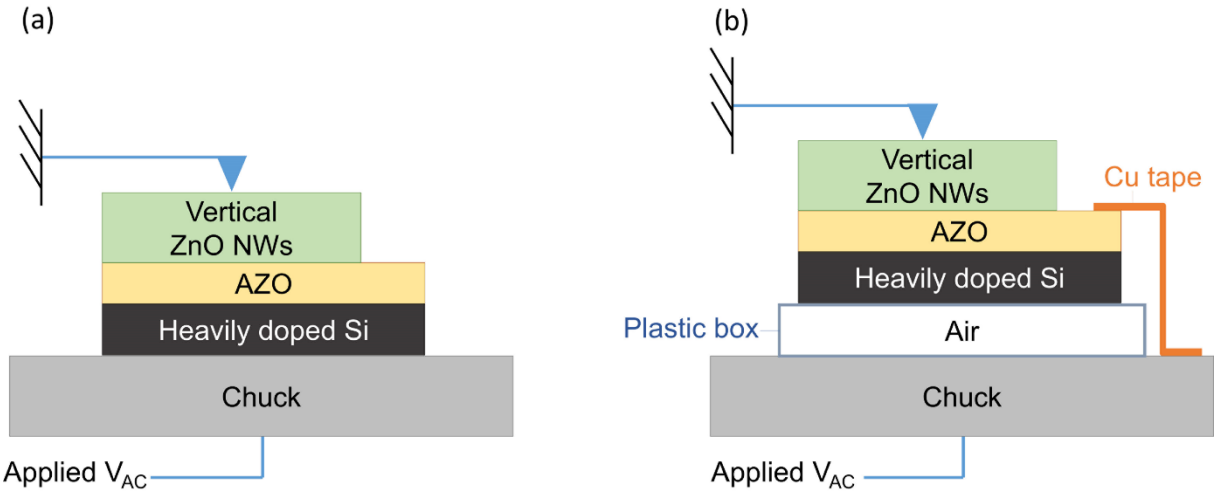

Figure 5.15: Schematic of the setups for PFM measurements. (a) The 1st setup, the voltage applied to the ZnO NW array through the heavily doped Si substrate and AZO layer. (b) The 2nd setup, the voltage applied to the ZnO NW array through the Cu tape and AZO layer.

After the datacube PFM measurement, the piezoelectric amplitude and phase images were recorded. Similar to our results shown in the previous Chapters, the phase responses of ZnO NWs grown by PLI-MOCVD are positive indicating the Zn-polarity. The negative phase responses are the artifacts generated when the AFM scans on the void between NWs. A data treatment was carried out to remove these artifact signals. In this data treatment, the data point with phase value > 50° was kept, while other data points were removed.

Figure 5.16 shows the amplitude histograms after data treatment of NWs on AZO layers measured in the 1st setup, where the voltage was applied through the Si substrate and the AZO layer. The results reveal that while the amplitude is varied from 0 to 37 pm on all NW samples, their amplitude distributions are different. In the histogram of NWs grown on Si substrate (**Figure 5.16a**), the piezoelectric amplitude with the highest count, namely most frequent value of the distribution (the mode), is around 15 – 19 pm. Interestingly, this mode value of NWs grown on all three AZO layers is higher than on Si substrates, which is around 23 – 27 pm. Regarding their structure property analysis, the XRD results showed that the NWs on Si substrates have a very high *c*-axis orientation similar to NWs on other AZO layers. All the NWs on Si substrates and AZO layers were grown simultaneously in the chamber. Thus, the difference in the piezoelectric amplitude was not caused by the growth atmosphere. Regarding the electrodes, because the resistivity of Si and AZO layer are similar at around 2 – 5 x 10^{-3} Ω.cm, the efficient applied voltage at the bottom electrical contact should be the same for all samples during the PFM measurement. However, the reason could be due to the difference between the Si substrate/ZnO NWs interface and the AZO layer/ZnO NWs interface. In the work of K. Pradel et al., they demonstrated that the piezoelectric output was significantly increased by forming a ZnO p-n homojunction.[75] The junction was formed by two ZnO layers containing different dopants, leading to creation of a depletion layer that interferes with the movement of free electrons inside ZnO to the electric pole. Thus, the screening effect was decreased, leading to increasing the piezoelectric efficiency. Similarly, Q. Wang et al. showed that free electrons can be trapped at ZnO-CuO heterojunction, resulting in enhancing the piezoelectric output.[92] The

formation of depletion layer between the ZnO and AZO layers was demonstrated by G. Li et al..[230] In our work, a depletion layer may also be created at the AZO/ZnO interface due to the fact that there are a large difference in the doping density between the AZO thin film and undoped ZnO NWs. This depletion layer could prevent the free electrons inside ZnO from coming to the bottom electrode, leading to reducing screening effect and increasing the piezoelectric amplitude. Among AZO layers, the mode value of NWs on AZO20 and AZO30 layer consists of 48.2 % of their distribution, while it is only 30.9 % on AZO10 layer. **Figure 5.16d** shows that the piezoelectric amplitude histogram on AZO10 layer has a broad distribution, which stretches to the low piezoelectric amplitude value. This can be explained by the randomly inclined NWs on this layer. When the AFM tip approached the NW on AZO20 and AZO30 layers during the datacube PFM measurement, it was in contact with the NW tip and the applied electric field direction coincided with the polar *c*-axis of the NWs thanks to their well-aligned NW array. In contrast, since there are many inclined NWs on AZO layer, the AFM tip can touch the NWs at their sidewall. At that position, the piezoelectric measurement was carried out on the ZnO semi-polar plane instead of the polar plane, resulting in the lower piezoelectric amplitude.

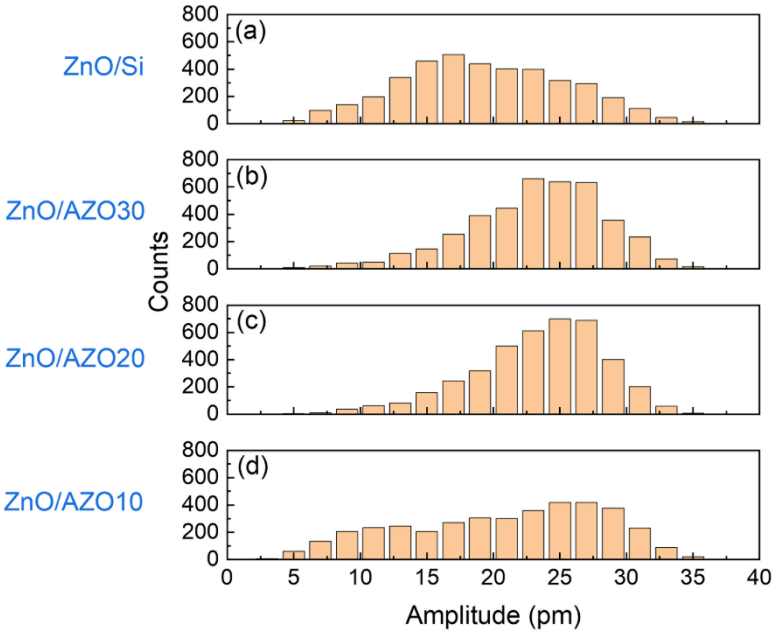

Figure 5.16: Piezoelectric amplitude histogram after data treatment of ZnO NWs grown by PLI-MOCVD on (a) Si substrate, (b) AZO30, (c) AZO20 and (d) AZO10 layers. The PFM measurements were performed in the 1st setup.

Figure 5.17 shows the piezoelectric amplitude histograms after data treatment of NWs on AZO layers measured in the 2nd setup, where the bottom electrical contact only went through the Cu tape and AZO layer while the Si substrates were isolated. The amplitude histograms of NWs on AZO30 and AZO20 layers in **Figures 5.17a-b** are similar to their histograms in **Figures 5.16b-c**.

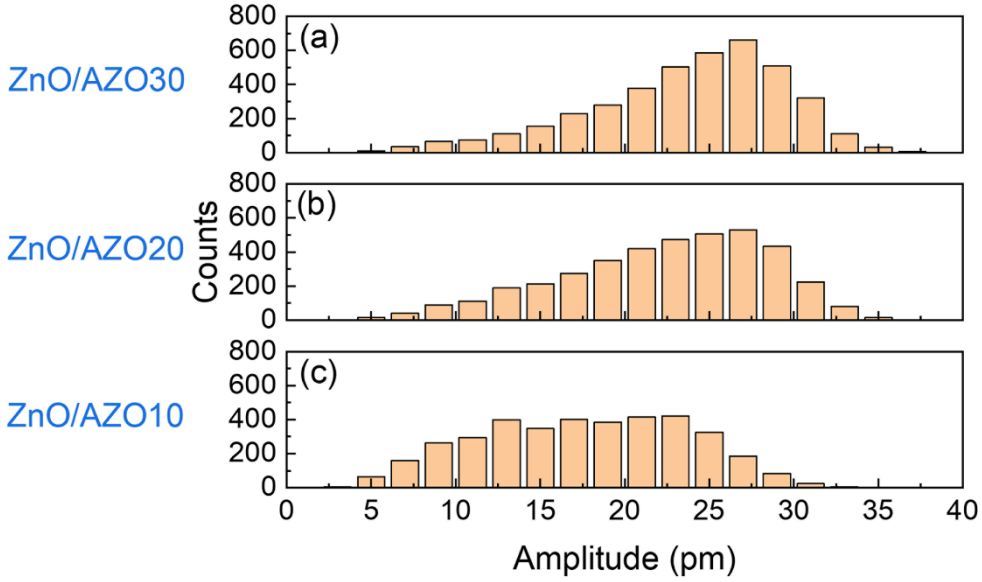

Figure 5.17: Piezoelectric amplitude histogram after data treatment of ZnO NWs grown by PLI-MOCVD on (a) AZO30, (b) AZO20 and (c) AZO10 layers. The PFM measurements were performed in the 2nd setup.

The average amplitude of all samples measured in the 1st and the 2nd setups were calculated and show in **Figure 5.18**. In the 1st setup, the piezoelectric amplitude values are 19.4, 23.2, 23.4 and 20.7 pm for NWs grown on Si substrate, AZO30, AZO20 and AZO10 layers, respectively. The average piezoelectric amplitude of NWs grown on AZO30 and AZO20 layers in the 2nd setup are 23.7 and 22.4 pm, respectively, which are similar to their values measured in the 1st setup. These piezoelectric amplitude values are higher compared to those of NW arrays shown in **Section 4.2** and are also the highest values obtained so far. Correspondingly, the highest piezoelectric coefficient d_{33} of 4.7 pm/V is deduced, considering the 5 V voltage applied during the PFM. The more uniform and higher average amplitude values on AZO30 and AZO20 layers suggest that they can have better piezoelectric performance. The similar results measured by 2 setups not only shows that a good electrical contact between the copper tape and the AZO layer was established, but also indicates that those AZO layers have good electrical conductivity to be used as an electrode in piezoelectric applications. On the other hand, **Figure 5.17c** shows that the amplitude of NWs on the AZO10 layer measured in the 2nd setup also has a similar broad distribution compared to the 1st setup due to the inclined NWs (**Figure 5.16d**). However, its piezoelectric amplitude distribution is shifted to a lower value, and the average amplitude is also decreased to 17.6 pm (**Figure 5.18**). Since the resistivity of AZO10 layer is similar to AZO20 and AZO30 layers after the NWs growth (around 5 x 10^{-3} Ω.cm), the reason could be due to the poor electrical contact between copper tape and the AZO10 layer that leaded to a drop voltage at the bottom electrode and hence a lower piezoelectric amplitude. This result shows that a good electrical contact is important for piezoelectric devices.

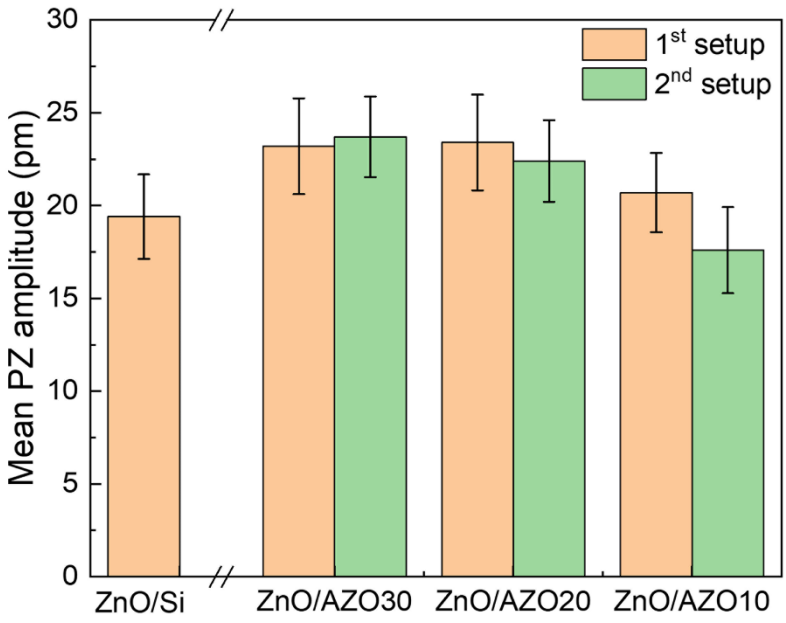

Figure 5.18: Mean piezoelectric amplitudes after data treatment of ZnO NWs grown by PLI-MOCVD on heavily doped p-type Si substrate, AZO30, AZO20 and AZO10 layers.

5.2 Summary of the chapter

In summary, we have demonstrated the AZO thin film depositions using different Zn/Al precursor cycle ratio in ALD process. These AZO layers were then used as platforms for the ZnO NW growth by PLI-MOCVD process. By varying the Al dopant concentration during the ALD process, different AZO morphologies were observed. The XRD analysis revealed that the *c*-axis orientation of thin film was improved when the Al dopant was increased until a certain point. Simultaneously, the charge concentration was also increased with the incorporation of Al dopants as shallow donors inside the ZnO structure, leading to increasing the conductivity. With further doping, the AZO thin film crystallinity was degraded and became partially crystallized film due to the large distortion inside the crystal lattice. The conductivity was also decreased in partially crystallized AZO thin film. Moreover, the high transparency of AZO thin films and ZnO NWs in the visible light region shows that they are good candidates for optoelectronic devices.

The ZnO NW growth direction strongly depended on the orientation of the AZO layer used as a platform. This in turn affected the piezoelectric amplitude distribution of the ZnO NW array. Interestingly, the PFM measurement also presented that the piezoelectric amplitude of ZnO NWs grown on the AZO layer was higher compared to those grown directly on Si substrate. The reason could be due to a depletion layer formation at the AZO layer/ZnO NW interface, which reduced the free electron movement inside ZnO NWs, leading to increase the piezoelectric efficiency. We also demonstrated that the ZnO NWs grown on a highly *c*-axis oriented AZO layer can have a good alignment similar to when they were grown on ZnO substrates. These results show that a piezoelectric device using only eco-friendly materials can be fabricated by the ALD and PLI-MOCVD processes, which are compatible with industrial scale production. At the bottom, the AZO electrode with high *c*-axis orientation and high conductivity can be obtained by using decent Al dopant

concentration. At the top, the vertically well-aligned ZnO NW array can be formed thanks to the good orientation of the AZO layer, leading to enhancing the amplitude and uniformity of its piezoelectric response. The highest piezoelectric coefficient in this PhD thesis is obtained on these ZnO NW array with the eco-friendly AZO layer as a bottom electrode. The optimization in ZnO and AZO growth processes combining with doping method can be done in future work to further improve the piezoelectric performance. Besides, more investigations on the electrical properties of ZnO NWs and ZnO NWs/AZO layer structures are also necessary before integrating them into devices.

Conclusion and perspectives

In conclusion, we have demonstrated the ZnO thin film and nanowire growths by using PLI-MOCVD process with different parameters, namely the growth temperature, the O- and Zn-precursor flow rates along with their O_2/DEZn molar flow rate ratio, and the substrates. By using different characterization techniques, the ZnO structural, electrical, and piezoelectric properties affected by the growth conditions are investigated. The strong correlations of properties are also revealed.

First, the effect of the growth temperature was studied. By increasing the growth temperature from 400 to 750 °C, the SEM images shows that the ZnO morphology transformed from a stack thin film to a vertical NW array. The structural analysis by XRD and Raman spectra indicate the wurtzite structure of ZnO thin films and nanowires with the preferential growth direction along the *c*-axis. Along with the transition from thin film to nanowires, the *c*-axis orientation is improved, and the internal strains are relaxed. By analyzing the TEM images, the growth of ZnO NWs on the Si substrate can be described as a self-assembled process: The strong Zn and O atom desorption combined with the highly *c*-axis oriented growth at high temperature led to the nucleation and formation of isolated islands, on which the *c*-axis orientation prevails over other directions. Thanks to the highly *c*-axis oriented growth and the enhanced diffusion length of atoms at high growth temperature, the elongation of NWs was continued on those islands in the vertical direction normal to the substrate. The structural and optical analysis also implied the presence of defects inside ZnO structures such as C and Al impurities or stacking faults, which could affect the electrical as well as the piezoelectric performance of ZnO. A direct comparison in piezoelectric responses of thin films and nanowires with the same thickness/length was also performed using PFM, showing that the average piezoelectric coefficient on the NW array is higher than on thin films. Moreover, the NW array also has a Zn-polar uniformity while the thin film has both Zn- and O-polar domains. These results show that the PLI-MOCVD growth at high temperatures can lead to the formation of ZnO NWs with better piezoelectric performance compared to its thin film counterpart.

After the study on temperature growth, the effect of the post-annealing at different temperatures on ZnO properties was also investigated. The thin films grown at 500 °C were annealed under O_2 atmosphere at temperatures ranging from 600 to 1000 °C, resulting in the crystallization. Similar to the growth temperature, the *c*-axis orientation and the crystallinity are improved when the annealing temperature is raised. The carbon impurities from the PLI-MOCVD process are also removed after the annealing at 800 °C or higher temperature. The resistivity of the ZnO thin film is also increased with the annealing temperature. Correspondingly, the average piezoelectric coefficient on Zn-polar domain is increased from 1.8 pm/V in as-grown thin film to 2.7 pm/V in annealed thin films at 800 °C or higher temperatures. The enhancement of the piezoelectric coefficient after annealing can be due to the improvement in the structural orientation along the polar *c*-axis and the decrease of screen effect caused by free charge carriers that reduce the piezoelectric potential. Although the piezoelectric coefficient of annealed thin films is still lower compared to the NW array (4.4 pm/V) grown in the previous experiment, this result shows the possibility to further increase the piezoelectric coefficient of ZnO thin films after the growth by using

post-annealing process. Interestingly, the PFM images reveal that there is a change in piezoelectric polar domains on the ZnO thin film along with the grain coarsening and growth process after the annealing. The annealing at 600 °C leads to the development of O-polar grains due to its lower energy, but then the Zn-polar grains prevails at higher annealing temperature thanks to its higher grain boundary mobility. This again shows that the Zn-polarity is more stable than O-polarity at high temperature. The post-annealing under O_2 atmosphere at higher temperature improves not only the piezoelectric coefficient but also the Zn-polar uniformity of the ZnO thin film.

After that, the investigation on the effect of precursor flow rates on the ZnO properties was performed. At first, the O_2 and DEZn flow rates were sequentially varied while the growth temperature was kept at 500 °C. The results show that all ZnO deposits are thin films regardless of the flow rate conditions. The growth time was adjusted in order to have thin films with the same thickness, so that the influence of the film thickness is decoupled from this investigation. The evolution of growth rate with the flow rate condition indicates that the ZnO growth is limited by the Zn-reactant. The SEM images of thin films display different morphologies, evidencing the impact of flow rate conditions on the ZnO growth process. The XRD shows that all thin films have a wurtzite structure with good *c*-axis orientation. However, the PFM images revealed that some thin films have a preferential growth in the c^+-axis direction (Zn-polarity), while other thin films have a preferential growth in the c^--axis direction (O-polarity). Different from the previous investigations about the temperature effect, the thin film with O-polar predominance was formed in certain flow rate conditions, indicating the ability to switch between the Zn- and O-polarities of the ZnO thin film by controlling the growth parameters. This change of polarity with the flow rate conditions can be attributed to the variation of the oxygen chemical potential during the PLI-MOCVD growth process, influencing the surface energies of ZnO crystalline planes as well as its growth directions. The Raman spectra analysis shows that the O/Zn atom ratio in the composition of ZnO thin film is strongly correlated to the O_2/DEZn flow rate ratio, which again implies the effect of oxygen chemical potential in the growth environment. Furthermore, the results of structural, electrical and piezoelectric characterizations also express the strong correlations of these properties. By comparing the piezoelectric response images with the topography and the morphology image, it is revealed that the Zn-polar grains have hexagonal or round shape, while the O-polar grains are composed of large-irregular-shape-clusters comprising many smaller grains. Other comparisons of PFM measurement with the XRD and resistivity also show that there are differences in the growth mechanism, the structural orientation, microstructural defects and the resistivity between two polarities. In particular, it is suggested that the O-polar domains could contain more donor impurities that screen the piezoelectric potential, as compared to the Zn-polar domains. This is supported by the lower resistivity of predominant O-polar thin film and the lower piezoelectric amplitude response on O-polar domains regardless of the flow rate conditions. Nevertheless, these results present the large ability of the PLI-MOCVD system to tune the polarity the ZnO growth as well as its other properties. The higher piezoelectric coefficient on the Zn-polar domains compared to the O-polar domains shows that the ZnO structure with Zn-polar uniformity is more favorable for higher piezoelectric efficiency.

Then, the effect of O_2 and DEZn flow rates on ZnO growth was studied with the growth temperature maintained at 700 °C. At this temperature, all growths result in the formation of vertical ZnO NW arrays regardless of the flow rate conditions. In addition, the PFM results show that all these NWs have a Zn-polarity, which is different from the thin film growths at 500 °C. This again indicates the preferential growth along the c^+-direction at high temperature. The Zn-polar ZnO NWs were also grown on the identified Zn- and O-polar ZnO substrates, verifying that the NW grown by our PLI-MOCVD process is limited to Zn-polarity. Despite that, the uniform Zn-polar ZnO NW array is favourable for the piezoelectric applications. Besides, the piezoelectric coefficient of NWs exhibits a strong correlation with their geometry. On NW arrays with the length below than 800 nm, the piezoelectric coefficient is low regardless of the diameter due to the lower *c*-axis oriented structure. Among NW arrays with longer length, the piezoelectric coefficient is higher on the NW arrays with the diameter lower than 65 nm thanks to the more efficient depletion of free electrons at the NW side-wall. Nevertheless, the NWs grown at 700 °C have higher piezoelectric coefficients (2.2 – 3.8 pm/V) compared to those of ZnO thin films (1.6 – 2.2 pm/V) grown with the same PLI-MOCVD process as well the growth conditions. This again indicates the superior piezoelectric efficiency of ZnO NWs compared to thin films.

Finally, the possibility of using AZO thin film grown by the ALD process as a bottom electrode was investigated. The Al-dopant concentration was varied during the ALD growth, which not only changes the structural and electrical properties of AZO thin films, but also affects the following ZnO NW growth by PLI-MOCVD process. Different AZO morphologies along with the large variation of structural orientation were observed when the Al dopant concentration is changed. The residual strain of the AZO thin film is increased with the Al-content, implying the incorporation of Al atoms into the ZnO lattice that causes the lattice distortion. Simultaneously, the charge carrier density and mobility as well as the resistivity are also varied with the Al dopant concentration. By adding a sufficient Al dopant amount, the *c*-axis orientation of AZO thin film is improved and its conductivity is also enhanced. An over-doping causes the degradation in both crystallinity and conductivity of AZO thin film. As a growth platform, the orientation of the AZO thin film affected the ZnO NW growth direction since the AZO and ZnO lattices have an epitaxial relation, which is different from the Si substrate. The ZnO growth on a highly *c*-oriented AZO thin film leads to the formation of a well-vertically aligned ZnO NW array, which is nearly as good as those NWs grown on single crystal ZnO substrates. In contrast, the growth on a poorly oriented AZO thin film results in a randomly inclined ZnO NW array. The ZnO NW array with good vertical alignment exhibits a more uniform piezoelectric amplitude. Meanwhile, the randomly inclined ZnO NW array has a broad piezoelectric response distribution, in which the amplitude stretches to lower value due to the inclined ZnO NWs, resulting in decreasing the average piezoelectric efficiency. Interestingly, a comparison with the piezoelectric coefficient of ZnO NWs grown directly on the highly doped Si substrate shows that the ZnO NWs grown on the AZO thin films exhibit higher values. This can be attributed to the effect of the AZO thin film/ZnO NW interface, which interferes with the screening effect that leads to increase the piezoelectric efficiency. The highest average piezoelectric coefficient of 4.7 pm/V is obtained on these ZnO NWs grown on the AZO thin film. These results show the high potential of using AZO thin films as an eco-friendly and efficient material for the electrode in the piezoelectric devices.

Moreover, the AZO thin films and the ZnO NWs also have a high transmittance in the visible light region, showing that they are also good candidates for optoelectronic devices.

Along with the investigations mentioned above, further improvement of the ZnO piezoelectric performance can be achieved by adding different dopants such as copper (Cu) or iron (Fe), which are non-critical elements. Beside the AZO thin film, other eco-friendly materials can also be used as electrodes to develop the piezoelectric devices such as fluorine-doped zinc oxide (FZO), graphene, etc. Furthermore, it is necessary to investigate the electrical and mechanical properties of ZnO NWs in order to integrate them into the piezoelectric devices. As shown by some optical characterization results in this thesis, an expanding study on the ZnO optical properties can help not only the advancement of its applications in piezoelectric but also other fields.

References

(1) Curie, J.; Curie, P. Développement Par Compression de l'électricité Polaire Dans Les Cristaux Hémièdres à Faces Inclinées. *Bull. la Société minéralogique Fr.* **1880**, *3*, 90–93.

(2) Gabriel Lippmann. The Principle of the Conservation of Electricity. *Ann. Chim. Phys.* **1881**, *24*, 145.

(3) Curie, J.; Curie, P. Contractions et Dilatations Produites Par Des Tensions Dans Les Cristaux Hémièdres à Faces Inclinées. *Comptes Rendus* **1881**, *93*, 1137–1140.

(4) Katzir, S. Who Knew Piezoelectricity? Rutherford and Langevin on Submarine Detection and the Invention of Sonar. *Notes Rec. R. Soc.* **2012**, *66*, 141–157.

(5) Kholkin, A.; Pertsev, N. A.; Goltsev, A. V. Piezoelectricity and Crystal Symmetry. *Piezoelectric Acoust. Mater. Transducer Appl.* **2008**, 17–38. https://doi.org/10.1007/978-0-387-76540-2.

(6) Std, A. IEEE Standard on Piezoelectricity. *IEEE Stand.* **1988**, 176–1987.

(7) Falconi, C.; Mantini, G.; D'Amico, A.; Ferrari, V. Modeling of Piezoelectric Nanodevices. In *Piezoelectric Nanomaterials for Biomedical Applications*; 2012; pp 93–133.

(8) Ballato, A. Basic Material Quartz and Related Innovations. In *Piezoelectricity*; 2008; pp 9–35.

(9) Acosta, M.; Novak, N.; Rojas, V.; Patel, S.; Vaish, R.; Koruza, J.; Rossetti, G. A. J.; J., R. BaTiO3-Based Piezoelectrics: Fundamentals, Current Status, and Perspectives. *Appl. Phys. Rev.* **2017**, *4*, 041305. https://doi.org/10.1063/1.4990046.

(10) Leontsev, S. O.; Eitel, R. E. Progress in Engineering High Strain Lead-Free Piezoelectric Ceramics. *Sci. Technol. Adv. Mater.* **2010**, *11*, 044302. https://doi.org/10.1088/1468-6996/11/4/044302.

(11) Bechmann, R. Elastic, Piezoelectric, and Dielectric Constants of Polarized Barium Titanate Ceramics and Some Applications of the Piezoelectric Equations Rudolf. *J. Acoust. Soc. Am.* **2017**, *28*, 347. https://doi.org/10.1121/1.1908324.

(12) Panda, P. K.; Sahoo, B. PZT to Lead Free Piezo Ceramics: A Review. *Ferroelectrics* **2015**, *474* (1), 128–143. https://doi.org/10.1080/00150193.2015.997146.

(13) Panda, P. K. Review : Environmental Friendly Lead-Free Piezoelectric Materials. *J. Mater. Sci.* **2009**, *44*, 5049–5062. https://doi.org/10.1007/s10853-009-3643-0.

(14) Ibn-mohammed, T.; Reaney, I. M.; Koh, S. C. L.; Acquaye, A.; Sinclair, D. C.; Randall, C. A.; Abubakar, F. H.; Smith, L.; Schileo, G.; Ozawa-meida, L. *Life cycle assessment and environmental profile evaluation of lead-free piezoelectrics in comparison with lead zirconate titanate*. Journal of the European Ceramic Society. https://doi.org/10.1016/j.jeurceramsoc.2018.06.044.

(15) Wani, A. L.; Ara, A.; Usmani, J. A. Lead Toxicity : A Review. *Interdiscip. Toxicol.* **2015**, *8* (2), 55–64. https://doi.org/10.1515/intox-2015-0009.

(16) U.S. Geological Survey. *Mineral Commodity Summaries 2020*; 2020.

(17) Zhang, W.; Yang, J.; Wu, X.; Hu, Y.; Yu, W.; Wang, J.; Dong, J.; Li, M.; Liang, S.; Hu, J.; Kumar, R. V. A Critical Review on Secondary Lead Recycling Technology and Its Prospect. *Renew. Sustain. Energy Rev.* **2016**, *61*, 108–122.

(18) ILZSG December 2021. *International Lead and Zinc Study Group*; 2021.

(19) Karaki, T.; Yan, K.; Miyamoto, T.; Adachi, M. Lead-Free Piezoelectric Ceramics with Large Dielectric and Piezoelectric Constants Manufactured from BaTiO3 Nano-Powder. *Jpn. J. Appl. Phys.* **2007**, *46* (4), L97–L98. https://doi.org/10.1143/JJAP.46.L97.

(20) Wada, S.; Takeda, K.; Muraishi, T.; Kakemoto, H.; Tsurumi, T.; Kimura, T.; Takeda, K.; Muraishi, T.; Kakemoto, H.; Tsurumi, T. Domain Wall Engineering in Lead-Free Piezoelectric Grain-Oriented Ceramics Domain Wall Engineering in Lead-Free Piezoelectric. *Ferroelectrics* **2008**, *373* (1), 11–21. https://doi.org/10.1080/00150190802408531.

(21) Roscow, J. I.; Lewis, R. W. C.; Taylor, J.; Bowen, C. R. Acta Materialia Modelling and Fabrication of Porous Sandwich Layer Barium Titanate with Improved Piezoelectric Energy Harvesting Fi Gures of Merit. *Acta Mater.* **2017**, *128*, 207–217. https://doi.org/10.1016/j.actamat.2017.02.029.

(22) Wei, H.; Wang, H.; Xia, Y.; Cui, D.; Shi, Y.; Dong, M.; Liu, C.; Ding, T.; Zhang, J.; Ma, Y.; Wang, N.; Wang, Z.; Sun, Y.; Wei, R.; Guo, Z. An Overview of Lead-Free Piezoelectric Materials and Devices. *J. Mater. Chem. C* **2018**, *6* (46), 12446. https://doi.org/10.1039/c8tc04515a.

(23) Subbarao, E. C. A Family of Ferroelectric Bismuth Compounds. *J. Phys. Chem. Solids* **1962**, *23* (6), 665–676. https://doi.org/10.1016/0022-3697(62)90526-7.

(24) Adhikary, P.; Garain, S.; Mandal, D. The Co-Operative Performance of a Hydrated Salt Assisted Sponge like P(VDF-HFP) Piezoelectric Generator: An Effective Piezoelectric Based Energy Harvester. *Phys. Chem. Chem. Phys.* **2015**, *17* (11), 7275–7281. https://doi.org/10.1039/c4cp05513f.

(25) Zhang, W.; Wang, J.; Gao, P.; Tan, S.; Zhu, W.; Zhang, Z. Synthesis of Poly(Vinylidene Fluoride–Trifluoroethylene) via a Controlled Silyl Radical Reduction of Poly(Vinylidene Fluoride–Chlorotrifluoroethylene). *J. Mater. Chem. C* **2017**, *5* (26), 6433–6441. https://doi.org/10.1039/c7tc01051f.

(26) Sriphan, S.; Nawanil, C.; Vittayakorn, N. Influence of Dispersed Phase Morphology on Electrical and Fatigue Properties of BaTiO3/PDMS Nanogenerator. *Ceram. Int. J.* **2018**, *44*, S38–S42. https://doi.org/10.1016/j.ceramint.2018.08.264.

(27) Bairagi, S.; Ali, S. W. A Unique Piezoelectric Nanogenerator Composed of Melt-Spun PVDF/KNN Nanorod-Based Nanocomposite Fibre. *Eur. Polym. J.* **2019**, *116*, 554–561.

(28) Park, I. W.; Kim, K. W.; Hong, Y.; Yoon, H. J.; Lee, Y.; Gwak, D. Recent Developments and Prospects of M13- Bacteriophage Based Piezoelectric Energy Harvesting Devices. *Nanomaterials* **2020**, *10* (1), 93.

(29) Shin, D.; Han, J.; Kim, W.; Kim, E. Bioinspired Piezoelectric Nanogenerators Based on Vertically Aligned Phage Nanopillars. *Energy Environ. Sci.* **2015**, *8* (11), 3198–3203. https://doi.org/10.1039/c5ee02611c.

(30) Kholkin, A.; Amdursky, N.; Bdikin, I.; Gazit, E.; Rosenman, G. Strong Piezoelectricity in Bioinspired Peptide Nanotubes. *ACS Nano* **2010**, *4* (2), 610–614. https://doi.org/10.1021/nn901327v.

(31) Zhang, Y.; Liu, Y.; Wang, Z. L. Fundamental Theory of Piezotronics. *Adv. Mater.* **2011**, *23* (27), 3004–3013. https://doi.org/10.1002/adma.201100906.

(32) Fraga, M. A.; Furlan, H.; Pessoa, R. S.; Massi, M. Wide Bandgap Semiconductor Thin Films for Piezoelectric and Piezoresistive MEMS Sensors Applied at High Temperatures : An Overview. *Microsyst. Technol.* **2014**, *20*, 9–21. https://doi.org/10.1007/s00542-013-2029-z.

(33) Nguyen, Q. K.; Janos, R.; Zsolt, E. H.; Saeedeh, S.; Binderiya, O.; Janos, V. The Effect of Substrate Bias on the Piezoelectric Properties of Pulse DC Magnetron Sputtered AlN Thin Films. *J. Mater. Sci. Mater. Electron.* **2020**, *31*, 22833–22843. https://doi.org/10.1007/s10854-020-04810-9.

(34) Zúñiga-Pérez, J.; Consonni, V.; Lymperakis, L.; Kong, X.; Trampert, A.; Fernández-Garrido, S.; Brandt, O.; Renevier, H.; Keller, S.; Hestroffer, K.; Wagner, M. R.; Reparaz, J. S.; Akyol, F.; Rajan, S.; Rennesson, S.; Palacios, T.; Feuillet, G. Polarity in GaN and ZnO: Theory, Measurement, Growth, and Devices. *Appl. Phys. Rev.* **2016**, *3* (4). https://doi.org/10.1063/1.4963919.

(35) Le, A. T.; Ahmadipour, M.; Pung, S. A Review on ZnO-Based Piezoelectric Nanogenerators : Synthesis, Characterization Techniques, Performance Enhancement and Applications. *J. Alloys Compd.* **2020**, *844* (5), 156172. https://doi.org/10.1016/j.jallcom.2020.156172.

(36) Goel, S.; Kumar, B. A Review on Piezo-/ Ferro-Electric Properties of Morphologically Diverse ZnO Nanostructures. *J. Alloys Compd.* **2020**, *816*, 152491. https://doi.org/10.1016/j.jallcom.2019.152491.

(37) Consonni, V.; Lord, A. M. Polarity in ZnO Nanowires : A Critical Issue for Piezotronic and Piezoelectric Devices. *Nano Energy* **2021**, *83*, 105789. https://doi.org/10.1016/j.nanoen.2021.105789.

(38) Momida, H.; Teshigahara, A.; Oguchi, T. Strong Enhancement of Piezoelectric Constants in ScxAl1−xN: First-Principles Calculations. *AIP Adv.* **2016**, *6* (6), 065006.

https://doi.org/10.1063/1.4953856.
(39) Guy, I. L.; Muensit, S.; Goldys, E. M. Extensional Piezoelectric Coefficients of Gallium Nitride and Aluminum Nitride. *Appl. Phys. Lett.* **1999**, *75*, 4133.
(40) Lueng, C. M.; Chan, H. L. W.; Surya, C.; C. L. Choy. Piezoelectric Coefficient of Aluminum Nitride and Gallium Nitride. *J. Appl. Phys.* **2000**, *88* (9), 5360.
(41) Curtis, S. M.; Wolff, N.; Dengiz, D.; Lewitz, H.; Jetter, J.; Bumke, L.; Hayes, P.; Yarar, E.; Thormählen, L.; Kienle, L.; Meyners, D.; Quandt, E. Integration of AlN Piezoelectric Thin Fi Lms on Ultralow Fatigue TiNiCu Shape Memory Alloys. *J. Mater. Res.* **2020**, *35* (10), 1298. https://doi.org/10.1557/jmr.2020.106.
(42) Bernardini, F.; Fiorentini, V. First-Principles Calculation of the Piezoelectric Tensor d of III-V Nitrides. *Appl. Phys. Lett.* **2002**, *80* (22), 4145.
(43) Minary-Jolandan, M.; Bernal, R. A.; Kuljanishvili, I.; Parpoil, V.; Espinosa, H. D. Individual GaN Nanowires Exhibit Strong Piezoelectricity in 3D. *Nano Lett.* **2012**, *12* (2), 970–976.
(44) Karanth, D.; Fu, H. Large Electromechanical Response in ZnO and Its Microscopic Origin. *Phys. Rev. B* **2005**, *72* (6), 064116. https://doi.org/10.1103/PhysRevB.72.064116.
(45) Zhao, M.; Wang, Z.; Mao, S. X. Piezoelectric Characterization of Individual Zinc Oxide Nanobelt Probed by Piezoresponse Force Microscope. *Nano Lett.* **2004**, *4* (4), 587–590.
(46) Christman, J. A.; Woolcott, R. R.; Kingon, A. I.; Nemanich, R. J. Piezoelectric Measurements with Atomic Force Microscopy. *Appl. Phys. Lett.* **1998**, *73* (26), 3851–3853. https://doi.org/10.1063/1.122914.
(47) Ghosh, M.; Rao, M. G. Growth Mechanism of ZnO Nanostructures for Ultra-High Piezoelectric D33 Coefficient. *Mater. Express* **2013**, *3* (4), 319–327. https://doi.org/10.1166/mex.2013.1134.
(48) Wang, Z. L. Towards Self-Powered Nanosystems : From Nanogenerators to Nanopiezotronics. *Adv. Funct. Mater.* **2008**, *18*, 3553–3567. https://doi.org/10.1002/adfm.200800541.
(49) Masato, U.; Takaaki, M.; Yasuhiro, A.; Hiroshi, Y.; Umeda, K.; Morito, A. Increase in the Piezoelectric Response of Scandium-Doped Gallium Nitride Thin Films Sputtered Using a Metal Interlayer for Piezo MEMS Increase in the Piezoelectric Response of Scandium-Doped Gallium Nitride Thin Films Sputtered Using a Metal Interlayer Fo. *Appl. Phys. Lett.* **2019**, *114* (1), 012902. https://doi.org/10.1063/1.5066613.
(50) Yang, Y. C.; Song, C.; Wang, X. H.; Zeng, F.; Pan, F. Giant Piezoelectric Coefficient D33 in Ferroelectric Vanadium Doped ZnO Films. *Appl. Phys. Lett.* **2008**, *92* (1), 012907. https://doi.org/10.1063/1.2830663.
(51) Moezzi, A.; Mcdonagh, A. M.; Cortie, M. B. Zinc Oxide Particles : Synthesis , Properties and Applications. *Chem. Eng. J.* **2012**, *185–186*, 1–22. https://doi.org/10.1016/j.cej.2012.01.076.
(52) Kołodziejczak-radzimska, A.; Jesionowski, T. Zinc Oxide—From Synthesis to Application: A Review. *Materials (Basel).* **2014**, *7* (4), 2833–2881. https://doi.org/10.3390/ma7042833.
(53) Mostoni, S.; Milana, P.; Credico, B. Di; Arienzo, M. D.; Scotti, R. Zinc-Based Curing Activators : New Trends for Reducing Zinc Content in Rubber Vulcanization Process. *Catalysts* **2019**, *9*, 664. https://doi.org/10.3390/catal9080664.
(54) Özgür, Ü.; Alivov, Y. I.; Liu, C.; Teke, A.; Reshchikov, M. A.; Doğan, S.; Avrutin, V.; Cho, S. J.; Morkç, H. A Comprehensive Review of ZnO Materials and Devices. *J. Appl. Phys.* **2005**, *98* (4), 1–103. https://doi.org/10.1063/1.1992666.
(55) Frydrych, A.; Arcf, J.; Kasiura, K. Zinc: A Critical Importance Element. *J. Appl. Cosmetol.* **2004**, *22*, 1–13.
(56) Abendrot, M.; Kalinowska-Lis, U. Zinc-Containing Compounds for Personal Care Applications. *Int. J. Cosmet. Sci.* **2018**, *40*, 319–327. https://doi.org/10.1111/ics.12463.
(57) Liu, H.; Gan, W.; Rengel, Z.; Zhao, P. Effects of Zinc Fertilizer Rate and Application Method on Photosynthetic Characteristics and Grain Yield of Summer Maize. *J. Soil Sci. Plant Nutr.* **2016**, *16* (2), 550–562.
(58) Meylan, G.; Reck, B. K. The Anthropogenic Cycle of Zinc : Status Quo and Perspectives. *Resour. Conserv. Recycl.* **2017**, *123*, 1–10. https://doi.org/10.1016/j.resconrec.2016.01.006.

(59) Cossuet, T.; Appert, E.; Thomassin, J.; Consonni, V. Polarity-Dependent Growth Rates of Selective Area Grown ZnO Nanorods by Chemical Bath Deposition. *Langmuir* **2017**, *33* (25), 6269–6279. https://doi.org/10.1021/acs.langmuir.7b00935.
(60) Borah, D.; Baruah, M. K.; Saikia, P. P.; Senapoty, K. K.; Barua, M.; Singha, R. Structural Characterization and Surface Environment of ZnO Nanoflowers. *J. Mater. Environ. Sci.* **2016**, *7* (1), 331–336.
(61) Wang, Z. L. Zinc Oxide Nanostructures : Growth , Properties and Applications Applications. *J. Phys. Condens. Matter* **2004**, *16* (25), R829. https://doi.org/10.1088/0953-8984/16/25/R01.
(62) Janotti, A.; Walle, C. G. Van De. Native Point Defects in ZnO. *Phys. Rev. B* **2007**, *76*, 165202. https://doi.org/10.1103/PhysRevB.76.165202.
(63) Janotti, A.; Van De Walle, C. G. Fundamentals of Zinc Oxide as a Semiconductor. *Reports Prog. Phys.* **2009**, *72* (12). https://doi.org/10.1088/0034-4885/72/12/126501.
(64) McCluskey, M. D.; Jokela, S. J. Defects in ZnO. *J. Appl. Phys.* **2009**, *106* (7). https://doi.org/10.1063/1.3216464.
(65) Chris G. Van de Walle. Hydrogen as a Cause of Doping in Zinc Oxide. *Phys. Rev. Lett.* **2000**, *85* (5), 1012.
(66) Villafuerte, J.; Donatini, F.; Kioseoglou, J.; Sarigiannidou, E.; Chaix-pluchery, O.; Pernot, J.; Consonni, V. Zinc Vacancy − Hydrogen Complexes as Major Defects in ZnO Nanowires Grown by Chemical Bath Deposition. *J. Phys. Chem. C* **2020**, *124* (30), 16652−16662. https://doi.org/10.1021/acs.jpcc.0c04264.
(67) Mohammadbeigi, F.; Kumar, E. S.; Alagha, S.; Anderson, I.; Watkins, S. P. Carbon Related Donor Bound Exciton Transitions in ZnO Nanowires. *J. Appl. Phys.* **2014**, *116* (5). https://doi.org/10.1063/1.4892090.
(68) Frodason, Y. K.; Johansen, K. M.; Bjørheim, T. S.; Svensson, B. G. Zn Vacancy-Donor Impurity Complexes in ZnO. *Phys. Rev. B* **2018**, *97* (10), 104109. https://doi.org/10.1103/PhysRevB.97.104109.
(69) Znaidi, L.; Touam, T.; Vrel, D.; Souded, N.; Yahia, S. Ben; Brinza, O.; Fischer, A.; Boudrioua, A. AZO Thin Films by Sol-Gel Process for Integrated Optics. *Coatings* **2013**, *3* (3), 126–139. https://doi.org/10.3390/coatings3030126.
(70) Deschanvres, J. L.; Rey, P.; Delabouglise, G.; Labeau, M.; Joubert, J. C.; Peuzin, J. C. Characterization of Piezoelectric Properties of Zinc Oxide Thin Films Deposited on Silicon for Sensors Applications. *Sensors Actuators A. Phys.* **1992**, *33* (1–2), 43–45. https://doi.org/10.1016/0924-4247(92)80223-P.
(71) Li, S.; Zhao, X.; Bai, Y.; Li, Y.; Ai, C.; Wen, D. Fabrication Technology and Characteristics Research of the Acceleration Sensor Based on Li-Doped ZnO Piezoelectric Thin Films. *Micromachines* **2018**, *9* (4), 178. https://doi.org/10.3390/mi9040178.
(72) Gardeniers, J. G. E.; Rittersma, Z. M.; Burger, G. J. Preferred Orientation and Piezoelectricity in Sputtered ZnO Films. *J. Appl. Phys.* **1998**, *83* (12), 7844–7854. https://doi.org/10.1063/1.367959.
(73) Wang, X. B.; Song, C.; Li, D. M.; Geng, K. W.; Zeng, F.; Pan, F. The Influence of Different Doping Elements on Microstructure, Piezoelectric Coefficient and Resistivity of Sputtered ZnO Film. *Appl. Surf. Sci.* **2006**, *253* (3), 1639–1643. https://doi.org/10.1016/j.apsusc.2006.02.059.
(74) Bhatia, D.; Sharma, H.; Meena, R. S.; Palkar, V. R. A Novel ZnO Piezoelectric Microcantilever Energy Scavenger : Fabrication and Characterization. *Sens. Bio-Sensing Res.* **2016**, *9*, 45–52. https://doi.org/10.1016/j.sbsr.2016.05.008.
(75) Pradel, K. C.; Wu, W.; Ding, Y.; Wang, Z. L. Solution-Derived ZnO Homojunction Nanowire Films on Wearable Substrates for Energy Conversion and Self-Powered Gesture Recognition. *Nano Lett.* **2014**, *14* (12), 6897–6905. https://doi.org/10.1021/nl5029182.
(76) Tao, K.; Yi, H.; Tang, L.; Wu, J.; Wang, P.; Wang, N.; Hu, L. Surface & Coatings Technology Piezoelectric ZnO Thin Films for 2DOF MEMS Vibrational Energy Harvesting. *Surf. Coat. Technol.* **2019**, *359*, 289–295. https://doi.org/10.1016/j.surfcoat.2018.11.102.
(77) Fanni, L.; Aebersold, A. B.; Morales-masis, M.; Alexander, D. T. L.; Hessler-wyser, A.; Nicolay, S.

Increasing Polycrystalline Zinc Oxide Grain Size by Control of Film Preferential Orientation. *Cryst. Growth Des.* **2015**, *15* (12), 5886−5891.

(78) Cai, X.; Liang, H.; Xia, X.; Shen, R.; Liu, Y.; Luo, Y.; Du, G. Influence of Cu Dopant on the Structure and Optical Properties of ZnO Thin Films Prepared by MOCVD. *J. Mater. Sci. Mater. Electron.* **2015**, *26* (3), 1591–1596. https://doi.org/10.1007/s10854-014-2580-0.

(79) Fang, Z. B.; Yan, Z. J.; Tan, Y. S.; Liu, X. Q.; Wang, Y. Y. Influence of Post-Annealing Treatment on the Structure Properties of ZnO Films. *Appl. Surf. Sci.* **2005**, *241* (3–4), 303–308. https://doi.org/10.1016/j.apsusc.2004.07.056.

(80) Asghar, M.; Noor, H.; Awan, M. S.; Naseem, S.; Hasan, M. A. Post-Annealing Modification in Structural Properties of ZnO Thin Films on p-Type Si Substrate Deposited by Evaporation. *Mater. Sci. Semicond. Process.* **2008**, *11* (1), 30–35. https://doi.org/10.1016/j.mssp.2008.07.008.

(81) Daniel, G. P.; Justinvictor, V. B.; Nair, P. B.; Joy, K.; Koshy, P.; Thomas, P. V. Effect of Annealing Temperature on the Structural and Optical Properties of ZnO Thin Films Prepared by RF Magnetron Sputtering. *Phys. B Condens. Matter* **2010**, *405* (7), 1782–1786. https://doi.org/10.1016/j.physb.2010.01.039.

(82) Luo, J. T.; Yang, Y. C.; Zhu, X. Y.; Chen, G.; Zeng, F.; Pan, F. Enhanced Electromechanical Response of Fe-Doped ZnO Films by Modulating the Chemical State and Ionic Size of the Fe Dopant. *Phys. Rev. B* **2010**, *82* (1), 014116. https://doi.org/10.1103/PhysRevB.82.014116.

(83) Du, S.; Jia, Y.; Chen, S. T.; Zhao, C.; Sun, B.; Arroyo, E.; Seshia, A. A. A New Electrode Design Method in Piezoelectric Vibration Energy Harvesters to Maximize Output Power. *Sensors Actuators, A Phys.* **2017**, *263*, 693–701. https://doi.org/10.1016/j.sna.2017.06.026.

(84) Schmidt-Mende, L.; MacManus-Driscoll, J. L. ZnO - Nanostructures, Defects, and Devices. *Mater. Today* **2007**, *10* (5), 40–48. https://doi.org/10.1016/S1369-7021(07)70078-0.

(85) Consonni, V.; Briscoe, J.; Kärber, E.; Li, X.; Cossuet, T. ZnO Nanowires for Solar Cells : A Comprehensive Review. *Nanotechnology* **2019**, *30* (36), 362001.

(86) Wang, X.; Song, J.; Liu, J.; Wang, Z. L. Direct-Current Nanogenerator Driven by Ultrasonic Waves. *Science (80-.).* **2007**, *316* (5821), 102–105.

(87) Yang, R.; Qin, Y.; Dai, L.; Wang, Z. L. Power Generation with Laterally Packaged Piezoelectric Fine Wires. *Nat. Nanotechnol.* **2009**, *4* (1), 34–39. https://doi.org/10.1038/nnano.2008.314.

(88) Yan, X.; Li, W.; Aberle, A. G.; Venkataraj, S. Textured AZO for Thin-Film Si Solar Cells : Towards Understanding the Effect of AZO Film Thickness on the Surface Texturing Properties. *Procedia Eng.* **2016**, *139*, 134–139. https://doi.org/10.1016/j.proeng.2015.09.214.

(89) Tao, R.; Mouis, M.; Ardila, G. Unveiling the Influence of Surface Fermi Level Pinning on the Piezoelectric Response of Semiconducting Nanowires. *Adv. Electron. Mater.* **2017**, *4* (1), 1700299. https://doi.org/10.1002/aelm.201700299.

(90) Chang, Y.; Chen, J.; Yang, T. Excellent Piezoelectric and Electrical Properties of Lithium-Doped ZnO Nanowires for Nanogenerator Applications. *Nano Energy* **2014**, *8*, 291–296. https://doi.org/10.1016/j.nanoen.2014.06.014.

(91) Rafique, S.; Kasi, A. K.; Kasi, J. K.; Aminullah; Bokhari, M.; Shakoor, Z. Fabrication of Silver-Doped Zinc Oxide Nanorods Piezoelectric Nanogenerator on Cotton Fabric to Utilize and Optimize the Charging System. *Nanomater. Nanotechnol.* **2020**, *10*, 1–12. https://doi.org/10.1177/1847980419895741.

(92) Wang, Q.; Qiu, Y.; Yang, D.; Li, B.; Zhang, X.; Tang, Y.; Hu, L. Improvement in Piezoelectric Performance of a ZnO Nanogenerator by Modulating Interface Engineering of CuO-ZnO Heterojunction. *Appl. Phys. Lett.* **2018**, *113* (5). https://doi.org/10.1063/1.5035309.

(93) Jalali, N.; Briscoe, J.; Woolliams, P.; Stewart, M.; Weaver, P. M.; Cain, M.; Dunn, S. Passivation of Zinc Oxide Nanowires for Improved Piezoelectric Energy Harvesting Devices. *J. Phys. Conf. Ser.* **2013**, *476* (1). https://doi.org/10.1088/1742-6596/476/1/012131.

(94) Yao, B. D.; Chan, Y. F.; Wang, N. Formation of ZnO Nanostructures by a Simple Way of Thermal Evaporation. *Appl. Phys. Lett.* **2002**, *81* (4), 757. https://doi.org/10.1063/1.1495878.

(95) Carcia, P. F.; McLean, R. S.; Reilly, M. H.; Nunes Jr., G. Transparent ZnO Thin-Film Transistor

Fabricated by Rf Magnetron Sputtering. *Appl. Phys. Lett.* **2003**, *82* (7), 1117. https://doi.org/10.1063/1.1553997.

(96) Abdel-Fattah, E.; Elsayed, I. A.; Fahmy, T. Substrate Temperature and Laser Fluence Effects on Properties of ZnO Thin Films Deposited by Pulsed Laser Deposition. *J. Mater. Sci. Mater. Electron.* **2018**, *29* (23), 19942–19950. https://doi.org/10.1007/s10854-018-0124-8.

(97) Ogata, K.; Sakurai, K.; Fujita, S.; Fujita, S.; Matsushige, K. Effects of Thermal Annealing of ZnO Layers Grown by MBE. *J. Cryst. Growth* **2000**, *214–215*, 312–315.

(98) Tran, H. H.; Kim, Y.; Ternon, C.; Langlet, M.; Riassetto, D.; Lee, D. Lubricant Depletion-Resistant Slippery Liquid-Infused Porous Surfaces via Capillary Rise Lubrication of Nanowire Array. *Adv. Mater. Interfaces* **2021**, *8* (7), 2002058. https://doi.org/10.1002/admi.202002058.

(99) Liu, Y.; Gorla, C. R.; Liang, S.; Emanetoglu, N.; Lu, Y.; Shen, H.; Wraback, M. Ultraviolet Detectors Based on Epitaxial ZnO Films Grown by MOCVD. *J. Electron. Mater.* **2000**, *29* (1), 69–74.

(100) Ye, J. D.; Gu, S. L.; Qin, F.; Zhu, S. M.; Liu, S. M.; Zhou, X.; Liu, W.; Hu, L. Q.; Zhang, R.; Shi, Y.; Zheng, Y. D.; Ye, Y. D. MOCVD Growth and Properties of ZnO Films Using Dimethylzinc and Oxygen. *Appl. Phys. A Mater. Sci. Process.* **2005**, *81* (4), 809–812. https://doi.org/10.1007/s00339-004-2865-x.

(101) Guziewicz, E.; Godlewski, M.; Krajewski, T.; Wachnicki, Ł.; Szczepanik, A.; Kopalko1, K.; Wójcik-Głodowska, A.; Przeździecka, E.; Paszkowicz, W.; Łusakowska, E.; Kruszewski, P.; Huby, N.; Tallarida, G.; Ferrari, S. ZnO Grown by Atomic Layer Deposition : A Material for Transparent Electronics and Organic Heterojunctions ZnO Grown by Atomic Layer Deposition : A Material for Transparent Electronics and Organic Heterojunctions. *J. Appl. Phys.* **2009**, *105* (12), 122413. https://doi.org/10.1063/1.3133803.

(102) Fan, H. J.; Lee, W.; Hauschild, R.; Alexe, M.; Rhun, G. Le; Scholz, R.; Dadgar, A.; Nielsch, K.; Kalt, H.; Krost, A.; Zacharias, M.; Gösele, U. Template-Assisted Large-Scale Ordered Arrays of ZnO Pillars for Optical and Piezoelectric Applications. *Small* **2006**, *2* (4), 561–568. https://doi.org/10.1002/smll.200500331.

(103) Li, T.; Li, Y. T.; Qin, W. W.; Zhang, P. P.; Chen, X. Q.; Hu, X. F.; Zhang, W. Piezoelectric Size Effects in a Zinc Oxide Micropillar. *Nanoscale Res. Lett.* **2015**, *10* (1). https://doi.org/10.1186/s11671-015-1081-2.

(104) Zhang, K. M.; Zhao, Y. P.; He, F. Q.; Liu, D. Q. Piezoelectricity of ZnO Films Prepared by Sol-Gel Method. *Chinese J. Chem. Phys.* **2007**, *20* (6), 721–726. https://doi.org/10.1088/1674-0068/20/06/721-726.

(105) Scrymgeour, D. A.; Sounart, T. L.; Simmons, N. C.; Hsu, J. W. P. Polarity and Piezoelectric Response of Solution Grown Zinc Oxide Nanocrystals on Silver. *J. Appl. Phys.* **2007**, *101* (1), 014316. https://doi.org/10.1063/1.2405014.

(106) Scrymgeour, D. A.; Hsu, J. W. P. Correlated Piezoelectric and Electrical Properties in Individual ZnO Nanorods. *Nano Res.* **2008**, *8* (8), 2204–2209.

(107) Lim, T.; Ico, G.; Jung, K.; Bozhilov, K. N.; Nam, J.; Martinez-Morales, A. A. Crystal Growth and Piezoelectric Characterization of Mechanically Stable ZnO Nanostructure Arrays. *CrystEngComm* **2018**, *20* (38), 5688. https://doi.org/10.1039/c8ce00799c.

(108) Seomoon, K.; Lee, J.; Jang, P.; Jung, C.; Kim, K. Synthesis and Characterization of ZnO Thin Films Deposited via PE-MOCVD. *Curr. Appl. Phys.* **2011**, *11* (4), S26–S29. https://doi.org/10.1016/j.cap.2011.01.049.

(109) Manasevit, H. M. SINGLE-CRYSTAL GALLIUM ARSENIDE ON INSULATING SUBSTRATES. *Appl. Phys. Lett.* **1968**, *12* (4), 156.

(110) Manasevit, H. M.; Simpson, W. I. The Use of Metal-Organics in the Preparation of Semiconductor Materials. *J. Electrochem. Soc.* **1969**, *116* (12), 1725.

(111) Wang, C. A. Early History of MOVPE Reactor Development. *J. Cryst. Growth* **2019**, *506*, 190–200. https://doi.org/10.1016/j.jcrysgro.2018.10.004.

(112) Dupuis, R. D.; Dapkus, P. D.; Yingling, R. D.; Moudy, L. A. High-Efficiency GaAlAs/GaAs Heterostructure Solar Cells Grown by Metalorganic Chemical Vapor Deposition. *Appl. Phys.*

Lett. **1977**, *31* (3), 201.
(113) Amano, H.; Kito, M.; Hiramatsu, K.; Akasaki, I. P-Type Conduction in Mg-Doped GaN Treated with Low-Energy Electron Beam Irradiation (LEEBI). *Jpn. J. Appl. Phys.* **1989**, *28* (12), L2112–L2114.
(114) Li, J.; Gan, H.; Xu, Y.; Wang, C.; Gu, F. L.; Wang, G. Chemical Reaction-Transport Model of Oxidized Diethylzinc Based on Quantum Mechanics and Computational Fluid Dynamics Approaches. *RSC Adv.* **2018**, *8* (2), 1116–1123. https://doi.org/10.1039/c7ra11534b.
(115) Kaufmann, T.; Fuchs, G.; Webert, M.; Frieske, S.; Gackle., M. MOCVD Layer Growth of ZnO Using Adducts of Dimethyl- and Diethylzinc. *Cryst. Res. Technol.* **1989**, *24* (3), 269–274.
(116) Ye, J.; Gu, S.; Zhu, S.; Liu, S.; Liu, W.; Zhou, X.; Hu, L.; Zhang, R.; Shi, Y.; Zheng, Y. Comparative Study of Diethylzinc and Dimethylzinc for the Growth of ZnO. *J. Cryst. Growth* **2005**, *274* (3–4), 489–494. https://doi.org/10.1016/j.jcrysgro.2004.10.044.
(117) Cossuet, T.; Donatini, F.; Lord, A. M.; Appert, E.; Pernot, J.; Consonni, V. Polarity-Dependent High Electrical Conductivity of ZnO Nanorods and Its Relation to Hydrogen. *J. Phys. Chem. C* **2018**, *122* (39), 22767–22775. https://doi.org/10.1021/acs.jpcc.8b07388.
(118) Kirchner, C.; Gruber, T.; Reu, F.; Thonke, K.; Waag, A.; Gieβenb, C.; Heuken, M. MOVPE Growth of ZnO Using Various Oxygen Precursors. *J. Cryst. Growth* **2003**, *248*, 20–24.
(119) Oleynik, N.; Adam, M.; Krtschil, A.; J.Bl.asing; Dadgar, A.; Bertram, F.; Forster, D.; Diez, A.; Greiling, A.; Seip, M.; Christen, J.; Krost, A. Metalorganic Chemical Vapor Phase Deposition of ZnO with Different O-Precursors. *J. Cryst. Growth* **2003**, *248*, 14–19.
(120) Sallet, V.; Rommeluere, J. F.; Lusson, A.; Rivie, A. MOCVD Growth of ZnO on Sapphire Using Tert-Butanol. *Phys. Status Solidi* **2002**, *229* (2), 903–906.
(121) Chen, Y. J.; Shih, Y. Y.; Ho, C. H.; Du, J. H.; Fu, Y. P. Effect of Temperature on Lateral Growth of ZnO Grains Grown by MOCVD. *Ceram. Int.* **2010**, *36* (1), 69–73. https://doi.org/10.1016/j.ceramint.2009.06.018.
(122) Bang, K.; Hwang, D.; Lim, S.; Myoung, J. Effects of Growth Temperature on the Properties of ZnO / GaAs Prepared by Metalorganic Chemical Vapor Deposition. *J. Cryst. Growth* **2003**, *250* (3–4), 437–443. https://doi.org/10.1016/S0022-0248(02)02456-9.
(123) Park, J. Y.; Lee, D. J.; Yun, Y. S.; Moon, J. H.; Lee, B.; Kim, S. S. Temperature-Induced Morphological Changes of ZnO Grown by Metalorganic Chemical Vapor Deposition. *J. Cryst. Growth* **2005**, *276* (1), 158–164. https://doi.org/10.1016/j.jcrysgro.2004.11.326.
(124) Malandrino, G.; Blandino, M.; Fragala, M. E.; Losurdo, M.; Bruno, G. Relationship between Nanostructure and Optical Properties of ZnO Thin Films. *J. Phys. Chem. C* **2008**, *112* (26), 9595–9599.
(125) Montenegro, D. N.; Souissi, A.; Martinez-Tomas, C.; Munoz-Sanjose, V.; Sallet, V. Morphology Transitions in ZnO Nanorods Grown by MOCVD. *J. Cryst. Growth* **2012**, *359*, 122–128. https://doi.org/10.1016/j.jcrysgro.2012.08.038.
(126) Wu, C. C.; Wuu, D. S.; Lin, P. R.; Chen, T. N.; Horng, R. H. Effects of Growth Conditions on Structural Properties of ZnO Nanostructures on Sapphire Substrate by Metal – Organic Chemical Vapor Deposition. *Nanoscale Res. Lett.* **2009**, *4* (4), 377–384. https://doi.org/10.1007/s11671-009-9257-2.
(127) Chiu, H.-M.; Tsai, H.-J.; Hsu, W.-K.; Wu, J.-M. Experimental and Computational Insights in the Growth of Gallium-Doped Zinc Oxide Nanostructures with Superior Field Emission Properties. *CrystEngComm* **2013**, *15* (29), 5764–5775. https://doi.org/10.1039/c3ce40101d.
(128) Kar, J. P.; Das, S. N.; Choi, J. H.; Lee, T. I.; Myoung, J. M. Study of the Morphological Evolution of ZnO Nanostructures on Various Sapphire Substrates. *Appl. Surf. Sci.* **2010**, *256* (16), 4995–4999. https://doi.org/10.1016/j.apsusc.2010.03.040.
(129) Gruber, T.; Kirchner, C.; Waag, A. MOCVD Growth of ZnO on Different Substrate Materials. *Phys. Status Solidi Basic Res.* **2002**, *229* (2), 841–844. https://doi.org/10.1002/1521-3951(200201)229:2<841::AID-PSSB841>3.0.CO;2-J.
(130) Versteeg, V. A.; Avedisian, C. T.; Raj, R. Metalorganic Chemical Vapor Deposition by Pulsed Liquid Injection Using an Ultrasonic Nozzle: Titanium Dioxide on Sapphire from Titanium(IV)

Isopropoxide. *J. Am. Ceram. Soc.* **1995**, *78* (10), 2763–2768.
(131) Binnig, G.; Quate, C. F.; Gerber, C. Atomic Force Microscope. *Phys. Rev. Lett.* **1986**, *56* (9), 930.
(132) Güthner, P.; Dransfeld, K. Local Poling of Ferroelectric Polymers by Scanning Force Microscopy. *Appl. Phys. Lett.* **1992**, *61* (9), 1137.
(133) Seol, D.; Kim, B.; Kim, Y. Non-Piezoelectric Effects in Piezoresponse Force Microscopy. *Curr. Appl. Phys.* **2017**, *17* (5), 661–674. https://doi.org/10.1016/j.cap.2016.12.012.
(134) Calahorra, Y.; Smith, M.; Datta, A.; Benisty, H.; Kar-Narayan, S. Mapping Piezoelectric Response in Nanomaterials Using a Dedicated Non-Destructive Scanning Probe Technique. *Nanoscale* **2017**, *9*, 19290–19297. https://doi.org/10.1039/c7nr06714c.
(135) Kim, S.; Seol, D.; Lu, X.; Alexe, M.; Kim, Y. Electrostatic-Free Piezoresponse Force Microscopy. *Sci. Rep.* **2017**, *7*, 41657. https://doi.org/10.1038/srep41657.
(136) Jungk, T.; Hoffmann, Á.; Soergel, E. Quantitative Analysis of Ferroelectric Domain Imaging with Piezoresponse Force Microscopy. *Appl. Phys. Lett.* **2006**, *89* (16). https://doi.org/10.1063/1.2362984.
(137) Consonni, V.; Feuillet, G.; Gergaud, P. Plasticity Induced Texture Development in Thick Polycrystalline CdTe: Experiments and Modeling. *J. Appl. Phys.* **2008**, *103* (6). https://doi.org/10.1063/1.2895382.
(138) Zak, A. K.; Majid, W. H. A.; Abrishami, M. E.; Youse, R. X-Ray Analysis of ZnO Nanoparticles by Williamson-Hall and Size-Strain Plot Methods. *Solid State Sci.* **2011**, *13* (1), 251–256. https://doi.org/10.1016/j.solidstatesciences.2010.11.024.
(139) Mote, V. D.; Purushotham, Y.; Dole, B. N. Williamson-Hall Analysis in Estimation of Lattice Strain in Nanometer-Sized ZnO Particles. *J. Theor. Appl. Phys.* **2012**, *6* (6), 2251–7235.
(140) Zhang, B. P.; Wakatsuki, K.; Binh, N. T.; Usami, N.; Segawa, Y. Effects of Growth Temperature on the Characteristics of ZnO Epitaxial Films Deposited by Metalorganic Chemical Vapor Deposition. *Thin Solid Films* **2004**, *449* (1–2), 12–19. https://doi.org/10.1016/S0040-6090.
(141) Thompson, C. V. Structure Evolution during Processing of Polycrystalline Films. *Annu. Rev. Mater. Sci.* **2000**, *30*, 159–190.
(142) Glas, F. Critical Dimensions for the Plastic Relaxation of Strained Axial Heterostructures in Free-Standing Nanowires. *Phys. Rev. B* **2006**, *74*, 121302(R). https://doi.org/10.1103/PhysRevB.74.121302.
(143) Cuscó, R.; Alarcón-lladó, E.; Ibáñez, J.; Artús, L.; Jiménez, J.; Wang, B.; Callahan, M. J. Temperature Dependence of Raman Scattering in ZnO. *Phys. Rev. B* **2007**, *75* (16), 165202. https://doi.org/10.1103/PhysRevB.75.165202.
(144) Ferrari, A. C.; Robertson, J. Interpretation of Raman Spectra of Disordered and Amorphous Carbon. *Phys. Rev. B* **2000**, *61* (20), 14095.
(145) Munuera, C.; J.Zuniga-Perez; Rommeluere, J. F.; Sallet, V.; Triboulet, R.; Soria, F.; Munoz-Sanjose, V.; Ocal, C. Morphology of ZnO Grown by MOCVD on Sapphire Substrates. *J. Cryst. Growth* **2004**, *264* (1–3), 70–78. https://doi.org/10.1016/j.jcrysgro.2003.12.056.
(146) Guillemin, S.; Appert, E.; Roussel, H.; Parize, R.; Boudou, T.; Bremond, G.; Consonni, V. Controlling the Structural Properties of Single Step , Dip Coated ZnO Seed Layers for Growing Perfectly Aligned Nanowire Arrays. *J. Phys. Chem. C* **2015**, *119* (37), 21694–21703. https://doi.org/10.1021/acs.jpcc.5b06180.
(147) Meyer, B. K.; Alves, H.; Hofmann, D. M.; Kriegseis, W.; Forster, D.; Bertram, F.; Christen, J.; Hoffmann, A.; Straßburg, M.; Dworzak, M.; Haboeck, U.; Rodina, A. V. Bound Exciton and Donor – Acceptor Pair Recombinations in ZnO. **2004**, *260* (2), 231–260. https://doi.org/10.1002/pssb.200301962.
(148) Wagner, M. R.; Callsen, G.; Reparaz, J. S.; Schulze, J.; Kirste, R.; Cobet, M.; Ostapenko, I. A.; Rodt, S.; Nenstiel, C.; Kaiser, M.; Hoffmann, A. Bound Excitons in ZnO : Structural Defect Complexes versus Shallow Impurity Centers. **2011**, *035313*, 1–18. https://doi.org/10.1103/PhysRevB.84.035313.
(149) Lavrov, E. V; Herklotz, F.; Weber, J. Identification of Two Hydrogen Donors in ZnO. *Phys. Rev. B* **2009**, *79* (16), 165210. https://doi.org/10.1103/PhysRevB.79.165210.

(150) Heinhold, R.; Neiman, A.; Kennedy, J. V; Markwitz, A.; Reeves, R. J.; Allen, M. W. Hydrogen-Related Excitons and Their Excited-State Transitions in ZnO. *Phys. Rev. B* **2017**, *95* (5), 054120. https://doi.org/10.1103/PhysRevB.95.054120.
(151) Sieber, B.; Addad, A.; Szunerits, S.; Boukherroub, R. Stacking Faults-Induced Quenching of the UV Luminescence in ZnO. **2010**, 3033–3038. https://doi.org/10.1021/jz101267t.
(152) Yang, S.; Kuo, C. C.; Liu, W.-R.; Lin, B. H.; Hsu, H.-C.; Hsu, C.-H.; Hsieh, W. F. Photoluminescence Associated with Basal Stacking Faults in C-Plane ZnO Epitaxial Film Grown by Atomic Layer Deposition. *Appl. Phys. Lett.* **2012**, *100* (10), 101907. https://doi.org/10.1063/1.3692730.
(153) Khranovskyy, V.; Eriksson, M. O.; Radnoczi, G. Z.; Khalid, A.; Zhang, H.; Holtz, P. O.; Hultman, L.; Yakimova, R. Photoluminescence Study of Basal Plane Stacking Faults in ZnO Nanowires. *Phys. B Condens. Matter* **2014**, *439*, 50–53. https://doi.org/10.1016/j.physb.2013.12.020.
(154) Lyons, J. L.; Varley, J. B.; Steiauf, D.; Janotti, A.; Walle, C. G. Van de. First-Principles Characterization of Native- Defect-Related Optical Transitions in ZnO. *J. Appl. Phys.* **2017**, *122* (3), 035704. https://doi.org/10.1063/1.4992128.
(155) Tao, R.; Parmar, M.; Ardila, G.; Oliveira, P.; Marques, D.; Montès, L.; Mouis, M. Performance of ZnO Based Piezo-Generators under Controlled Compression. *Semicond. Sci. Technol.* **2017**, *32* (6), 064003.
(156) Consonni, V.; Sarigiannidou, E.; Appert, E.; Bocheux, A.; Guillemin, S.; Donatini, F.; Robin, I.-C.; Kioseoglou, J.; Robaut, F. Selective Area Growth of Well-Ordered ZnO Nanowire Arrays with Controllable Polarity. *ACS Nano* **2014**, *8* (5), 4761–4770.
(157) Wander, A.; Harrison, N. M. An Ab Initio Study of ZnO(10-10). *Surf. Sci.* **2000**, *457* (1–2), L342–L346.
(158) Wander, A.; Schedin, F.; Steadman, P.; Norris, A.; Mcgrath, R.; Turner, T. S.; Thornton, G.; Harrison, N. M. Stability of Polar Oxide Surfaces. *Phys. Rev. Lett.* **2001**, *86* (17), 3811. https://doi.org/10.1103/PhysRevLett.86.3811.
(159) Kim, D. S.; Gösele, U.; Zacharias, M. Surface-Diffusion Induced Growth of ZnO Nanowires. *J. Cryst. Growth* **2009**, *311* (11), 3216–3219. https://doi.org/10.1016/j.jcrysgro.2009.03.026.
(160) María de la Mata; Zamani, R. R.; Martí-Sánchez, S.; Eickho, M.; Xiong, Q.; Fontcuberta, A.; Caro, P.; Arbiol, J. The Role of Polarity in Nonplanar Semiconductor Nanostructures. *Nano Lett.* **2019**, *19* (6), 3396−3408. https://doi.org/10.1021/acs.nanolett.9b00459.
(161) Lautenschlaeger, S.; Sann, J.; Volbers, N.; Meyer, B. K. Asymmetry in the Excitonic Recombinations and Impurity Incorporation of the Two Polar Faces of Homoepitaxially Grown ZnO Films. *Phys. Rev. B* **2008**, *77* (14), 1441085. https://doi.org/10.1103/PhysRevB.77.144108.
(162) Smith, G. L.; Pulskamp, J. S.; Sanchez, L. M.; Potrepka, D. M.; Proie, R. M.; Ivanov, T. G.; Rudy, R. Q.; Nothwang, W. D.; Bedair, S. S.; Meyer, C. D.; Polcawich, R. G. PZT-Based Piezoelectric MEMS Technology. *J. Am. Ceram. Soc.* **2012**, *95* (6), 1777–1792. https://doi.org/10.1111/j.1551-2916.2012.05155.x.
(163) Zhan, K.; Su, M.; Han, H.; Xie, S. F.; Zhu, Y. K.; Wang, D.; Cheng, H. B.; Wang, X. Y. Effect of Annealing Temperature on Piezoelectric and Mechanical Properties of (Bi0.5Na0.5)TiO3–(Bi0.5K0.5)TiO3–BaTiO3 Thin Film. *Ceram. Int.* **2016**, *42* (1), 1627–1632. https://doi.org/10.1016/j.ceramint.2015.09.114.
(164) Bhagavannarayana, G.; Budakoti, G. C.; Maurya, K. K.; Kumar, B. Enhancement of Crystalline , Piezoelectric and Optical Quality of LiNbO3 Single Crystals by Post-Growth Annealing and Poling. *J. Chem. Phys.* **2005**, *282* (3–4), 394–401. https://doi.org/10.1016/j.jcrysgro.2005.05.025.
(165) Vergara, L.; Olivares, J.; Iborra, E.; Clement, M.; Sanz-Hervás, A.; Sangrador, J. Effect of Rapid Thermal Annealing on the Crystal Quality and the Piezoelectric Response of Polycrystalline AlN Films. *Thin Solid Films* **2006**, *515* (4), 1814–1818. https://doi.org/10.1016/j.tsf.2006.07.002.
(166) Richardson, J. J.; Goh, G. K. L.; Le, H. Q.; Liew, L.; Lange, F. F.; Denbaars, S. P. Thermally Induced Pore Formation in Epitaxial ZnO Films Grown from Low Temperature Aqueous

Solution. *Cryst. Growth Des.* **2011**, *11* (8), 3558–3563. https://doi.org/10.1021/cg200528e.
(167) Gritsenko, L. V; Abdullin, K. A.; Gabdullin, M. T.; Kalkozova, Z. K.; Kumekov, S. E.; Mukash, Z. O.; Sazonov, A. Y.; Terukov, E. I. Effect of Thermal Annealing on Properties of Polycrystalline ZnO Thin Films. *J. Cryst. Growth* **2017**, *457*, 164–170. https://doi.org/10.1016/j.jcrysgro.2016.07.026.
(168) Yi, G. R.; Kim, H. S.; Lee, D. H.; Kim, B.; Kim, C. K. Effect of Annealing on Performance of ZnO Thin Film Transistors. *Mol. Cryst. Liq. Cryst.* **2019**, *678* (1), 43–52. https://doi.org/10.1080/15421406.2019.1597527.
(169) Nijikovsky, B.; Richardson, J. J.; Garbrecht, M.; Denbaars, S. P.; Kaplan, W. D. Microstructure of ZnO Films Synthesized on MgAl2O4 from Low-Temperature Aqueous Solution: Growth and Post-Annealing. *J. Mater. Sci.* **2013**, *48* (4), 1614–1622. https://doi.org/10.1007/s10853-012-6918-9.
(170) Consonni, V.; Rey, G.; Roussel, H.; Bellet, D. Thickness Effects on the Texture Development of Fluorine-Doped SnO2 Thin Films : The Role of Surface and Strain Energy. *J. Appl. Phys.* **2012**, *111* (3), 033523. https://doi.org/10.1063/1.3684543.
(171) Consonni, V.; Rey, G.; Roussel, H.; Doisneau, B.; Blanquet, E.; Bellet, D. Preferential Orientation of Fluorine-Doped SnO2 Thin Films : The Effects of Growth Temperature. *Acta Mater.* **2013**, *61* (1), 22–31. https://doi.org/10.1016/j.actamat.2012.09.006.
(172) Nix, W. D.; Clemens, B. M. Crystallite Coalescence: A Mechanism for Intrinsic Tensile Stresses in Thin Films. *J. Mater. Res.* **1999**, *14* (8), 3467–3473.
(173) Floro, J. A.; Hearne, S. J.; Hunter, J. A.; Kotula, P.; Chason, E.; Seel, S. C.; Thompson, C. V. The Dynamic Competition between Stress Generation and Relaxation Mechanisms during Coalescence of Volmer – Weber Thin Films. *J. Appl. Phys.* **2001**, *89* (9), 4886. https://doi.org/10.1063/1.1352563.
(174) Jou, J.-H.; Han, M.-Y.; Cheng, D.-J. Substrate Dependent Internal Stress in Sputtered Zinc Oxide Thin Films. *J. Appl. Phys.* **1992**, *71* (9), 4333.
(175) Wright, A. F. Elastic Properties of Zinc-Blende and Wurtzite AlN, GaN, and InN. *J. Appl. Phys.* **1997**, *82* (6), 2833.
(176) Wagner, J.; Bechstedt, F. Properties of Strained Wurtzite GaN and AlN : Ab Initio Studies. *Phys. Rev. B* **2002**, *66* (11), 115202. https://doi.org/10.1103/PhysRevB.66.115202.
(177) Hong, R.; Shao, J.; He, H.; Fan, Z. Influence of Buffer Layer Thickness on the Structure and Optical Properties of ZnO Thin Films. *Appl. Surf. Sci.* **2006**, *252* (8), 2888–2893. https://doi.org/10.1016/j.apsusc.2005.04.041.
(178) Scepanovic, M.; Grujic-Brojcin, M.; Vojisavljevic, K.; Bernik, S.; Sreckovi, T. Raman Study of Structural Disorder in ZnO Nanopowders. *J. Raman Spectrosc.* **2010**, *41* (9), 914–921. https://doi.org/10.1002/jrs.2546.
(179) Tang, C.; Spencer, M. J. S.; Barnard, A. S. Activity of ZnO Polar Surfaces: An Insight from Surface Energies. *Phys. Chem. Chem. Phys.* **2014**, *16* (40), 22139–22144. https://doi.org/10.1039/c4cp03221g.
(180) Lee, J.; Wiederhorn, S. M. Effects of Polarity on Grain-Boundary Migration in ZnO. *J. Am. Ceram. Soc.* **2004**, *87* (7), 1319–1323.
(181) Lim, T.; Mirabedini, P. S.; Jung, K.; Greaney, P. A. High-Index Crystal Plane of ZnO Nanopyramidal Structures : Stabilization , Growth , and Improved Photocatalytic Performance. *Appl. Surf. Sci.* **2021**, *536*, 147326. https://doi.org/10.1016/j.apsusc.2020.147326.
(182) Saedi, A.; Rost, M. J. Thermodynamics of Deposition Flux-Dependent Intrinsic Film Stress. *Nat. Commun.* **2016**, *7*. https://doi.org/10.1038/ncomms10733.
(183) Ma, Y.; Chang, Y. C.; Yin, J. Z. Evaluation of Lattice Strain in ZnO Thin Films Based on Williamson-Hall Analysis. *J. Optoelectron. Adv. Mater.* **2019**, *21* (11–12), 702–709.
(184) DRIFT, A. van der. Evolutionary Selection, a Principle Governing Growth Orientation in Vapour-Deposited Layers. *Philips Res. Reports* **1967**, *22*, 267–288.
(185) Synhaivskyi, O.; Albertini, D.; Ga, P.; Chauveau, J.; Consonni, V.; Gautier, B.; Bremond, G. Evidence of Piezoelectric Potential and Screening Effect in Single Highly Doped ZnO:Ga and

ZnO:Al Nanowires by Advanced Scanning Probe Microscopy. *J. Phys. Chem. C* **2021**, *125* (28), 15373–15383. https://doi.org/10.1021/acs.jpcc.1c00926.

(186) Li, W.; Shi, E.; Zhong, W.; Yin, Z. Growth Mechanism and Growth Habit of Oxide Crystals. **1999**, *203* (July 1998), 186–196.

(187) Perillat-Merceroz, G.; Thierry, R.; Jouneau, P.-H.; Ferret, P.; Feuillet, G. Compared Growth Mechanisms of Zn-Polar ZnO Nanowires on O-Polar ZnO and on Sapphire. *Nanotechnology* **2012**, *23* (12), 125702. https://doi.org/10.1088/0957-4484/23/12/125702.

(188) Sallet, V.; Sartel, C.; Vilar, C.; Lusson, A.; Galtier, P. Opposite Crystal Polarities Observed in Spontaneous and Vapour-Liquid-Solid Grown ZnO Nanowires. *Appl. Phys. Lett.* **2013**, *102* (18). https://doi.org/10.1063/1.4804254.

(189) Wang, Z. L.; Kong, X. Y.; Zuo, J. M. Induced Growth of Asymmetric Nanocantilever Arrays on Polar Surfaces. *Physcial Rev. Lett.* **2003**, *91* (18), 185502. https://doi.org/10.1103/PhysRevLett.91.185502.

(190) Schuster, F.; Laumer, B.; Zamani, R. R.; Mage, C.; Morante, J. R.; Arbiol, J.; Stutzmann, M. P-GaN/n-ZnO Heterojunction Nanowires: Optoelectronic Properties and the Role of Interface Polarity. *ACS Nano* **2014**, *8* (5), 4376–4384.

(191) Gao, P. X.; Wang, Z. L. Substrate Atomic-Termination-Induced Anisotropic Growth of ZnO Nanowires/Nanorods by the VLS Process. *J. Phys. Chem. B* **2004**, *108* (23), 7534–7537.

(192) Ellmer, K. Past Achievements and Future Challenges in the Development of Optically Transparent Electrodes. *Nat. Photonics* **2012**, *6*, 809–817. https://doi.org/10.1038/NPHOTON.2012.282.

(193) Kawajiri, K.; Tahara, K.; Uemiya, S. Lifecycle Assessment of Critical Material Substitution: Indium Tin Oxide and Aluminum Zinc Oxide in Transparent Electrodes. *Resour. Environ. Sustain.* **2022**, *7* (April 2021), 100047. https://doi.org/10.1016/j.resenv.2022.100047.

(194) Lim, C. H.; Han, J.; Cho, H.; Kang, M. Studies on the Toxicity and Distribution of Indium Compounds According to Particle Size in Sprague-Dawley Rats. *Toxicalogical Reseach* **2014**, *30* (1), 55–63.

(195) Badding, M. A.; Fix, N. R.; Orandle, M. S.; Barger, M. W.; Dunnick, K. M.; Cummings, K. J.; Leonard, S. S. Pulmonary Toxicity of Indium-Tin Oxide Production Facility Particles in Rats. *J. Appl. Toxicol.* **2015**, *36* (4), 618–626. https://doi.org/10.1002/jat.3253.

(196) Sarma, B.; Barman, D.; Sarma, B. K. AZO (Al:ZnO) Thin Films with High Figure of Merit as Stable Indium Free Transparent Conducting Oxide. *Appl. Surf. Sci.* **2019**, *479*, 786–795.

(197) Tuan, A.; Pham, T.; Minh, N.; Kieu, O.; Le, T.; Hoang, D. Van; Huu, T.; Bach, T.; Cao, V. Journal of Science : Advanced Materials and Devices High-Mobility Sputtered F-Doped ZnO Films as Good-Performance Transparent-Electrode Layers. *J. Sci. Adv. Mater. Devices* **2021**, *6* (3), 446–452. https://doi.org/10.1016/j.jsamd.2021.05.004.

(198) Way, A.; Luke, J.; Evans, A. D.; Li, Z.; Kim, J.-S.; Durrant, J. R.; Lee, H. K. H.; Tsoi, W. C. Fluorine Doped Tin Oxide as an Alternative of Indium Tin Oxide for Bottom Electrode of Semi-Transparent Organic Photovoltaic Devices. *AIP Adv.* **2019**, *9* (8), 085220. https://doi.org/10.1063/1.5104333.

(199) Madeira, A.; Papanastasiou, D. T.; Toupance, T.; Servant, L.; Bellet, D.; Goldthorpe, I. A. Rapid Synthesis of Ultra-Long Silver Nanowires for High Performance Transparent Electrodes. *Nanoscale Adv.* **2020**, *2* (9), 3804. https://doi.org/10.1039/d0na00392a.

(200) Rana, K.; Singh, J.; Ahn, J. A Graphene-Based Transparent Electrode for Use in Fl Exible Optoelectronic Devices. *J. Mater. Chem. C* **2014**, *2* (15), 2646. https://doi.org/10.1039/c3tc32264e.

(201) Mereu, R. A.; Marchionna, S.; Donne, A. Le; Ciontea, L.; Binetti, S.; Acciarri, M. Optical and Electrical Studies of Transparent Conductive AZO and ITO Sputtered Thin Films for CIGS Photovoltaics. *Phys. Status Solidi C* **2014**, *11* (9), 1464–1467. https://doi.org/10.1002/pssc.201300631.

(202) Yu, W.; Han, D.; Dong, J.; Cong, Y.; Cui, G.; Wang, Y.; Zhang, S. AZO Thin Film Transistor Performance Enhancement by Capping an Aluminum Layer. *IEEE Trans. Electron Devices* **2017**,

64 (5), 2228–2232.
(203) Liu, H.; Liu, Y.; Xiong, P.; Chen, P.; Li, H.; Hou, J.; Kang, B.; Duan, Y. Aluminum-Doped Zinc Oxide Transparent Electrode Prepared by Atomic Layer Deposition for Organic Light Emitting Devices. *IEEE Trans. Nanotechnol.* **2017**, *16* (4), 634–638.
(204) Hjiri, M.; Mir, L. El; Leonardi, S. G.; Pistone, A.; Mavilia, L.; Neri, G. Sensors and Actuators B : Chemical Al-Doped ZnO for Highly Sensitive CO Gas Sensors. *Sensors Actuators B. Chem.* **2014**, *196*, 413–420. https://doi.org/10.1016/j.snb.2014.01.068.
(205) Justeau, C.; Tlemcani, T. S.; Poulin-vittrant, G.; Nadaud, K.; Alquier, D. A Comparative Study on the Effects of Au, ZnO and AZO Seed Layers on the Performance of ZnO. *Materials (Basel).* **2019**, *12* (16), 2511.
(206) Pung, S.-Y.; Choy, K.-L.; Hou, X.; Shan, C. Preferential Growth of ZnO Thin Films by the Atomic Layer Deposition Technique. *Nanotechnology* **2008**, *19* (43), 435609. https://doi.org/10.1088/0957-4484/19/43/435609.
(207) Kim, J. Y.; Choi, Y.-J.; Park, H.-H.; Golledge, S.; Johnson, D. C. Effective Atomic Layer Deposition Procedure for Al-Dopant Distribution in ZnO Thin Films. *J. Vac. Sci. Technol. A* **2010**, *28* (January 2010), 1111. https://doi.org/10.1116/1.3460905.
(208) Wu, Y.; Cao, F.; Ji, X. Optical and Electrical Properties of Al-Doped ZnO Thin Films by Atomic Layer Deposition. *J. Mater. Sci. Mater. Electron.* **2020**, *31* (20), 17365–17374. https://doi.org/10.1007/s10854-020-04292-9.
(209) Geng, Y.; Guo, L.; Xu, S.; Sun, Q.; Ding, S.; Lu, H.; Zhang, D. W. Influence of Al Doping on the Properties of ZnO Thin Films Grown by Atomic Layer Deposition. *J. Phys. Chem. C* **2011**, *115* (25), 12317–12321.
(210) Dasgupta, N. P.; Neubert, S.; Lee, W.; Trejo, O.; Lee, J.; Prinz, F. B. Atomic Layer Deposition of Al-Doped ZnO Films : Effect of Grain Orientation on Conductivity. *Chem. Mater.* **2010**, *22* (16), 4769–4775. https://doi.org/10.1021/cm101227h.
(211) Park, S. K.; Lee, Y. E. Controlling Preferred Orientation of ZnO Thin Films by Atomic Layer Deposition. *J. Mater. Sci.* **2004**, *39*, 2195–2197.
(212) Dhakal, T.; Vanhart, D.; Christian, R.; Nandur, A.; Sharma, A.; Westgate, C. R. Growth Morphology and Electrical/Optical Properties of Al-Doped ZnO Thin Films Grown by Atomic Layer Deposition Films Grown by Atomic Layer Deposition. *J. Vac. Sci. Technol. A* **2012**, *30* (2), 021202.
(213) Banerjee, P.; Lee, W.-J.; Bae, K.-R.; Lee, S. B.; Rubloff, G. W. Structural, Electrical, and Optical Properties of Atomic Layer Deposition Al-Doped ZnO Films. *J. Appl. Phys.* **2010**, *108* (4), 043504. https://doi.org/10.1063/1.3466987.
(214) Luka, G.; Wachnicki, L.; Witkowski, B. S.; Krajewski, T. A.; Jakiela, R.; Guziewicz, E.; Godlewski, M. The Uniformity of Al Distribution in Aluminum-Doped Zinc Oxide Films Grown by Atomic Layer Deposition. *Mater. Sci. Eng. B* **2011**, *176* (3), 237–241. https://doi.org/10.1016/j.mseb.2010.11.014.
(215) Luka, G.; Krajewski, T. A.; Witkowski, B. S.; Wisz, G.; Virt, I. S.; Guziewicz, E.; Godlewski, M. Aluminum-Doped Zinc Oxide Films Grown by Atomic Layer Deposition for Transparent Electrode Applications. *J. Mater. Sci. Mater. Electron.* **2011**, *22*, 1810–1815. https://doi.org/10.1007/s10854-011-0367-0.
(216) Nguyen, V. H.; Resende, J.; Jiménez, C.; Deschanvres, J.-L.; Carroy, P.; Muñoz, D.; Bellet, D.; Muñoz-Rojas, D. Deposition of ZnO Based Thin Films by Atmospheric Pressure Spatial Atomic Layer Deposition for Application in Solar Cells. *J. Renew. Sustain. Energy* **2017**, *9* (2), 021203. https://doi.org/10.1063/1.4979822.
(217) Seweryn, A.; Pietruszka, R.; Witkowski, B. S.; Wierzbicka, A.; Jakiela, R.; Sybilski, P.; Godlewski, M. Structural and Electrical Parameters of ZnO Thin Films Grown by ALD with Either Water or Ozone as Oxygen Precursor. *Cryst. 2019* **2019**, *9* (11), 554.
(218) Mishra, S.; Przezdziecka, E.; Wozniak, W.; Adhikari, A.; Jakiela, R.; Paszkowicz, W.; Sulich, A.; Ozga, M.; Kopalko, K.; Guziewicz, E. Structural Properties of Thin ZnO Films Deposited by ALD under O-Rich and Zn-Rich Growth Conditions and Their. *Materials (Basel).* **2021**, *14* (14), 4048.

(219) Xia, B.; Ganem, J. J.; Briand, E.; Steydli, S.; Tancrez, H.; Vickridge, I. The Carbon and Hydrogen Contents in ALD-Grown ZnO Films Define a Narrow ALD Temperature Window. *Vacuum* **2021**, *190*, 110289. https://doi.org/10.1016/j.vacuum.2021.110289.
(220) Wang, A.; Chen, T.; Lu, S.; Wu, Z.; Li, Y.; Chen, H.; Wang, Y. Effects of Doping and Annealing on Properties of ZnO Films Grown by Atomic Layer Deposition. *Nanoscale Res. Lett.* **2015**, *10*, 75. https://doi.org/10.1186/s11671-015-0801-y.
(221) Lin, S.; Huang, J.; Sajgalik, P. The Properties of Heavily Al-Doped ZnO Films before and after Annealing in the Different Atmosphere. *Surf. Coat. Technol.* **2004**, *185* (2–3), 254–263. https://doi.org/10.1016/j.surfcoat.2003.12.007.
(222) Tonny, K. N.; Rafique, R.; Sharmin, A.; Bashar, M. S.; Mahmood, Z. H. Electrical, Optical and Structural Properties of Transparent Conducting Al Doped ZnO (AZO) Deposited by Sol-Gel Spin Coating. *AIP Adv.* **2018**, *8* (6), 065307. https://doi.org/10.1063/1.5023020.
(223) Joseph, B.; Manoj, P. K.; Vaidyan, V. K. Studies on the Structural , Electrical and Optical Properties of Al-Doped ZnO Thin Films Prepared by Chemical Spray Deposition. *Ceram. Int.* **2006**, *32*, 487–493. https://doi.org/10.1016/j.ceramint.2005.03.029.
(224) Jeong, J.; Shin, H.; Choi, K.; Kim, H. Flexible Al-Doped ZnO Films Grown on PET Substrates Using Linear Facing Target Sputtering for Flexible OLEDs. *J. Phys. D. Appl. Phys.* **2010**, *43*, 465403. https://doi.org/10.1088/0022-3727/43/46/465403.
(225) Chen, Z.; Li, W.; Li, R.; Zhang, Y.; Xu, G.; Cheng, H. Fabrication of Highly Transparent and Conductive Indium − Tin Oxide Thin Films with a High Figure of Merit via Solution Processing. *Langmuir* **2013**, *29* (45), 13836−13842.
(226) Khrypunova, A.; Kudii, D.; Khrypunova, I. The Optical and Electrical Properties ITO Thin Film. *2018 IEEE 3rd Int. Conf. Intell. Energy Power Syst.* **2018**, 229–234.
(227) Park, S.; Ikegami, T.; Ebihara, K. Investigation of Transparent Conductive Oxide Al-Doped ZnO Films Produced by Pulsed Laser Deposition. *Jpn. J. Appl. Phys.* **2005**, *44* (11), 8027–8031. https://doi.org/10.1143/JJAP.44.8027.
(228) Ayinde, S. A.; Fasakin, O.; Olofinjana, B.; Adedeji, A. V; Oyedare, P. O.; Eleruja, M. A.; Ajayi, E. O. B. Optical, Structural and Electrical Properties of Aluminum Doped Zinc Oxide Thin Films by MOCVD Technique. *J. Electron. Mater.* **2019**, *48*, 3655–3661. https://doi.org/10.1007/s11664-019-07123-8.
(229) Gong, S. C.; Choi, Y.-J.; Kim, H.; Park, C.-S.; Park, H.-H.; Jang, J. G.; Chang, H. J.; Yeom, G. Y. Aluminum-Doped Zinc Oxide Formed by Atomic Layer Deposition for Use as Anodes in Organic Light Emitting Diodes. *J. Vac. Sci. Technol. A* **2013**, *31* (1), 01A101. https://doi.org/10.1116/1.4738749.
(230) Li, G.; Zhao, X.; Jia, X.; Li, S.; He, Y. Characterization of Impact Ionization Coefficient of ZnO Based on a P-Si/i-ZnO/n-AZO Avalanche Photodiode. *Micromachines* **2020**, *11* (8), 740.

Sommaire de la thèse

De nos jours, « l'internet des objets » (IoT) est devenu un élément important dans notre vie quotidienne. De nombreux objets physiques tels que des capteurs, des actionneurs et des dispositifs électroniques de tous les jours (les smartphones, les ordinateurs, les contrôleurs dans les voitures, etc.) sont connectés à l'internet, ce qui permet la collecte, le traitement et la transmission automatiques de données ainsi que des communications entre les objets et les humaines. Le développement de nouvelles technologies et de dispositifs IoT nécessite l'utilisation de matériaux comprenant des éléments rares ou toxiques (Gallium (Ga), Indium (In), Plomb (Pb), etc.). La consommation continue de ces éléments critiques peut entraîner un risque d'approvisionnement ainsi que d'autres problèmes environnementaux et économiques dans un avenir proche. Il est donc nécessaire de trouver d'autres moyens de réduire ou de remplacer l'utilisation des éléments critiques pour les applications IoT.

Dans ce contexte, le projet « NanoElectroniquE Durable (NEED) pour IoT » est proposé pour répondre à ce problème critique. Ce projet vise à développer des méthodologies et des technologies pour le développement durable des dispositifs micro-nano-électroniques. Les objectifs sont d'identifier les risques de la chaîne d'approvisionnement des dispositifs émergents IoT, de réduire ou de remplacer la consommation d'éléments critiques par des matériaux plus abondants ou en utilisant des conceptions plus efficaces, et d'intégrer de nouvelles technologies et de nouveaux matériaux aux chaînes de production et aux dispositifs. Concernant la technologie des matériaux, le défi consiste à trouver des matériaux alternatifs non critiques qui ont également la même fonction avec une efficacité élevée que le matériau remplacé. Ces matériaux doivent également être compatibles avec une production industrielle à grande échelle. Les domaines d'application comprennent les capteurs, les mémoires, l'optoélectronique, la spintronique et la piézoélectricité. Ma thèse fait partie de ce projet, qui participe au développement d'un matériau durable pour les applications piézoélectriques.

Les matériaux piézoélectriques sont présents dans de nombreux types de dispositifs. Ils sont utilisés pour les capteurs de pression, les actionneurs ou les composants des dispositifs à ondes acoustiques de surface (SAW) qui sont utilisés pour les outils de mesure précis et les systèmes automatiques dans la recherche et la production industrielle. Ils sont utilisés comme transducteurs à ultrasons pour la navigation ou dans les traitements médicaux. Dans la vie quotidienne, nous les trouvons dans les microphones, les écouteurs, les filtres de fréquence des téléphones portables, les alarmes, les imprimantes à jet d'encre, les briquets à allumage, etc. Ils ont également le potentiel d'être une source d'énergie pour les appareils mobiles grâce à leur capacité à récolter l'énergie mécanique du milieu environnant et à la convertir en électricité. Ainsi, la demande de matériaux piézoélectriques continuera sans aucun doute à croître à l'avenir. L'un des matériaux les plus couramment utilisés pour les applications piézoélectriques est le zirconate-titanate de plomb (PZT) en raison de ses performances piézoélectriques exceptionnelles. Cependant, l'élément plomb (Pb) contenu dans ce matériau est extrêmement toxique pour l'environnement et les humains. L'oxyde de plomb (PbO) et le plomb contenu dans les produits PZT peuvent être volatils et libérés dans l'environnement au cours de leur cycle de vie, d'où le plomb peut pénétrer dans le corps humain et

causer de graves dommages. Il est donc nécessaire de trouver un autre matériau piézoélectrique qui puisse remplacer le PZT pour le développement durable des technologies avancées.

D'autre part, l'oxyde de zinc (ZnO) est un candidat potentiel pour remplacer ce matériau piézoélectrique. Ce composé semi-conducteur présente des avantages, notamment celui d'être un matériau abondant et biocompatible qui possède également des propriétés piézoélectriques grâce à sa structure wurtzite. En fait, ce matériau n'est pas nouveau. C'est un matériau multifonctionnel qui a été produit et présenté dans de nombreuses applications dont les caoutchoucs, les produits cosmétiques, les traitements antibactériens, etc. Ses propriétés ont également été étudiées et utilisées dans des applications électroniques et optoélectroniques. L'étude des propriétés piézoélectriques du ZnO est encore assez récente et est devenue récemment une solution intéressante pour le développement durable. Comparé au PZT, le coefficient piézoélectrique du ZnO est encore assez faible, mais il peut être amélioré. Le principal défi du ZnO pour son utilisation dans les dispositifs piézoélectriques est son dopage résiduel élevé de type n. Quelles que soient les méthodes de fabrication, la structure du ZnO contient une grande quantité d'électrons libres. Lorsque le ZnO est polarisé, ces électrons libres peuvent se déplacer vers le pôle positif, faisant écran au potentiel piézoélectrique et réduisant l'efficacité piézoélectrique. Il est donc nécessaire d'éliminer ou de compenser ces électrons libres afin d'augmenter l'efficacité piézoélectrique du ZnO. Les autres défis, moins mentionnés mais également essentiels pour la performance piézoélectrique, sont l'exigence d'une bonne orientation et d'une polarité uniforme. Le caractère aléatoire de l'orientation et des domaines polaires peut conduire à l'annulation des signaux piézoélectriques entre les domaines, entraînant la diminution voire la disparition du potentiel piézoélectrique. Ces propriétés du ZnO sont fortement influencées par son procédé de fabrication. Ainsi, ses performances piézoélectriques peuvent être considérablement améliorées en adaptant sa formation à l'aide de conditions de fabrication appropriées.

Parmi les différentes techniques de fabrication, le dépôt chimique en phase vapeur par injection de liquide pulsé (PLI-MOCVD) a été choisi pour faire croître les structures en ZnO. Cette technique permet de faire croître le ZnO rapidement, sur de grandes surfaces, sans nécessiter d'ultravide, tout en obtenant une qualité structurelle élevée, ce qui la rend compatible avec une production à l'échelle industrielle. Il s'agit également d'un processus complexe qui offre de nombreux paramètres contrôlables tels que la température de croissance, les débits, la pression, les dopants et les substrats, ce qui permet de modifier largement les propriétés du ZnO afin de l'adapter à différentes applications. Il y a nombreuses recherches sur l'effet des paramètres MOCVD sur la croissance du ZnO ont été réalisées, la plupart des travaux se sont concentrés sur les propriétés structurelles, optiques et électriques du ZnO. Cependant, il manquait des informations sur les propriétés piézoélectriques, en particulier, le coefficient piézoélectrique et la polarité. Selon la littérature, les propriétés piézoélectriques ont de fortes corrélations avec d'autres propriétés, ce qui suggère que les propriétés piézoélectriques peuvent également être largement modifiées lorsque les conditions de croissance sont variées. En d'autres termes, il est possible d'améliorer le coefficient piézoélectrique du ZnO en ajustant les paramètres de croissance.

Dans le cadre du projet NEED, cette thèse vise à développer un dispositif piézoélectrique utilisant uniquement des matériaux écologiques tout en garantissant des performances comparables aux dispositifs PZT existants et sa capacité à s'intégrer dans la production industrielle. Pour cela, le matériau durable ZnO est choisi pour le composant piézoélectrique. La technique PLI-MOCVD est choisie pour la croissance du ZnO car elle a non seulement le potentiel d'améliorer les propriétés piézoélectriques du ZnO mais elle est également adaptée à la production à grande échelle dans l'industrie. Le matériau compatible pour l'électrode du dispositif sera également soigneusement sélectionné en tenant compte de la criticité des matières premières.

Puisque la compréhension et le contrôle des conditions de croissance PLI-MOCVD est le point clé pour améliorer les performances piézoélectriques du ZnO, l'objectif principal de ma thèse est d'étudier l'influence de ces conditions de croissance sur les propriétés du ZnO. Différents paramètres PLI-MOCVD sont systématiquement variés et étudiés, à savoir la température de croissance, les débits des précurseurs O- et Zn- ainsi que leur rapport de débit molaire O_2/DEZn, et les substrats. Les propriétés structurelles du ZnO sont analysées par microscopie électronique à balayage à émission de champ (FE-SEM/MEB), diffraction des rayons X (XRD), spectroscopie de diffusion Raman, microscopie électronique à transmission (TEM). Les caractérisations optiques sont effectuées en utilisant la cathodoluminescence (CL) et la spectrophotométrie Ultraviolet-Visible-Près Infrarouge (UV-Vis-NIR). La résistivité, la densité et la mobilité de charge sont mesurées par la méthode de mesure de la ligne de transmission (TLM) et la mesure de l'effet Hall. Enfin, les propriétés piézoélectriques sont caractérisées par la microscopie à force de réponse piézoélectrique (PFM). La PFM est un outil puissant qui permet de cartographier simultanément la topographie et les réponses piézoélectriques. En analysant soigneusement l'évolution des propriétés piézoélectriques du ZnO (i.e. le coefficient piézoélectrique et la polarité) en fonction des conditions de fabrication, ainsi que ses corrélations avec d'autres propriétés structurelles et électriques, la méthode permettant d'améliorer l'efficacité piézoélectrique du ZnO peut être réalisée.

Dans la première expérience de cette thèse, l'effet de la température de croissance sur les propriétés du ZnO a été étudié. Les substrats de Si de type p fortement dopés ont été utilisés comme électrodes inférieure pour la mesure de la PFM. En augmentant la température de 400 à 750 °C, les images MEB montrent que la morphologie du ZnO s'est transformée d'une couche mince à les nanofils verticaux. L'analyse structurelle par XRD et spectres Raman indique la structure wurtzite des couches minces et des nanofils de ZnO avec la direction de croissance préférentielle le long de l'axe *c*. Avec la transition du couche mince aux nanofils, l'orientation de l'axe *c* est améliorée et les contraintes internes sont relâchées. En analysant les images TEM, la croissance des nanofils de ZnO sur le substrat de Si peut être décrite comme un processus d'auto-assemblage: La forte désorption des atomes de Zn et de O combinée à la croissance hautement orientée selon l'axe *c* à haute température a conduit à la nucléation et à la formation d'îles isolés, sur lesquels l'orientation selon l'axe *c* prévaut sur les autres directions. Grâce à la croissance hautement orientée selon l'axe *c* et à l'augmentation de la longueur de diffusion des atomes à haute température de croissance, l'allongement des nanofils s'est poursuivi sur ces îles dans la direction verticale normale au substrat. L'analyse structurelle et optique a également impliqué la présence de défauts à l'intérieur des structures de ZnO, tels que des impuretés de carbone et aluminium ou des défauts d'empilement,

qui pourraient affecter les performances électriques et piézoélectriques du ZnO. Une comparaison directe des réponses piézoélectriques des couches minces et des nanofils de même épaisseur/longueur a également été réalisée à l'aide du PFM, montrant que le coefficient piézoélectrique sur les nanofils verticaux est plus élevé que sur les couches minces. De plus, les nanofils présentent également une uniformité de polarité Zn alors que la couche mince présente des domaines de polarité Zn- et O-. Ces résultats montrent que la croissance PLI-MOCVD à haute température peut conduire à la formation des nanofils de ZnO avec de meilleures performances piézoélectriques par rapport à son homologue en couche mince.

Après l'étude de la croissance à température, l'effet du post-recuit à différentes températures sur les propriétés du ZnO a également été étudié. Les couches minces développées à 500 °C ont été recuits sous atmosphère d'O_2 à des températures allant de 600 à 1000 °C, entraînant la cristallisation. Comme pour la température de croissance, l'orientation de l'axe *c* et la cristallinité sont améliorées lorsque la température de recuit est élevée. Les impuretés de carbone provenant du processus PLI-MOCVD sont également éliminées après le recuit à 800 °C ou plus. La résistivité de la couche mince de ZnO augmente également avec la température de recuit. En conséquence, le coefficient piézoélectrique moyen sur le domaine polaire Zn est augmenté de 1.8 pm/V dans la couche mince obtenue par croissance à 2.7 pm/V dans les couches minces recuites à 800 °C ou plus. L'augmentation du coefficient piézoélectrique après recuit peut être due à l'amélioration de l'orientation structurelle le long de l'axe *c* polaire et à la diminution de l'effet d'écran causé par les porteurs de charges libres qui réduisent le potentiel piézoélectrique. Bien que le coefficient piézoélectrique de couches minces recuites soit toujours inférieur à celui des nanofils (4.4 pm/V) obtenues par croissance dans l'expérience précédente, ce résultat montre la possibilité d'augmenter encore le coefficient piézoélectrique des couches minces de ZnO après la croissance en utilisant un processus de post-recuit. Fait intéressant, les images PFM révèlent qu'il y a un changement dans les domaines polaires piézoélectriques sur la couche mince de ZnO avec le processus de grossissement des grains et de croissance après le recuit. Le recuit à 600 °C conduit au développement de grains polaires O en raison de sa plus faible énergie, mais les grains polaires Zn prédominent à une température de recuit plus élevée grâce à sa plus grande mobilité aux limites du grain. Cela montre à nouveau que la polarité Zn est plus stable que la polarité O à haute température. Le post-recuit sous atmosphère O_2 à haute température améliore non seulement le coefficient piézoélectrique mais aussi l'uniformité de la polarité Zn du couche mince de ZnO.

Sur la base de ces résultats, l'étude de l'effet des débits de précurseurs sur les propriétés du ZnO a été réalisée. D'abord, les débits d'O_2 et de DEZn ont été variés séquentiellement tandis que la température de croissance était maintenue à 500 °C. Les résultats montrent que tous les dépôts de ZnO sont des couches minces indépendamment des conditions de débit. Le temps de croissance a été ajusté afin d'obtenir des couches minces de même épaisseur, de sorte que l'influence de l'épaisseur de la couche mince est découplée de cette étude. L'évolution du taux de croissance avec les conditions de débit indique que la croissance du ZnO est limitée par le réactif Zn. Les images MEB des couches minces présentent différentes morphologies, mettant en évidence l'impact des conditions de débit sur le processus de croissance du ZnO. La XRD montre que tous les couches

minces ont une structure wurtzite avec une bonne orientation de l'axe *c*. Cependant, les images PFM ont révélé que certaines couches minces ont une croissance préférentielle dans la direction de l'axe c^+ (polarité Zn), tandis que d'autres couches minces ont une croissance préférentielle dans la direction de l'axe c^- (polarité O). Contrairement aux études précédentes sur l'effet de la température, la couche mince avec une prédominance de polarité O a été formée dans certaines conditions de débit, ce qui indique la possibilité de passer de la polarité Zn à la polarité O du film mince de ZnO en contrôlant les paramètres de croissance. Ce changement de polarité avec les conditions de débit peut être attribué à la variation du potentiel chimique de l'oxygène pendant le processus de croissance PLI-MOCVD, influençant les énergies de surface des plans cristallins de ZnO ainsi que ses directions de croissance. L'analyse des spectres Raman montre que le rapport atomique O/Zn dans la composition de la couche mince de ZnO est fortement corrélé au rapport de débit O_2/DEZn, ce qui implique à nouveau l'effet du potentiel chimique de l'oxygène dans l'environnement de croissance. De plus, les résultats des caractérisations structurelles, électriques et piézoélectriques expriment également les fortes corrélations de ces propriétés. En comparant les images de réponse piézoélectrique avec la topographie et l'image de morphologie, il est révélé que les grains polaires de Zn ont une forme hexagonale ou ronde, tandis que les grains polaires de O sont composés de grands amas de forme irrégulière comprenant de nombreux grains plus petits. D'autres comparaisons de la mesure PFM avec la XRD et la résistivité montrent également qu'il existe des différences dans le mécanisme de croissance, l'orientation structurelle, les défauts microstructures et la résistivité entre les deux polarités. En particulier, il est suggéré que les domaines de polarité O pourraient contenir plus d'impuretés donneuses qui font écran au potentiel piézoélectrique, par rapport aux domaines de polarité Zn. Ceci est confirmé par la résistivité plus faible de la couche mince prédominant de polarité O et la réponse d'amplitude piézoélectrique plus faible sur les domaines de polarité O indépendamment des conditions de débit. Néanmoins, ces résultats montrent la grande capacité du système PLI-MOCVD à régler la polarité de la croissance du ZnO ainsi que ses autres propriétés. Le coefficient piézoélectrique plus élevé sur les domaines polaires Zn par rapport aux domaines polaires O montre que la structure ZnO avec une uniformité polaire Zn est plus favorable pour une efficacité piézoélectrique plus élevée.

Ensuite, l'effet des débits d'O_2 et de DEZn sur la croissance de ZnO a été étudié avec la température de croissance maintenue à 700 °C. A cette température, toutes les croissances aboutissent à la formation des nanofils verticaux de ZnO indépendamment des conditions de débit. De plus, les résultats de la PFM montrent que tous ces nanofils ont une polarité Zn, ce qui est différent des croissances de couches minces à 500 °C. Cela indique à nouveau la croissance préférentielle le long de la direction c^+ à haute température. Les nanofils de ZnO polaires au Zn ont également été développés sur les substrats de ZnO polaires au Zn et au O identifiés, vérifiant que les nanofils développés par notre procédé PLI-MOCVD sont limités à la polarité Zn. Malgré cela, les nanofils de ZnO avec une polarité Zn uniforme est favorable aux applications piézoélectriques. De plus, le coefficient piézoélectrique des nanofils montre une forte corrélation avec leur géométrie. Sur les nanofils de longueur inférieure à 800 nm, le coefficient piézoélectrique est faible, quel que soit le diamètre, en raison de la structure orientée vers l'axe *c* inférieur. Parmi les nanofils de plus grande et longueur, le coefficient piézoélectrique est plus élevé sur les nanofils de diamètre inférieur à 65 nm

grâce à l'épuisement plus efficace des électrons libres sur la paroi latérale du nanofil. Néanmoins, les nanofils développés à 700 °C ont des coefficients piézoélectriques plus élevés (2.2 - 3.8 pm/V) comparés à ceux des couches minces de ZnO (1.6 - 2.2 pm/V) développés avec le même procédé PLI-MOCVD ainsi que les mêmes conditions de croissance. Ceci indique à nouveau l'efficacité piézoélectrique supérieure des nanofils de ZnO par rapport aux couches minces.

Enfin, la possibilité d'utiliser une couche mince d'AZO obtenu par le procédé ALD comme électrode inférieure a été étudiée. La concentration de dopant Al a été modifiée pendant la croissance ALD, ce qui non seulement change les propriétés structurelles et électriques des couches minces d'AZO, mais affecte également la croissance suivante de nanofils de ZnO par le processus PLI-MOCVD. Différentes morphologies d'AZO ainsi qu'une grande variation de l'orientation structurelle ont été observées lorsque la concentration de dopant Al est modifiée. La déformation résiduelle de la couche mince d'AZO augmente avec le dopant Al, ce qui implique l'incorporation d'atomes d'Al dans la structure de ZnO qui provoque la distorsion du réseau structurel du matériau. Simultanément, la densité et la mobilité des porteurs de charge ainsi que la résistivité varient également avec la concentration du dopant Al. En ajoutant une quantité suffisante de dopant Al, l'orientation de l'axe *c* de la couche mince d'AZO est améliorée et sa conductivité est également augmenté. Cependant, un excès de dopant Al entraîne une dégradation de la cristallinité et de la conductivité de la couche mince d'AZO. En tant que plateforme de croissance, l'orientation de la couche mince d'AZO a affecté la direction de croissance des nanofils de ZnO puisque les réseaux structurels d'AZO et de ZnO ont une relation épitaxie. La croissance de ZnO sur une couche mince d'AZO fortement orienté *c* conduit à la formation les nanofils de ZnO bien aligné verticalement, qui est presque aussi bon que les nanofils formés sur des substrats de ZnO monocristallin. Par contre, la croissance sur une couche mince d'AZO mal orienté entraîne les nanofils de ZnO incliné de manière aléatoire. Les nanofils de ZnO avec un bon alignement vertical présentent une amplitude piézoélectrique plus uniforme. En revanche, les nanofils de ZnO incliné de manière aléatoire présente une large distribution de la réponse piézoélectrique, dans laquelle l'amplitude s'étend vers une valeur plus faible en raison de l'inclinaison des nanofils, ce qui entraîne une diminution de l'efficacité piézoélectrique moyenne. Fait intéressant, une comparaison avec le coefficient piézoélectrique des nanofils de ZnO formés directement sur le substrat de Si fortement dopé montre que les nanofils de ZnO formés sur les couches minces d'AZO présentent des valeurs plus élevées. Ceci peut être attribué à l'effet de l'interface couch mince AZO/nanofil de ZnO, qui interfère avec l'effet d'écran qui conduit à l'augmentation de l'efficacité piézoélectrique. Le coefficient piézoélectrique moyen le plus élevé de 4.7 pm/V est obtenu sur ces nanofils de ZnO formés sur le couche mince d'AZO. Ces résultats montrent le fort potentiel de l'utilisation des couches minces d'AZO comme matériau écologique et efficace pour l'électrode dans les dispositifs piézoélectriques. De plus, les couches minces d'AZO et les nanofils de ZnO ont également une transmittance élevée dans la région de la lumière visible, montrant qu'ils sont également de bons candidats pour les dispositifs optoélectroniques.

En conclusion, les croissances des couches minces et de nanofils de ZnO en utilisant le procédé PLI-MOCVD avec différents paramètres ont été démontrées. En utilisant différentes techniques de caractérisation, les propriétés structurelles, électriques et piézoélectriques du ZnO

affectées par les conditions de croissance sont étudiées. Les fortes corrélations entre les propriétés sont également révélées. Les résultats montrent une grande flexibilité du PLI-MOCVD pour modifier les propriétés du ZnO. Les nanofils de ZnO présentant un coefficient piézoélectrique élevé et une polarité uniforme formés dans des conditions de croissance appropriées constituent un matériau durable prometteur pour les applications piézoélectriques.